MSc. Thesis

Advantages of a supersonic split line nozzle over a submerged movable nozzle

S. Ravnan

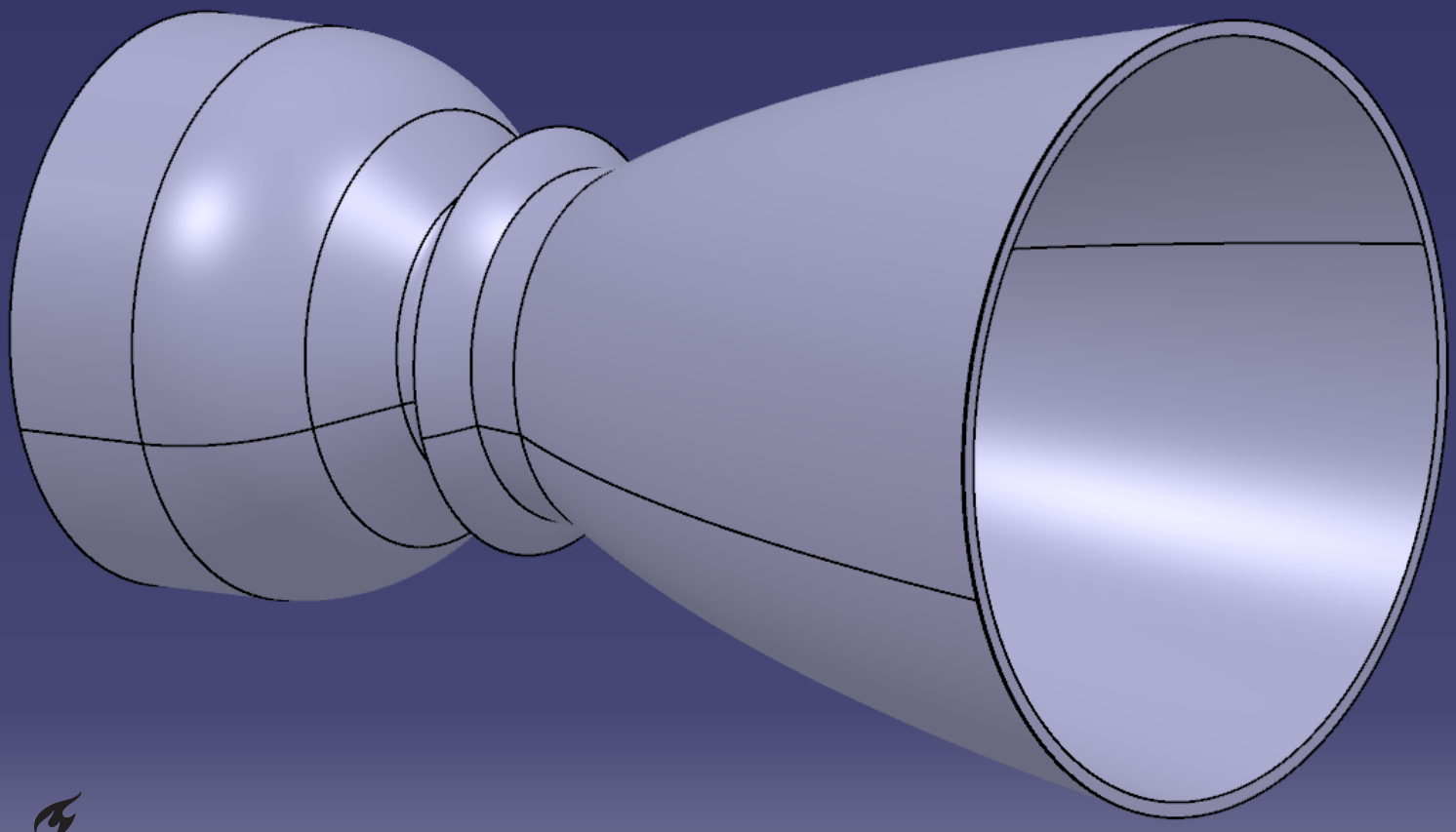

TU Delft

MSc. Thesis

Advantages of a supersonic split line nozzle over a submerged movable nozzle

by

S. Ravnan

to obtain the degree of Master of Science
at the Delft University of Technology,
to be defended publicly on 11 of March 2021 at 09:00

Student number:	4159160	
Project duration:	April, 2020 – March, 2021	
Thesis committee:	Ir. B. T. C. Zandbergen	TU Delft, Supervisor
	Prof. dr. E. K. A. Gill	TU Delft, Committee chair
	Dr. ir. A. H. van Zuijlen	TU Delft, Committee examiner
	Dr. M. G. Faenza	Nammo Raufoss, External supervisor

An electronic version of this thesis is available at http://repository.tudelft.nl/.

TU Delft

Preface

This MSc thesis presents the work that has been done in order to complete my Master of Science education in the field of Aerospace Engineering at the department of Space Systems Engineering at Delft University of Technology.
This work represents the final step of my education. The journey to this point has not been easy and I have had many ups and downs. However, it has been a long time coming.
I would like to thank Barry, my supervisor from the TU Delft, for all his support and patience during this project, as well as the excellent answers to my questions. I would like to thank Martina, from Nammo Raufoss, for giving me the opportunity to do this thesis in cooperation with Nammo, for her help and guidance during this project. I would like to thank Alexander for being part my exam committee, and I would like to thank Eberhard for being chair of my exam committee.
Furthermore, I would like to thank Marcus and Elke for raising the idea to run distributed simulations, as well as lending me their laptop. I would also like to thank Aubin for letting me work at his place and for his advice on the thesis. I would like to thank Gerrit for reading my long texts and giving valuable input. Additionally, I would like to thank my old room mates Aubin, Gerrit, Wessel and Hans for still trying to be social in these hard times (Covid-19) with many rounds of Axis and Allies.
Finally, I would like to thank my family for letting me study at my own pace and still support me. I would also like to give a extra big thanks to my biggest sponsor, Gerda, my grandmother. My last thanks goes to someone that has had to endure the most of the bad and the good, my girlfriend José. José has always had my back and encouraged me on. So an extra big thanks to you José!

S. Ravnan
Delft, February 2021

Abstract

The supersonic split line (SSSL) nozzle has been considered for years in the use of solid rocket motors. The SSSL nozzle is an attractive alternative to the more conventional submerged movable (SM) nozzle. The SSSL nozzle can save up to 43% on nozzle mass and 25% on the thrust vector control (TVC) system mass. The SSSL nozzle also has the benefit of the amplification factor, which is a result of the SSSL nozzle turning the flow in the supersonic region. The shock waves formed deflect the flow more than the mechanical deflection. The amplification factor is defined as the flow deflection divided by the mechanical deflection. The greatest disadvantage of the SSSL nozzle is the high temperature experienced around the split area.

Only limited research is available on the SSSL nozzle. This thesis aims to expand on the knowledge of the SSSL nozzle in cooperation with Nammo Raufoss. Nammo has proposed a project to look into the amplification factor of the SSSL nozzle while changing various aspects of the nozzle. The aspects that are researched in detail are as following: The effect on the amplification factor when moving the split and changing the expansion ratio of the nozzle. Furthermore, to determine how well the SSSL nozzle compares to a more traditional SM nozzle, a comparison between the SSSL and the SM nozzle is performed at equal performance. This comparison has a focus on the mass differences of the nozzles and TVC systems of the SSSL and SM nozzle.

The performances of the SM nozzle and the SSSL nozzle are determined by simulations with computational fluid dynamics (CFD). The nozzles are constructed by creating a basic nozzle shape that can then be drawn into a 3D modelling program. From the CFD simulations, the amplification factor of the SSSL nozzle was determined. In order to compare the SSSL nozzle and the SM nozzle a mass model is developed. The model uses the calculated performance from the CFD simulations to calculate the mass difference between the two nozzle and TVC systems.

The results show that the amplification factor increases when moving the split further down stream. Furthermore, when increasing the expansion ratio the amplification factor decreases. For the SSSL nozzle with a total expansion ratio of 12 and the split location at an expansion ratio of 1.75, the maximum amplification factor is 1.57. Additionally, a linear relationship between the amplification factor and the ratio of the expansion ratio at the split to the total expansion ratio of the nozzle is observed. The SSSL nozzle experiences increasing thrust and Isp losses while vectoring when the split is located further downstream, while receiving only a slight increase in the amplification factor. The results from the mass model show that the SSSL nozzle is on average 37% lighter than the SM nozzle for a vectoring duty cycle of 0.25.

To conclude, for an increasing ratio between the expansion ratio at the split to the total expansion ratio of the nozzle, the amplification factor increases. Additionally, the SSSL nozzle is the lighter option when only the aerodynamic effects are considered. Other effects such as the interstage length and thermal protection of the split were not considered in this study, but these might have an influence on the overall system mass for the SSSL nozzle. It was also seen that the temperature and heat flux around the split area was high, to overcome this the SSSL nozzle might need additional thermal protection which could potentially lead to a higher mass. It was observed that the largest mass difference between the SSSL and SM nozzle system was found when the split of the SSSL nozzle is located at an expansion ratio that gives the highest possible Isp.

Contents

List of symbols and abbreviations

List of symbols

Symbol	Description	Unit
A	Area	m^2
AF	Amplification Factor	-
A_e	Nozzle exit area	m^2
A_t	Nozzle throat area	m^2
α_{div}	Divergence angle	degree
α_{needed}	Needed nozzle deflection	degree
$\beta_{required}$	The required angle of thrust vectoring	degree
c^*	Characteristic velocity	$m \cdot s^{-1}$
C_F	Thrust coefficient	-
c_p	Specific Heat Capacity at Constant Pressure	$J{\cdot}K^{-1}{\cdot}kg^{-1}$
C_d	Discharge coefficient	-
D	Diameter of nozzle	m
D_t	Throat diameter	m
δ	Nozzle deflection angle	degrees
ΔV	Delta V, time integration of the acceleration produced by the rocket engine	ms^{-1}
$\Delta\epsilon_{H_2O-CO_2}$	Correction factor emissivity for water vapour and carbon-dioxide	-
ϵ_1	Emissivity of medium 1	-
ϵ_{CO_2}	Emissivity of carbon-dioxide	-
ϵ_{div}	Divergence loss efficiency	-
ϵ_{H_20}	Emissivity of water vapour	-
ϵ_{tot}	Total emissivity of gas mixture	-
ϵ	Area expansion ratio	-
ϵ_{Ratio}	Ratio of expansion ratios	-
$\epsilon_{\text{Split location}}$	Expansion ratio at the split	-
ϵ_{Nozzle}	Total expansion ratio of the nozzle	-
F	Thrust force	N
γ	Specific heat ratio	-
G	Shear modulus	Pa
h	Height	m
h_α	Convective heat transfer coefficient	$W{\cdot}\ m^{-2}\cdot K$
I_{sp}	Specific impulse, measure of effectiveness	s
$\dot{m}$	Mass flow	$kg \cdot s^{-1}$
m_0	Initial total mass of the rocket	kg
m_1	Final total mass of the rocket	kg
m_p	Propellant mass	kg
M	Mach number	-
M_e	Mach number at nozzle exit	-
M_m	Molar mass	$kg \cdot mol^{-}1$

μ	Dynamic viscosity	kg·m^{-1}·s^{-1}
n	Number of elastomer layers	-
π	Mathematical constant Pi (3.14159)	-
p_0	Ambient pressure	Pa
p_c	Chamber pressure	Pa
p_e	Nozzle exit pressure	Pa
p_t	Total pressure	Pa
Pr	Prandtl number	-
q_{1-2}	Heat transfer from medium 1 to medium 2	W ·m^{-2}
r	Radius	m
r_t	Throat radius	m
r_c	Radius of curvature nozzle throat	m
R	Specific gas constant	J · K^{-1} · mol^{-1}
R_a	Universal gas constant (8.31446)	J · K^{-1} · mol^{-1}
σ	Stefan–Boltzmann constant (5.670374419E-8)	W ·m^{-2}· K^{-4}
θ	Nozzle wall angle	degrees
t_r	Thickness of elastomer layer	m
T_e	Nozzle exit temperature	K
T_t	Total temperature	K
$T_{w,g}$	Gas temperature at the wall	K
v_e	Nozzle exit velocity	m · s^{-1}
v_{eq}	Nozzle equivalent exit velocity	m · s^{-1}
v_x	Exit velocity in x direction	m · s^{-1}
v_y	Exit velocity in y direction	m · s^{-1}
ξ_F	Nozzle quality factor	-
ξ_c	Combustion quality factor	-
ξ_s	Motor quality factor	-

List of abbreviations

Abbreviation	Description
CAD	Computer Aided Design
CFD	Computational Fluid Dynamics
EET	Engineering Estimation Techniques
Isp	Specific impulse, measure of effectiveness
LITVC	Liquid Injection Thrust Vectoring Control
MITVC	Mechanical Intervention Thrust Vectoring Control
NASA	The National Aeronautics and Space Administration
PW	Pratt and Whitney
SEP	Société Européenne de Propulsion
SM	Submerged Movable
SOW	Statement Of Work
SSSL	Supersonic Split Line
TVC	Thrust Vectoring Control

List of Figures

List of Tables

1 Introduction

In this master thesis a comparison between the Super Sonic Split Line (SSSL) nozzle and a more conventional Submerged Movable (SM) nozzle has been performed. Additionally, the SSSL nozzle has been studied in more detail, especially the unique feature of the SSSL nozzle namely the Amplification Factor (AF). The thesis was done in collaboration with Nammo Raufoss. Nammo Raufoss is a multinational defence and space company based in Norway. In this chapter background information is presented as well as the research objectives and the research approach. First, some background information is presented. Second, the research objectives, research questions and hypotheses are presented. Third, the general methodology of the thesis is outlined and finally the outline of the thesis is presented.

1.1. Background information

In order to alter flight direction rockets need a form of control. There are various methods that can achieve this [34]. One method that can be used is thrust vector control (TVC). TVC manipulates the rocket exhaust in order to turn the rocket [13, 34, 40]. This can be achieved in several different ways. One approach is by the use of movable nozzles. Movable nozzles deflect the hot gas flow by mechanically deflecting the nozzle to the desired angle of thrust vectoring [40]. A second method is to use mechanical intervention devices, these achieve thrust vectoring by extending a mechanical device into the hot gas flow in order to deflect the exhaust gasses [40]. A third method is by injecting a liquid or gas into the hot gas flow to induce a shock wave that in turn turns the flow [25]. The two methods of thrust vectoring control that are dealt with in this thesis are the SSSL nozzle and the SM nozzle, which are both movable nozzles [23]. The SSSL nozzle and the SM nozzle can be seen as a ball and socket joint with a hollow middle. For the SSSL nozzle the ball and socket is located in the super sonic region of the nozzle, this is downstream of the nozzle throat. When the downstream part of the SSSL nozzle is rotated around the socket, the hot gas flow is turned and two super sonic flow phenomena occur [43, 52]. At the bottom, displayed in figure 1.1, a shock wave forms due to the nozzle turning. On the top there are expansion waves since the gas has to expand around the corner. These two effects result in an additional turning of the gas flow. The SSSL nozzle can therefore turn the gas flow more than the mechanical deflection of the nozzle. This is called the amplification factor, which is defined as [23, 43]:

$$AF = \frac{\text{Aerodynamic flow deflection}}{\text{Mechanical flow deflection}} \tag{1.1}$$

figure 1.2 is a representation of a SSSL nozzle that was tested against a SM nozzle. The upper nozzle is the SM nozzle and the lower nozzle is the SSSL nozzle. For the SM nozzle the ball and socket is located at the end of the combustion chamber. This means that the whole nozzle turns and the flow is turned before the throat of the nozzle. No supersonic flow phenomena can occur due to the nozzle deflection since the exhaust gasses are tuned before they reach super sonic speeds. The SSSL nozzle is the lower of the two nozzles in the figure. The figure is adapted from the paper by Ellis and Berdoyes [23].

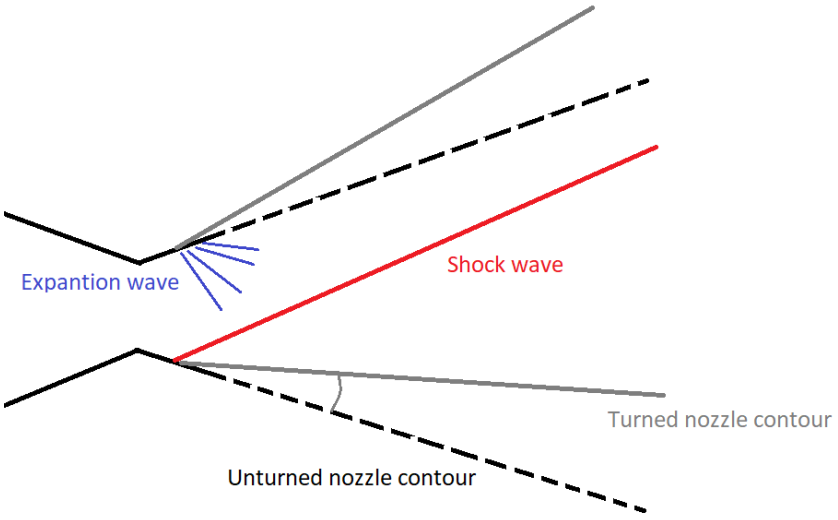

Figure 1.1: A simplified example of a SSSL nozzle with the expansion waves and shock waves indicated

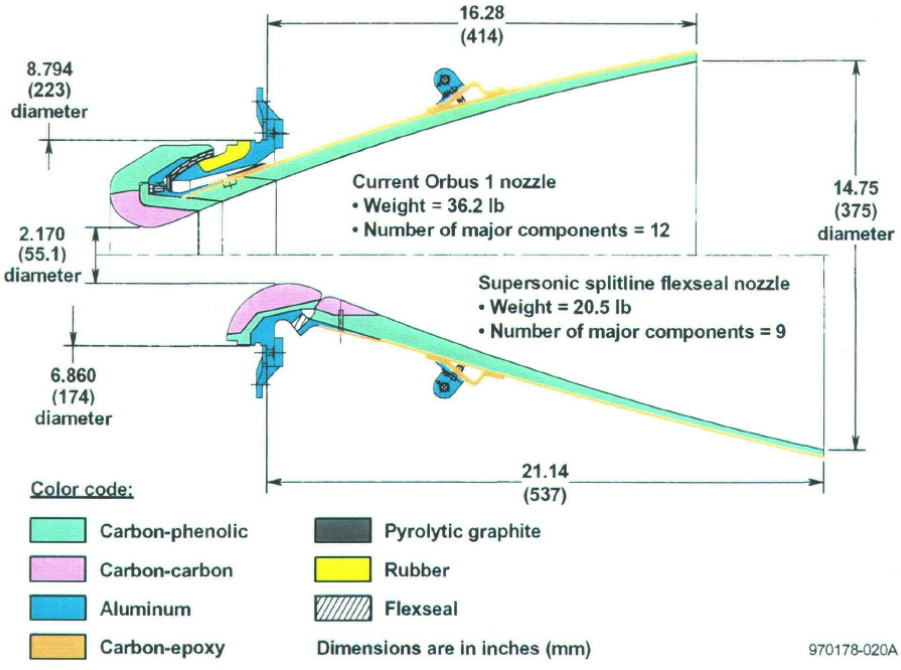

Figure 1.2: Figure of a sectioned view of a SM and SSSL nozzle. The Upper nozzle is the SM nozzle and the lower nozzle is the SSSL nozzle. Figure adapted from [23]

The two simulated nozzles in this thesis use a hybrid rocket motor for the combustion chamber conditions. This rocket motor is under development by Nammo Raufoss. This hybrid rocket uses a solid fuel grain and a liquid oxidiser in order to create thrust. The engine is designed to produce 100kN of thrust. The engine will be used in the North Star rocket family and micro launcher [53].

The last couple of years the development of rockets has increased rapidly. Especially within the field of TVC with SpaceX. The SSSL nozzle has however not yet been used extensively for TVC. This is due to the limited research on the SSSL nozzle. However, around the 1970s, the SSSL was studied extensively for the use of TVC. SSSL nozzles never became of great importance in the rocket industry

due to excessive heating around the split. This was the main pitfall for the SSSL nozzle preventing a breakthrough [21, 25, 44]. The last years however, the SSSL has received renewed attention. This is mainly due to the usage of composite materials. The composite materials overcame the excessive heating which has prevented the SSSL nozzle from being a success [11, 14, 23, 43]. One of the advantages of the SSSL nozzle is its low structural mass. A contributing factor is the use of composite materials and a less complicated design [23]. The mass of the SSSL nozzle is lower than alternatives such as the SM nozzle, Liquid Injection Thrust Vector Control (LITVC) and Mechanical Intervention Thrust Vector Control (MITVC), while still maintaining a good performance [23, 25, 34]. One of the hazards of the SSSL nozzle remains the limited experience and the fact that there is no public knowledge of flown rockets that have used the SSSL nozzle for TVC. In the literature review performed for this thesis a clear overview of the few articles that have been written about the SSSL nozzle is given [48]. The literature review revealed that the SSSL nozzle needs additional and up to date research on the SSSL nozzle. However, some relevant insights were obtained, specifically from the study by Ellis and Berdoyes [23]. They found that for the same test engine the SSSL nozzle had a mass saving of 43% compared to the SM nozzle [23]. In this test, the mass reduction resulted in a 7.1 kg lighter nozzle when looking at only the nozzle structure. Ellis and Berdoyes argue that this is due to the less complicated design and the fact that less material is needed for the construction [23]. During the test described in the paper, the torque required to turn the SSSL nozzle was drastically reduced by 63%. This resulted in a 25% reduction in the actuator mass. According to Ellis and Berdoyes the reduction in the torque was due to a combination of the amplification factor, aerodynamic torque and the less stiff joint [23].
The amplification factor of the SSSL nozzle has also been studied in the paper by Ørbekk [43]. In this paper the SSSL nozzle is tested on a small solid rocket motor. Ørbekk explores the relationship between the split location and the amplification gained and concludes that there is a maximum to be found [43]. He also argues that when increasing the overall expansion ratio the optimum split location moves as well.

In summary, the most beneficial aspects of the SSSL nozzle in comparison to the SM nozzle are the following: Firstly, the mass of the nozzle structure can be reduced substantially (of order 40%) [23]. Secondly, the SSSL nozzle has the unique benefit of the amplification factor [43]. The amplification factor has the result of reducing the actuator mass by 25% [23]. Finally, the specific impulse of the SSSL nozzle is on average 1-2s higher than for the SM nozzle [23].
The two papers by Ørbekk and Ellis & Berdoyes are the most comprehensive papers about the SSSL nozzle and the benefit of the SSSL nozzle over a SM nozzle. However, both papers do not deliver all their data and therefore the claims that are stated in the papers are hard to verify. Therefore, a clear gap in the knowledge of the SSSL nozzle has been found. In order to confirm or refute the statements by Ellis & Berdoyes and Ørbekk additional research is needed into the topic. In addition, Nammo Raufoss is interested in using the SSSL nozzle for the North Star.

1.2. Research objectives

This thesis focuses on the comparison between the SSSL nozzle and the SM nozzle. The amplification factor of the SSSL nozzle is also studied in more detail. The research focusses on the aerodynamic differences between the two nozzles. Other differences such as structural, cooling and manufacturing differences will not be taken into account as these aspects are deemed outside the scope of the thesis. Additionally, the amplification factor is only effected by the aerodynamic differences. Below is a list of research objectives for the thesis.

1. The first objective of the thesis is to find the difference in performance between the SM nozzle and the SSSL nozzle. The performance is divided in aerodynamic moment, vectoring performance, and specific impulse (Isp) loss. The vectoring performance is calculated by finding the the amplification factor. A model is created in order to compare the nozzle and TVC system mass. If the performance of the nozzles changes this can then be observed as a mass change in the model. The mass of the nozzle system is of importance because the largest benefit of the SSSL nozzle over the SM nozzle is the lower mass.

2. The second objective of the thesis is to explore the amplification factor in more detail:

   (a) Find the relationship between the amplification factor and the position of the split along the nozzle wall.
   (b) Find the effect of throttling the engine.

   Both effects on the amplification factor will then be linked to the mass increase or decrease through the developed model. The nozzle is analysed at three angles of mechanical nozzle deflection, three split locations and three thrust settings.

3. The third objective of the thesis is to determine the effect on the amplification factor when increasing the total expansion ratio. This is performed in order to find the effect on the amplification factor for a potential upper stage motor of the North Star.

4. The final objective of the work is to determine the effect of scaling the nozzle down to a smaller nozzle size. This is done to see the effect on the amplification factor for a smaller rocket such as the Nucleus sounding rocket [26].

1.3. Research questions

In order to achieve all the research objectives of this thesis, a set of research questions have been formulated. The main research questions for the thesis are listed below with additional research questions to aid the process on reaching the research objectives. The research questions are adapted from the project plan for this thesis [47].

1. What is the mass difference between the SSSL nozzle and the SM nozzle for a 100kN hybrid rocket motor with a burn time of 90s?
   (a) What is the mass difference due to the amplification factor?
   (b) What is the mass difference due to the aerodynamic moment?
   (c) What is the mass difference due to the Isp loss?

2. What is the effect on the amplification factor when changing the parameters of the nozzle and engine?
   (a) What is the effect on the amplification factor when moving the split, while keeping everything else constant?
   (b) What is the effect on the amplification factor when changing the mass flow, while keeping the split at a constant location?
   (c) What is the effect on the amplification factor when increasing the expansion ratio of the nozzle, while keeping the same throat area?
   (d) What is the effect on the amplification factor when decreasing the scale of the nozzle down to a 29kN engine?

1.3.1. Hypotheses

Accompanying the objectives and the research questions are a set of hypotheses that are listed below. The hypotheses are adapted from the project plan for this thesis [47].

1. In the first objective, the goal is to find the performance difference between the SSSL nozzle and the SM nozzle. From literature it is expected that the SSSL nozzle will outperform the SM nozzle in vectoring performance and aerodynamic moment, which results in a lower vectoring system mass [23]. However, the SSSL nozzle will probably suffer from a lower Isp while vectoring. Since, this has been reported in literature [1].

2. The hypothesis for what happens to the amplification factor when moving the split is: The amplification factor will have a maximum at a location of the split where the area ratio is around 2 [48]. On each side of the maximum the amplification factor will be lower.

3. Varying the mass flow for the same nozzle geometry the prediction is that the amplification factor will increase as the mass flow is reduced. The momentum of the flow is lower and hence less force is needed to divert the flow. Therefore, the shock wave is able to deflect the flow more.

4. Increasing the area expansion ratio the prediction is that the maximum point for the amplification ratio is located further downstream as the nozzle is longer. As the nozzle length increases it is expected that the effect of the shock will dissipate further downstream. Since the flow is expanded more than for a lower expansion ratio nozzle.

5. Finally when scaling the nozzle it is expected that it will have no effect on the amplification factor. This hypothesis is based on the different size engines in literature. [11, 15, 23, 25, 43, 52]

1.4. General methodology

This section will discuss the general methodology of the thesis. Each subsection deals with a specific portion of the thesis. The methodology is written as presented in the project plan for this thesis [47].

1.4.1. Basic nozzle generation and performance calculation

”In order to make sure that both nozzles can be compared, their basic nozzle shape has to be the same. The basic nozzle shape is defined as the shape from the throat to the exit. The chamber to throat region will differ because of the submergence of the SM nozzle, since the SSSL nozzle is not submerged. This difference is designed with the guidelines of Ellis [24]. The basic nozzle shape is created by the methods described in the book by Sutton, the course notes from Zandbergen and in other sources [13, 32, 40, 42]. These methods give an approximation of an ideal nozzle. Nammo has requested a bell shape nozzle with a length similar to 80% of a 15°conical nozzle. In order to create the nozzle shape and calculate the performance a python program is written to change the design if needed.
When the nozzle shape has been determined the nozzle performance is calculated with the ideal rocket theory by Sutton [40]. The calculations will use a typical nozzle quality factor, combustion quality factor and motor quality factor. In order to produce a more realistic answer, the quality factors used are based on the lecture notes by Zandbergen [13]. The performance of the nozzle will then be compared to the requirements by Nammo. At a later stage, the answers with the quality factors can be compared to the simulations done by the Computational Fluid Dynamics (CFD) simulations. Additional information on the CFD methodology is given in chapter 6
The mass model is created in python as well where the three parameters amplification factor, aerodynamic torque and Isp are used as inputs. The model can then calculate the effect on the mass of the nozzle and TVC system. The amplification factor is linked to the mass via the reduced angle of deflection needed. The values for the spring torque is estimated and adjusted based on engine size from the papers by Donat, Zandbergen, Ellis & Berdoyes and Ørbekk [13, 22, 23, 43]. The aerodynamic turning moment is linked to the mass by comparing the moments to the values obtained in the study by Ellis and Berdoyes. The Isp loss is linked to the mass of the system in the form of the additional propellant needed for the 90s burn time by the use of the ideal rocket equation [13]. The three python programs are discussed in detail in sections 2.1 and 2.2 and chapter 3.”
- (Ravnan 2020, [47])

1.4.2. Verification of Ansys

”To verify that the Ansys Fluent creates the right solution, and that Ansys is setup correctly, a test case is created and compared to the results of Kumar and Devarajan [33]. Ansys is a engineering software toolbox with a great variety of tools. The specific tools used for this thesis are highlighted in chapter 6. The nozzle in the test case is created to the same specification as in the paper. This is done in order to properly compare the nozzle performance of the paper to the one in this thesis. In chapter 6 a detailed description of this process is given.”
- (Ravnan 2020, [47])

1.4.3. Supersonic split line and submerged movable nozzle design and comparison

”This part of the thesis aims to answer research question 1 and test hypothesis 1. The SM nozzle and the SSSL nozzle specifics are designed and drawn in a Computer Assisted Design (CAD) program, when the basic shape has been analysed and Ansys has been verified. The SM nozzle will have a submerged part inside the combustion chamber. This part is designed with the guidelines of

Ellis [24].The SSSL nozzle will have a split located at around 1.75 in area expansion ratio, as various previous designs are located around this point. This was extensively explored in the literature study [48]. Both nozzles will then be analysed with Ansys Fluent [4]. Ansys uses the CAD model created earlier to determine the boundaries of the nozzle and the mesh is drawn on the surface of the nozzle wall. Reference sources from literature have shown that Ansys is more than capable of calculating the flow solution of a rocket nozzle [29, 41, 48]. The SM nozzle and the SSSL nozzle are tested at three different vectoring angles in Ansys Fluent to compare the performance of the two nozzles. Each of the different angles needs a separate CAD and mesh in order to simulate the different angles. The following performance parameters that are tested: thrust, specific impulse, aerodynamic torque, thrust coefficient, nozzle coefficient and thrust loss due to vectoring. Additionally the amplification factor is calculated by dividing the flow deflection by the mechanical deflection. When the Ansys simulations are done, the performance parameters are added to the mass model and the mass of the SSSL nozzle and the SM nozzle can be compared. Both nozzles will also be compared to the requirements by Nammo."
- (Ravnan 2020, [47])

1.4.4. Supersonic split line nozzle investigation

"This part of the thesis aims to answer research question 2a and 2b and test hypothesis 2 and 3. In part two of the thesis the SSSL nozzle design is redesigned. The changed parameter is the location of the split. The different split locations are tested on three different angles to determine the effect of changing the split location on the amplification factor. Three different split positions are tested. Additionally, the pressure field and temperature field around the split are characterized. This is done in Ansys Fluent as it will calculate these two parameters in the simulation. From this an estimation of the heat transfer to the nozzle wall can be established by coupling the CFD calculations with the Bartz equation [10]. This method has been used by several other studies as shown in the literature study [48]. The results of the different amplification factors are compared with the values from the various previous studies on a SSSL nozzle [11, 15, 19, 23, 24, 43, 52]. This will confirm that the values gained from the analysis are comparable.
The mass flow is varied by varying the total pressure of the simulation. In order to save time this option is run on the previously analysed nozzle configurations. The only parameters that needs to change is the total pressure. The results can then be analysed and compared with hypothesis number 3."
- (Ravnan 2020, [47])

1.4.5. Higher expansion ratio and scaled supersonic split line nozzle

"The nozzle is redesigned with a higher expansion ratio to simulate the second stage of a launch vehicle. The requirements for this nozzle are given in appendix A. The higher expansion ratio for the 107kN engine is 45. The new nozzle will then be analysed and compared against the lower expansion ratio nozzle for two or more split locations and angles. The analysis is done in the same manner as for the lower expansion ration nozzle. After this, the behaviour of the amplification factor can be determined when going to a higher expansion ratio. This effect was also explored to some extend by Ørbekk [43]. By comparing this analysis against the work of Ørbekk, the statements from Ørbekk can be verified and be expanded on by additional data on the amplification factor. This can be seen in figure 1.3.

When the above tasks have been reviewed a downscaled version of the nozzle is created with a thrust of 29 kN. The downscaled nozzle requirements are shown in the statement of work (SOW) by Nammo chapter A. This nozzle will then be analysed in the same manner as for the 107kN engine. In order to find the effect of scaling the engine.
This part of the thesis aims to answer research question 2c and 2d and tests hypothesis 4 and 5."
- (Ravnan 2020, [47])

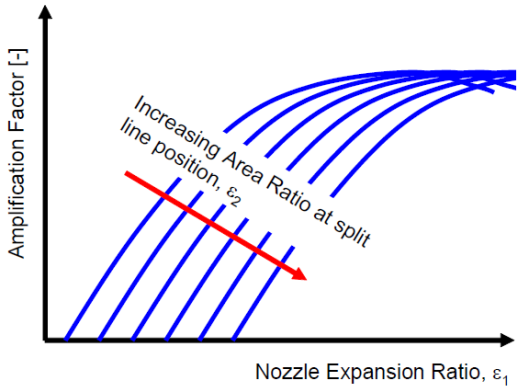

Figure 1.3: Illustration of the effect of moving the split down stream on the amplification factor. Figure taken from [43].

1.5. Thesis layout

In this section the layout of the thesis is presented with an overview what can be found in each chapter.

- **Chapter 2 - Baseline nozzle definition:** In this chapter the baseline nozzle is created for both the SM nozzle and the SSSL nozzle. The baseline nozzle parameters are calculated with the help of a python program. The creation and verification of the python program is also discussed in this chapter.
- **Chapter 3 - Python mass model program:** The mass model that is used in the comparison between the SSSL nozzle system and the SM nozzle system is developed in this chapter. Each of the aspects of the program is explained and a example calculation is shown.
- **Chapter 4 - Supersonic split line and submerged movable nozzle design:** This chapter discusses the design of the SSSL nozzle and the SM nozzle. Additionally, the usage of a CAD program is outlined.
- **Chapter 5 - Heat transfer:** In this chapter the approach taken to calculate the heat transfer to the nozzle walls is discussed, two sources of heat transfer are used, convective and radiative. Both are explained in their own section.
- **Chapter 6 - Ansys approach:** In this chapter the use of Ansys for the CFD calculations is described. A verification simulation of the CFD analysis is performed by comparing the results to literature. Additionally, a comparison of turbulence models is shown and the convergence criteria are set. Finally the simulation plan is presented.
- **Chapter 7 - Results and discussion on the comparison between the supersonic split line nozzle and the submerged movable nozzle:** The results of the comparison between the SSSL nozzle and the SM nozzle is presented in this chapter including a discussion of the results. This includes the mass model results and the performance results of both nozzles.
- **Chapter 8 - Results and discussion of amplification factor research:** The results of the effect of moving the split, changing the expansion ratio and scaling the nozzle is presented in this chapter. The results will also be discussed
- **Chapter 9 - Results and discussion on temperature distribution and heat flux:** This chapter will present the results of the investigation into the temperature distribution and the heat flux experienced by the nozzle. These results will then also be discussed.
- **Chapter 10 - Conclusion and recommendations:** This chapter will present the conclusions of the thesis and provide recommendations for further studies.

2

Baseline nozzle definition

In this chapter the creation of the Python programs used to define the basic nozzle shape and the predicted performance of the basic nozzle shape are discussed. For all nozzle representations the flow of gases goes from the left to the right. At the end of the chapter the programs are validated against a test case and compared to literature. First, the shape program is discussed. Second, the performance program is presented. Third, the programs are validated and finally the results for the three different nozzle shapes are presented. For all nozzle representations the flow of gases goes from the left to the right.

2.1. Python Shape program

In this section the Python program created for drawing the initial nozzle shape is presented. The equations used and methods of obtaining the nozzle shape is briefly discussed. The program is written in Python 3 as this is a widely available programming language and the software is open source. The first approach to the shape program was taken from the book by Sutton and the lecture notes by Zandbergen [13, 40]. The first approach uses a parabolic equation to create the nozzle shape and relies on 3 boundary conditions. This approach is simple and quick, but it was found that it did not produce an adequate nozzle shape. Therefore, a second approach was found and compared to the first approach. This approach is based on the methods by Huzel, Rao, Chikitkin et al. and Ogawa et al. [16, 31, 32, 42]. The second approach is a bit more complicated and uses 4 boundary conditions to create a skewed parabolic nozzle shape. By comparing the two methods it was found that the second approach created a better nozzle shape. Therefore, the second approach was chosen and is presented below. The first approach can be found in appendix C.

2.1.1. Shape calculation

The second approach to the shape calculation is by the use of a Bézier curve [16, 31, 37]. A Bézier curve creates a smooth curve along a set of control points [37]. The control points are found by using the $x-p$ point and the $x-e$ point as shown in figure C.2. However, in order to create a curve there has to be a third control point. This third control point is created from the intersection of two lines originating from the $x-p$ point and the $x-e$ point. The angle of these lines are determined from the angles given in the book by Sutton in the chapter on nozzle design [40]. These angles have been determined from various experimental tests and approximate the optimal angles for a certain length of a bell nozzle. The length is expressed in the % length of a 15°conical nozzle. The two angles can be found by choosing the appropriate expansion ratio and finding the angles from figure 2.1.

When the two angles are set, the intersection of the two points can be found by the using algebra. Lets call the lines L_1 and L_2. The lines both have two points.For L_1 this is (x_{11}, y_{11}) and (x_{12}, y_{12}) and for L_2 this is (x_{21}, y_{21}) and (x_{22}, y_{22}). In this case (x_{12}, y_{12}) is not yet known. The second point is created by stretching a line from the first known point ($x-p$ or (x_{11}, y_{11})) at the angle found in figure 2.1. The x-coordinate of the second point will be located at a x distance equal to the x-coordinate of $x-e$ or (x_{21}, y_{21}). Thereby the y coordinate can be calculated using $y_{12} = tan(\theta) \cdot (x_{21} - x_{11})$. Now both points for L_1 have been determined. This is repeated for L_2, however now the known point is $x-e$ and the

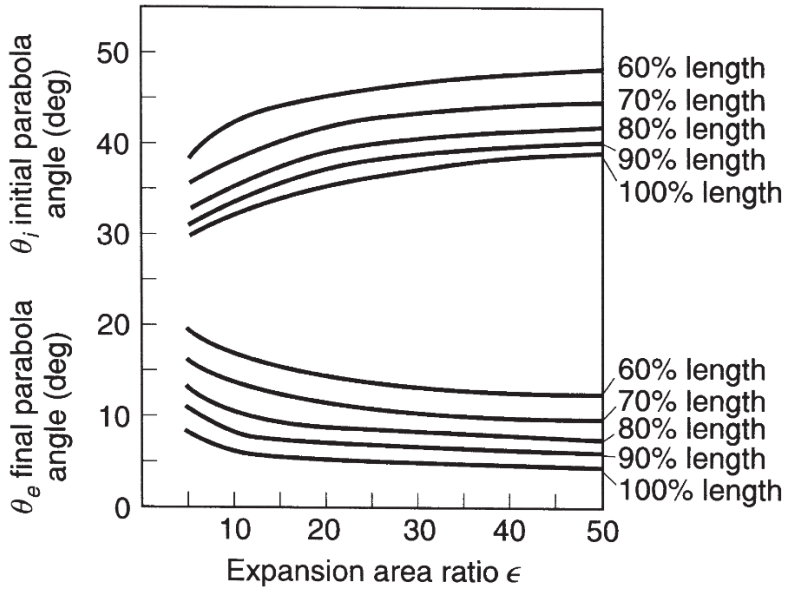

Figure 2.1: Figure showing the nozzle entry and exit angles for a certain expansion ratio. The length percentage is the length of the bell nozzle compared to a 15°conical nozzle. Source for the image [40].

exit angle should be used. In figure 2.2 a graphical example of the nozzle coordinates is shown. The point (x_{11}, y_{11}) is the known $x - p$ point and the (x_{12}, y_{12}) is created with the initial angle. For the red line the (x_{22}, y_{22}) is the known $x - e$ point and the (x_{21}, y_{21}) is created with the exit angle.
The intersection point can clearly be seen in figure 2.2, but the exact point can also be calculated by the use of determinants. From equation (2.1) and equation (2.2) the intersection point can be found. Where I_x and I_y are the x and y coordinates for the intersection point respectively.

$$I_x = \frac{\begin{vmatrix} \begin{vmatrix} x_{11} & y_{11} \\ x_{12} & y_{12} \end{vmatrix} & \begin{vmatrix} x_{11} & 1 \\ x_{12} & 1 \end{vmatrix} \\ \begin{vmatrix} x_{21} & y_{21} \\ x_{22} & y_{22} \end{vmatrix} & \begin{vmatrix} x_{21} & 1 \\ x_{22} & 1 \end{vmatrix} \end{vmatrix}}{\begin{vmatrix} \begin{vmatrix} x_{11} & 1 \\ x_{12} & 1 \end{vmatrix} & \begin{vmatrix} y_{11} & 1 \\ y_{12} & 1 \end{vmatrix} \\ \begin{vmatrix} x_{21} & 1 \\ x_{22} & 1 \end{vmatrix} & \begin{vmatrix} y_{21} & 1 \\ y_{22} & 1 \end{vmatrix} \end{vmatrix}} \quad (2.1) \qquad I_y = \frac{\begin{vmatrix} \begin{vmatrix} x_{11} & y_{11} \\ x_{12} & y_{12} \end{vmatrix} & \begin{vmatrix} x_{11} & 1 \\ x_{12} & 1 \end{vmatrix} \\ \begin{vmatrix} x_{21} & y_{21} \\ x_{22} & y_{22} \end{vmatrix} & \begin{vmatrix} x_{21} & 1 \\ x_{22} & 1 \end{vmatrix} \end{vmatrix}}{\begin{vmatrix} \begin{vmatrix} x_{11} & 1 \\ x_{12} & 1 \end{vmatrix} & \begin{vmatrix} y_{11} & 1 \\ y_{12} & 1 \end{vmatrix} \\ \begin{vmatrix} x_{21} & 1 \\ x_{22} & 1 \end{vmatrix} & \begin{vmatrix} y_{21} & 1 \\ y_{22} & 1 \end{vmatrix} \end{vmatrix}} \quad (2.2)$$

With all the required points the calculation of the Bézier curve can be done. For a curve with 3 control points the Bézier curve formula is described by equation (2.3). x_1, x_2 and x_3 are the x-coordinates for the control points. The y version works the same only y_1, y_2 and y_3 are used. The control points used in this program are $x - p$, I and $x - e$. I is the intersection point calculated as described before. t is a 'time-step' that goes from 0 to 1. When this is calculated the resulting curve creates a smooth nozzle shape. The section right after the throat is calculated by using a circular arc with radius equal to 0.382 times the throat radius [32]. The final shape for the nozzle can be calculated, this is shown in figure 2.3.

$$\begin{aligned} x &= (1-t)^2 x_1 + 2(1-t)t \cdot x_2 + t^2 x_3 \\ y &= (1-t)^2 y_1 + 2(1-t)t \cdot y_2 + t^2 y_3 \end{aligned} \quad (2.3)$$

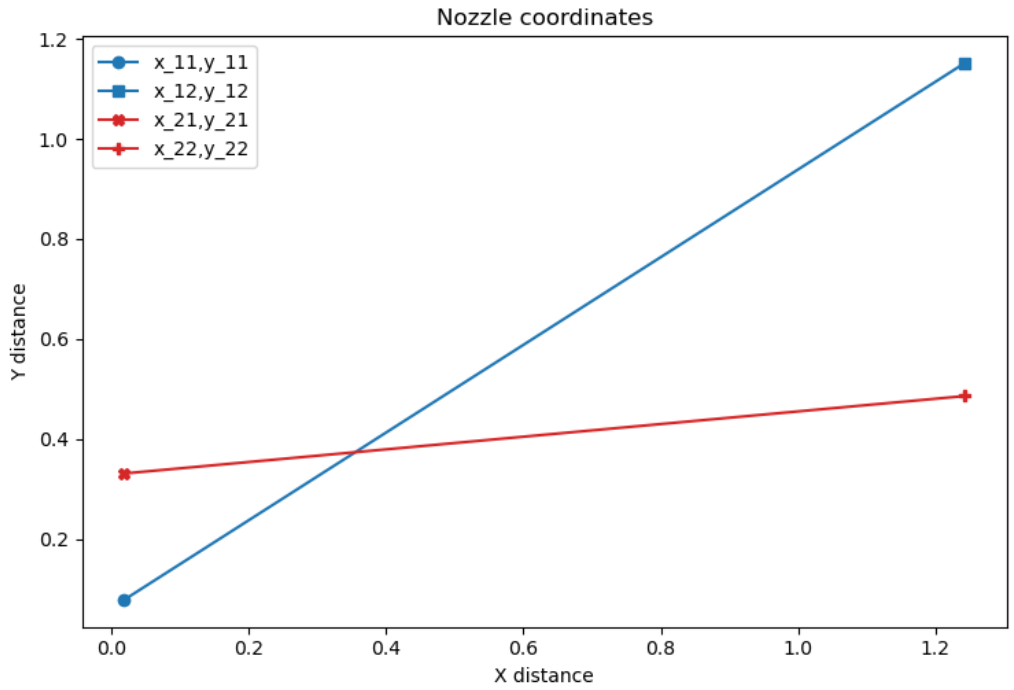

Figure 2.2: Figure showing an example of the nozzle coordinates calculation.

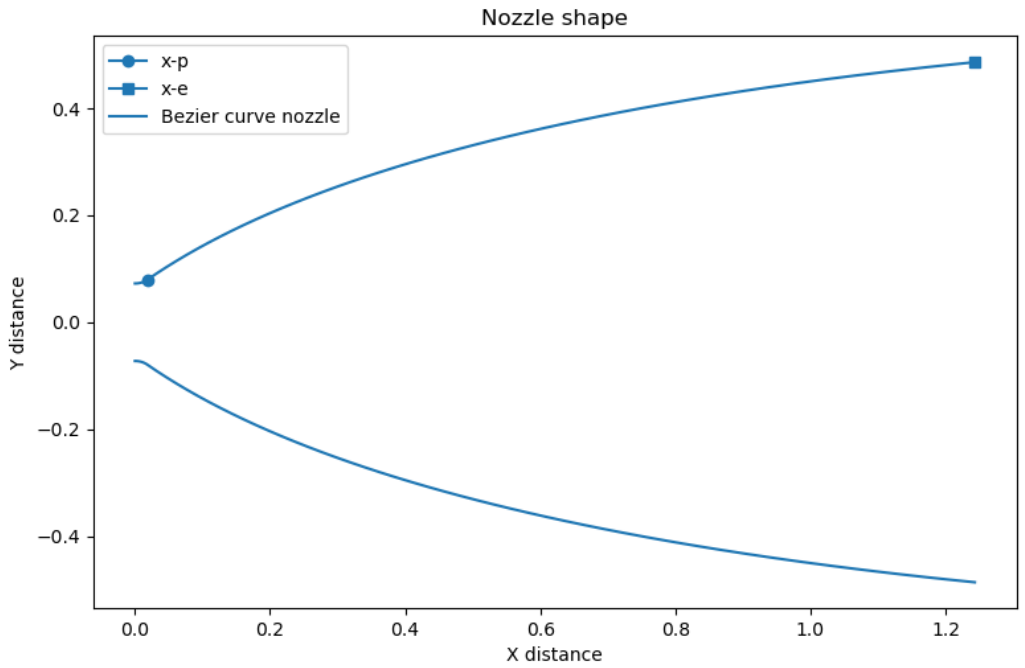

Figure 2.3: Figure showing an example of the nozzle shape calculation.

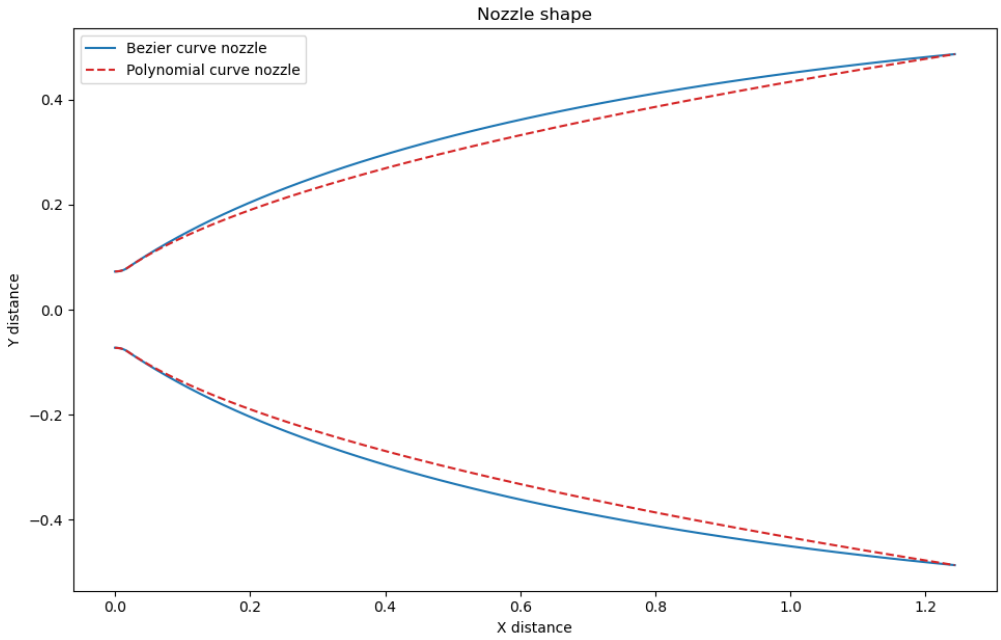

Figure 2.4: Figure showing an example of the difference between the two nozzle shape programs.

2.1.2. Differences between shape calculation approach 1 and 2

The biggest difference between shape calculation approach 1 and 2 is the exit angle of the nozzle. The Bézier curve shows a slightly steeper angle towards the I control point and is to some extent more aggressive in turning back towards the nozzle exit. This creates the difference in nozzle exit angle. In shape program 1, the polynomial tends to become quite straight towards the exit. This can be seen in figure 2.4. In this figure both shape programs have been run for the same nozzle with the same nozzle entry angle. The figure demonstrates that the Bézier curve creates a wider nozzle profile in the region after the throat than the polynomial nozzle. The Bézier curve method creates the same shape as the method described by Huzel in his paper [32]. Huzel uses skewed parabolas in order to create the nozzle shape. Since both methods use the same boundary conditions the shape of the nozzle becomes the same. This line is not shown in figure 2.4 as it overlaps the Bézier curve nozzle

2.2. Python performance program

In this section the approach for the initial performance calculation of the nozzle is discussed. Furthermore, all the equations used will also be highlighted.

To find the predicted performance of the nozzle, a program is written in Python to calculate the performance from the given input parameters. The input parameters are the total pressure (p_t), total temperature (T_t), molar mass of the combustion products (M_m), specific heat ratio (γ), throat radius (r_t) and expansion ratio (ϵ). These inputs are given by Nammo, they can be found in the SOW in appendix A. The output of the program will include the predicted thrust and Isp as these two need to be compared to the requirements.
For the calculation of the predicted performance the performance program uses ideal rocket theory. Ideal rocket theory calculates the ideal performance of a rocket without losses. A number of assumptions are used in order to calculate the performance. The assumptions are listed below [40].

- The working substance is homogeneous.
- The working fluid is considered as gaseous.
- The working fluid follow the ideal gas law.

- The flow has no friction and boundary layer effects are neglected.
- There are no shock waves and no discontinuities in the nozzle wall.
- The flow is considered a frozen flow, hence there are no chemical reactions happening.
- The flow is considered isentropic and one-dimensional.
- The exit flow is uniform and leaves the nozzle normal to the nozzle axis.

All these assumptions make sure that the calculations of the initial performance parameters can be made. The assumptions result in some discrepancies with a real rocket motor. The difference can be seen in validation of the performance calculations in section 2.3

The first step performed by the program is to calculate the mass flow ($\dot{m}$) of the motor based on the total temperature (T_t), total pressure (p_t), ratio of specific heats γ, specific gas constant R and the throat area (A_t). It is assumed that the velocity of the gas in the combustion chamber is zero. Furthermore it is also amused that γ is constant. This is shown in equation (2.4) [13, 40]. The throat area is determined from the input parameter by Nammo. Since the throat diameter is given the throat area can be computed to be: 0.016513m^2. The specific gas constant is also supplied by Nammo and equals: 1.13.

$$\dot{m} = \frac{p_t \cdot A_t}{R \cdot T_t} \cdot \sqrt{\gamma \cdot R \cdot T_t} \cdot \left(\frac{2}{\gamma+1}\right)^{\left(\frac{\gamma+1}{2(\gamma-1)}\right)} \tag{2.4}$$

R is the specific gas constant for the combustion products which is calculated by equation (2.5). R_a is the universal gas constant and M_m is the molar mass of the combustion products.

$$R = \frac{R_a}{M_m} \tag{2.5}$$

The next step is to find the exit Mach number using the supplied area expansion ratio and γ. However, this equation can not be algebraically solved for the Mach number. The equation is shown in equation (2.6). The equation has to be iteratively solved in order to find the Mach number at the exit. From a initial guess a gradient is computed with respect to the expansion ratio, after which the Mach number is updated using a step size relative to the gradient. The program solves the equation until the difference between the expected expansion ratio and the computed expansion ratio is less than 1E-6. The last guess of the Mach number is taken as the Mach number at the exit.

$$\frac{A_e}{A_t} = \left(\frac{\gamma+1}{2}\right)^{-\left(\frac{\gamma+1}{2(\gamma-1)}\right)} \frac{\left(1+\frac{\gamma-1}{2}M_e^2\right)^{\frac{\gamma+1}{2(\gamma-1)}}}{M_e} \tag{2.6}$$

Where A_e is the exit area, A_t is the throat area, γ is the ratio of specific heats and M_e is the Mach number at the exit. When the exit Mach number is known the next step is to find the exit temperature and the exit pressure. These are found using isentropic relations. The equations for the exit temperature and exit pressure are given by equations (2.7) and (2.8) respectively. T_t is the total temperature, T_e is the exit temperature, p_t is the total pressure and p_e is the exit pressure.

$$\frac{T_e}{T_t} = \left(1+\frac{\gamma-1}{2}M_e^2\right)^{-1} \tag{2.7}$$

$$\frac{p_e}{p_t} = \left(1+\frac{\gamma-1}{2}M_e^2\right)^{-\frac{\gamma}{\gamma-1}} \tag{2.8}$$

From the exit temperature the exit velocity can be found. This is shown in equation (2.9).Where v_e is the exit velocity. As the nozzle created will not expel all the exhaust gases in parallel to the nozzle axis. Therefore, the thrust equation will have a loss associated to the velocity component. This loss is called

the divergence loss and is defined by equation (2.10). θ_{exit} is the exit angle of the nozzle and α_{div} is the divergence angle which is defined as shown in figure 2.5.

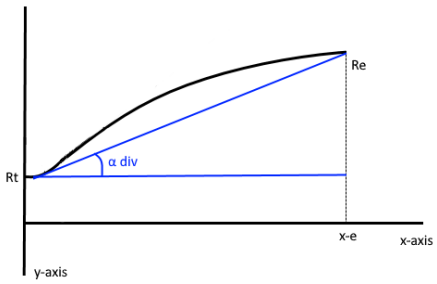

Figure 2.5: Figure showing the definition of the divergence angle for divergence loss

$$v_e = M_e\sqrt{\gamma R T_e} \tag{2.9}$$

$$\epsilon_{div} = 0.5 \cdot \left(1 - cos\left(\frac{\theta_{exit} + \alpha_{div}}{2}\right)\right) \tag{2.10}$$

The nozzle created will not be perfectly adapted to the ambient conditions and hence the thrust of the engine has an additional term dependent on the pressure. The combination of the velocity term and the pressure term can be called the equivalent exit velocity. This can be seen in equation (2.11). From this the motor thrust can be computed by multiplying the mass flow with the exit velocity and the additional pressure term, this is shown in equation (2.12). The Isp of the engine can be computed from the equivalent exit velocity and the gravity constant, and is defined by equation (2.13). Other interesting characteristics of the engine can now also be computed such as the characteristic velocity and the thrust coefficient. The definition of these can be found in equations (2.14) and (2.15) respectively. From all these equations the theoretical performance of the rocket engine can be found.

$$v_{eq} = v_e \cdot + \frac{p_e - p_0}{\dot{m}} \cdot A_e \tag{2.11}$$

$$F = v_e \cdot \epsilon_{div} \cdot \dot{m} + (p_e - p_0) \cdot A_e \tag{2.12}$$

$$I_{sp} = \frac{v_{eq}}{g_0} \tag{2.13}$$

$$c^* = \frac{p_t \cdot A_t}{\dot{m}} \tag{2.14}$$

$$C_F = \frac{F}{p_t \cdot A_t} \tag{2.15}$$

2.3. Verification and validation of python shape and performance program

The verification of the performance program was done by doing hand calculations of the exact same input parameters. Additionally, each section of the program was unit tested to prevent mistakes from one part of the program translating to the next part. All of the calculations were within 0.01% and the difference can be acclaimed to rounding off errors in the hand calculations. For the unit tests it was found that none of the program parts caused problems and they performed as they should.

For the validation of the results a test case from literature is used. The test case that is used is the RS-25 engine, or better known as the Space Shuttle Main Engine [46]. The values are taken from a

presentation on the RS-25 engine [46]. In table 2.1 all the different values of the engine are given with the calculated values from the performance program included. As can be seen in table 2.1 the values are quite close. The difference in thust is 1.66% and the difference in Isp is 1.55%. The performance program overestimates the thrust and Isp by some margin. Two other engines were also tested and validated against, the Vulcain 2 and the LE-7 engine [27, 50]. Their data can be found in tables 2.2 and 2.3. The values of the thrust difference range from 0.41% to 2% and the Isp difference range from 1.55% to 3.6%. The values for the shape program were expected to be a bit higher as the program uses ideal rocket theory.
The shape calculated from the shape program can be seen overlaid on the RS-25 engine, Vulcain engine and the LE-7 engine in figures 2.6 to 2.8. The figures are adapted from various sources on the engines [27, 36, 39]. The red broken line is the shape calculated from the shape program. As can be seen the shapes calculated are close to the real nozzle shape, based on visual inspection.

The results of the validation study are close to the real rocket engine values and for this thesis the programs created are deemed sufficiently valid. As the programs show an expected behaviour, such as the little higher performance than the real engines, and the shape of the nozzle being close to the real shape. The shape is not exact as the method used uses an approximate method for constructing the nozzle shape.
If the performance program did not produce the expected results the program can not be considered valid and it would need some revision. This revision would include checking the equations and comparing the input to the model with the real engine. If the input is not the same as for the real engine the performance program will produce a different answer.

Table 2.1: Comparison between the RS-25 engine and the performance program.

Parameter	RS-25	Performance program	Percentage difference
Chamber pressure	207.4 Bar	207.4 Bar	-
Chamber temperature	3588.7 K	3588.7 K	-
Throat diameter	276 mm	276 mm	-
Expansion ratio	69	69	-
Molar mass of combustion products	13.1 g/mol	13.1 g/mol	-
Ratio specific heat γ	1.196	1.196	-
Thrust	2282.41 kN	2320.30 kN	1.66%
Isp	452 s	459 s	1.55%

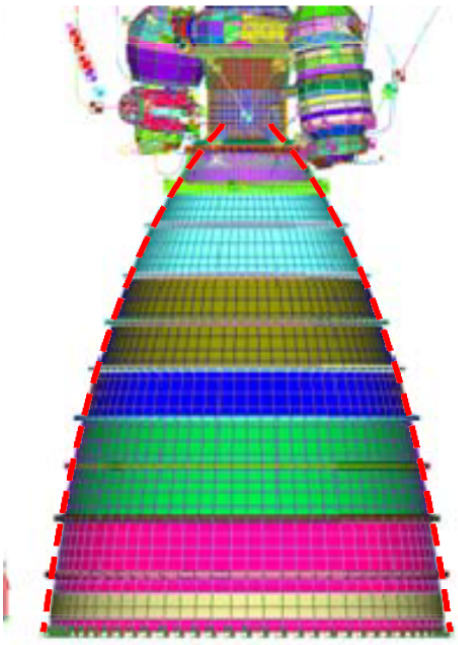

Figure 2.6: Figure showing the RS-25 engine with a dashed line indicating the shape calculated from the shape program

Table 2.2: Comparison between the Vulcain 2 engine and the performance program.

Parameter	Vulcain 2	Performance program	Percentage difference
Chamber pressure	115 Bar	115 Bar	-
Chamber temperature	3588.7 K	3588.7 K	-
Throat diameter	281 mm	281 mm	-
Expansion ratio	58.8	58.8	-
Molar mass of combustion products	14 g/mol	14 g/mol	-
Ratio specific heat γ	1.194	1.194	-
Thrust	1340.00 kN	1367.84 kN	2.01%
Isp	431 s	447 s	3.60%

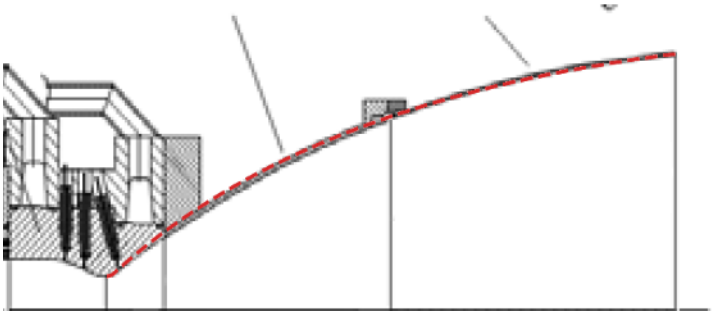

Figure 2.7: Figure showing the Vulcain 2 engine with a dashed line indicating the shape calculated from the shape program

Table 2.3: Comparison between the LE-7 engine and the performance program.

Parameter	LE-7	Performance program	Percentage difference
Chamber pressure	127 Bar	127 Bar	-
Chamber temperature	3570 K	3570 K	-
Throat diameter	241 mm	241 mm	-
Expansion ratio	52	52	-
Molar mass of combustion products	13.3 g/mol	13.3 g/mol	-
Ratio specific heat γ	1.198	1.198	-
Thrust	1098.00 kN	1102.54 kN	0.41%
Isp	438 s	446 s	1.79%

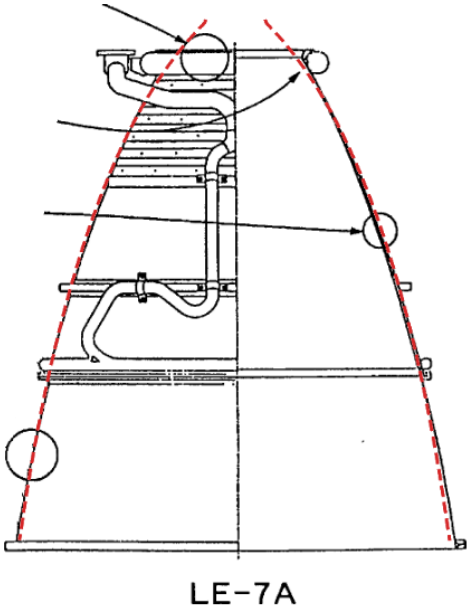

Figure 2.8: Figure showing the LE-7 engine with a dashed line indicating the shape calculated from the shape program

2.4. Baseline rocket shape and performance numbers

In this section the basic nozzle shape and performance numbers are calculated with the method developed in the previous sections. Three nozzle shapes are constructed for the use in this study, including a nominal nozzle with an expansion ratio of 12, an upper stage nozzle with the same throat size as the nominal nozzle but with an expansion ratio of 45 and a sounding rocket version which is a scaled down version with an expansion ratio of 6.5. These expatiation ratios are selected as Nammo has requested these nozzles to be tested.

2.4.1. Nominal expansion ratio nozzle

The input parameters used for the performance program are shown in table 2.4. The input parameters are taken from the SOW in appendix A and from finding the initial angle and final angle from figure 2.1. The nozzle created is the nominal nozzle with expansion ratio of 12. The shape of the nozzle is a bell shaped nozzle with a 80% length.

Table 2.4: Baseline rocket input parameters for the performance program

Parameter	Value
Total temperature	2721 K
Total pressure	35 bar
Molar mass	22 g/mol
Ratio specific heats (γ)	1.13
Throat diameter	145 mm
Area expansion ratio	12
Initial angle	36
Final angle	10

The python program calculated the following shape and performance. The performance parameters are given in table 2.5 and the shape is shown in figure 2.9.

Table 2.5: Baseline rocket performance parameters calculated from the performance program

Parameter	Value	Requirement by Nammo
Thrust vacuum	104.58 kN	100 kN
Isp vacuum	293.6 s	289.5 s
Thrust coefficient	1.802	-
Characteristic velocity	1598.04 m/s	-
Exit velocity	2668.31 m/s	-
Mass flow	36.17 kg/s	-
Mach number	3.191	-
Exit pressure	42326.29 Pa	-
Exit temperature	1637.33 K	-

As can be seen in table 2.5, the basic nozzle shape satisfies the requirements by Nammo, the thrust and Isp is a little higher than requested. The shape of the nominal nozzle can be seen in figure 2.9 and has a shape that is comparable to other nozzles in literature [13, 24, 43, 46]. The exact parameters of the nozzle are found in table 2.6.

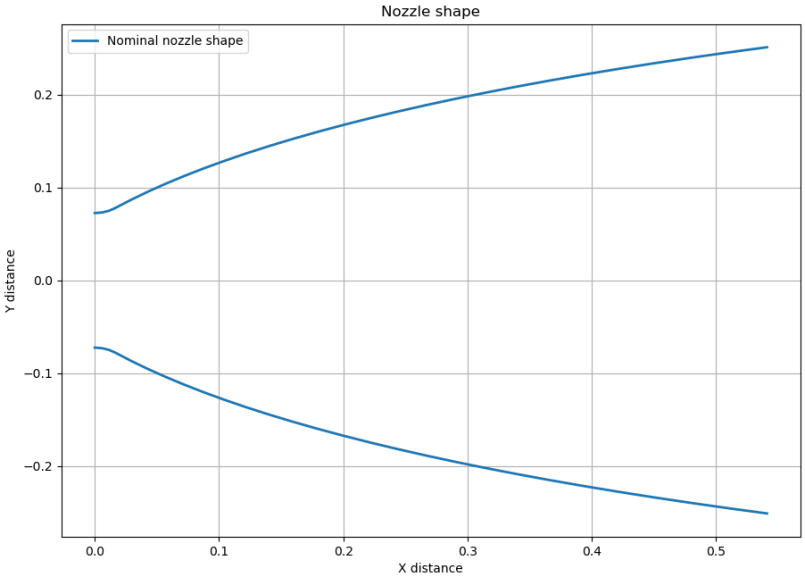

Figure 2.9: Figure showing the basic nozzle shape generated by the shape program

Table 2.6: Basic nozzle shape parameters for the nominal nozzle

Parameter	Value
Throat radius	72.50 mm
Nozzle length	541.01 mm
Nozzle exit radius	251.15 mm
Expansion ratio	12
Initial angle	36
Final angle	10
Throat radius of curvature	27.70 mm

2.4.2. Upper stage nozzle

The input parameters used for the performance program are shown in table 2.7 the inputs are gathered the same way as the nominal nozzle. The nozzle created is the upper stage nozzle with expansion ratio of 45.

Table 2.7: Second stage rocket input parameters for the performance program

Parameter	Value
Total temperature	2721 K
Total pressure	35 bar
Molar mass	22 g/mol
Ratio specific heats (γ)	1.13
Throat diameter	145 mm
Area expansion ratio	45
Initial angle	41.2
Final angle	7.2

The python program calculated the following shape and performance. The performance parameters are given in table 2.8 and the shape is shown in figure 2.10. The exact nozzle parameters are given in table 2.9

Table 2.8: Second stage rocket performance parameters calculated from the performance program

Parameter	Value	Requirement by Nammo
Thrust vacuum	113.99 kN	107.7 kN
Isp vacuum	321.3 s	311.8 s
Thrust coefficient	1.972	-
Characteristic velocity	1598.04 m/s	-
Exit velocity	2992.01 m/s	-
Mass flow	36.17 kg/s	-
Mach number	3.928	-
Exit pressure	8351.51 Pa	-
Exit temperature	1358.46 K	-

Table 2.9: Basic nozzle shape parameters for the upper stage nozzle

Parameter	Value
Throat radius	72.50 mm
Nozzle length	1243.23 mm
Nozzle exit radius	486.34 mm
Expansion ratio	45
Initial angle	41.2
Final angle	7.2
Throat radius of curvature	27.70 mm

As can be seen, the basic nozzle shape for the upper stage nozzle satisfies the requirements by Nammo, the thrust and Isp is a little higher than requested. The shape seen in figure 2.9 has a shape that is comparable to other nozzles in literature [13, 24, 43, 46].

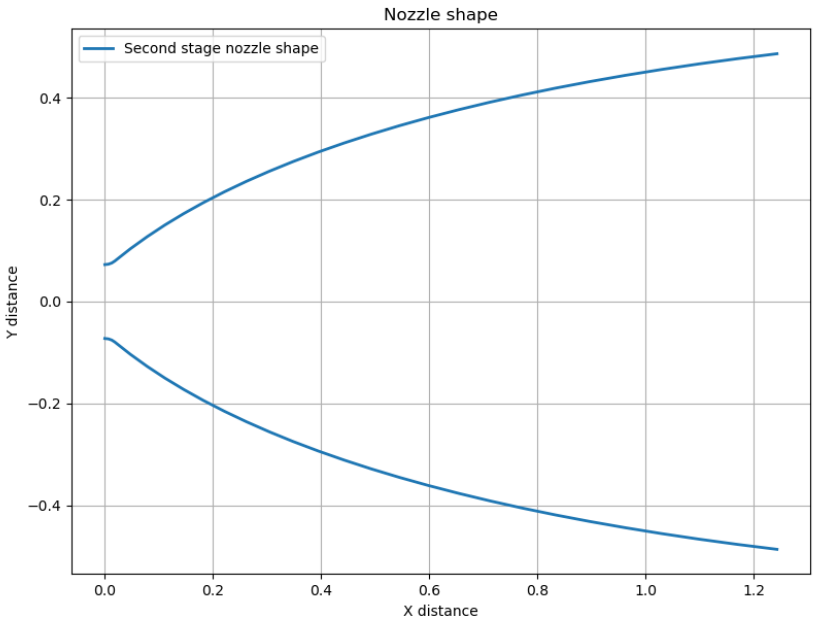

Figure 2.10: Figure showing the second stage nozzle shape generated by the shape program

2.4.3. Sounding rocket nozzle

The input parameters used for the performance program are shown in table 2.10. The nozzle tested is the sounding rocket nozzle with expansion ratio of 6.5.

Table 2.10: Sounding rocket nozzle input parameters for the performance program

Parameter	Value
Total temperature	2721 K
Total pressure	35 bar
Molar mass	22 g/mol
Ratio specific heats (γ)	1.13
Throat diameter	83 mm
Area expansion ratio	6.5
Initial angle	33.5
Final angle	12

The python program calculated the following shape and performance. The performance parameters are given in table 2.11 and the shape is shown in figure 2.11. The exact nozzle shape parameters can be found in table 2.12.

Table 2.11: Sounding rocket nozzle performance parameters calculated from the performance program

Parameter	Value	Requirement by Nammo
Thrust vacuum	32.22 kN	29.0 kN
Isp vacuum	277.2 s	275.4 s
Thrust coefficient	1.701	-
Characteristic velocity	1598.04 m/s	-
Exit velocity	2472.07 m/s	-
Mass flow	11.85 kg/s	-
Mach number	2.827	-
Exit pressure	92253.40 Pa	-
Exit temperature	1790.87 K	-

As can be seen, the basic nozzle shape satisfies the requirements by Nammo, the thrust and Isp is slightly higher than requested. The rest of the output from the performance program shows that the basic nozzle has an ample performance. The shape seen in figure 2.9 has a shape that is comparable to other nozzles in literature [13, 24, 43, 46].

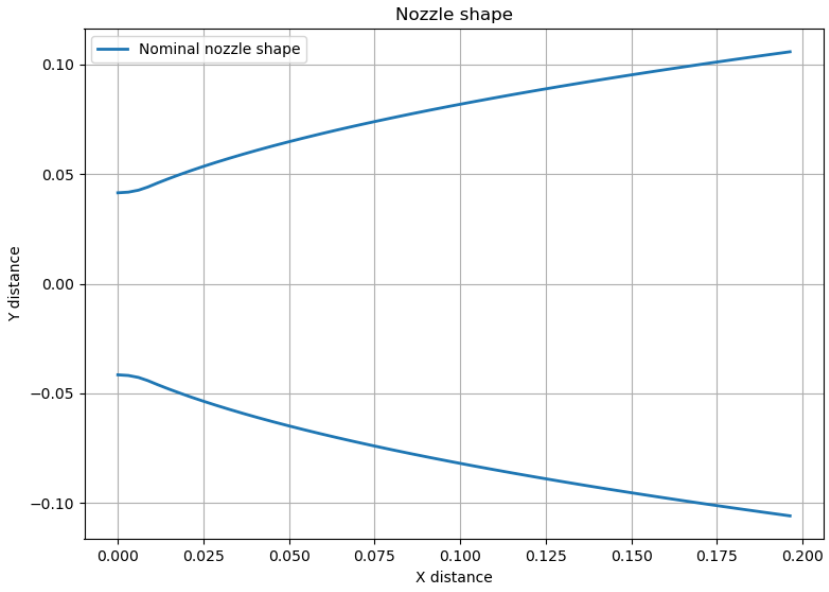

Figure 2.11: Figure showing the sounding rocket nozzle shape generated by the shape program

Table 2.12: Basic nozzle shape parameters for the sounding rocket nozzle

Parameter	Value
Throat radius	41.50 mm
Nozzle length	196.36 mm
Nozzle exit radius	105.80 mm
Expansion ratio	6.5
Initial angle	33.5
Final angle	12
Throat radius of curvature	15.85 mm

2.5. Discussion and summary of shape and performance programs

In this section a brief discussion and a summary of the created methods is given.

2.5.1. Discussion on shape calculation approach

The shape calculation of the basic nozzle shape was done with the first shape calculation approach for the first iteration of the CFD calculations. Unfortunately, it was discovered that the first shape calculation approach would produce excessive angles for cases with higher expansion ratios. The initial angle would go to 50 degrees for a nozzle with expansion ratio of 45. This was a limitation of the method used for calculation the shape and it can be concluded that this method only produced adequate results for lower expansion ratio nozzles. Therefore, the first set of CFD simulations could be discarded. At this point, it was decided to find a second approach for the shape calculation. The chosen method was to use Beziér curves to create the nozzle shape. This approach uses skewed parabolas instead of a normal parabolic shape [16, 31, 32, 37]. With the use of skewed parabolas one additional boundary condition could be used, thereby constraining the shape to have the desired initial and final angle as well as defining the length of the nozzle. The second shape calculation approach is fully explained in section 2.1.1. The Beziér curve method was also validated with literature. The validation of this method can be found in section 2.3. Additionally, a comparison between the two shape approaches can be found in section 2.1.2. With the new shape calculation for the baseline nozzle, the CFD calculations could be redone without the excessive angles at the initial angle of the nozzle. The explanation of shape program 1 is given in the appendix and can be found in appendix C. The shape of the nozzles created with the shape program are close to the validation nozzles. The main objective of this work is to compare the SSSL nozzle and the SM nozzle and find the general trend in the effects on the amplification factor when changing certain aspects of the nozzle. Therefore, a perfect shape is not needed, the effects of the non perfect shape will be on all the nozzles simulated and hence the general trend and a comparison can still be performed. Hence for this work the shape program is deemed accurate enough.

2.5.2. Discussion on performance program

The performance program calculates the ideal rocket performance of the nozzles and does not take any quality factors into account. The main task of the performance program is to see the predicted performance and to compare with the results from the CFD. It is expected that the CFD results have a little lower performance than the performance program as the CFD calculations take into account some of the losses that occur in a rocket nozzle. If the CFD simulations show a large difference with the results from the performance program, then the results from the CFD needs to be checked or a new simulation has to be run. The performance program was also tested against some validating cases. The performance program calculated an expected result and was deemed sufficiently validated for this work.

2.5.3. Summary of shape and performance program

In this chapter a method of determining the ideal rocket nozzle performance was created in order to verify the CFD calculations and to compare to the requirements by Nammo. Additionally, a method was created to generate a nozzle shape from the throat of the nozzle to the exit of the nozzle by the

use of skewed parabolas. This method was used to create the three different basic nozzle shapes for the nominal, upper stage and sounding rocket nozzles that are used in this study. The programs were validated against three cases from literature and found to be valid enough for this work. Even though the methods do not produce a perfect nozzle, the nozzles created are compared to each other and therefore the inaccuracies of the method does not have a large impact for the comparison. Therefore, the methods produced are deemed valid for the use in this work.

3

Python mass model program

In this chapter the model that converts the different performance parameters to a mass difference between the SSSL and SM nozzle is discussed. The model is created in order to find the mass difference between the two nozzles. The model will take the different performance parameters as input and convert this to a mass gain based on the Isp and the required torque to actuate the nozzle. The chapter starts by finding all the parameters needed for the model. Then an explanation of the different functions of the program is presented. Finally, an example calculation is given. For all nozzle representations the flow of gases goes from the left to the right.

The nozzles are compared in the following three aspects: Specific impulse (Isp), aerodynamic torque and amplification factor. The Isp contribution is computed last as the two other categories influence the empty and take-off mass of the rocket which are needed to calculate the delta V. Where delta V is the velocity change that the rocket can achieve with the amount of propellants used. In figure 3.1 a flow chart of the inputs and outputs to the mass model program is presented. Each section of the program is discussed in the following sections. As the Isp influences the amount of propellant needed, the contribution to the mass from the Isp is called the propellant penalty.

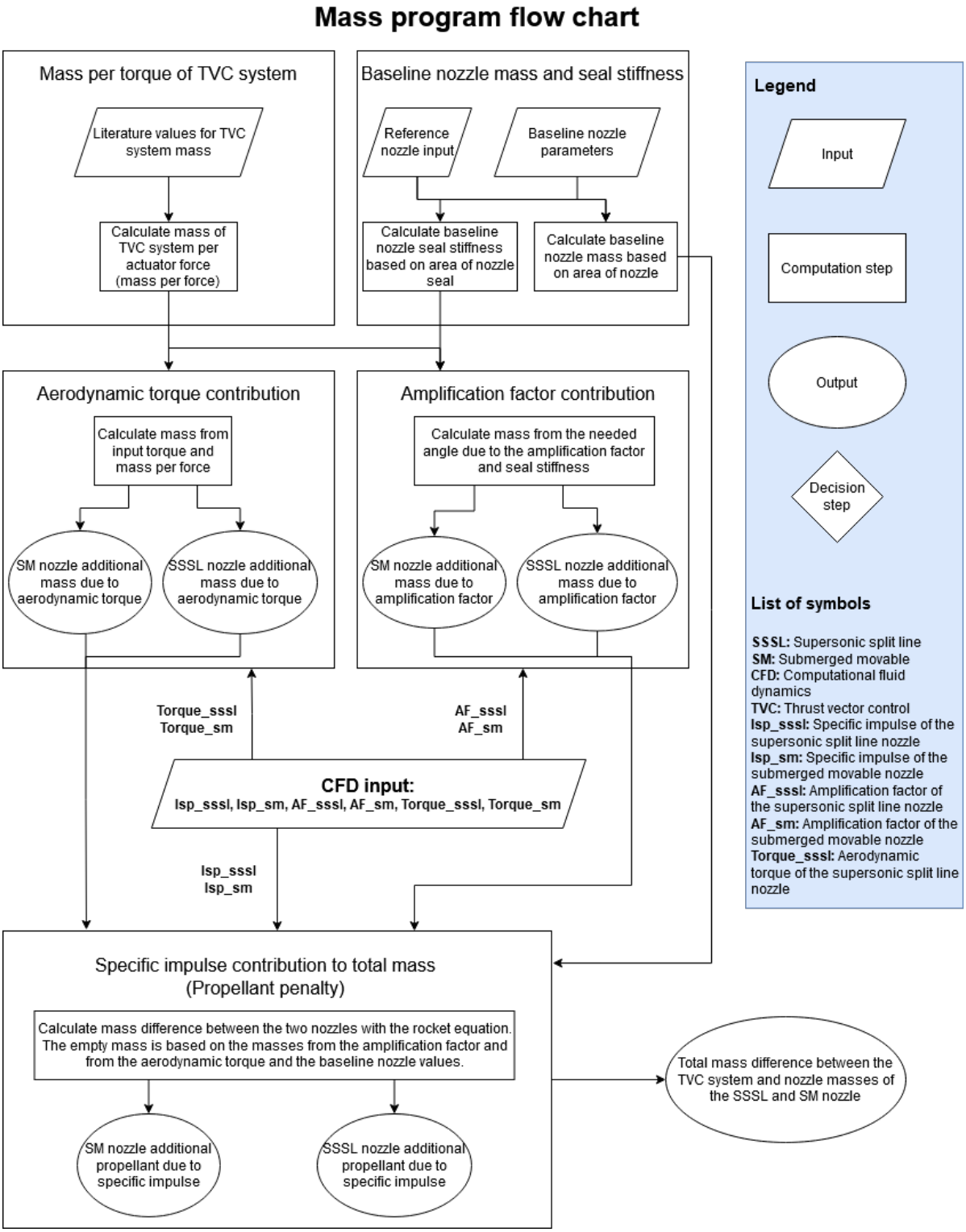

Figure 3.1: Figure of the computations steps in the mass model program. The figure shows all the interconnections between the inputs and outputs.

3.1. Baseline rocket parameters

The baseline rocket parameters are computed in the baseline nozzle mass and seal stiffness part of the flow chart shown in figure 3.1. The baseline rocket parameters are also used in the computation of the propellant penalty.

The baseline rocket mass for the mass model is calculated from the propellant mass, using the relations by Zandbergen to find the empty mass of the rocket [13]. The dry mass of the rocket is around 15.85% of the propellant mass [13]. The relation between the propellant mass and the dry mass is developed on solid rocket motors. Since there are some similarities between solid rocket motors and hybrid rocket motors, such as the solid fuel grain, the relation can give a decent estimate. There are also differences between solid and hybrid rocket motors such as the storage of the liquid oxidizer, feed system and pumps. However, even though the estimate would be more around 25% of the propellant mass it would not alter the general comparison between the two nozzles since they will use the same base mass. This is explored in the sensitivity analysis at the end of this chapter.
The propellant mass of the baseline nozzle is calculated by multiplying the mass flow with the required burn time. The required burn time by Nammo is 90s and can be found in the SOW in appendix A. From equation (2.4) the mass flow of the rocket is found and can then be multiplied by the 90s burn time resulting in the propellant mass. If the burn time is extended to 180s the nozzle with the highest Isp would perform better than with a burn time of 90s. This is explored in the sensitivity analysis at the end of this chapter.
The nozzle mass that is used for the baseline rocket is a scaled up version of the nozzle in the study by Ellis and Berdoyes [23]. This nozzle is used as the study also compares the SSSL and SM nozzle systems. The nozzle is scaled on the surface area of the nozzle. It is assumed that the nozzle mass scales linearly with the nozzle surface area. The surface area is approximated with a truncated cone that has the same inlet and outlet diameter as the real nozzle. The area of a truncated cone can be computed with equation (3.1). The outer radius is denoted by r_o and the inner radius by r_i. In figure 3.2 the definition of these radii are shown, in the figure the cone is seen head on. The height of the cone is denoted by h. A denotes the surface area. The calculated values are presented in table 3.1. It can be seen that the mass per area is quite high, this is a result of not taking into account the surface area before the throat. The SM nozzle has a larger area before the throat and it can be seen that its mass per area is higher than the SSSL nozzle. Due to this estimation, the assumption of a linear relation will not hold for a nozzle much larger than the one in the study by Ellis and Berdoyes [23]. However the size difference is quite similar with only a size factor of 1.53, therefore for this work the estimation of nozzle mass is accurate enough. The table also includes the scaled nozzle mass. The SM nozzle mass and the TVC system mass for the baseline rocket are used to calculate the empty mass excluding these two systems. The dry mass excluding nozzle and TVC system can be found in table 3.4.

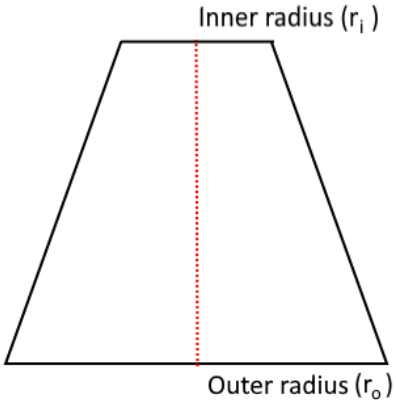

Figure 3.2: Definition of the inner and outer radius of a truncated cone, the cone is seen head on

$$A = \pi(r_i + r_o)\sqrt{h^2 + (r_o - r_i)^2}) \tag{3.1}$$

Table 3.1: Table showing the scaled nozzle mass of the baseline nozzle based on values from literature

Parameter	Literature nozzle [23]	Baseline nozzle
Throat radius	27.55 mm	72.50 mm
Exit radius	187.50 mm	251.15 mm
Nozzle length	537.55 mm	541.01 mm
Area	0.38m^2	0.58 m^2
Scaling factor	1	1.53
Mass SM nozzle	16.42 kg	25.13 kg
Mass SSSL nozzle	9.30 kg	14.23 kg

3.2. Seal stiffness

The seal stiffness computation takes part in the baseline nozzle mass and seal stiffness block in the flow chart in figure 3.1. The seal stiffness is used in the computation of the amplification factor contribution.

The torque needed to actuate the nozzle is calculated based on values for seal stiffness taken from literature [23]. The SSSL nozzle has the benefit of having a self sealing split [43]. This means that the torque to overcome the seal stiffness is much less (65%) for the SSSL nozzle than the SM nozzle. The values from the paper by Ellis and Berdoyes are used for the seal stiffness [23]. However, the stiffness is scaled on the approximate area of the nozzle seal. It is assumed that the seal stiffness scales linearly with seal area. Since the seal is made from alternating layers of elastomers and metal sheets the stiffness will increase as the area of the seal increases. From the report of Cooke on the design of a flex seal nozzle the equation for the force by the seal can be described as shown in equation (3.2) [18]. F is the force needed to deflect the seal to δ degrees, G is the shear modulus, A is the area, n is the number of layers of elastomers and t_r is the thickness of the layers. From this equation it can be seen that the force is directly proportional to the seal area. Therefore, it was chosen to scale the seal torque on the approximate seal area. The seal area of the nozzle from Ellis and Berdoyes is computed from the approximate inner and outer diameter of the seal. The approximation is made with help from the illustrations of the nozzle in the paper [23]. The seal in the baseline rocket will have the same width and start at the same distance from the throat as in the paper. An illustration of this approximation is shown in figure 3.3. The values for the flex seal area, distance, scaling factor and seal stiffness are presented in table 3.2. It can be seen that the SSSL nozzle has a lower seal stiffness than the SM nozzle this is due to the self sealing property of the SSSL nozzle and the fact that the pressure is much lower at the split of the SSSL nozzle than the split of the SM nozzle [11, 15, 23, 43].

$$F = \frac{\delta \cdot G \cdot A}{n \cdot t_r} \tag{3.2}$$

Table 3.2: Scaled nozzle stiffness based on the seal area for the nozzle from literature and the baseline nozzle

Parameter	Literature nozzle [23]	Baseline nozzle
Throat diameter	55.10 mm	145.00 mm
Seal inner diameter	150.00 mm	240.00 mm
Seal outer diameter	200.00 mm	290.00 mm
Area seal	13744.47 mm^2	20813.05 mm^2
Scaling factor	1	1.51
SM nozzle stiffness	136.62 Nm/deg	206.88 Nm/deg
SSSL nozzle stiffness	48.30 Nm/deg	73.14 Nm/deg

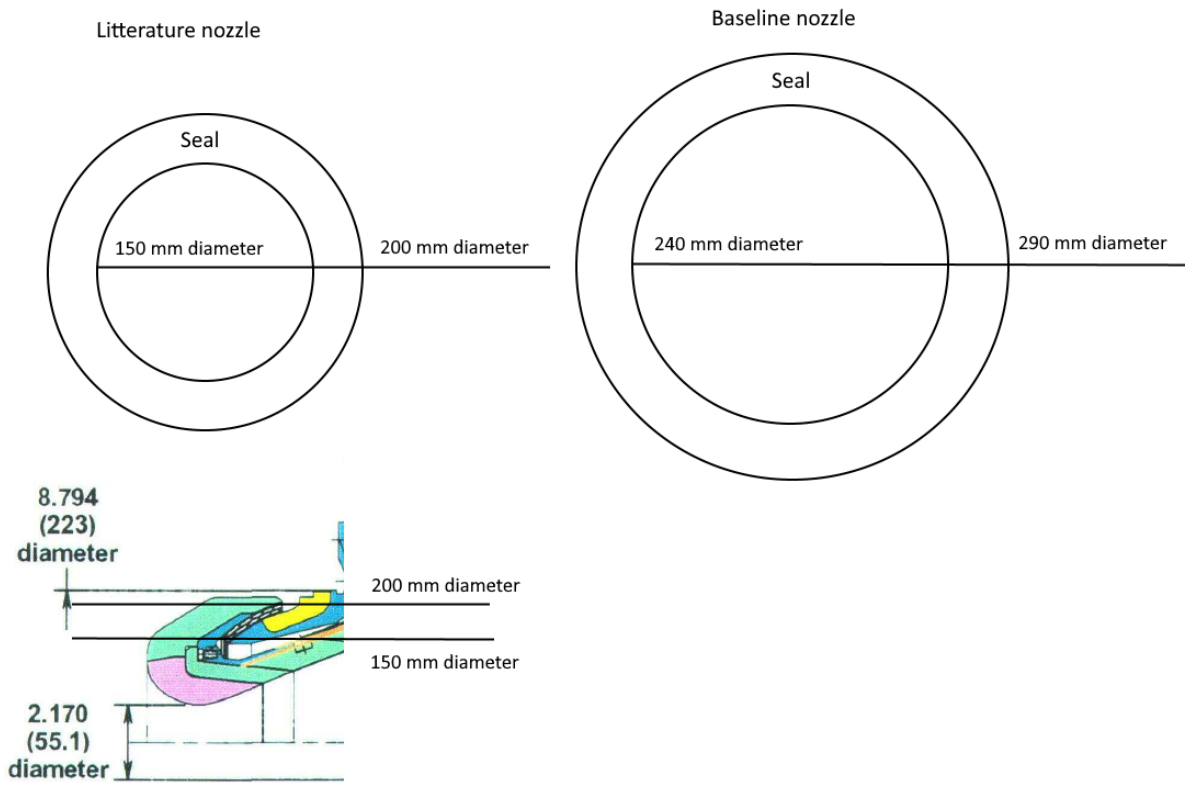

Figure 3.3: Figure of the approximated inner and outer diameter of the seal for the nozzle in the paper by Ellis and Berdoyes [23]. The approximated dimensions for the baseline rocket is also presented.

3.3. Torque to mass relation

The torque to mass relation is computed in the mass per torque of TVC system part of the flow chart shown in figure 3.1. The torque to mass relation is used in the computation of the aerodynamic torque contribution and the amplification factor contribution. Only the contributions from the aerodynamic torque and seal torque are included in the mass calculations. The torque from gravity, inertia and other external torques are neglected. To neglect these torques is of benefit to the SM nozzle as it has the higher mass of the two systems however, as the nozzles in this study are fairly small compared to large launchers it is assumed that the difference in the torque created from these sources are small.

To calculate the mass gain from the exerted torques a model to go from torque to mass is needed. However, as most actuators for TVC systems are rated in force, the mass per force is calculated. From the CFD calculations and from the seal stiffness a torque is obtained. To use the mass per force value the moment arm of the actuator is needed. The moment arm is approximated by comparing to the two nozzles in the paper by Ellis and Berdoyes [23]. When looking at the two nozzles, the attachment point for the actuator is located at different lengths from the centre line. The SM nozzle is located at around 175mm and the SSSL nozzle is located at around 130mm. These figures are based on the figure of the two nozzles in the paper by Ellis and Berdoyes, the figure is shown in figure 3.4 [23]. The measurements are shown in red. In the mass model it is assumed that both the SM and SSSL nozzle have the same attachment point and that the actuator works in a horizontal direction with respect to the centre line. In the paper by Ellis and Berdoyes the attachment point is located at around half the nozzle length. Using the same approach for both the SM and SSSL nozzle, the attachment point is located at around 175mm. The dimensions of the basic nozzle shape can be seen in figure 2.9. Thus, the moment arm in the mass model is taken as 175mm. The moment from the CFD calculations and from the seal stiffness can then be converted to a force on the actuator by dividing the torque with the moment arm.

The mass per force of the TVC system is found by using values from literature. Various different actuators for different size TVC systems are used to create a relation between the mass and the force of the

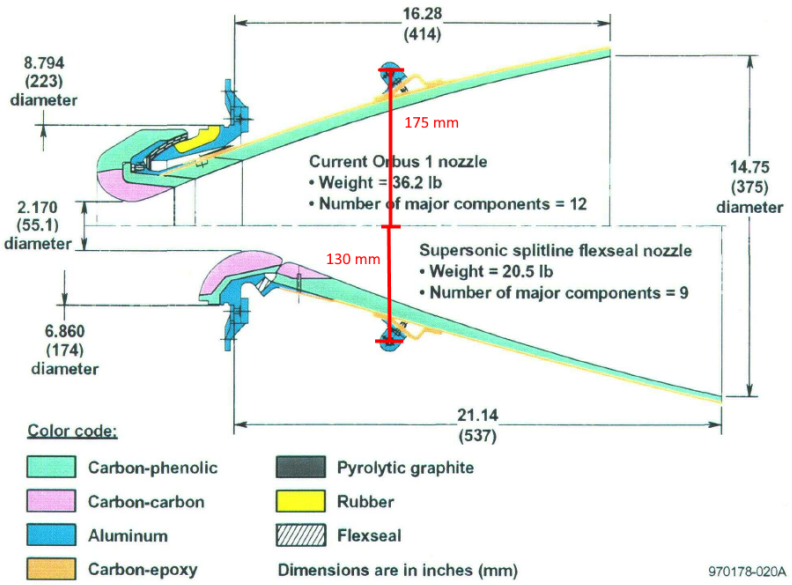

Figure 3.4: Figure showing the approximated length from the centre line to the attachment points for the SM and SSSL nozzle. These lengths are shown in red. Figure adapted from [23]

actuator. For the actuators that only have data for a single actuator it is assumed that two actuators are needed for the TVC system. Additionally, the controller mass has not been taken into account for these hypothetical systems. The data size for the model is relative small. However, both the SM nozzle and the SSSL nozzle will use the same mass per force number. Therefore, the accuracy of the mass per force figure has no impact on the comparison. In table 3.3 the numbers from literature are presented. The mass per force is computed from the trend that can be seen in figure 3.5. The calculated trend has the equation as presented in figure 3.5. Where y is the mass of the actuator and x is the force exerted upon the actuator. In this equation it can be seen that there is a base mass of around 5kg. This mass is added to the structural mass of the nozzle. Thereby, the mass contributions from the torques are clearly visible.
In a real rocket the actuator would have a safety margin on the largest exerted force however, for this mass model the linear relation between actuator mass and actuator force is used.

All the relations and equations needed for the mass model have been developed and a summary of all the values are given in table 3.4.

Table 3.3: Table showing mass of actuator system divided by actuator force values for various TVC systems

Actuator/Rocket	Actuator force [kN]	Mass of system/two actuators [kg]	Mass per force [kg/kN]
P120 [20]	135	120	0.89
Z40 [20]	55	60	1.09
SRB-A [35, 55]	106	83.8	0.79
Moog [51]	180.60	113.40	0.63
Moog [51]	96.65	51.71	0.53
Moog [51]	52.49	29.03	0.55
Moog [51]	20.61	11.79	0.57
Moog [51]	14.19	16.33	1.15
Moog [51]	3.31	7.26	2.15

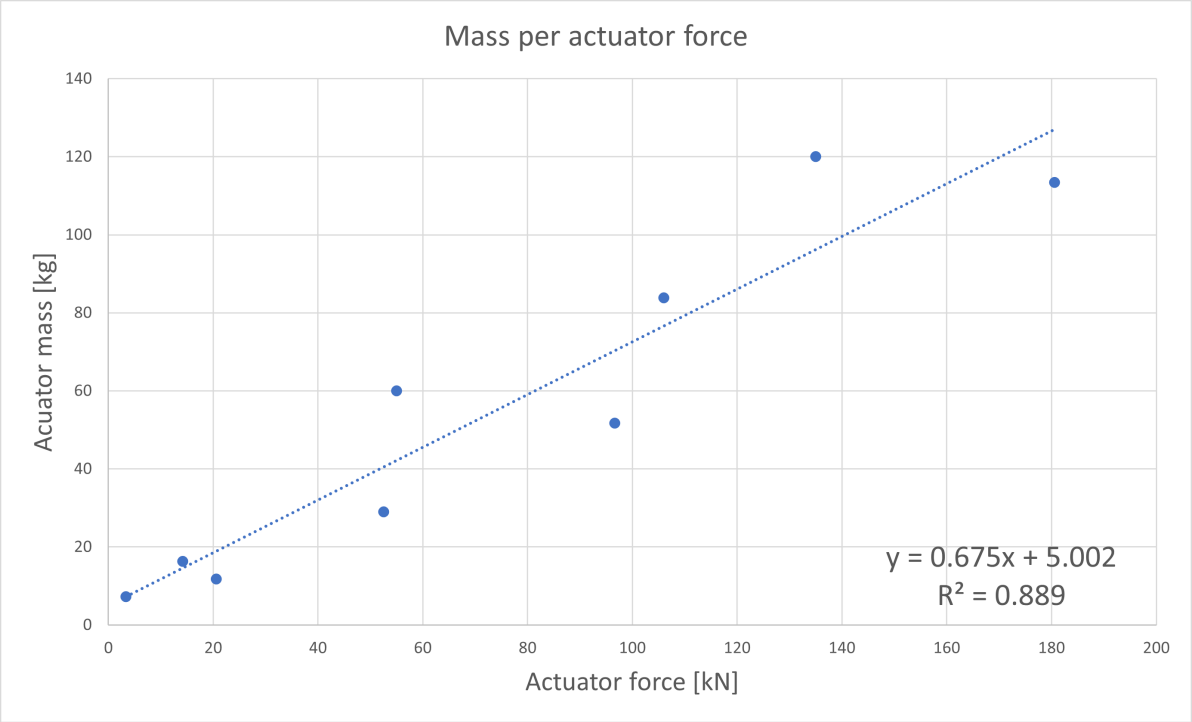

Figure 3.5: Figure showing the trend of actuator mass plotted against actuator force. In the right corner is the linear fit equation and R^2 value.

3.4. Aerodynamic torque contribution

The calculation of the aerodynamic torque contribution can be seen in the aerodynamic torque contribution block in the flow chart in figure 3.1. The additional mass of the aerodynamic torque is used later in the calculation of the propellant penalty.
The aerodynamic torque contribution is calculated by taking the aerodynamic torque from the input for both SSSL and SM nozzle and converting this torque to a force on the actuator. This is done by dividing the torque with the moment arm, which is 0.175m. The force is then multiplied with the mass per force figure established in the torque to mass relation. The mass per force equation is found in table 3.4.

3.5. Amplification factor contribution

The calculation of the amplification factor contribution can be seen in the amplification factor contribution block in the flow chart in figure 3.1. The additional mass of the amplification factor will then be used later in the calculation of the propellant penalty.
The contribution from the amplification factor is computed by using the seal stiffness and the mass per force figure. The amplification factor has the effect of reducing the angle needed to achieve the desired thrust vector angle. To find the actual needed angle, equation (3.3) is used. α_{needed} is the needed nozzle deflection to obtain the requested thrust vector angle. This angle is denoted by $\beta_{required}$. AF is the amplification factor of the nozzle.

$$\alpha_{needed} = \frac{\beta_{required}}{AF} \tag{3.3}$$

The angle obtained from the calculation will then be multiplied with the seal stiffness of the nozzle type. The torque obtained from this step is converted to a force on the actuator and this force is used in the mass per force equation. The equation can be found in table 3.4.

3.6. Propellant penalty

The calculation of the influence of the specific impulse can be seen in the propellant penalty block in the flow chart in figure 3.1. This is the final step in the calculation and the total mass difference between

Table 3.4: Summary of baseline rocket parameters and mass per force equation

Rocket part	Value
Fuel	3255.00 kg
Dry mass (excluding nozzle and TVC system)	456.95 kg
Payload mass (North star payload [53])	50.00 kg
SM nozzle mass	25.13 kg
SSSL nozzle mass	14.23 kg
SM nozzle seal stiffness	206.88 Nm/deg
SSSL nozzle seal stiffness	73.14 Nm/deg
Mass of TVC system based on actuator force	Actuator mass [kg] $= 0.675 \cdot$ (Actuator force [kN]) $+ 5.002$

the SSSL and SM nozzle systems are found from adding all the contributions to each other.
The calculation of the contribution from Isp is done by comparing the difference in delta V (ΔV) produced by the propellants. From the rocket equation the ΔV of the rocket can be found [40]. The ΔV of the rocket is the time integration of the acceleration produced by the rocket. The rocket equation is given in equation (3.4). Where m_0 is the total initial mass of the rocket and m_1 is the total final mass of the rocket. v_{eq} is the exit velocity of the exhaust gasses. To link the Isp to the rocket equation one can use equation (2.13). It is assumed that v_{eq} stays constant for the mass model. The initial mass and final mass of the rocket for the two nozzles is different due to the effect of the aerodynamic torque contribution and the amplification factor contribution. This also has an effect on the propellant penalty and hence the propellant penalty can only be calculated after the other two contributions have been determined.

$$\Delta V = v_{eq} \cdot ln\frac{m_0}{m_1} \tag{3.4}$$

When the difference in ΔV between the two nozzles is found, the difference can be used to determine the amount of propellant that needs to be added. The difference in ΔV is used to determine the propellant mass that would produce the ΔV difference between the two nozzles. Using equation (3.5), where m_p is the propellant mass used, the propellant penalty of one of the two nozzles can be found. The propellant penalty is a comparison between the two nozzles, which means that one of the nozzles will always have 0 kg addition in the mass model.

$$m_p = m_1(e^{\left(\frac{\Delta V}{v_{eq}}\right)} - 1) \tag{3.5}$$

3.7. Mass model example calculation

In this section an example calculation of the mass model is presented. The inputs to the mass model program are the following:

Parameter	SSSL nozzle	SM nozzle
Specific impulse	280 s	275 s
Aerodynamic torque	2000 Nm	500 Nm
Amplification factor	1.5	1

The program calculates the contribution from each parameter using the methods described in the preceding sections. The calculation of the aerodynamic torque contribution is straight forward. The torque is converted to a force and the mass is found from the mass per force equation found in table 3.4.

Nozzle	Actuator force [kN]	Actuator mass [kg]
SSSL nozzle	11.43	7.72
SM nozzle	2.86	1.93

The program continues on to calculate the contribution from the amplification factor. The actual vectoring angle needed is calculated first and the actual vectoring angle is multiplied by the seal stiffness. The torque is converted to mass with the same relations used in the aerodynamic torque step. This example will use the 5 degree case.

Nozzle	Amplification factor [-]	Angle needed [deg]	Actuator force [kN]	Actuator mass [kg]
SSSL nozzle	1.5	3.33	1.39	0.94
SM nozzle	1	5	5.91	3.99

The propellant penalty is calculated from the contributions obtained from the amplification factor and from the aerodynamic torque. The total rocket mass for the two systems is different and this influences the propellant penalty calculation. The following numbers are used in the calculations of the propellant penalty.

Nozzle	Isp [s]	Total mass [kg]	Empty mass [kg]	ΔV [m/s]	Fuel mass to equalize ΔV (propellant penalty) [kg]
SSSL nozzle	280	3789.84	534.84	5378.56	0
SM nozzle	275	3798.00	543.00	5247.45	24.55

The final calculation that is performed is the addition of all the mass contributions. In the final mass the nozzle mass is also included, the nozzle mass is including the 5 kg TVC base mass. The masses are shown in table 3.5. In this example it can be seen that the SSSL nozzle has a much lower total mass than the SM nozzle. The two main contributing factors to this is the nozzle structural mass and the addition to specific impulse.

Table 3.5: Table showing all the additions to the final nozzle mass from the mass model example calculation. The nozzle mass is including the 5 kg base mass of the TVC system.

Contribution	SSSL nozzle masses [kg]	SM nozzle masses [kg]
Aerodynamic torque	7.72	1.93
Amplification factor	0.94	3.99
Propellant penalty	0	24.55
Nozzle mass	19.23	30.13
Total mass	27.89	60.60

3.8. Duty cycle of the thrust vectoring

The thrust vectoring system does not need to vector during the whole flight time. Therefore, a duty cycle is defined in order to mimic a real world scenario. It is assumed that the vectoring is performed always at the maximum deflection of 5 deg. The duty cycle is defined as shown in equation (3.6). It is assumed that the duty cycle in this work is 0.25. Hence, the TVC system is vectoring at 5 degrees for 25% of the time and 75% of the time it is vectoring at 0 degrees. In order to find the sensitivity of the duty cycle the actual duty cycle needed for the SSSL and SM nozzle system mass to be equal is calculated in the results. In only one of the cases the masses could be equalized. In the other two cases the SSSL nozzle was the lighter option. In the case with where the masses could be equalized the duty cycle needed to be 0.90. Furthermore, the assumption that the TVC system always vectors at 5 degrees is an over estimation of the use of the TVC systems. The TVC system most likely vectors at much smaller angles for small adjustments. Therefore, for this work a duty cycle of 0.25 seems as

a reasonable estimate.

$$\text{Duty cycle} = \frac{\text{Duration needed of TVC activation}}{\text{Flight time}} \tag{3.6}$$

The mass of the nozzle system at a duty cycle of 0.25 is calculated by multiplying the duty cycle with the mass of the nozzle system a 5 degree thrust vectoring plus the mass of the nozzle system at 0 degree thrust vectoring multiplied with 1 minus the duty cycle. This is shown in equation (3.7), where m_{dc} is the mass of the nozzle system at specified duty cycle, m_{5deg} is the mass of the nozzle system at 5 degrees with duty cycle 1, dc is the duty cycle and m_{0deg} is the mass of the nozzle system at 0 degrees with duty cycle 1.

$$m_{dc} = m_{5deg} \cdot dc + m_{0deg} \cdot (1 - dc) \tag{3.7}$$

3.9. Sensitivity analysis and uncertainties

The mass model was designed as a tool for a direct comparison between the SSSL nozzle and the SM nozzle. This section will explore the sensitivity of the mass model to changes in the input parameters.

3.9.1. Uncertainties

The baseline nozzle parameters have been established by scaling the nozzle directly from another nozzle. Therefore, there are no uncertainties tied to the mass values of the baseline nozzle. In order to increase the accuracy of the mass per nozzle area a comprehensive model would need to be built. Only if the SSSL nozzle and the SM nozzle would use different models with different uncertainties the comparison between the two nozzle could be affected in a more comprehensive way. However as the two nozzles use the same model with the same uncertainty the comparison between the two nozzles is still valid.

The seal stiffness has been established in the same way as the baseline nozzle parameters and have therefore no direct uncertainty related to the seal stiffness.

The largest uncertainty comes from the relation between the actuator mass and the actuator force. From the linear regression the coefficients of the linear equation were calculated. These could then be used to calculate the actuator mass when the force on the actuator is known. The R^2 value for this equation was 0.889. Using the following two formulas the uncertainty on the linear regression can be established.
When considering the equation of type:

$$y = a \cdot x + b$$

The two constants a and b have the following uncertainties:

$$\sigma_a = a \cdot \sqrt{\frac{(\frac{1}{R^2} - 1)}{n - 2}}$$

Where n is the sample size and σ_a is the uncertainty of the constant a.

$$\sigma_b = \sigma_a \cdot \sqrt{\frac{\sum x^2}{n}}$$

Where σ_b is the uncertainty on the constant b. When both these uncertainties have been calculated the new equation is as follows:

$$y = (0.675 \pm 0.09) \cdot x + (5.002 \pm 8.4)$$

3.9.2. Sensitivity analysis

In order to see the sensitivity of the inputs on the outputs of the model the numbers from the results of the comparison between the nominal SSSL nozzle with the split located at 1.75 and the SM nozzle. In table 3.6 the output values are tracked vs the input change. The output is the difference in mass difference for a duty cycle of 0.25. All the inputs are increased with the given percentage. A negative percentage on the output means that the difference between the two nozzles has decreased if the percentage goes under -100% it means that the SM nozzle has become the lighter option. Only the amplification factor of the SSSL nozzle is tested as the amplification factor of the SM nozzle will not change. What can be seen is that the mass model is highly sensitive to a change in the Isp. The output changes with 138% when the Isp of the SSSL nozzle only changes with 2%. The other parameters did not change the output of the model in a high degree. Additionally, the sensitivity to a change in duty cycle, empty mass, burn time and seal stiffness were performed. For a change in duty cycle of 100% resulting in a duty cycle of 0.5 the mass difference changed with 23.18% in favour of the SM nozzle. For a change in empty mass of 10% the mass difference between the SSSL nozzle and SM nozzle system changed with 1.54% in favour of the SM nozzle. For a change in burn time from 90s to 180s (100% increase) the mass difference between the two nozzles changed with 21.92% in favour of the SM nozzle. Finally, a change in the seal stiffness of 10% results in a change of 0.98% in the mass difference in favour of the SSSL nozzle. It should be noted that the SSSL nozzle remained the lighter option for all the test cases of the sensitivity study.
To conclude, the mass model is very sensitive to a change in Isp and hence any errors in the Isp will have an impact on the mass model results. Therefore, the Isp will have to be checked to see if it make sense otherwise it might have a large impact on the mass model.

Table 3.6: Table showing the change of the output of the mass model when changing a input.

Input	Input change	Output change
Aerodynamic torque SM	10%	0.01%
Aerodynamic torque SSSL	10%	-2.31%
Propellant penalty (Isp) SM	2%	-66.17%
Propellant penalty (Isp) SSSL	2%	138.10%
Amplification factor SSSL	10%	0.28%
Duty cycle	100%	-23.18%
Empty mass	10 %	-1.54%
Burn time	100 %	-21.92%
Stiffness of seal	10%	0.98%

3.10. Summary and conclusion to mass model

In this chapter a method of comparing the SSSL nozzle and the SM nozzle system mass has been developed. The model uses the amplification factor, Isp and aerodynamic moment as input and calculates the mass difference between the nozzle systems. The model has some uncertainties, but for the comparison between the two nozzle systems these uncertainties play no major role as both nozzles use the same model. Additionally it was found that the model is highly sensitive to a change in Isp. Therefore, the Isp of the nozzles is checked against the performance program to see if they are reasonable. Furthermore, the numbers used for the seal stiffness, empty mass, duty cycle and burn time did not have a large effect on the outcome when these numbers were changed.
To conclude, the mass model is a tool to compare the SSSL nozzle and SM nozzle system and can not predict the exact mass of the systems. This is however not of importance as the objective is to find the mass difference. For this work the mass model is deemed valid enough, however some extra attention to the Isp should be used in order to verify that the Isp used for the model has a reasonable value.

4

Supersonic split line and submerged movable nozzle design

In this chapter the usage of a CAD program is described and also the design philosophy of the SM and SSSL nozzle is discussed. Additionally a CAD render and dimensions of the nozzles are presented. There are four sections that explain the design method of the various nozzles. The nozzles are presented in the following order: SSSL expansion ratio 12, SM nozzle, SSSL expansion ratio 45 and the scaled down SSSL nozzle with expansion ratio 6.5. For all nozzle representations the flow of gases goes from the left to the right.

4.1. Design of the nozzle

The design of the two nozzles is performed in Catia V5. Catia is available for students at the university and is a CAD tool with many features. The nozzle shape created in the python shape program in section 2.4 is imported into the CAD program and incorporated in the design. All the nozzles will consist of two parts that can rotate around each other. The SM and SSSL nozzles will have the same combustion chamber diameter. This diameter is 356mm.
When designing the SSSL nozzle with a higher area expansion ratio of 45, the same chamber diameter is used as it uses the same combustion chamber. The scaled down combustion chamber has a diameter of 178mm.

4.1.1. Supersonic split line nozzle expansion ratio 12

For the SSSL nozzle the main design point is the split. By looking at other SSSL nozzle designs in various papers, it was decided to round off the nozzle wall around the split [11, 15, 23, 24, 43]. The rounding towards the split was set to a circle of radius of 3mm and the radius of the rounding away from the split was set to 10mm. This can be seen on the cut out of the nozzle in figure 4.1. The two rounding edges are indicated with arrows and the radius of the rounding is described. Additionally, the interface between the upper part and lower part can clearly be seen.

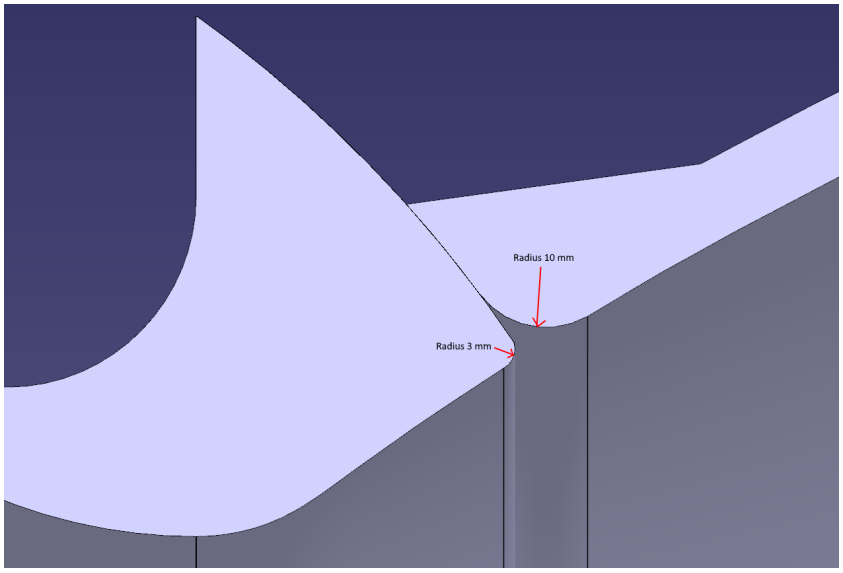

Figure 4.1: Figure of the split area of a sectioned view of the SSSL nozzle

The centre of rotation was determined by taking the tangent of the nozzle wall at the split location. Where the tangent crossed the neutral line was taken as the rotation point. The nozzle wall thickness was set to 10mm, however this was more for the ease of meshing later and will probably not be the final thickness of the nozzle wall. The chamber to throat region was determined with the methods from Zandbergen and Huzel [13, 32]. The radius of curvature from the combustion chamber wall was set to 0.4 times the chamber diameter (142.4mm). The angle of the converging wall was set to 45 degrees. The final radius of curvature toward the nozzle throat was set to the throat radius (72.5mm). These design points can be seen in figure 4.2 with the rest of the assembled nozzle.

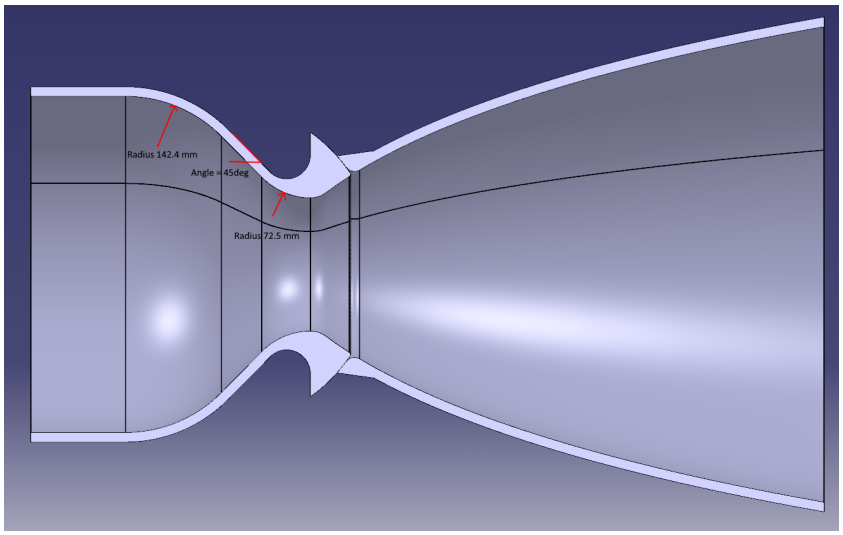

Figure 4.2: Figure of the SSSL nozzle cut through the middle

The full upper and lower parts can be seen in figures 4.3a and 4.3b. Finally the assembled nozzle can be seen in figure 4.4

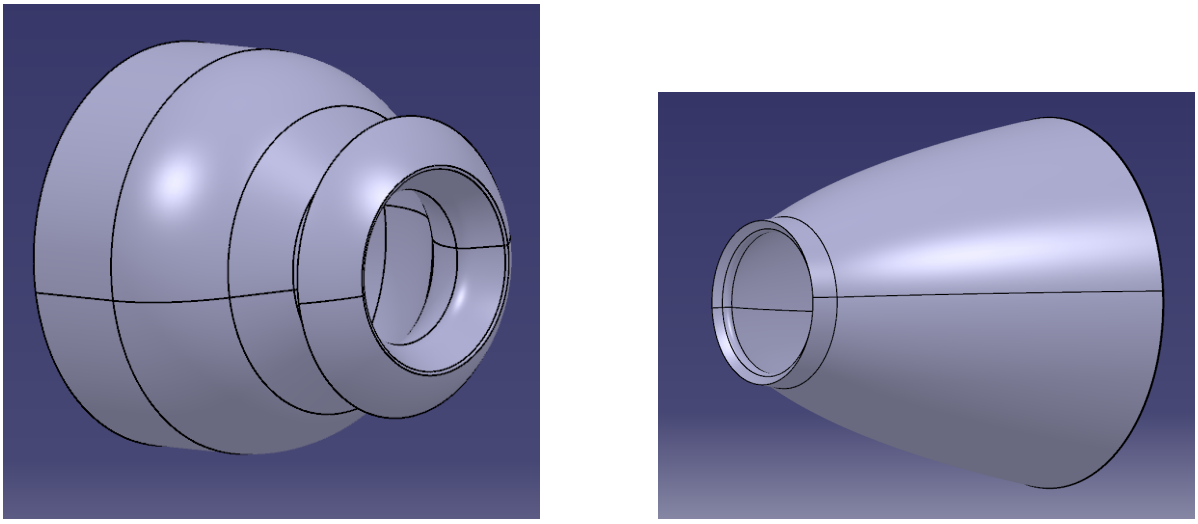

(a) Upper part of the SSSL nozzle with expansion ratio 12

(b) Lower part of the SSSL nozzle with expansion ratio 12

Figure 4.3: The upper and lower part of the SSSL nozzle with expansion ratio 12

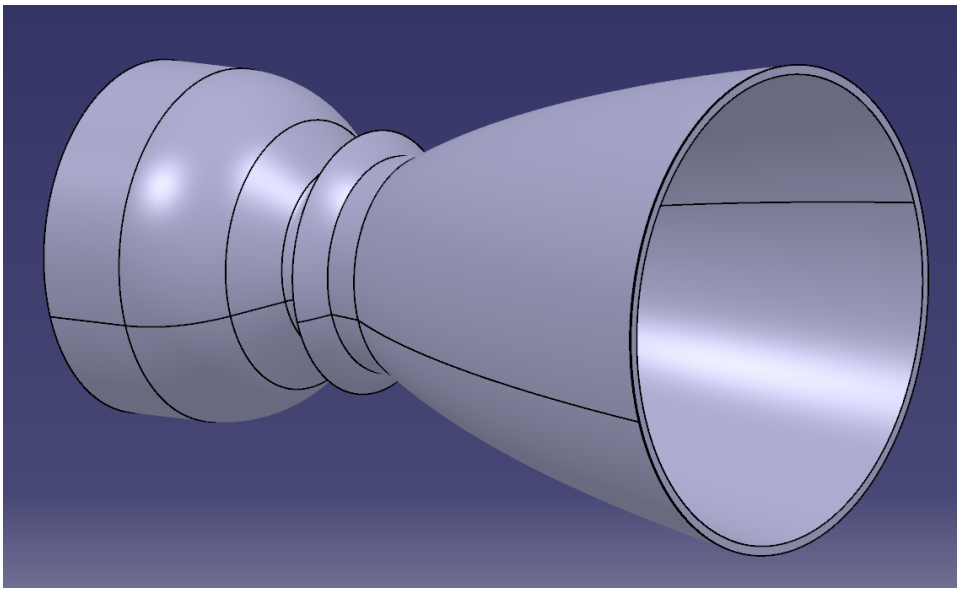

Figure 4.4: Figure of the assembled SSSL nozzle with expansion ratio 12

4.1.2. Submerged movable nozzle

For the SM nozzle the main design point is the entrance towards the throat. This was designed with the guidelines by Ellis [24]. In figure 4.5 a representation of the design points for the entrance to the throat is presented, the figure is adapted from [24]. The entrance of the SM nozzle is modelled as an ellipse with the leading edge at an expansion ratio of 2 with respect to the throat. This is the tip radius in figure 4.5 and its value is 102.5 mm. The distance to the leading edge of the ellipse was set to the throat diameter, which is 145 mm. In figure 4.5 this is called the entry length. A detailed view of the SM nozzle entry contour can be seen in figure 4.6. The rotation point was set at 1/3 throat diameter behind the nozzle throat. The section from the combustion chamber to the nozzle was designed as straight wall with a curved wall section at the end. The end of the curved section contains the interface surface to the ball and socket. The parts can be seen in figures 4.7 and 4.9. A sectioned view of the nozzle can be seen in figure 4.8. Finally the assembled nozzle can be seen in figure 4.9

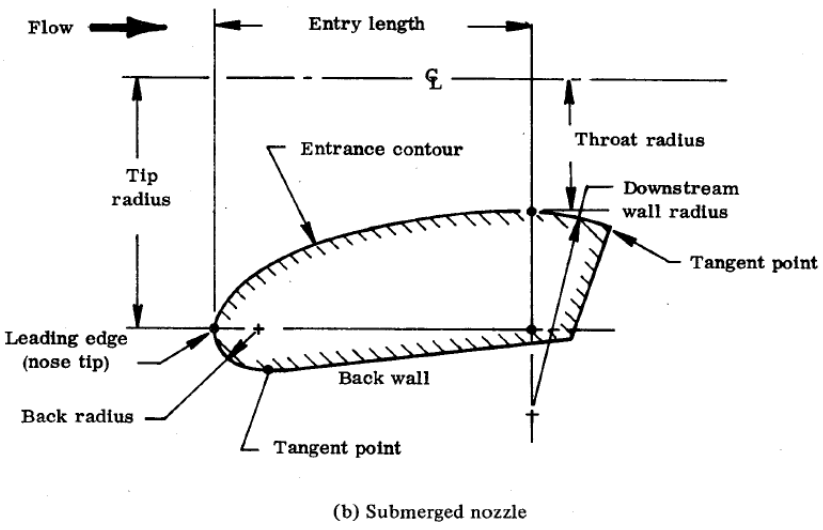

Figure 4.5: Figure the design of the entrance to a submerged nozzle.

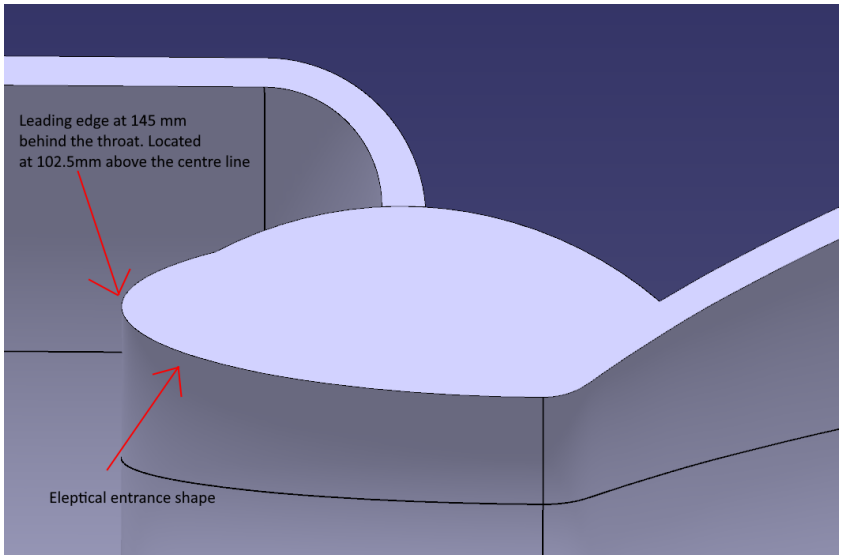

Figure 4.6: Figure of the entry contour of the SM nozzle

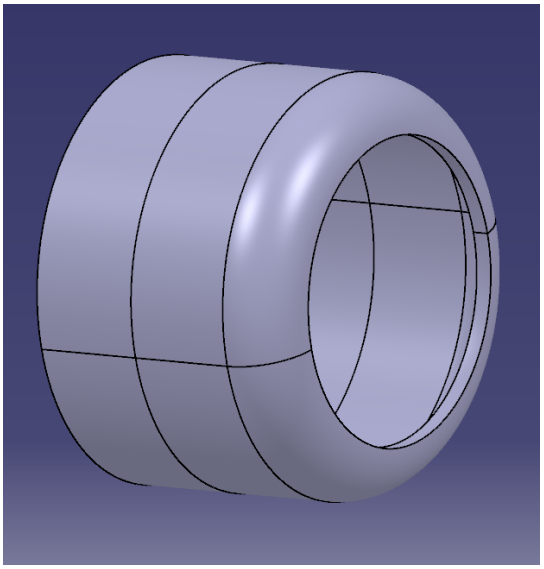

(a) Upper part of the SM nozzle

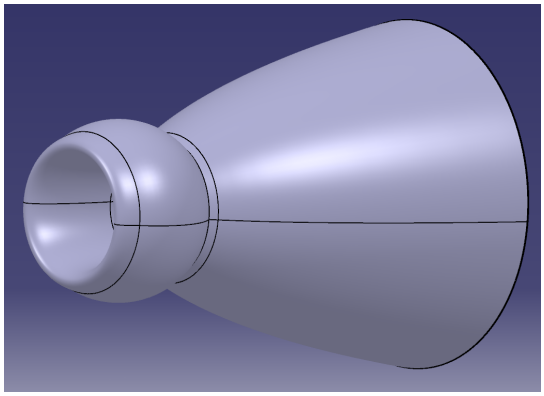

(b) Lower part of the SM nozzle

Figure 4.7: The upper and lower part of the SM nozzle

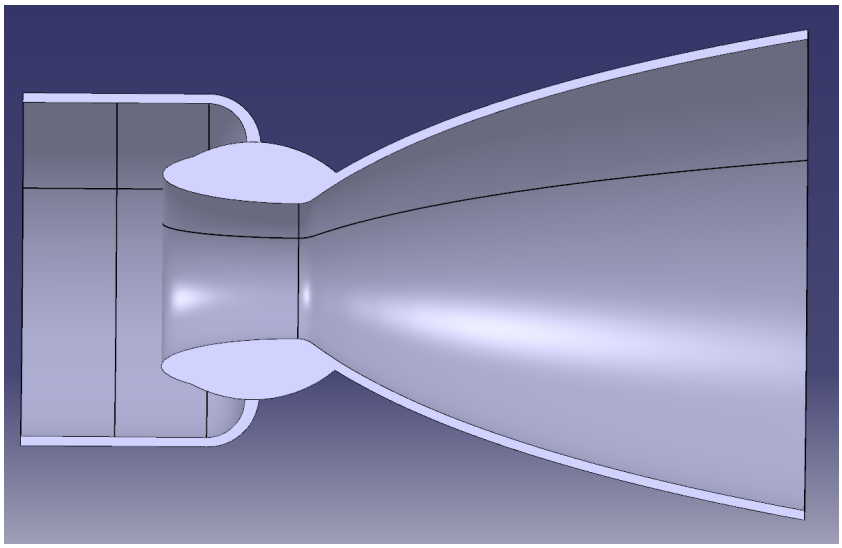

Figure 4.8: Figure of the sectioned SM nozzle

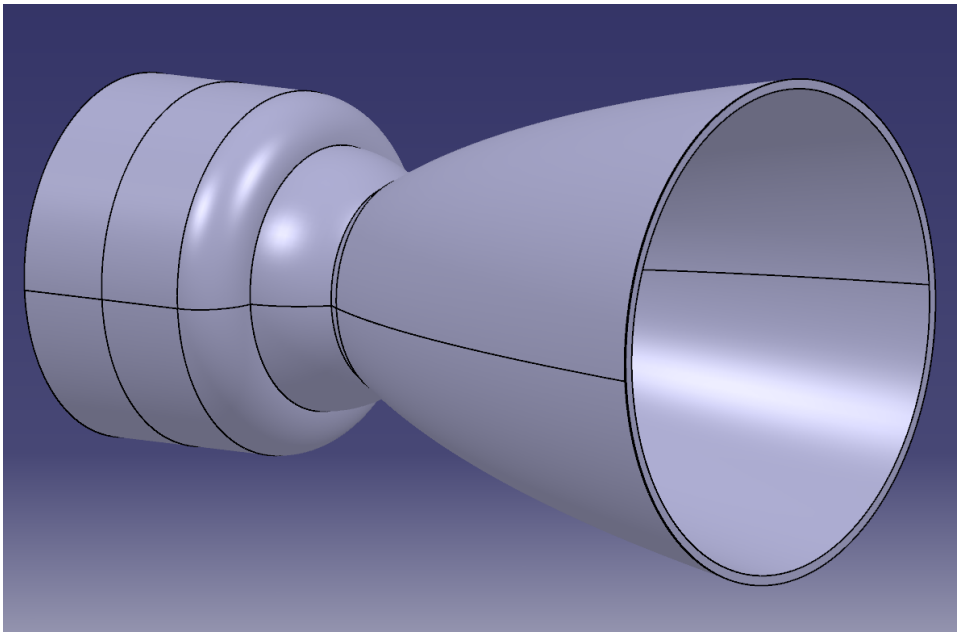

Figure 4.9: Figure the assembled SM nozzle.

4.1.3. Supersonic split line nozzle expansion ratio 45

The design of the SSSL nozzle with an expansion ratio of 45 ($\epsilon 45$) follows the same design logic as the SSSL nozzle with an expansion ratio of 12 ($\epsilon 12$). Both nozzles use the same chamber to throat design. The only difference is the contour of the nozzle after the throat. The $\epsilon 45$ nozzle has a larger initial angle and the total nozzle length is much longer. The rounding at the split is done in the same manner as the $\epsilon 12$ nozzle. In figures 4.10 to 4.12 are several representations of the nozzle design shown.

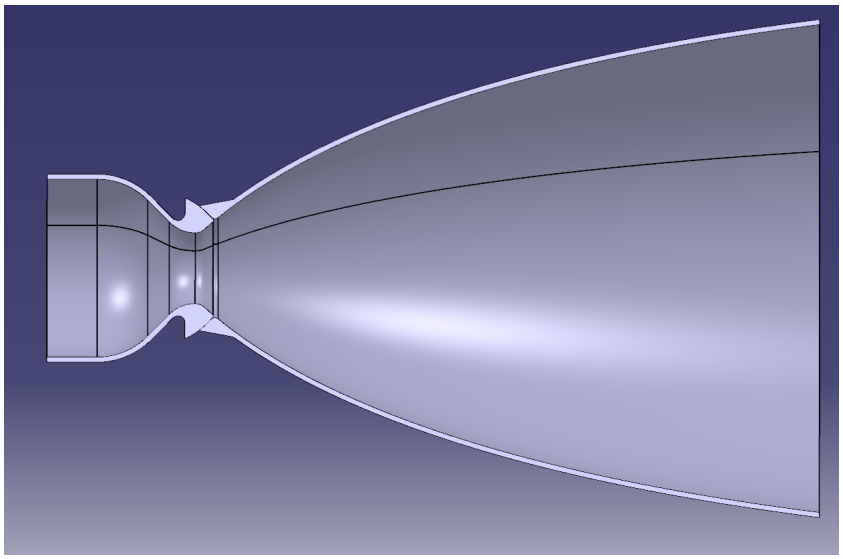

Figure 4.10: Figure of the SSSL nozzle with expansion ratio 45 cut through the middle

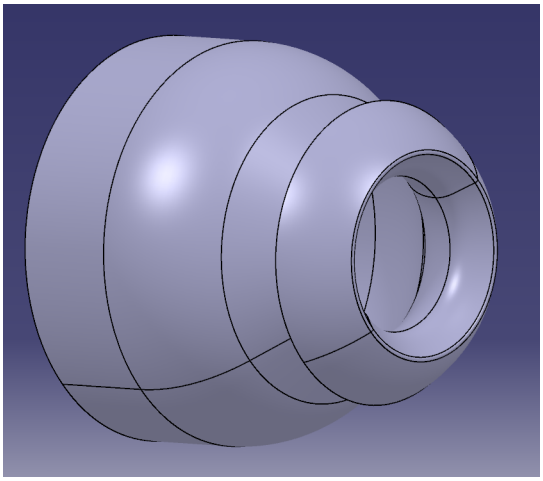

(a) Upper part of the SSSL nozzle with expansion ratio 45

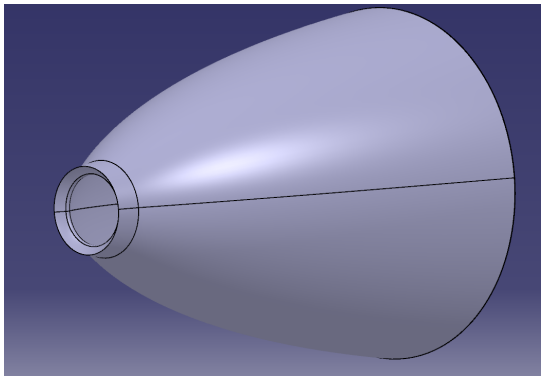

(b) Lower part of the SSSL nozzle with expansion ratio 45

Figure 4.11: The upper and lower part of the SSSL nozzle with expansion ratio 45

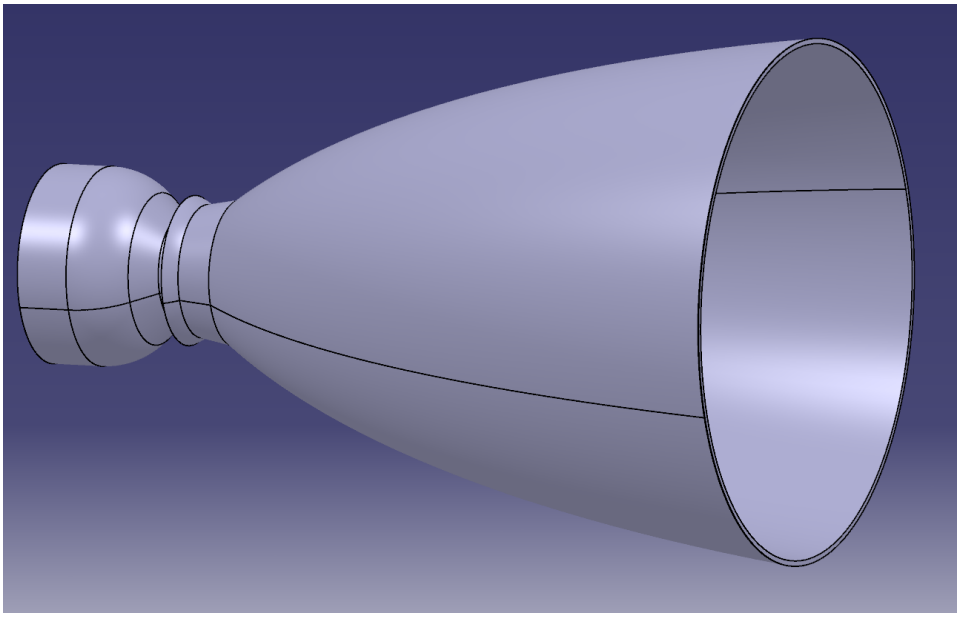

Figure 4.12: Figure the assembled SSSL nozzle with expansion ratio 45

4.1.4. Supersonic split line nozzle scaled down version

The scaled down version of the SSSL nozzle differs a little from the other two designs. The combustion chamber to throat region is a bit sharper and steeper. The scaled SSSL nozzle has an area expansion ratio of 6.5. Additionally the rounding of the split is smaller due to the smaller size of the nozzle. The rounding towards the split was chosen a 1.5 mm radius and the rounding away from the split was chosen as 5 mm. This can be seen in the zoomed in figure of the split area that is shown in figure 4.13.

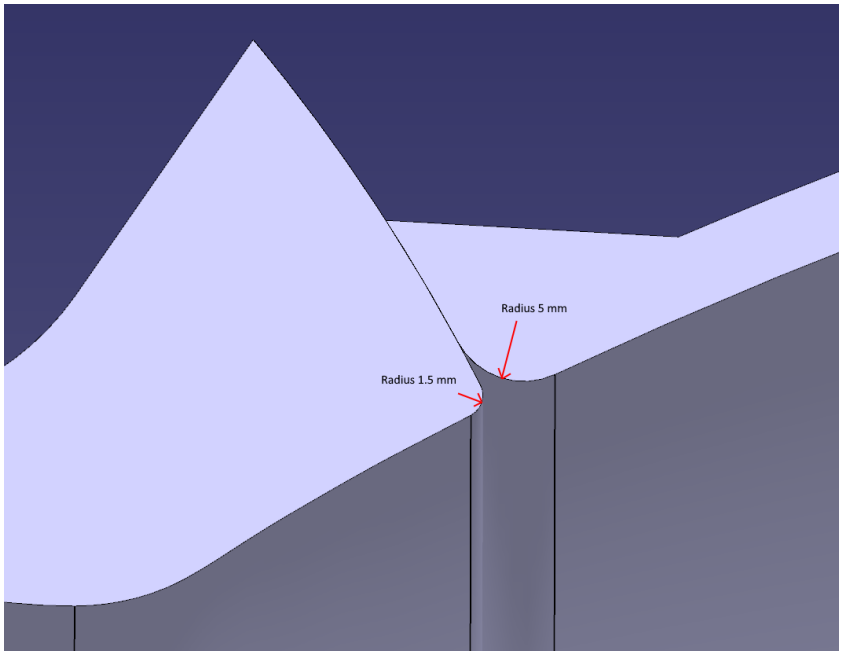

Figure 4.13: Figure of the split area of a sectioned view of the scaled down SSSL nozzle

The combustion chamber to throat region also has some differences. The first rounding was set to 1/3 of the combustion chamber diameter (29.67 mm). The angle of the converging part towards the throat was set to 55 deg. Finally the rounding towards the throat was set to half the throat diameter (41.5 mm). All these values can be seen in figure 4.14.

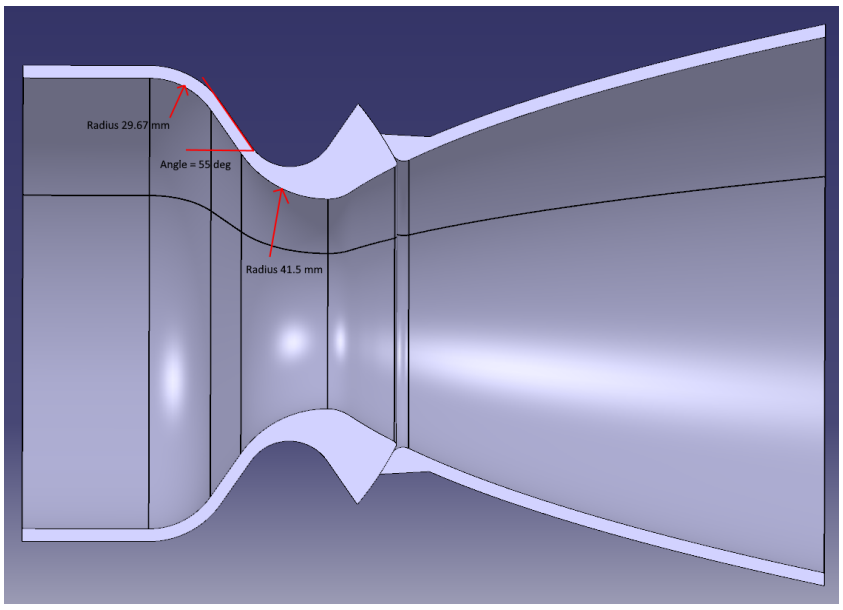

Figure 4.14: Figure of the scaled down SSSL nozzle cut through the middle

The full upper and lower parts of the scaled down SSSL nozzle can be seen in figures 4.15a and 4.15b. Finally the assembled nozzle can be seen in figure 4.16.

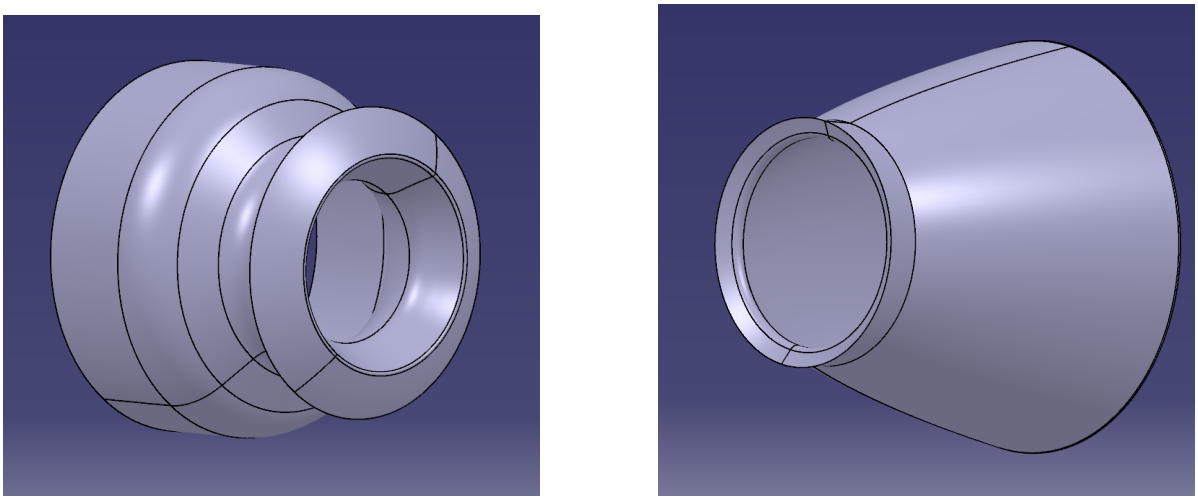

(a) Upper part of the scaled down SSSL nozzle

(b) Lower part of the scaled down SSSL nozzle

Figure 4.15: The upper and lower part of the scaled down SSSL nozzle

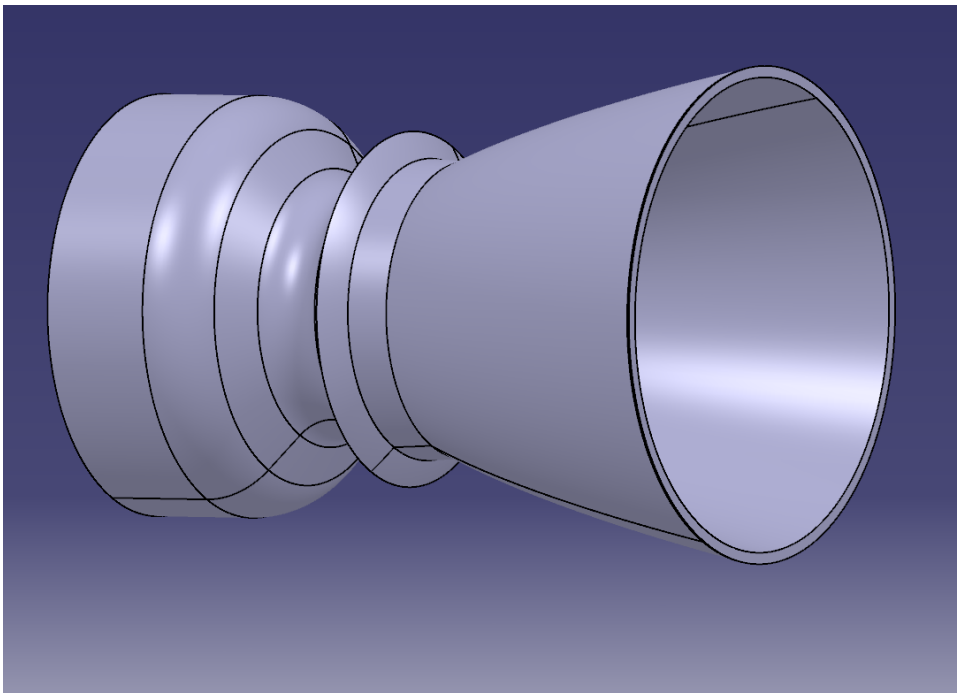

Figure 4.16: Figure the assembled scaled down SSSL nozzle

4.1.5. Nozzle area

When constructing the mass model in chapter 3 the surface area of a truncated cone was used to scale the nozzle from the paper by Ellis and Berdoyes [23]. The real surface area of the nominal nozzle has now been checked with the use of the CAD software. The surface area is 0.64 m^2, compared to the 0.58 m^2 of the truncated cone. This leads to an increase in nozzle structural mass of 9%. However, when looking at the sensitivity analysis for the change in empty mass of 10% the change in the mass difference between the two nozzles was only 1.54% in favour of the SM nozzle. This is a small change and therefore it was decided not to change the mass model.

4.2. Summary and conclusion to nozzle generation

In this chapter the CAD models of the various nozzles are constructed. These CAD models are used for the generation of the mesh for the CFD simulations. From the mesh, the CFD simulations can be run. Additionally, the surface area of the nominal nozzle was compared to the assumption of a truncated cone used in the mass model. It was found that it had negligible effect on the mass model result.
The method by importing the general nozzle shape into CATIA from python proved an easy solution to create the desired nozzle shape. The other elements of the nozzle were then drawn around this nozzle divergent shape.

5

Heat transfer

In this chapter the method used to determine the heat transfer is provided. Nammo has requested an estimate of the heat transfer in order to see if extra care is needed in the design with regards to cooling. Approximation methods found in literature are used to calculate the heat transfer. In the first section the explanation of the convective heat-transfer is given. In the second section the explanation for the radiative heat transfer is provided.

5.1. Convective heat transfer

In a rocket nozzle the convective heat transfer amounts to around 70-80% of the total heat transfer for supersonic nozzle flow [13, 24]. The convective heat transfer of the gas in the nozzle can be approximated by the use of the Bartz equation [10]. The Bartz equations tend to give a slight over estimation of the heat flux, however as only an estimate of the heat flux is needed it is deemed accurate enough for this work [49, 54]. The Bartz equation is given in equation (5.1), with the following parameters:

c^*	Characteristic velocity
c_p	Specific heat capacity at constant pressure
D	Diameter of nozzle section
D_t	Diameter of nozzle throat
γ	Specific heat ratio
M	Mach number
μ	Dynamic viscosity
p_c	Chamber pressure
Pr	Prandtl number
r_c	Radius of curvature downstream of throat
T_t	Total temperature
T_w	Wall temperature
$T_{w,g}$	Gas temperature at the wall
h_α	Convective heat transfer coefficient

$$h_\alpha = \left(\frac{0.026}{D_t^{0.2}}\right)\left(\frac{\mu^{0.2}\cdot c_p}{Pr^{0.6}}\right)\left(\frac{p_c}{c^*}\right)^{0.8}\left(\frac{D_t}{r_c}\right)^{0.1}\left(\frac{D_t}{D}\right)^{1.8}\left(\frac{\left[1+M^2\cdot\left(\frac{\gamma-1}{2}\right)\right]^{-0.12}}{\left[0.5+0.5\left(\frac{T_{w,g}}{T_t}\right)\left(1+M^2\left(\frac{\gamma-1}{2}\right)\right)\right]^{0.68}}\right) \tag{5.1}$$

$$q_\alpha = h_\alpha \cdot (T_{w,g} - T_w) \tag{5.2}$$

Using equation (5.1) together with the results from the CFD calculations and equation (5.2) an estimate of the convective heat transfer can be found. Where q_α is the convective heat transfer, The following

parameters are obtained from the CFD simulation: Pr, T_t, $T_{w,g}$, M and μ. It is assumed that the wall temperature stays constant and that the specific heat capacity at constant pressure is constant as well. It is assumed that the wall temperature stays constant at 1200K, this is a requirement from Nammo that can be found in the SOW in appendix A. The resulting heat transfer will only be an estimate and cannot effectively predict the heat transfer at the split due to the shock wave and expansion fans at these locations. The calculation is done in Ansys Post in order to get a contour plot of the heat transfer. The contour is on the inside surface of the nozzle wall.

5.2. Radiative heat transfer

The radiative heat transfer amounts to much less than the convective heat transfer. However, to create a more precise picture an estimate of the radiative heat transfer is also included.
The following assumptions are used for the radiative heat transfer.

1. The gasses are assumed as a grey body
    (a) The gasses are in real life also a grey body so this assumption has little to no impact on the heat flux
2. The nozzle is assumed as a black body
    (a) The nozzle walls will never be like a black body, but if a carbon-carbon material is used for the nozzle wall, the absorptivity and emissivity of the nozzle wall is high. Therefore this assumption results in an overestimation of the heat flux
3. It is assumed that the absorptivity and emissivity is equal
    (a) This assumption is in general true when the temperature of the wall and the gas are around the same temperature (Kirchoffs law [45]). This assumption will result in an over estimation.
4. The emissivity is set to a constant that does not change with temperature or pressure
    (a) The emissivity of the gas changes with pressure and temperature and hence this will lead to an under estimation in the combustion chamber and an over estimation towards the end of the nozzle
5. It is assumed that the view factor of the gas and wall is 1
    (a) The view factor is less than 1 since the nozzle has an exit that the radiation can escape from. Additionally, the view factor will change through the nozzle. This will lead to an over estimation of the heat flux

The radiative heat transfer is only about 20-30% of the total heat transfer [13, 24]. Additionally, only an estimate of the total heat transfer is needed and hence the radiative heat transfer is simplified with the assumptions used.

In order to calculate the radiative heat transfer, the emissivity of the gas is needed. To find the exact emissivity of the gas mixture is a complicated process. However, using assumption 4 an approximate emissivity of the gas mixture is used on the whole domain. Using the chart and methods developed by Alberti et.al. an approximate emissivity can be found [2]. The charts needed for this work are found in chapter B The accuracy of the method is within 1% of the measured emissivity of a gas mixture [2]. In order to use the charts in the paper by Alberti et.al. the pressure path of the gas is needed. The pressure path is the integration of pressure times path length over the length of the nozzle. When looking at the pressure trace along the wall for the SSSL nozzle that is shown in figure 7.2, it can be seen that the pressure stays at around 35 bar for around 25 cm. Then there is a large drop down to a pressure of 4 bar over the next 6 cm. The rest of the nozzle the pressure drops from 4 bar down to around 0.4 bar over the next 52 cm. For the sections that have a drop in pressure, the average pressure of the start and end pressure is used in the pressure path calculation. The resulting overall pressure path length is then:

$$35 \cdot 25 + (35 - 4)/2 \cdot 6 + (4 - 0.4)/2 \cdot 52 = 1061.6 \text{ bar-cm}$$

For the nozzle with an expansion ratio of 45 the same pressure path is used as mostly the high pressure path is determining for the pressure path length. It is assumed that the scaled down nozzle has the same emissivity as the larger nozzles.
By using this pressure path length and an approximate gas temperature of 2000 K the emissivity of the gas mixture can be found. The temperature of 2000 K is used as this is approximately the average temperature throughout the nozzle. It is assumed that only the water vapour and the carbon-dioxide contributes to the emissivity as they are the dominant species in the gas mixture. The total emissivity of the gas mixture can then be approximated by equation (5.3). ϵ_{tot} is the total emissivity of the gas mixture, ϵ_{H_2O} is the emissivity of water vapour, ϵ_{CO_2} is the emissivity of carbon-dioxide and $\Delta\epsilon_{H_2O-CO_2}$ is the correction factor for a mixture with water vapour and carbon-dioxide.

$$\epsilon_{tot} = \epsilon_{H_2O} + \epsilon_{CO_2} - \Delta\epsilon_{H_2O-CO_2} \tag{5.3}$$

From reading out the charts in the paper by Alberti et.al. the following emissivities can be found for the chosen path length and the temperature. The charts can also be found in appendix B.

Table 5.1: Table showing the emissivity for the four nozzles. Pressure path length = 1061.6 bar-cm, temperature = 2000 K, ratio CO_2 to H_2 = 0.54

Parameter	Emissivity
ϵ_{H_2O}	0.51
ϵ_{CO_2}	0.11
$\Delta\epsilon_{H_2O-CO_2}$	0.15
ϵ_{tot}	0.47

The radiative heat transfer of the rocket motor can be computed with equation (5.4). This equation is only valid with the current assumptions. Where q_{1-2} is the heat transfer from the hot gasses to the nozzle wall, ϵ_1 is the emissivity of the hot gasses, σ is the Stefan–Boltzmann constant, T_1 is the temperature of the gas and T_2 is the temperature of the wall. The temperature of the gas is taken from the CFD simulations which will vary throughout the nozzle.

$$q_{1-2} = \epsilon_1 \cdot \sigma \left(T_1^4 - T_2^4\right) \tag{5.4}$$

The total heat transfer that the wall experiences is a combination of the radiative heat transfer and the convective heat transfer. The heat transfer is calculated in Ansys post in order to access all the wall data that has been computed during the CFD calculations. The estimate of the radiative heat transfer is a quite simple model that overestimates the contribution from radiation. This is due to the assumption of a view factor of 1, that the nozzle walls are treated as a black body and also that the emissivity of the gas is quite high as all the estimates of the pressure path length and the temperatures were taken on the high side. The total heat flux is calculated as shown in equation (5.5). Where q_{tot} is the total heat flux, q_{rad} is the radiative heat flux and q_{conv} is the convective heat flux.

$$q_{tot} = q_{rad} + q_{conv} \tag{5.5}$$

5.3. Discussion and conclusion to heat flux calculations

The methods chosen for the heat flux calculations both have inaccuracies and are an overestimation of the heat flux. However, as the work compares two nozzles it is of interest to see what the difference between the two nozzles are. Therefore, the model used to calculate the heat flux does not have a large impact on the comparison. To conclude, the method of calculating the heat flux is deemed valid for the comparison between the nozzles. And the results are an indication of the total heat flux in the nozzle.

6

Ansys approach

In this chapter the usage of Ansys is discussed. Additionally, a verification of the Ansys set-up is performed. In order to establish if the tool is used correctly. This is done by comparing the results of the CFD calculations to the results from literature. The paper that is used for the comparison is a study by Kumar and Devarajan [33]. In the first section, the usage of Ansys is explained. In the second section, a verification of the CFD analysis method is performed. In the third section, the 3D mesh method is explained. Finally, in the fourth section, the input to the CFD analysis performed in this thesis is explained. For all nozzle representations the flow of gases goes from left to right.

6.1. Computational fluid dynamics analysis

In order to meet the research objectives, the two nozzles need to be analysed with a CFD tool. The CFD tool chosen for this task is Ansys Fluent 19.3 [4]. Ansys Fluent is available for students at the university and is a CFD tool for analysing several fluid dynamic problems [5]. It has been used for various other studies involving rocket nozzles [29, 33, 41].

In order to perform a CFD simulation, the nozzles must first be designed in a CAD drawing program. The program used for this is Catia V5, as this is also readily available for students at the university. Once the geometry is drawn, the meshing program can load the geometry from the CAD file in order to create the mesh. The mesh is drawn in ICEM. ICEM is part of the Ansys package and can export the mesh directly to Ansys Fluent. ICEM is chosen as the meshing program for the 2D case as it offers good control over the meshing process. When the mesh has been loaded into Ansys Fluent, the setup for the CFD analysis can be done. When the boundary conditions, fluid properties and the solver methods are set, the simulation can start. All the setup parameters are noted down and reported together with the results. When the simulation has converged, the results can be exported to CFD-Post. The convergence criteria is set to 1E-3. In CFD-Post, which is a program in the Ansys package, the results can be analysed. In CFD-Post, all the contour plots, graphs and data is created in order to analyse the results. In figure 6.1 a step by step process on the steps taken towards the CFD simulations is shown.

6.2. Verification of the computational fluid dynamics analysis method

In this section, the verification of the use of Ansys Fluent and the other tools used from Ansys is performed. The section will describe the nozzle generation, meshing, CFD input parameters and finally, compare the results to a case from literature. The comparison is done to verify that the usage of Ansys is done correctly and that the results in this work are of sufficient quality. It was chosen to use an easy 2D case in order to verify Ansys as a complex 3D case was hard to find a good source for in literature. The following criteria are used in order to verify the Ansys approach. The values given in the paper and the verification analysis shall not exceed 2%. This figure was chosen in order to give room for mesh differences and solver differences. The solver used for this thesis is Ansys Fluent 2019 R3, while the solver used in the paper is Ansys Fluent R14.5. All the nozzle design parameters and the simulation inputs are the same as in the paper by Kumar and Devarajan [33].

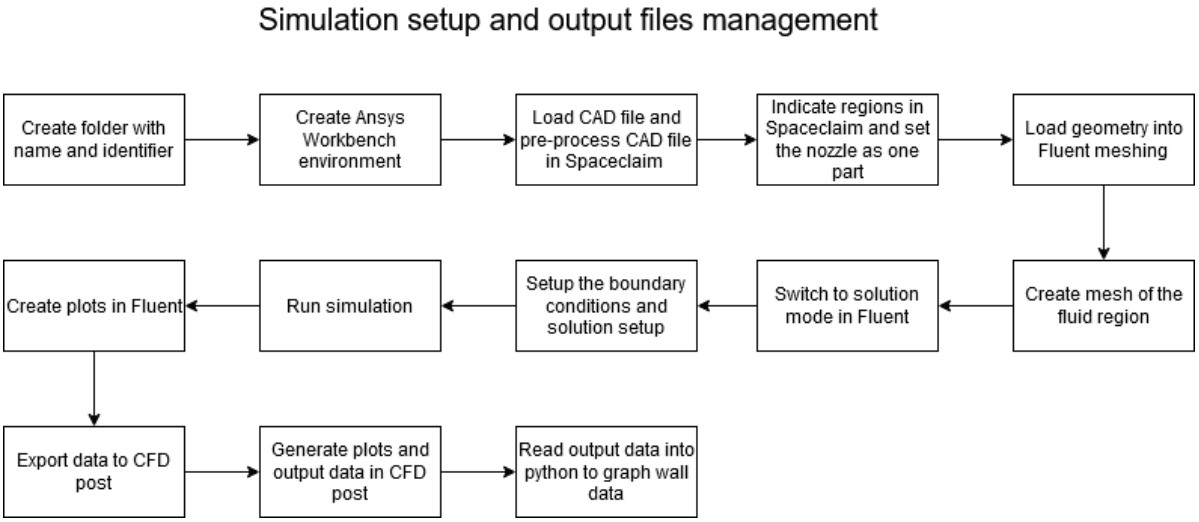

Figure 6.1: Figure of the simulation set-up and steps.

6.2.1. Verification nozzle design

The nozzle design used in the paper by Kumar and Devarajan is a conical nozzle with the parameters as listed in table 6.1. A drawing of the nozzle is presented in figure 6.2. All the dimensions are in millimeters. From the CAD drawing, the mesh can be created. The mesh for the verification nozzle was created with 120 cell divisions along the vertical axis. Cells were spaced closer towards the nozzle wall with a minimum size of 0.13 mm. The cell divisions in the horizontal direction were divided up in two sections. One section before the throat and one after the throat. The section before the throat had 90 cell divisions with decreasing cell size towards the throat. The smallest cell size was set to 0.2 mm. The section after the throat was set to 120 divisions with increasing cell size towards the exit. In total 25080 nodes were used. The mesh orthogonality was reported as between 0.86 an 1. The orthogonality refers to how orthogonal two neighbouring mesh cells are with each other. The closer to 1 the better the quality as there are no translations needed to move from the one control volume to the next. The mesh is shown in figure 6.3.

Table 6.1: Verification nozzle design parameters

Part	Dimensions
Inlet diameter	25 mm
Throat diameter	10 mm
Outlet diameter	35 mm
Nozzle divergence length	50 mm
Total nozzle length	75 mm
Throat longitudinal radius	0 mm

6.2.2. Verification nozzle simulation input

The fluid used for the verification nozzle is considered to be air. The air is modelled with the ideal gas law for the density. The specific heat was set to a constant value of 1006.43 J/kg-K. The thermal conductivity of the gas was set to a constant of 0.0242 W/mK. The viscosity of the gas was modelled with the Sutherland viscosity law [12]. The simulation was set to a laminar flow that evaluated the energy equation of the flow. The molecular weight of the gas was set to a constant of 28.966 g/mol. The other input parameters for the boundary conditions are given in table 6.2.

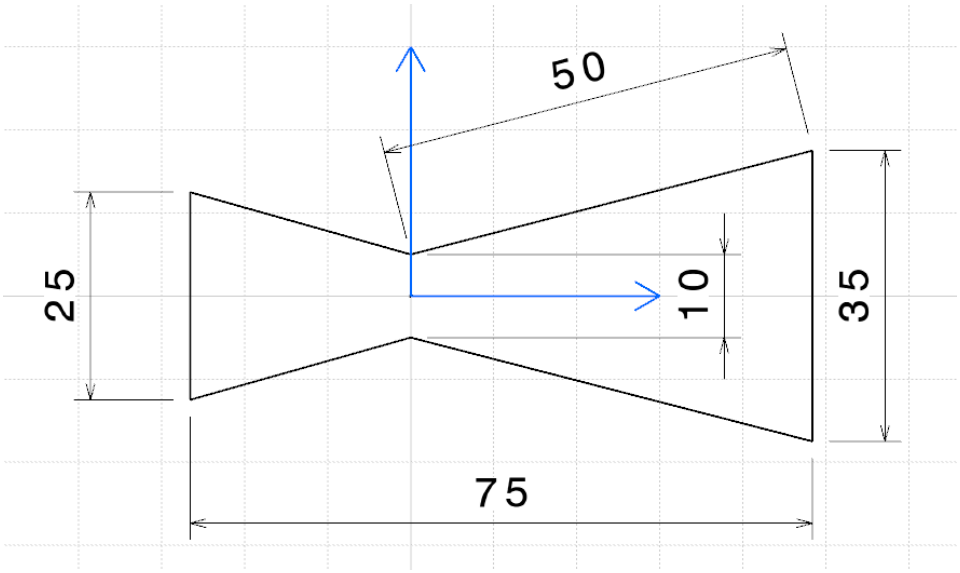

Figure 6.2: Figure showing the drawing for the Ansys verification nozzle.

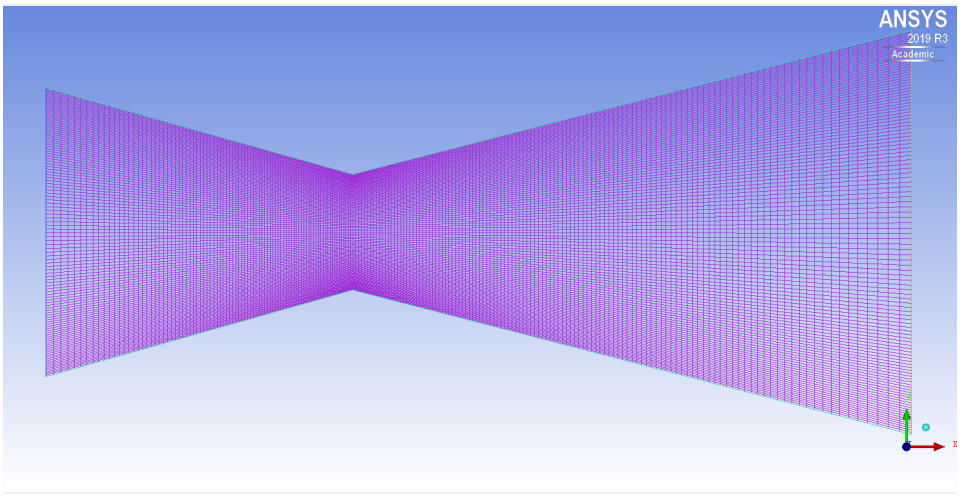

Figure 6.3: Figure showing the mesh for the Ansys verification nozzle.

Table 6.2: Table showing the setup parameters for the verification nozzle CFD analysis

Procedure	Details
General-Solver	Type: Density based Velocity formation: Absolute Time: Steady 2D space: Planar
Models	Energy: On Viscous: Laminar
Materials	Fluid: Air Density: Ideal Gas Viscosity: Sutherland
Boundary conditions	Inlet: Pressure Inlet Gauge Total Pressure (pa): 3E5 Temperature: 300K Outlet: Pressure Outlet Operating pressure Pressure (pa): 0
Reference values	Compute from: Inlet Reference zone: Solid surface body
Initialization	Standard initialization Compute from inlet
Solution	Solution control Courant number = 5

6.2.3. Verification nozzle analysis

The setup for the CFD calculation used the parameters that are shown in table 6.2. When all the parameter were set, the check case function of Ansys Fluent was used and it reported no problems. The solution was set to run 1000 iterations but was converged after 281 iterations. The convergence criteria was set to 1E-3 for velocity, continuity and energy residuals. The paper by Kumar and Devarajan [33] had the same convergence criteria. Figure 6.4 shows a trace of the residuals for the simulation. As seen the residuals decrease until the convergence criteria is met.

The results were analysed in CFD-Post and the results were compared to the values obtained by Kumar and Devarajan. The results are summarized in table 6.4. The contour plots of Mach number, velocity and static pressure are also compared and can be seen in figures 6.5 to 6.7. The authors of the paper have decided to not show the flow field in great detail for the Mach number and the pressure. However, the velocity contour shown in figure 6.7 shows some more detail. It can be seen that oblique shock waves are formed right after the nozzle throat. This is right after the thin red line after the nozzle throat. It can be seen that the two oblique shock waves meet in the middle and are reflected outwards toward the exit. As seen in the pressure contour in figure 6.5, the pressure decreases from the inlet towards the outlet. The pressure is denoted as negative at the exit since in this simulation the gauge pressure is used. In order to obtain the absolute pressure, the reported pressure should be added to the ambient conditions. The ambient conditions in this case is 101325Pa. The results from the paper and the results from the CFD simulation are almost identical. The results are compared in table 6.4. The largest difference is in the temperature at the outlet which is 3% smaller that the reported result in literature. However, as all the other results are around 1% or less. The differences between the two simulations can have multiple sources, the two most likely sources are: Firstly, the mesh can be different, thereby creating a small difference in the output. Secondly, the solver used is different, the one used in the paper is version 14.5 and the one used for this thesis is version 19.3. The newer solver

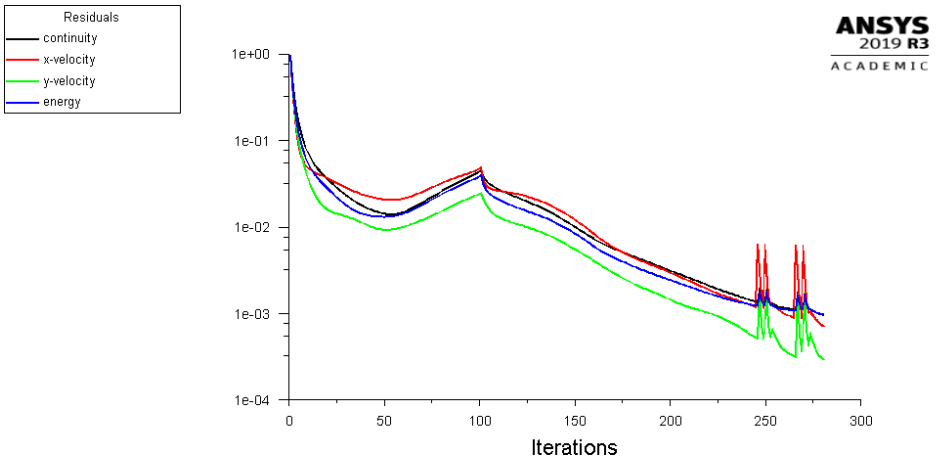

Figure 6.4: Figure showing the residuals for the Ansys verification nozzle.

might calculate some aspects of the nozzle flow with greater accuracy.
In addition, the nozzle quality factors of the verification nozzle are compared to the quality factors in the book by Sutton and the design guidelines of Huzel [32, 40]. Three quality factors are evaluated. Nozzle quality factor ξ_F, Combustion quality factor ξ_c and motor quality factor ξ_s. These three factors can be calculated by using the following three equations [13, 32, 40].

$$\xi_F = \frac{(C_F)_{experimental}}{(C_F)_{ideal}} \tag{6.1}$$

$$\xi_c = \frac{(c^*)_{experimental}}{(c^*)_{ideal}} \tag{6.2}$$

$$\xi_s = \frac{(Isp)_{experimental}}{(Isp)_{ideal}} \tag{6.3}$$

The quality factors can be related in the following way.

$$\xi_s = \xi_c \cdot \xi_F \tag{6.4}$$

The results for the nozzle quality factors are shown in table 6.3. It can be seen that the quality factors of the verification nozzle are within the values that are listed in literature. From the similar results that are shown in table 6.4 and from the quality factors listed in table 6.3 it can be concluded that the Ansys approach has been verified. There is one peculiar value between the quality factors. The combustion quality factor is larger than 1. This does not however imply that there is free energy produced. Additionally, this breaks the relation between the quality factors given in equation (6.4). The explanation to this lies in the discharge coefficient. There exists a boundary layer along the wall of the nozzle. This has the effect of reducing the real throat area. This in turn has an effect on the mass flow of the system as well. The discharge coefficient can be found by using the following relation.

$$C_d = \frac{\dot{m}_{experimental}}{\dot{m}_{ideal}} \tag{6.5}$$

The relation for the discharge coefficient is only valid for a cold non reacting flow. The flow in the CFD simulation is a non reacting flow and hence we can use the above relation. The discharge coefficient for this nozzle is 0.974. This indicates that the there is some boundary layer forming in the throat which effects the calculation of the quality factors. Especially the combustion quality factor is affected by the discharge coefficient and hence the combustion quality factor is larger than 1 for this case.

Table 6.3: Quality factor values for the CFD simulation with a comparison to literature

Parameter	CFD value	Values from Sutton [40]	Values from Huzel [32]
ξ_F	0.945	0.92 - 0.96	0.92 - 1.00
ξ_c	1.027	0.85 - 0.98	0.87 - 1.03
ξ_s	0.938	0.8 - 0.9	0.85 - 0.98
C_d	0.974	-	-

Table 6.4: Table summarizing the difference between the verification nozzle and the nozzle from literature

Parameter	Verification nozzle	Literature nozzle	Percentage difference
Velocity magnitude (Maximum)	608.423 ms^{-1}	609.346 ms^{-1}	0.15%
Pressure (Inlet/Outlet)	397527Pa / 14033.2Pa	393224Pa / 14155.1Pa	1.08% / 0.86%
Temperature (Inlet/Outlet)	298.8797K / 125.9K	298.195K / 129.838K	0.23% / 3.03%
Mach number (Maximum)	2.818	2.82	0.07%

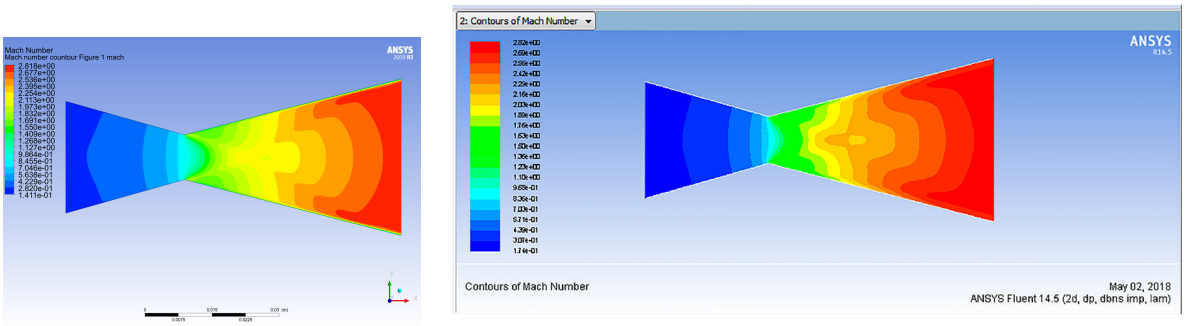

(a) Verification nozzle Mach number contour (b) Literature nozzle Mach number contour

Figure 6.6: Side by side comparison between the verification nozzle and the nozzle from literature. The compared value is Mach number

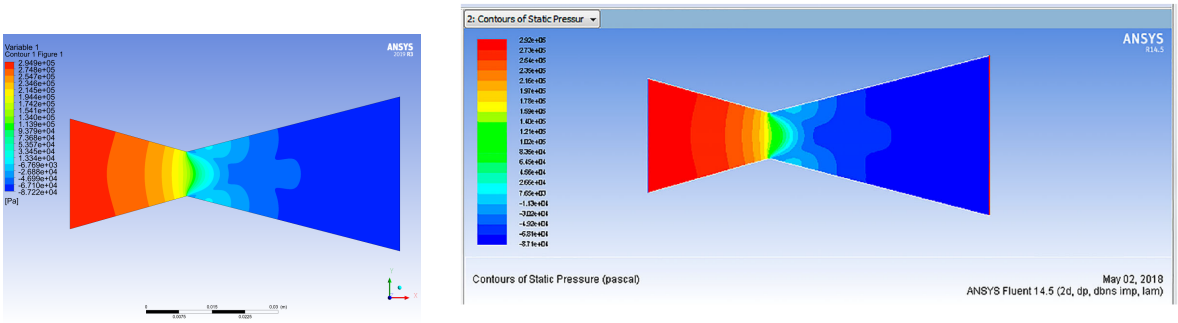

(a) Verification nozzle static pressure contour (b) Literature nozzle static pressure contour

Figure 6.5: Side by side comparison between the verification nozzle and the nozzle from literature. The compared value is static pressure. Note to obtain absolute pressure add 101325Pa

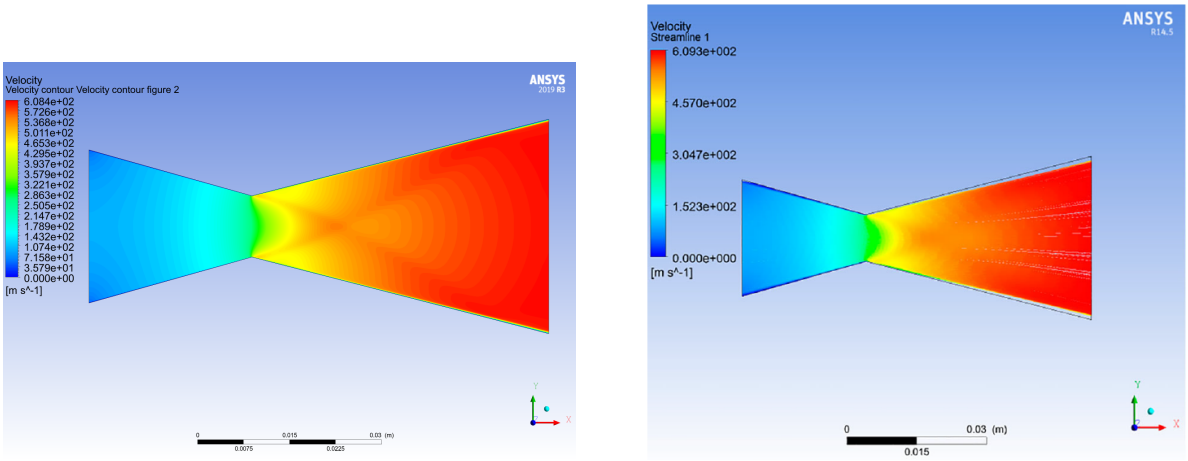

(a) Verification nozzle velocity contour

(b) Literature nozzle velocity contour

Figure 6.7: Side by side comparison between the verification nozzle and the nozzle from literature. The compared value is velocity

6.2.4. Conclusion to verification of Ansys

The results from the verification study show that Ansys has been used in the correct way and that Ansys produces the correct results. The small difference between the case from literature and the verification study are due to mesh differences and solver differences. Therefore, the results were not identical, but the correct use of Ansys has been demonstrated. Therefore, the method of using Ansys for the CFD simulations is proved valid for the use in this work.

6.3. 3D mesh method

Although ICEM can create very accurate meshes, it struggled to create a mesh for the SSSL nozzle due to the small indentation in the split. It was therefore decided to switch to the more automatic meshing method of Ansys Fluent for the 3D mesh for the CFD analysis. In order to create the mesh in Fluent the CAD drawings have to be modified in SpaceClaim. SpaceClaim is also a CAD software however, it allows the creation of zones and named sections that Fluent can understand. The sections that are created are Inlet, Outlet and the region around the split and throat. The region at the split and throat are created in order to refine the mesh in this region.
Once the geometry of the nozzle has been established, it can be loaded into Fluent meshing. In Fluent meshing, there is a preloaded work path in order to create a mesh. This work path consists of several steps. These steps are listed below. The settings used for the SSSL and SM nozzles are also mentioned.

1. Import geometry: In this step the geometry is loaded from SpaceClaim to Fluent meshing.

2. Add local sizing: This step is an optional step. In this case we want to add a local sizing around the split and the throat. For this step, the section created in SpaceClaim is used. Each local sizing gets its own sub step where the size of the local sizing is set. In the case of the SSSL nozzle, the local sizing set around the split is 3mm. The program will then try to create mesh cells that are no larger than 3 mm.

3. Create surface mesh: This creates the mesh on the surface of the body. This enables the program to have a reference point for the volume mesh created later. For this step there are several options that can be changed. The minimum and maximum size of the cells can be set. Furthermore, there are more advanced options that are not used for this thesis. For the SSSL nozzle, the minimum cell size was set to 5.5mm and the maximum size to 20mm.

4. Describe geometry: In order for the program to detect the inlet and outlet, the user has to specify these areas. This is done by using the sections created in SpaceClaim and setting the type of inlet and outlet. The type used is a pressure inlet and outlet. In this step, the walls of the nozzle are specified as a solid body. Additionally, the fluid regain can be inspected in order to observe if it is correct.

5. Create volume mesh: This is the step that creates the volume mesh for the fluid. This section has a couple of options that are of interest. The fist option is the specification of boundary layers at the walls of the domain. In this case, the number of boundary layers are set to four. The final option that is changed is the maximum length of each cell. This is set to 20 mm.

6. Improve volume mesh: Finally, the program will try to improve the mesh by moving vertices of the mesh cells to increase the orthogonality of the mesh cells. The best mesh has a orthogonality of 1, however with the corners and turns in the SSSL nozzle this is hard to achieve. The final orthogonality was 0.42 which is still a good quality mesh [28].

Figure 6.8 and 6.9 show an example of a mesh created in Fluent meshing. The figures show an overview of the whole mesh and there is also a more detailed version around the split.

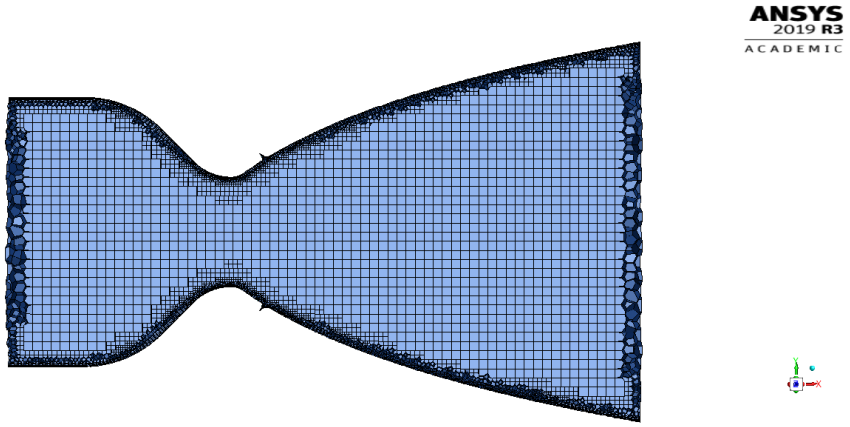

Figure 6.8: Figure showing the mesh for the second mesh approach.

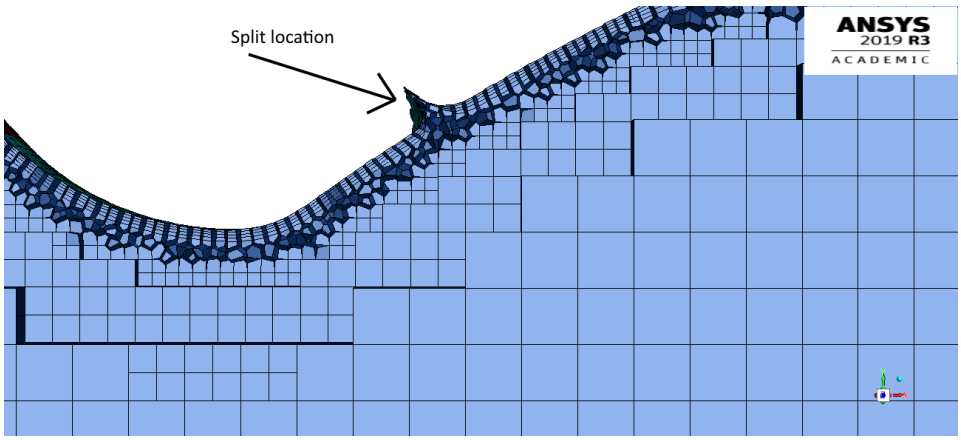

Figure 6.9: Figure showing the mesh for the second mesh approach, with higher detail around the split area. This is indicated with an arrow

6.3.1. Mesh convergence study

A mesh convergence study was performed in order to determine if the mesh was of sufficient quality. If the mesh is not detailed enough, the results from the CFD analysis are less accurate. However, as the licence for Ansys Fluent is a student version the highest number of mesh elements is set to 512000. The convergence study was therefore performed backwards in order to see if the result from the CDF analysis changed. The study was performed over 3 simulations of the same nozzle. This nozzle was the SSSL nozzle with expansion ratio 12, the split located at an expansion ratio of 1.75 and the thrust vectoring set to 5 degrees. The mesh density was 480000, 350000 and 250000 mesh elements. The number of mesh elements are hard to control directly therefore, it was chosen to get as close as possible. Several parameters were checked at the exit in order to see if the mesh had a significance on the result. In table 6.5 the results are given for the various meshes.

Table 6.5: Results from the mesh convergence study

Parameter	Mesh density 480000	Mesh density 350000	Mesh density 250000
Pressure	45127.46 Pa	45266.69 Pa	45329.80 Pa
Exit velocity	2609.07 ms^{-1}	2604.93 ms^{-1}	2604.50 ms^{-1}
Temperature	1678.53 K	1681.55 K	1681.75 K

From table 6.5 it can be seen that the parameters keep changing towards the highest mesh density in the study. This indicates that the mesh is not yet converged. The results from the CFD study will

therefore be slightly less accurate than compared to a higher density mesh. The changes between the different meshes are not significant, 0.31% for pressure, 0.16% for velocity and 0.18% for temperature. The percentages are calculated between the 480000 and the 350000 mesh density case. Due to the mesh not being fully converged, it is recommended that a follow up study researches at what point the mesh is converged and how large the differences are with the results from this thesis.

6.4. Turbulence model

It was chosen to use the Shear Stress Transport (SST) k-omega turbulence model for the simulations since it yields good results for rocket nozzles. The SST k-omega is a combination of two models. It uses the k-omega model close to the walls as this model can predict shock waves and wall behaviour accurately. In the free stream, the model uses the k-epsilon model as this model is accurate in the free stream. A comparison between many turbulence models on a rocket nozzle has been explored in the paper by Balabel et al. [9]. The paper concludes that the SST k-omega turbulence model is the best model to use for computing the fluid flow in a rocket nozzle. The paper also states that the SST k-omega model was the best at computing the shock wave position and the flow parameters after the shock wave. As the SSSL nozzle relies on the shock wave for the amplification factor it was a clear choice to use the SST k-omega model. A comparison between the two models was performed on the SSSL nozzle with expansion ratio 12 and split at 1.75 for the 5 degree case. In figure 6.10, the split at the bottom side can be seen with a pressure contour. On the right is the CFD result of the SST k-omega turbulence model and on the right is the result for the k-epsilon. The k-epsilon model is known to not handle adverse pressure gradients and this can also be seen in figures 6.10 and 6.11 [9]. The SST k-omega model predicts a much lower pressure drop, due to the expansion wave at the split. When looking at the top portion of the nozzle, the same behaviour can be seen from the k-epsilon model. It predicts a much larger pressure gain after the shock wave. This can be seen in figure 6.11. It can also be seen that the shock wave in the k-epsilon model is at a steeper angle than the shock wave in the SST k-omega. The prediction of the shock wave angle and the calculation of the parameters behind the shock is also explored in the paper by Balabel et al.[9]. In the paper the SST k-omega performed the best with respect to the experimental data. The turbulence model also has an effect of on the Mach number contour. On the bottom of the nozzle, the flow reattaches much quicker for the k-epsilon model than for the SST k-omega model. On the top side of the nozzle, the k-epsilon model has a much larger region of lower Mach number behind the shock wave. These two effects can be seen in figures 6.12 and 6.13 respectively.

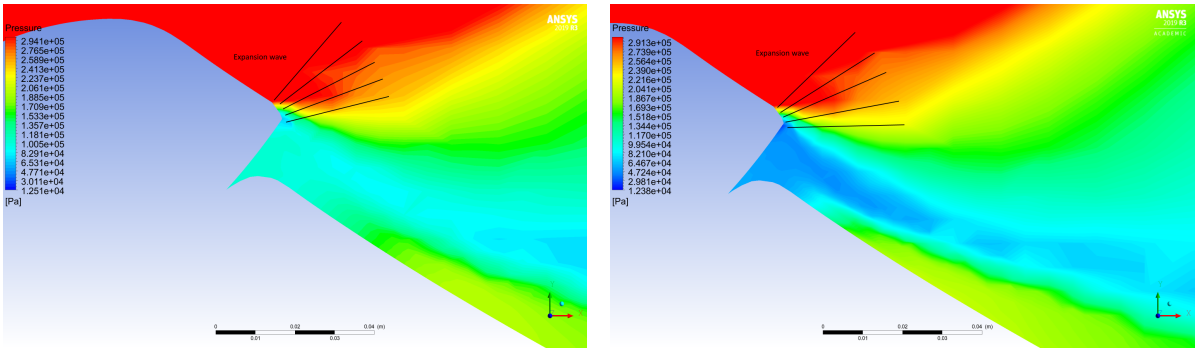

(a) SST k-omega

(b) k-epsilon

Figure 6.10: Pressure contour of the split at the bottom of the nozzle.

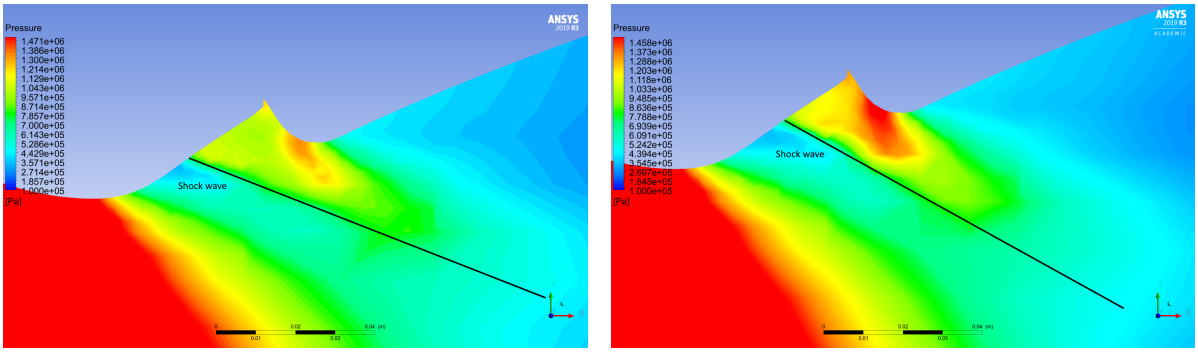

(a) SST k-omega (b) k-epsilon

Figure 6.11: Pressure contour of the split at the top of the nozzle.

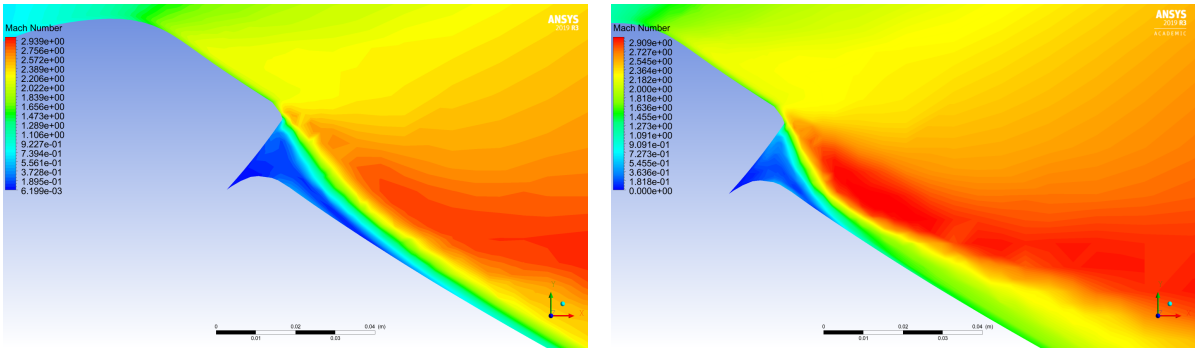

(a) SST k-omega (b) k-epsilon

Figure 6.12: Mach contour of the split at the bottom of the nozzle.

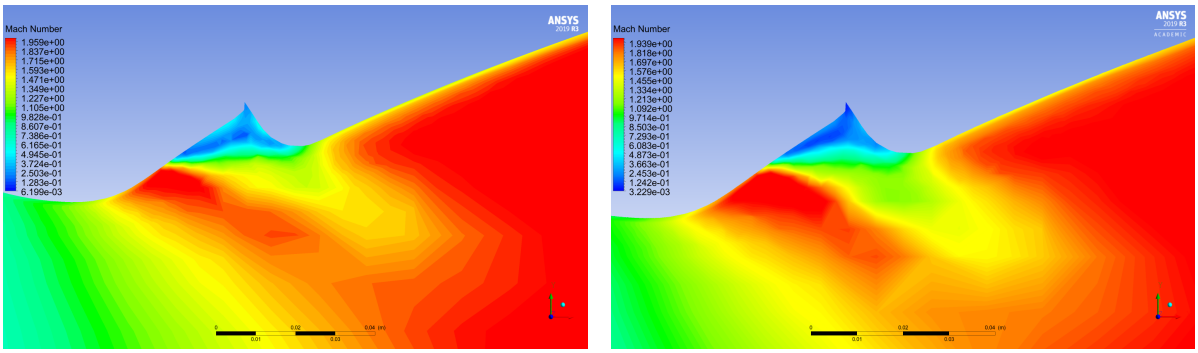

(a) SST k-omega (b) k-epsilon

Figure 6.13: Mach contour of the split at the top of the nozzle.

The turbulence model also has an effect on the parameters at the exit at the nozzle and a much larger effect on the aerodynamic torque on the nozzle. The difference between the two models is shown in table 6.6. The largest difference is in the aerodynamic torque, as most of the torque is created at the nozzle wall. The SST k-omega gives a higher value since it is more accurate at predicting pressure and shear values at the nozzle wall. The other values have much smaller differences, but the SST k-omega model predicts that the nozzle performs better than the k-epsilon model. In order to validate the results, a experimental test of the SSSL nozzle should be done to confirm that the SST k-omega turbulence model preforms the best. However, using literature to support the choice, the SST k-omega model is chosen as the turbulence model for the CFD simulations in this thesis.

Table 6.6: Results at the exit of the nozzle for the SST k-omega and k-epsilon turbulence models for the SSSL nozzle.

Parameter	SST k-omega turbulence model	k-epsilon turbulence model	Percentage difference
Pressure	45127.46 Pa	45476.62 Pa	0.77%
Mass flow	35.76 kg/s	35.75 kg/s	0.03%
Mach number	3.095	3.080	0.48%
Aerodynamic moment	1950.21 Nm	1816.78 Nm	6.84%
Thrust	101.70 kN	101.44 kN	0.26%
Specific impulse (Isp)	289.90 s	289.23 s	0.23%
Amplification factor	1.518	1.503	0.99%

6.5. Computational fluid dynamics convergence

In order to trust the CFD results there are a couple of criteria that have to be checked. Firstly, the residuals of the simulation are checked against the convergence criteria. This is set to 1E-3. The residuals are the error of the simulation and if they are too high the simulation result can not be trusted. However, there are cases when the steady state solution residuals keep oscillating around a certain value. This effect can have different causes. The first cause can be the mesh detail. If the mesh is too coarse, the solution may not converge properly. During this research, a student licence for Ansys was used. The student licence sets a limit to the amount of mesh nodes. The limit is set to 512000 nodes. The meshes in this study were configured to be as close to this limit as possible in order to get the best quality. A mesh convergence study was conducted but it was concluded that the mesh was not yet converged. However, for this thesis the error from the mesh convergence is considered small. The largest error was found in the pressure at the exit when moving from a mesh with 350000 element to the used mesh of 480000 elements. The maximum error was 0.3%. The second source of oscillating residuals can be caused by non-steady flow phenomena such as vortex formation [5–7]. Vortex formation is areas of rotating flow, these are inherently non steady and therefore the residuals can keep oscillating [3]. In this case, other parameters of the flow, such as mass flow and pressure forces, can be observed. If these remain constant and do not change as the simulation progresses, the solution can be considered converged even if the residuals have not reached the convergence criteria.
For most of the CFD calculations in this thesis, the residuals kept oscillating close to the convergence criteria. Therefore, it was chosen to look at various parameters in order to conclude if the solution was converged. The parameters considered were; aerodynamic moment, x/y/z-force and mass flow in and out. The most important of the above mentioned parameters is the mass flow in and out of the nozzle. If the mass flow in and out of the nozzle is not balanced and constant, the solution can not be considered converged. In figure 6.14, it can be seen that the residuals have not reached 1E-3. However, when looking at the aerodynamic moment, x/y/z force and mass flow it can be concluded that the solution has converged. This is due to the constant behaviour of these parameters. An example of this is illustrated in figures 6.15 and 6.16. Most of the CFD simulations ended up with oscillating residuals slightly over the convergence criteria. Therefore, it was chosen to look at the forces and mass flows of the solution in order to determine convergence. Especially the simulations of the SM nozzle had problems with vortex formation. Vortex formation can be seen from the streamlines of the SM nozzle at 0 degree thrust vectoring in figure 6.17. On the left figure, it can be seen that some of the streamlines are trapped and make spirals at the flex seal area. The formation of these vortexes affects the residuals. However, they have little to no effect on the exit conditions. This can be seen on the right figure as the vorticity has become symmetrical by the time the flow reaches the exit. When comparing the vorticity of the SM nozzle and the SSSL nozzle for the 5 degree case it can be seen that the SSSL nozzle has much less vorticity than the SM nozzle. The comparison can be seen in figure 6.18, the SSSL nozzle design A is the left figure and the SM nozzle is the right figure. Therefore the SSSL nozzle simulations were easier to converge to a solution.

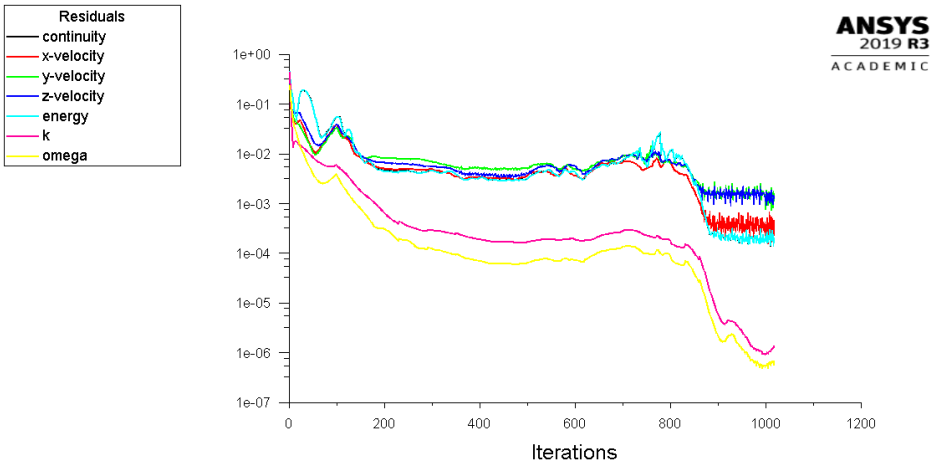

Figure 6.14: Figure of oscillating residuals of the CFD simulations

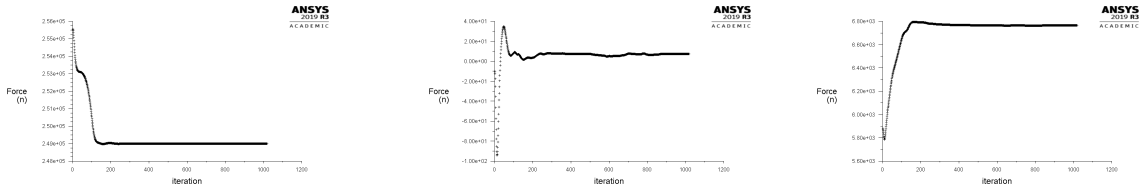

(a) Trace of the x-force on the nozzle over the iterations

(b) Trace of the y-force on the nozzle over the iterations

(c) Trace of the z-force on the nozzle over the iterations

Figure 6.15: Solution values for x, y and z force graphed against the iteration of the simulation

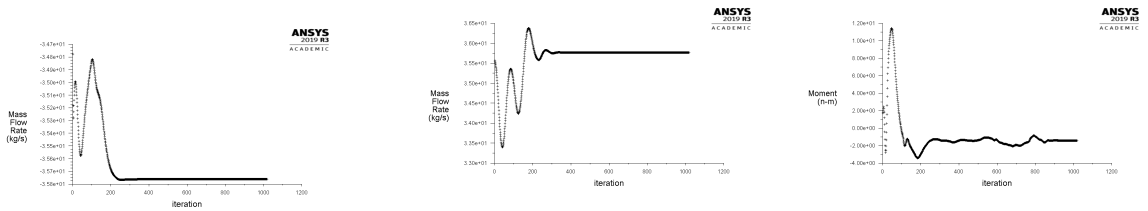

(a) Trace of the mass flow going in to the nozzle

(b) Trace of the mass flow going out of the nozzle

(c) Trace of the aerodynamic moment on the nozzle

Figure 6.16: Solution values for the mass flow in and out and the aerodynamic moment for the CFD simulation.

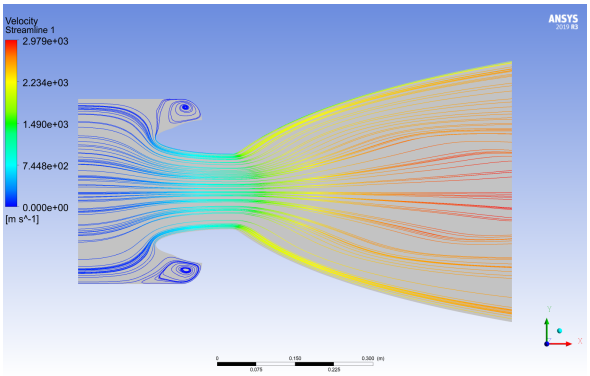

(a) Velocity streamlines of the SM nozzle at 0 degree thrust vectoring. The vortexes are formed in the flex seal area.

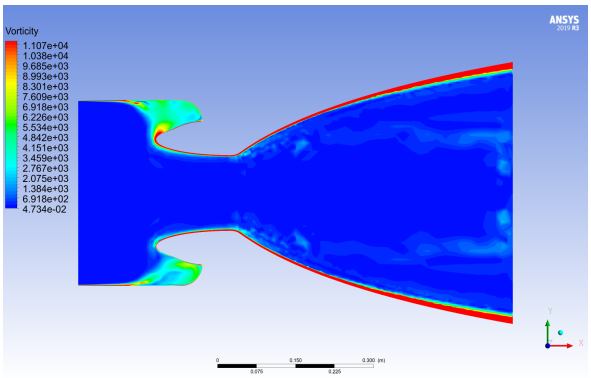

(b) Vorticity of the SM nozzle at 0 degree vectoring

Figure 6.17: Vorticity contour and velocity stream lines of the SM nozzle at 0 degree thrust vectoring

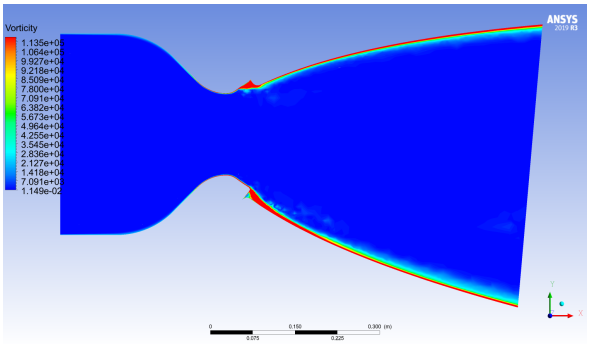

(a) Vorticity of the SSSL nozzle at 5 degree vectoring

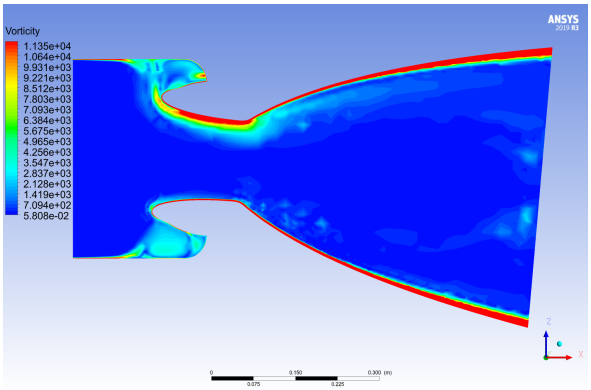

(b) Vorticity of the SM nozzle at 5 degree vectoring

Figure 6.18: Vorticity contour the SM nozzle and SSSL nozzle design A at 5 degree thrust vectoring

6.5.1. Criteria for convergence

For the CFD simulations, the following set of criteria are used to confirm that the solution has converged:

1. Residuals: Less than 1e-3
2. Mass flow in: No change the last 50 iterations in the mass flow in
3. Mass flow out: No change the last 50 iterations in the mass flow out
4. Total mass flow: Mass flow in minus mass flow out is equal to 0
5. X-Y-Z force: No change in the last 50 iterations
6. Aerodynamic moment: No change in the last 50 iterations

Each simulation is checked against the criteria above. If the simulation does not meet the required criteria, it will be looked at which parameter is not passed. Based on the parameter that did not pass the case is checked rigorously in order to determine if the solution has converged. In the case the residuals are higher than 1e-3 and the rest of the criteria is met, the solution can still be said to be converged. As was discussed in the previous section the residuals have a tenancy to oscillate around one value. If any of the other criteria are not met then a more rigorous check has to be performed by checking if the output is as expected and comparable to the other nozzles.
The convergence of each of the simulations are tracked by the use of the following table. The different symbols in table 6.7 have the following meaning: $\surd$ is the sign for a passed check. $\sim$ is the symbol for a nearly passed check. X is the symbol for a failed check. At the right side of the table is a section for some notes on the particular case.

Table 6.7: Convergence test matrix to determine if the simulation has been converged. R is residuals, $\dot{m}_i$ is mass flow in, $\dot{m}_o$ is mass flow out, $\dot{m}_{tot}$ is mass flow total, X-Y-Z is the X-Y-Z forces and AM is the aerodynamic moment.

Simulation	R	$\dot{m}_i$	$\dot{m}_o$	$\dot{m}_{tot}$	X-Y-Z	AM	Convergence	Notes
Test check	~	√	√	√	√	√	√	As all other criteria than the residuals are converged the total simulation is deemed converged.

6.5.2. Errors in the computational fluid dynamics simulations

The errors of the CFD calculations are hard to predict from the residuals alone. One way to classify the errors in the CFD simulations is to do an experimental test. An experimental test is however out of the scope of this thesis. In order to establish whether the CFD calculations make sense, the output of the CFD simulations are compared to the performance program which used ideal rocket theory. It is expected that the CFD simulations have slightly worse performance than the calculations from ideal rocket theory.

6.6. Simulation plan

All the methods have been developed for running the simulations and getting the desired output have been created. In this section the simulation plan and all the cases that are simulated are presented. In order to keep track of all the different cases a naming convention has been created. The naming convention of the folders and files were based on the type of nozzle, split location, expansion ratio and angle of thrust vectoring. Example: ”SSSL_1_75_e45_5deg” would be the name for the SSSL nozzle with the split located at an expansion ratio of 1.75. It is the nozzle with a total expansion ratio of 45 and it has a thrust vectoring of 5 deg.

In table 6.8 a overview of all the cases tested are shown. In the column with angles all the angles tested are separated with a comma. The rationale for the choice of the cases is discussed below. The angles 0, 2.5 and 5 degree were chosen since the maximum deflection requested by Nammo was 5 degree and it is desirable to know the 0 degree deflection. The 2.5 degree was then a logical mid point between the two other angles. The split locations of the nominal nozzle with expansion ratio 12 were chosen to be 1.75, 2, and 2.25 since these values span the range of most SSSL nozzles in literature [48]. For the upper stage nozzle with expansion ratio 45 and the sounding rocket nozzle with expansion ratio 6.5 the outer two split locations were chosen. By requirement from Nammo these should not be different than the split locations of the nominal nozzle in order to compare these nozzles. The total pressure was changed in order to see the effect of throttling the nozzle a decrease of 2.5 bar per simulation was chosen. The values were chosen arbitrarily. Nammo had requested the research on the throttling of the nozzle. All the requirements of Nammo can be found in the SOW in appendix A.

Table 6.8: List simulations that were performed. The split location is the area expansion ratio at the location of the split. Where multiple angles are mentioned one simulation for each of the angles were performed.

Type nozzle	Expansion ratio	Split location	Angle (degree)	Total pressure (Bar)
SM nozzle	12	-	0, 2.5, 5	35
SSSL nozzle	12	1.75	0, 2.5, 5	35
SSSL nozzle	12	2	0, 2.5, 5	35
SSSL nozzle	12	2.25	0, 2.5, 5	35
SSSL nozzle	45	1.75	0, 2.5, 5	35
SSSL nozzle	45	2.25	0, 2.5, 5	35
SSSL nozzle	6.5	1.75	0, 2.5, 5	35
SSSL nozzle	6.5	2.25	0, 2.5, 5	35
SSSL nozzle	12	1.75	5	32.5
SSSL nozzle	12	1.75	5	30

6.6.1. Input to the computational fluid dynamics simulation

The input to the different CFD simulations is discussed in this section. All the nozzles use the same operating gas. Likewise, the nozzles will mostly be using the same boundary conditions as well. Only the simulations exploring the effect on the amplification factor from changing the mass flow will have a different chamber pressure. In tables 6.9 to 6.12, the input values are given and additional notes are provided for the inputs that need clarification. Each table provides information about one segment of the simulation inputs.

Table 6.9: List of operating gas parameters

Gas property	Value	Notes
Density	Treated as ideal gas	-
Specific heat	3285.1 J/kgK	Set as a constant
Thermal conductivity	0.0242 W/mK	Set as a constant
Viscosity	Sutherland's law, Reference viscosity: 1.217e-5 kg/ms, Reference temperature: 320.12 K Effective temperature: 737.30 K	The viscosity constants are taken as a combination of water vapour and CO_2 using the ratio of water vapour to CO_2 to calculate the constants [17]. The ratio can be found in the SOW from Nammo in chapter A.
Molecular mass	22 g/mol	Input from Nammo in the SOW in appendix A

Table 6.10: List of boundary conditions

Boundary	Value	Notes
Free stream conditions	0 Pa	Treated as a vacuum
Gas pressure inlet	35e5 Pa	It is assumed that the gas has no velocity when entering the simulation domain
Gas temperature inlet	2721 K	-
Gas pressure outlet	1 Pa	The pressure at the outlet is set to 1 Pa in order to compute the density with the ideal gas law. Has no influence on the result.
Gas temperature outlet	300 K	Has no influence on the result other than the initial guess
Walls	Free slip condition	This means that there is no friction at the wall. As the material of the nozzle is designed to be as smooth as possible this is considered a valid assumption.

Table 6.11: List of models used

Model	Value	Notes
Time domain	Steady state	-
Energy equation	Turned on	Calculating if the energy is conserved and where losses occur
Continuity equation	Turned on	Calculating that the mass flow in equals the mass flow out
Momentum equation	Turned on	Calculating forces on the nozzle
Turbulence model	Shear Stress Transport k-omega	Reason behind was explored in section 6.4
Spatial discretization	Second order upwind	-

Table 6.12: List of solution controls

Controls	Value	Notes
Initialization	Hybrid	Creates an initial guess with a coarse version of the mesh
Solution steering	Supersonic	Letting know to Fluent that it will deal with supersonic flow
Courant number range	1-100	The courant number specifies the time step of the simulation. Even though the solution is steady state the program simulates the nozzle as a transient system until it does not change with time any more. Higher numbers means a larger time step [30]. At the end of the simulation the Courant number is set manually to 0.5 to get a good convergence.

6.6.2. Calculation of amplification factor and aerodynamic moment

In this section the method for calculating the amplification factor from the Ansys results is discussed and the method of finding the aerodynamic moment is discussed.
The amplification factor is found by finding the angle of thrust. The angle of thrust is found from equation (6.6), where δ_{thrust} is the angle of thrust, v_y is the y velocity of the exit flow and v_x is the x velocity of the exit flow. Then the amplification factor can be calculated by equation (1.1).

$$\delta_{thrust} = tan^{-1}\left(\frac{v_y}{v_x}\right) \tag{6.6}$$

The aerodynamic moment is calculated within Ansys Fluent. The moment centre is specified at the rotation point of the nozzle and then Ansys calculates the moments of the nozzle around that point.

6.7. Conclusion to the Ansys approach

In this chapter the explanation of the CFD analysis method has been given. The various aspects connected to the CFD simulations have been explored in detail, such as a mesh convergence study, turbulence model testing and general convergence criteria. It was found that the CFD simulations might be influenced by the non converged mesh but that it should not have a large impact for the comparison between the nozzles. The accuracy of the CFD calculations will not be perfect but since the goal is to compare the nozzles the accuracy of the CFD result is of less concern. Additionally, the values from the CFD calculations are checked against the values from the performance program to see if they are as expected. Therefore, it can be concluded that the CFD method used is of sufficient quality for the objectives in this work.

7

Results and discussion on the comparison between the supersonic split line nozzle and the submerged movable nozzle

In this chapter, the results from the research on the comparison between the SSSL nozzle system and the SM nozzle system is presented. Firstly, the performance of the nozzles is presented. Secondly, the results from the mass model are presented. After the results have been displayed, the results are discussed. The nozzle flow in all the figures in this chapter goes from left to right. For all nozzle representations, the flow of gases goes from left to right.

7.1. Results

In this section, the results of the comparison between the SSSL nozzle and SM nozzle are presented. The flow fields of the two nozzles are presented. Only the flow field for the 5 degree case are shown. Additional flow field representations at all angles can be found in appendix D. The two nozzles were tested with angles of 0, 2.5 and 5 degrees. The expansion ratio of both nozzles for this comparison was 12, as this was the expansion ratio requested by Nammo.
The naming convention for the SSSL nozzles is as following: The nozzle with the split at 1.75 expansion ratio is design A, the one at 2 is design B and the one at 2.25 is design C. In section 6.6 the full plan for the simulations can be found.

The additional flow fields that can be found in appendix D contain the following parameters.

- Mach number contour
- Pressure contours
- Temperature contour
- Turbulence contour
- Total temperature contour
- Heat flux contours
- Pressure and temperature trace along nozzle wall
- Residual plots

7.1.1. Convergence check

The convergence check for the nozzles: SSSL nozzle design A, B and C and the SM nozzle with expantion ratio 12 can be found in table 7.1

7.1.2. Flow field and nozzle performance results

In this section, a number of contour plots of the flow field of the SSSL nozzle and the SM nozzle are shown. The most interesting cases are shown in this section however, more flow field results are shown in appendix D.
Most detail of the shock wave and expansion wave can be seen in the 5 degree case of the SSSL nozzle. As a result, this case was selected to highlight the shock position and the expansion wave position. In figure 7.1 the pressure contour of design A of the SSSL nozzle is shown to the left and the SM nozzle is shown to the right. Both nozzles are at a vectoring angle of 5 degrees. The annotations on the SSSL nozzle show the approximate location of the shock wave and expansion wave that form due to the split.

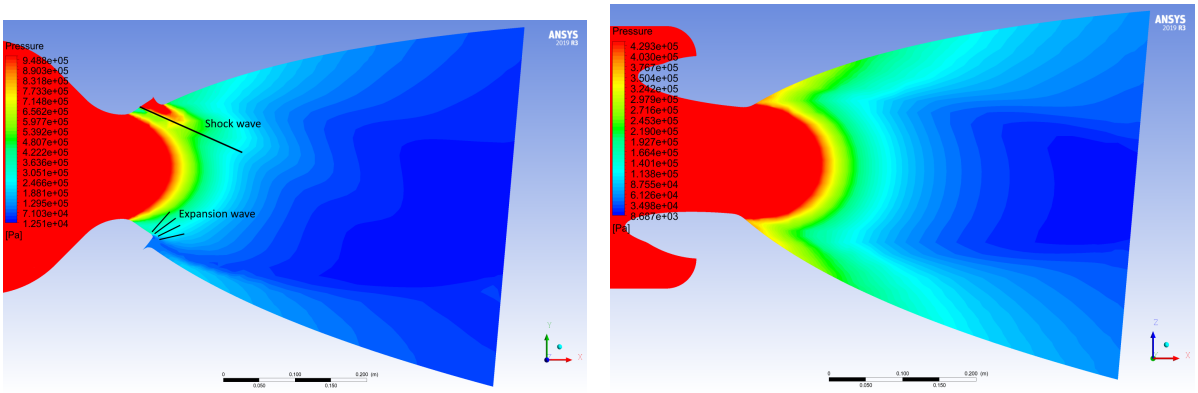

(a) SSSL nozzle at 5 degree vectoring

(b) SM nozzle at 5 degree vectoring

Figure 7.1: Pressure contour of the SSSL nozzle design A and the SM nozzle

It can be seen that the SM nozzle does not form any shock waves since it has turned the flow before the throat. The SM nozzle also has a symmetrical expansion of the gasses towards the exit whereas the SSSL nozzle has a highly asymmetrical distribution along the centreline. The asymmetry is what causes the amplification factor. When looking at the pressure distribution along the nozzle wall that is illustrated in figure 7.2, the asymmetrical pressure distribution is visible. The largest pressure difference between the top and bottom wall is located around the split area for the SSSL nozzle. The location of the split is indicated with a green dotted line. Additionally the throat is indicated with a orange dotted line. For the SM nozzle, the pressure distribution along the nozzle wall is the same for top and bottom. Only minor differences are shown around the x = -0.15. The spike in x direction for the pressure traces are due to the submergence of the SM nozzle. The pressure remains the same until the leading edge of the throat entrance. Therefore it looks as of the pressure trace turns back on itself.

Table 7.1: Convergence test matrix to determine if the simulation has been converged for the nozzles: SSSL nozzle design A, B and C and the SM nozzle with expantion ratio 12. R is residuals, $\dot{m}_i$ is mass flow in, $\dot{m}_o$ is mass flow out, $\dot{m}_{tot}$ is mass flow total, X-Y-Z is the X-Y-Z forces and AM is the aerodynamic moment.

Simulation	R	$\dot{m}_i$	$\dot{m}_o$	$\dot{m}_{tot}$	X-Y-Z	AM	Convergence	Notes
SSSL nozzle design A 0deg	~	√	√	√	√	√	√	As all other criteria than the residuals are converged the total simulation is deemed converged.
SSSL nozzle design A 2.5deg	~	√	√	√	√	√	√	As all other criteria than the residuals are converged the total simulation is deemed converged.
SSSL nozzle design A 5deg	~	√	√	√	√	√	√	As all other criteria than the residuals are converged the total simulation is deemed converged.
SSSL nozzle design B 0deg	~	√	√	√	√	√	√	As all other criteria than the residuals are converged the total simulation is deemed converged.
SSSL nozzle design B 2.5deg	~	√	√	√	√	√	√	As all other criteria than the residuals are converged the total simulation is deemed converged.
SSSL nozzle design B 5deg	~	√	√	√	√	√	√	As all other criteria than the residuals are converged the total simulation is deemed converged.
SSSL nozzle design C 0deg	~	√	√	√	√	√	√	As all other criteria than the residuals are converged the total simulation is deemed converged.
SSSL nozzle design C 2.5deg	~	√	√	√	√	√	√	As all other criteria than the residuals are converged the total simulation is deemed converged.
SSSL nozzle design C 5deg	~	√	√	√	√	√	√	As all other criteria than the residuals are converged the total simulation is deemed converged.
SM nozzle 0deg	X	~	√	~	√	√	√	The mass flow in for the SM nozzle was oscillating but the oscillations were small and the mass flow out was constant. Vorticity at the entrance prevents a steady state solution at the inlet. The results were further checked against the performance program and deemed converged enough.
SM nozzle 2.5deg	~	√	√	√	√	√	√	Same as 0 degrees
SM nozzle 5deg	~	√	√	√	√	√	√	Same as 0 degrees

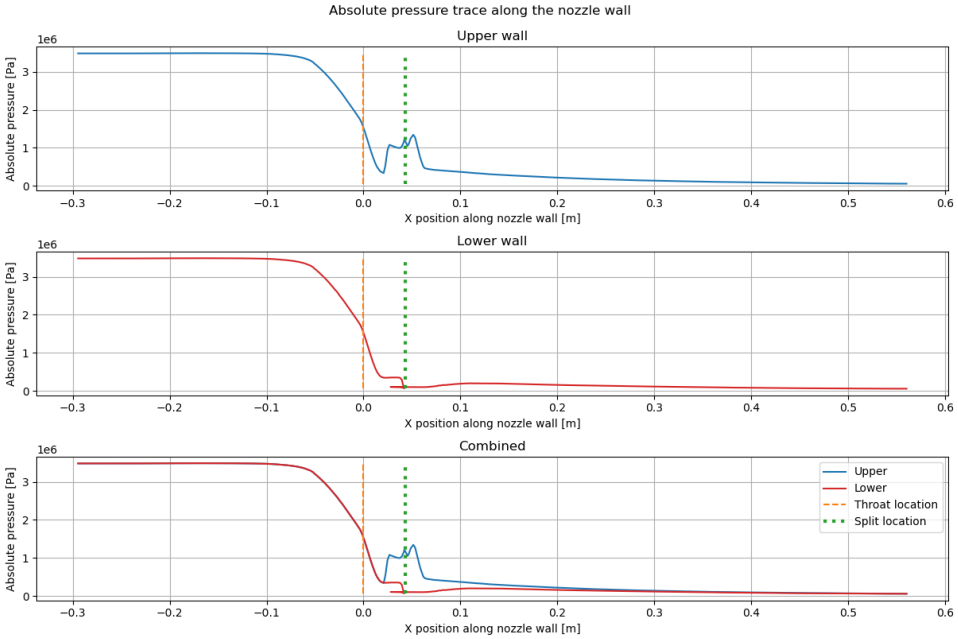

(a) SSSL nozzle at 5 degree vectoring

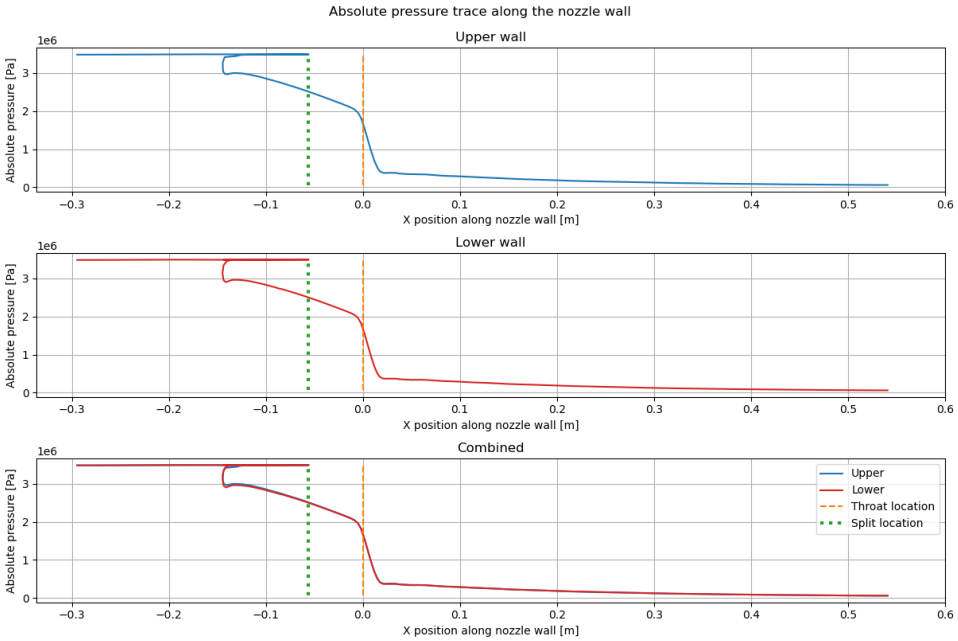

(b) SM nozzle at 5 degree vectoring

Figure 7.2: Pressure distribution along the nozzle wall of the SSSL nozzle design A and the SM nozzle

The same behaviour of the flow field can be seen in the Mach number contour. Again, the SM nozzle has a symmetrical distribution of Mach number while the SSSL nozzle is highly asymmetrical. This is illustrated in figure 7.3.

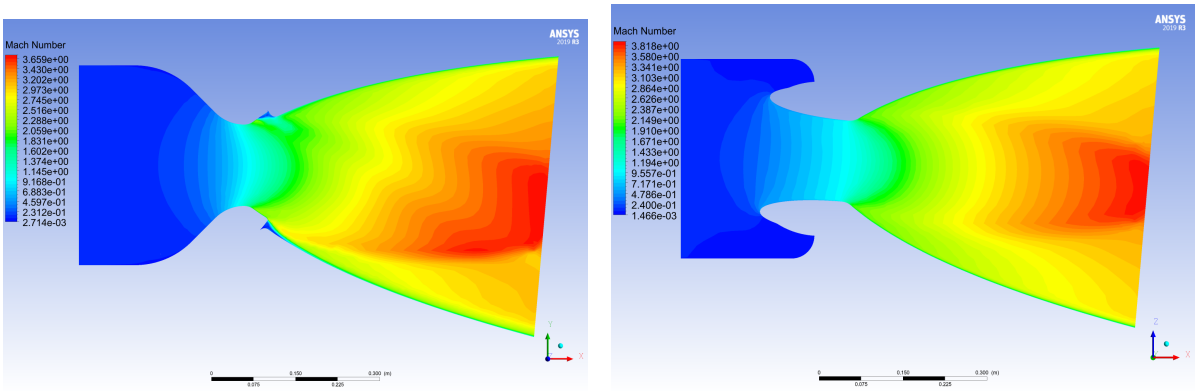

(a) SSSL nozzle at 5 degree vectoring (b) SM nozzle at 5 degree vectoring

Figure 7.3: Mach number contour of the SSSL nozzle design A and the SM nozzle

In figure 7.4 a comparison between the SSSL nozzle design A and the SM nozzle at 0 degree vectoring can be seen. The variable of the contour plot is the Mach number. It can be seen that both nozzles now have quite similar flow fields as the split has no large impact on the flow field. In figure 7.5 it can be seen that there are small expansion waves followed by weak shocks formed at the split. The expansion waves and shock waves have been indicated for clarity. The shocks formed at the splits will induce extra losses and the performance will be a lower than for an undisturbed flow field. For both the nozzles it can be seen that there are weak shocks formed after the throat. This is indicated on the SM nozzle in figure 7.4.

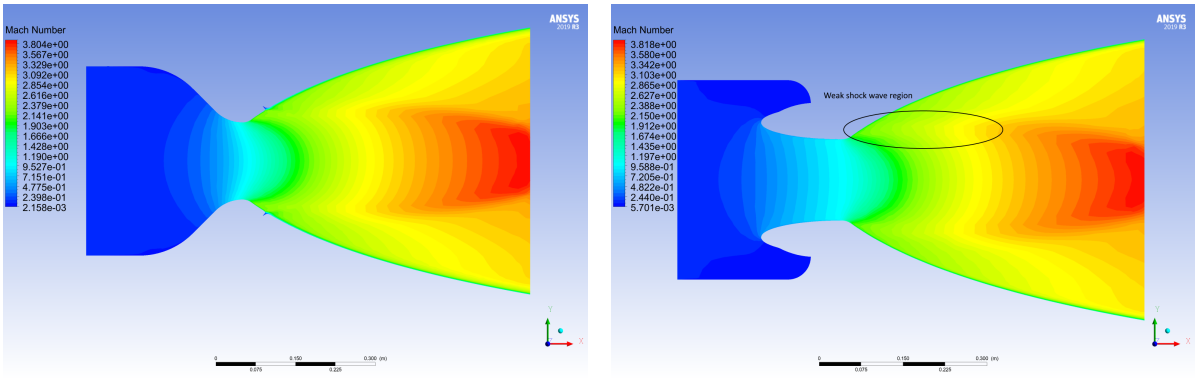

(a) SSSL nozzle at 0 degree vectoring (b) SM nozzle at 0 degree vectoring

Figure 7.4: Mach number contour of the SSSL nozzle design A and the SM nozzle

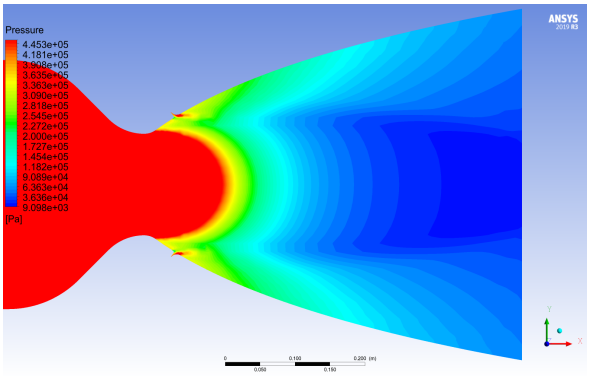

(a) SSSL nozzle at 0 degree vectoring

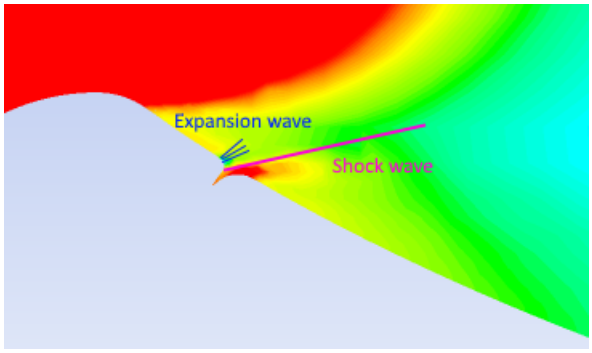

(b) Detailed view of the same nozzle with indications of expansion waves and shock waves

Figure 7.5: Pressure contour of the SSSL nozzle design A at 0 degrees

Two other split locations were investigated for the comparison between the SSSL nozzle and the SM nozzle. When looking at the Mach number contour of design B and C of the SSSL nozzle in figure 7.6, it can be seen that the shock wave produced at the split on the top side becomes stronger for a split at a higher expansion ratio. The influence of the shock is increasingly more clear for a higher expansion ratio split. This has been indicated in the figure with a circle around the affected area.

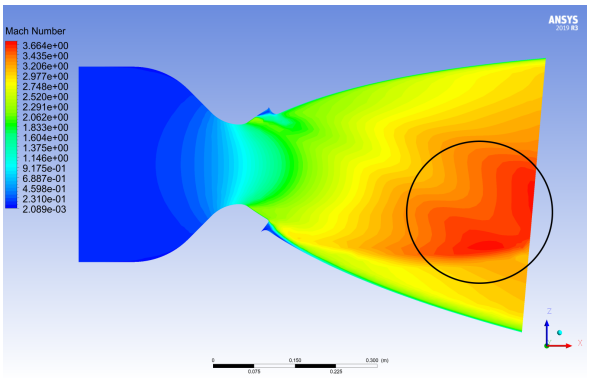

(a) SSSL nozzle design B at 5 degree vectoring

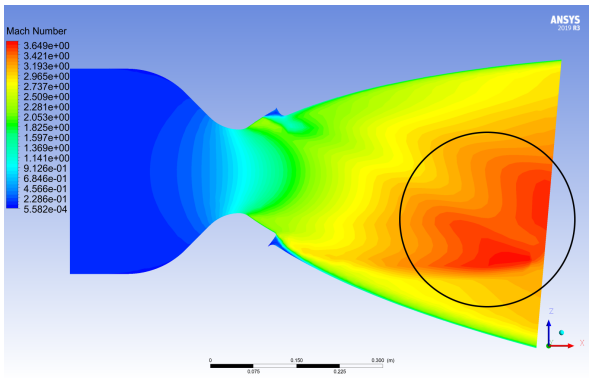

(b) SSSL nozzle design C at 5 degree vectoring

Figure 7.6: Mach number contour of the SSSL nozzle design B and C at 5 degree of vectoring

When looking at the turbulence for both the SM and the SSSL nozzle design A for 5 degree thrust vectoring, it can be seen that the SM nozzle has a large turbulent layer on the upper side of the nozzle. The SSSL nozzle however does not have this large layer. The SSSL nozzle does have a higher turbulence level close to the wall than the SM nozzle but this does not extend as far as the SM nozzle. The increased turbulence in this region is a result of the increased vorticity that is induced from the submergence of the SM nozzle. This was discussed in section 6.5

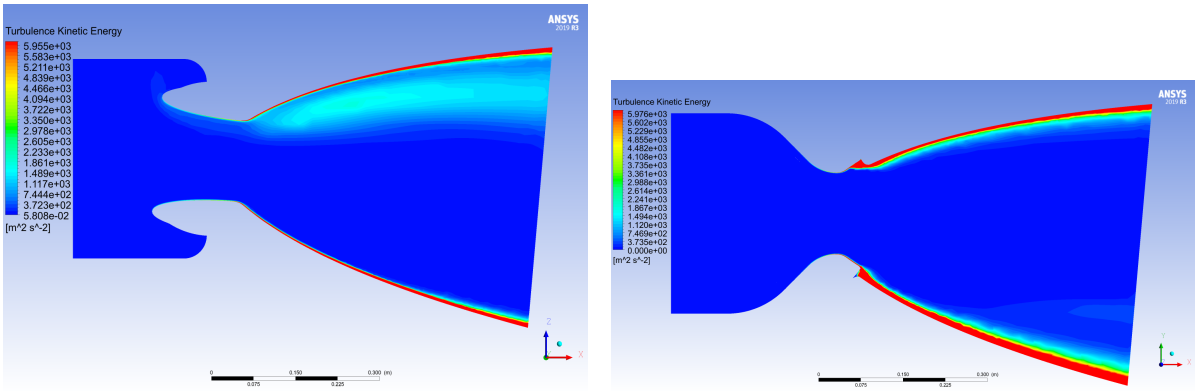

(a) SM nozzle at 5 degree vectoring

(b) SSSL nozzle design A at 5 degree vectoring

Figure 7.7: Turbulence kinetic energy contour of the SSSL nozzle design A and the SM nozzle at 5 degree of vectoring

The nozzle performance of the various nozzles tested are presented in tables 7.2 to 7.4. In table 7.2, the results from 0 degree thrust vectoring are shown. In tables 7.3 and 7.4, the thrust loss and Isp loss with respect to the 0 degree case are included. It can be seen that the SM nozzle has better performance than the SSSL nozzles. The thrust of the SM nozzle is 0.64% higher and the Isp is 0.16% higher than the SSSL nozzle at 0 degree vectoring. However, a straight comparison is not possible due to the higher mass flow of the SM nozzle. As both nozzles have the same exit area and the same throat area the mass flow should be the same. This indicates some errors in the CFD modelling. If the mass flow of the SM nozzle is set to the same as the SSSL nozzles and assuming that the rest of the flow parameters are constant the performance difference becomes: 0.19% higher thrust than the SSSL nozzle design A and 0.20% higher Isp. These values are so low that the performance at 0 degree are close to identical. In tables 7.2 to 7.4 the column called SM corrected are the values for the SM nozzle when applying the mass flow correction and assuming the rest of the flow parameters stay the same.
When vectoring at 5 degrees, the performance difference between the SSSL nozzle and the corrected SM nozzle increases to 0.77% and 0.77% for thrust and Isp respectively. The SSSL nozzles have worse performance due to the split interrupting the flow slightly. It can also be noted that the performance of the SSSL nozzle becomes worse when moving the split to a higher expansion ratio, this is around 0.05% for both thrust and Isp when going from design A to C for the 0 degree case. The loss increases to 0.62% for both Isp and thrust when vectoring at 5 degrees.
The performance loss of the SSSL nozzle is also larger than the SM nozzle while vectoring with respect to the non-vectoring state. The thrust and Isp loss is 1.15% for design C but reduces to 0.58% for design A at 5 degree thrust vectoring. The SM nozzle experiences at maximum 0.01% thrust loss and 0% Isp loss. The aerodynamic torque of the SSSL nozzle is larger than the SM nozzle which has almost no aerodynamic moment. The torque of the SM nozzle is 40.76 Nm and the torque of the SSSL nozzle around 2000 Nm for the 5 degree case. This can be explained by the fact that the SM nozzle has a almost symmetrical flow field while the SSSL nozzle does not.
The SSSL nozzle receives a larger amplification factor when moving the split to a higher expansion ratio. It goes from 1.52 to 1.59 when moving from design A to C for the 5 degree case. The largest change in amplification factor is for the 2.5 degree case which increases from 1.57 to 1.66 when going from design A to design C.

Table 7.2: Nozzle performance parameters for the 0 degree thrust vector angle case for the SSSL nozzle and SM nozzle at an expansion ratio of 12.

Parameter	SSSL design A	SSSL design B	SSSL design C	SM nozzle	SM corrected
Thrust	102.29 kN	102.27 kN	102.25 kN	102.95 kN	102.50 kN
Isp	291.57 s	291.51 s	291.45 s	292.04 s	292.16 s
Thrust vector angle	0 deg	0 deg	0 deg	0 deg	0 deg
Amplification factor	1	1	1	1	1
Mass flow	35.76 kg/s	35.76 kg/s	35.76 kg/s	35.94 kg/s	35.76 kg/s
Aerodynamic moment	4.15 Nm	2.85 Nm	1.59 Nm	3.58 Nm	3.58 Nm

Table 7.3: Nozzle performance parameters for the 2.5 degree thrust vector angle case for the SSSL nozzle and SM nozzle at an expansion ratio of 12. The thrust loss and isp loss are calculated by finding the difference with the 0 degree case of the same nozzle.

Parameter	SSSL design A	SSSL design B	SSSL design C	SM nozzle	SM corrected
Thrust	101.88 kN	101.81 kN	101.72 kN	102.95 kN	102.50 kN
Isp	290.41 s	290.20 s	289.95 s	292.04 s	292.16 s
Thrust vector angle	3.93 deg	4.034 deg	4.14 deg	2.50 deg	2.50 deg
Amplification factor	1.57	1.61	1.66	1	1
Mass flow	35.76 kg/s	35.76 kg/s	35.76 kg/s	35.93 kg/s	35.76 kg/s
Aerodynamic moment	1077.26 Nm	1109.79 Nm	1168.57 Nm	24.32 Nm	24.32 Nm
Thrust loss	0.40%	0.45%	0.51%	0.01%	0.01%
Isp loss	0.40%	0.45%	0.51%	0.00%	0.00%

Table 7.4: Nozzle performance parameters for the 5 degree thrust vector angle case for the SSSL nozzle and SM nozzle at an expansion ratio of 12. The thrust loss and isp loss are calculated by finding the difference with the 0 degree case of the same nozzle.

Parameter	SSSL design A	SSSL design B	SSSL design C	SM nozzle	SM corrected
Thrust	101.70 kN	101.48 kN	101.08 kN	102.94 kN	102.50 kN
Isp	289.90 s	289.25 s	288.07 s	292.04 s	292.16 s
Thrust vector angle	7.59 deg	7.76 deg	7.95 deg	5 deg	5 deg
Amplification factor	1.52	1.55	1.59	1	1
Mass flow	35.76 kg/s	35.76 kg/s	35.76 kg/s	35.93 kg/s	35.76 kg/s
Aerodynamic moment	1950.21 Nm	1997.21 Nm	1968.68 Nm	40.76 Nm	40.76 Nm
Thrust loss	0.58%	0.78%	1.15%	0.02%	0.01%
Isp loss	0.57%	0.77%	1.16%	0.00%	0.00%

The results of the nozzles were also checked against the performance program in order to establish if the results are reasonable. In tables 7.5 and 7.6 the difference between the CFD simulations and the performance program can be seen. Looking at the numbers in the tables it can be seen that the performance parameters from the CFD simulations stay around 1-2% lower than the values from the performance program. This is close to the range of difference seen in the validation of the performance program to the cases from literature found in section 2.3. The only value that is a bit large is the pressure difference. The pressure difference is around 5%. This can be explained by the fact that the CFD simulations do take into account turbulence and shock waves, thereby the gases are slightly less

expanded than in the ideal case.

Table 7.5: Nozzle performance parameters for the 0 degree thrust vector angle case for the SSSL nozzle with expansion ratio 12 compared to the performance program.

Parameter	SSSL nozzle design A	Performance program	Percentage difference
Thrust	102.29 kN	104.16 kN	1.79%
Isp	291.57 s	293.57 s	0.68%
Mass flow	35.76 kg/s	36.17 kg/s	1.13%
Mach number	3.129	3.191	1.94%
Pressure	44210.10 Pa	42326.29 Pa	4.45%

Table 7.6: Nozzle performance parameters for the 0 degree thrust vector angle case for the SM nozzle compared to the performance program.

Parameter	SM nozzle	Performance program	Percentage difference
Thrust	102.95 kN	104.16 kN	1.16%
Isp	292.04 s	293.57 s	0.52%
Mass flow	35.94 kg/s	36.17 kg/s	0.64%
Mach number	3.138	3.191	1.66%
Pressure	44267.79 Pa	42326.29 Pa	4.39%

In order to validate the motor performance the results are compared to the values obtained by the ideal rocket theory used in the performance program. The quality factors of the engine will then be calculated and compared with literature. They are compared to the quality factors in the book by Sutton and the design guidelines of Huzel [32, 40]. Three quality factors are evaluated. Nozzle quality factor ξ_F, Combustion quality factor ξ_c and motor quality factor ξ_s. These three factors can be calculated by using equations (6.1) to (6.3). The values are calculated for the 0 degree thrust vectoring case. As the difference in performance between the split locations is small only one of the split locations is calculated. The three different SSSL nozzles, expansion ratio 12, 45 and the scaled down nozzle, and the SM nozzle are compared to values from literature.
The calculated values and the values from literature are shown in table 7.7. All the nozzles have quite high numbers of combustion quality factors, this can have multiple sources for which one of them is due to the discharge factor which can be calculated using equation (6.5). The discharge factor is also added to table 7.7. As can be seen in table 7.7 all the quality factors are close to 1.

Table 7.7: Quality factor values for the CFD simulation with a comparison to literature

Parameter	SSSL e12	SSSL e45	SSSL e6	SM nozzle	Sutton [40]	Huzel [32]
ξ_F	0.98	0.98	0.98	0.98	0.92 - 0.96	0.92 - 1.00
ξ_c	1.01	1.01	1.01	1.01	0.85 - 0.98	0.87 - 1.03
ξ_s	0.99	0.99	0.99	0.99	0.80 - 0.90	0.85 - 0.98
C_d	0.99	0.99	0.99	0.99	-	-

7.1.3. Performance results summary

The main observations of the SSSL nozzles and the SM nozzle is that the SM nozzle and SSSL nozzle have comparable performance. The performance of the SSSL nozzles decreases when the vectoring angle increases. Additionally, when moving the split further downstream this performance loss is increased. It can also be noted that the amplification factor has a maximum at lower angles of thrust

vectoring. The amplification factor then decreases as the angle increases. The amplification factor also increases when moving the split further down stream. Finally, both nozzles have comparable performance to the values obtained from the performance program.

7.1.4. Mass model results

The input parameters for the Mass model have been generated in the previous section. Each of the nozzles are compared for the three different angles. The same naming convention is used for the SSSL nozzles. Each contribution addition is listed. As mentioned in the description of the mass model, the propellant penalty is a direct comparison between the SSSL nozzle and the SM nozzle and therefore one of the nozzles will have a 0 kg addition for the propellant penalty. This can be read in detail in section 3.6. Note that the SSSL nozzle would need a lower vectoring angle due to the amplification factor and therefore the Isp would be a bit higher than is used for this comparison. The results of the mass model are given in tables 7.8 to 7.10. The input values are presented as the first three rows and the rest is the results from the mass model. The corrected values for the difference in mass flow are used for the SM nozzle. The SM nozzle is listed three times for each angle due to the direct comparison between the SSSL nozzle and SM nozzle for the propellant penalty. The masses are calculated for a duty cycle of 1. Hence the vectoring is constantly at 0, 2.5 or 5 degrees. The total mass at the bottom of each table is the total TVC and nozzle system mass.

Table 7.8: Mass model results for the 0 degree thrust vector angle case at duty cycle = 1, abbreviations in the table are as following; Amplification Factor (AF) and Aerodynamic Torque (AT)

Parameter	**Design A**	**SM nozzle**	**Design B**	**SM nozzle**	**Design C**	**SM nozzle**
Isp	291.57 s	292.16 s	291.51 s	292.16 s	291.45 s	292.16 s
AF	1	1	1	1	1	1
AT	4.15 Nm	3.58 Nm	2.85 Nm	3.58 Nm	1.59 Nm	3.58 Nm
AF contribution	0.00 kg	0.00 kg	0.00 kg	0.00 kg	0.00 kg	0.00 kg
AT contribution	0.02 kg	0.01	0.01 kg	0.01 kg	0.01 kg	0.01 kg
Propellant penalty	0.00 kg	6.70 kg	0.00 kg	6.49 kg	0.00 kg	6.29 kg
Nozzle mass	19.23 kg	30.13 kg	19.23 kg	30.13 kg	19.23 kg	30.13 kg
Total mass	**19.25kg**	**36.85kg**	**19.24kg**	**36.64 kg**	**19.24 kg**	**36.44kg**

Table 7.9: Mass model results for the 2.5 degree thrust vector angle case at duty cycle = 1, abbreviations in the table are as following; Amplification Factor (AF) and Aerodynamic Torque (AT)

Parameter	**Design A**	**SM nozzle**	**Design B**	**SM nozzle**	**Design C**	**SM nozzle**
Isp	290.41 s	292.16 s	290.20 s	292.16 s	289.95 s	292.16 s
AF	1.57	1	1.61	1	1.66	1
AT	1077.26 Nm	24.32 Nm	1109.79 Nm	24.32 Nm	1168.57 Nm	24.32 Nm
AF contribution	0.45 kg	1.99 kg	0.44 kg	1.99 kg	0.43 kg	1.99 kg
AT contribution	4.16 kg	0.09 kg	4.28 kg	0.09 kg	4.51 kg	0.09 kg
Propellant penalty	0.00 kg	0.82 kg	0.00 kg	0.05 kg	0.94 kg	0.00 kg
Nozzle mass	19.23 kg	30.13 kg	19.23 kg	30.13 kg	19.23 kg	30.13 kg
Total mass	**23.84kg**	**33.04kg**	**23.95kg**	**32.27 kg**	**25.11 kg**	**32.22kg**

Table 7.10: Mass model results for the 5 degree thrust vector angle case at duty cycle = 1, abbreviations in the table are as following; Amplification Factor (AF) and Aerodynamic Torque (AT)

Parameter	Design A	SM nozzle	Design B	SM nozzle	Design C	SM nozzle
Isp	289.90 s	292.16 s	289.25 s	292.16 s	288.07 s	292.16 s
AF	1.52	1	1.55	1	1.59	1
AT	1950.21 Nm	40.76 Nm	1997.21 Nm	40.76 Nm	1968.68 Nm	40.76 Nm
AF contribution	0.93 kg	4.00 kg	0.91 kg	4.00 kg	0.8 9kg	4.00 kg
AT contribution	7.53 kg	0.16 kg	7.71 kg	0.16 kg	7.60 kg	0.16 kg
Propellant penalty	2.27 kg	0.00 kg	4.54 kg	0.00 kg	8.40 kg	0.00 kg
Nozzle mass	19.23 kg	30.13 kg	19.23 kg	30.13 kg	19.23 kg	30.13 kg
Total mass	**29.95kg**	**34.29kg**	**32.39kg**	**34.29 kg**	**36.12 kg**	**34.29kg**

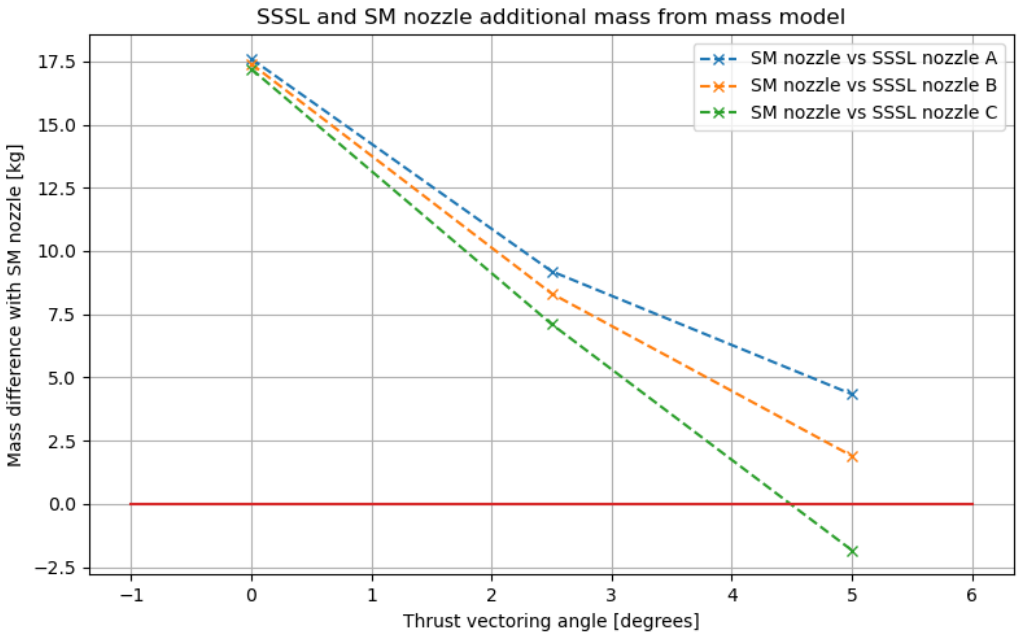

Figure 7.8: Figure showing the mass difference between the three SSSL nozzle designs and the SM nozzle. The red line indicates where the SM nozzle becomes the lighter option. The mass difference is defined as: Mass difference = SM nozzle mass – SSSL nozzle mass. The data points are for a duty cycle of 1.

As can be seen from tables 7.8 to 7.10, the SSSL nozzle is the lighter option with a mass of 19.24 kg on average between the designs. The SM nozzle has an average mass of 36.64 kg for the 0 degree thrust vectoring. However, due to the large aerodynamic torque the SSSL nozzle quickly becomes heavier for larger angles of thrust deflection. At 5 degrees, the additional mass due to the aerodynamic torque is on average 7.61 kg. Furthermore, as the angle of thrust vectoring increases the Isp of the SSSL nozzle decreases as well. This has the effect of increasing the propellant penalty to 8.4 kg for SSSL nozzle design C at 5 degree thrust vectoring. The mass difference between the SSSL nozzles and the SM nozzles are displayed in figure 7.8. In the figure, it can be seen that the mass difference is the largest at 0 degrees with an average of 17.40 kg mass difference. This reduces to a mass difference of 1.47 kg on average at 5 degree of thrust vectoring. Design C becomes 1.83 kg heavier than the SM nozzle at 5 degrees thrust vectoring. Where the mass difference becomes negative the SM nozzle is the lighter option and is indicated with a red line in figure 7.8.
From the sensitivity analysis of the mass model in section 3.9.2 it was found that the Isp was the largest

contributor to a change in the mass difference. This can also be seen in the mass difference change from design A to design C for the 5 degree case. The Isp changes with 1.83 s while the other inputs are nearly constant. The mass difference changes with 6.17 kg between the two designs.
The SM nozzle will only be the lighter option for C if the duty cycle exceeds 0.90. However, it was defined that the duty cycle of the TVC system was 0.25 in section 3.8. Therefore, the SSSL nozzle is the lighter option. The masses of all the nozzles are listed in table 7.11. It can be seen that all the three SSSL nozzle designs are lighter that the SM nozzle. The average mass difference between the SSSL nozzle and the SM nozzle for a duty cycle of 0.25 was 13.41 kg. This is a mass reduction of 37% when using a SSSL nozzle over a SM nozzle.

Table 7.11: The SSSL nozzle masses compared with the SM nozzle for a duty cycle of 0.25

Parameter	Design A	SM nozzle	Design B	SM nozzle	Design C	SM nozzle
Nozzle mass	21.93 kg	36.21 kg	22.53 kg	36.05 kg	23.46 kg	35.90 kg

7.1.5. Mass model results summary

The main observations form the mass model results, is that the SSSL nozzle system is the lighter option for all cases except the 5 degree case for SSSL nozzle design C. It was also observed that the Isp of the nozzle had a large impact on the mass of the systems which was also seen in the sensitivity study in section 3.9.2. The large difference in aerodynamic torque also had a large impact for the mass of the SSSL nozzle system. For a duty cycle of 0.25 the SSSL nozzle was on average 13.41 kg (37%) lighter than the SM nozzle.

7.2. Discussion of performance and mass model

The input parameters to the mass model program were obtained by using the corrected mass flow of the SM nozzle. Without the corrected mass flow of the SM nozzle the mass difference between the SSSL and SM nozzle system was on average is 13.81 kg (38%). This is only a slight increase from the results with the mass correction. The results were obtained using the assumption that the other flow parameters would stay constant. However, they would probably be slightly different as well. Furthermore, as the mass flow has a large influence on thrust and Isp, only the mass flow correction was taken into account. In order to verify this, new simulations need to be run on the SM nozzle and change the input pressure until the mass flow is the same as the SSSL nozzle. A possible outcome is that the pressure at the exit is slightly lower and hence the Isp would become lower as well.
When comparing the result of this study with the study of Ellis and Berdoyes, the mass difference between the two nozzle systems are very comparable [23]. The structural mass difference is the same in this work as in the study by Ellis and Berdoyes. Therefore, this will not be compared however, the calculated TVC system mass difference between the SSSL nozzle and the SM nozzle had a 30.5% difference, where the SSSL nozzle is the lighter option. In the study by Ellis and Berdoyes this is 25%. These numbers are close and can be said to be comparable.
There are other aspects that play a role in a real world scenario, such as the length of the interstage or skirt that surround the nozzles. Since the SM nozzle is shorter than the SSSL nozzle due to its submergence, the SM nozzle could save mass on these two aspects. The mass from an interstage or a skirt have not been included as the thesis focussed only on the mass addition due to aerodynamic effects only.
The mass difference between the two nozzles changes from 0 degree thrust vectoring to 5 degree thrust vectoring. The main contributor to this, is the large aerodynamic moment of the SSSL nozzle. This can be seen in tables 7.8 to 7.10. The aerodynamic torque of the SM nozzle is very low, this is due to the SM nozzle turning the flow before the throat and forming a more symmetrical flow field. The SSSL nozzle in this study had a backward pivot point. By having the pivot point forward would most likely reduce the aerodynamic moment. The design of the SSSL nozzle in this work has a backward pivot point which results in the upstream part being the ball and the downstream part being the socket. In this configuration the rotation point lies somewhere before the nozzle throat. With a forward pivot point this is reversed and the upstream part is the socket and the downstream part is the ball. Hence, the pivot point is somewhere after the throat. In this configuration some of the moments created could cancel each other out, thereby reducing the aerodynamic moment. A forward pivot point has also been

discussed in the test report by Strome [52]. However, none of the nozzles in literature have featured a forward pivot point, which may indicate that this is difficult to achieve.
The SSSL nozzle has the drawback of having the split that effects the nozzle flow. The SM nozzle does not have this disturbance and has therefore a higher Isp and thrust than the SSSL nozzle. This can be clearly seen in the results shown in tables 7.2 to 7.4. The SSSL nozzle has a 0.47 s lower Isp at 0 degree thrust vectoring. Additionally, the SSSL nozzle suffers from a larger performance loss when vectoring. It looses around from 1.67-3.38 s of Isp when vectoring depending on split location, while the SM nozzle does not have any loss. However, the Isp loss was expected as literature described the loss to be around 2s for vectoring angles under 5 degrees [38]. The downsides of the performance of the SSSL nozzle are compensated by the lower structural mass and the much lower seal stiffness due to the self sealing split [11, 15, 43]. The mass model does not take into account that the Isp loss would be less for the SSSL nozzle, due to the amplification factor reducing the angle needed to achieve 5 degrees of vectoring. Thereby, the Isp of the SSSL nozzle is lower than it would be in a real world scenario. This results in the SSSL nozzle system saving more mass compared to the SM nozzle system
As the torque relation only takes into account the aerodynamic torque and the seal torque the difference in the mass addition due to the torque could be higher. This is due to the SM nozzle having to move the whole nozzle and not only the bottom part. Additionally, the actuator placement and actuator arm was set to be the same for the comparison, but this is far from ideal. The nozzles will have an optimal actuator location which could lower the torque that the actuator needs to produce.
Since the discharge factor is lower than 1, it indicates that there is a boundary layer that effects the nozzle throat area and thereby the mass flow of the nozzle. This can be seen in table 7.7. As all the equations except the motor quality function use either the throat area or the mass flow or both, the effect of the boundary layer on the motor quality factors can be large. Secondly, the CFD calculations are not an experimental test and does not predict all the losses in the nozzle, such as the friction along the nozzle wall. The nozzle walls are simulated as having no friction. If the walls had friction, the losses in the nozzle would be larger and the quality factors might resemble the values from literature. The values are quite close to the upper bounds of the values from literature, and since the values from literature have been established from experimental tests it can be concluded that the motor performance in the CFD simulations are relatively high. But the comparison between the SM and SSSL nozzle is still valid since both nozzles have high values. Also the general trend of the amplification factor research can be observed even though the amplification factor is a bit high in some cases. To fully find the motor performance an experimental test should be done. However this is outside the scope of this work.

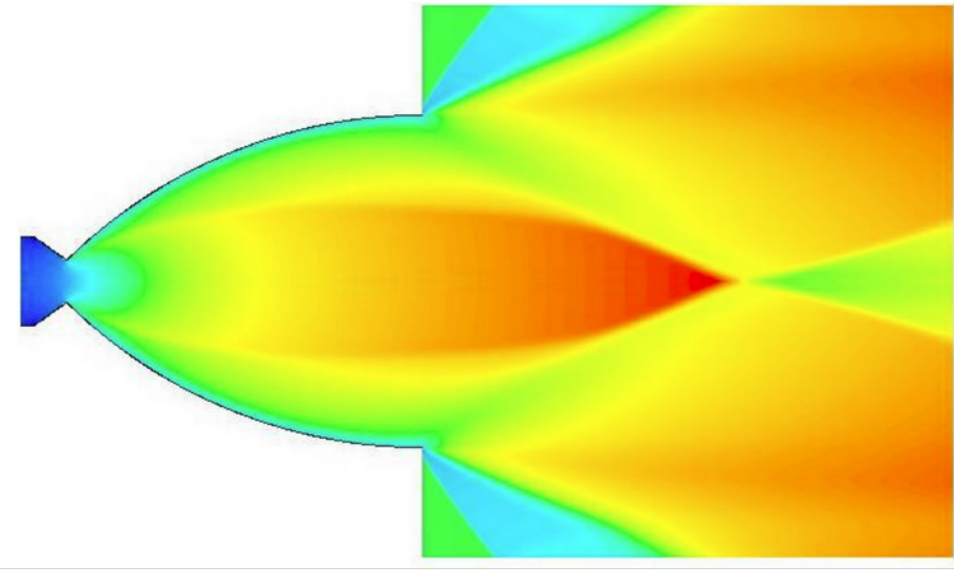

Figure 7.9: Figure of a nozzle experiencing under expansion. Figure taken from [8]

Looking at the Mach number contour in figure 7.4, it can be seen that oblique shock waves are formed right after the nozzle throat. This is due the the under-expansion of the rocket nozzle. The free stream

conditions are set to 0 Pa and the pressure of the nozzle flow is still higher than the ambient pressure. The flow will then form expansion waves at the exit as the flow keeps expanding. An example of this can be seen in figure 7.9 [8]. Comparing the nozzle flow in figures 7.4 and 7.9, it can be seen that they all form the same oblique shocks after the throat.

To summarize, the SSSL nozzle is the lighter choice of TVC nozzle when comparing the SSSL nozzle and the SM nozzle. Only the contributions from the aerodynamic effects have been considered. The SM nozzle does have slightly better performance with respect to thrust and Isp in the vectored state, which may make it more attractive in certain scenarios. However, in this thesis the research question is: ”What is the mass difference between the SSSL nozzle and the SM nozzle?” It can be answered with; on average the SSSL nozzle is 13.41 kg lighter than the SM nozzle when considering the aerodynamic effects only.
One part of hypothesis 1 was not correct. The hypothesis can be found in section 1.3.1 The aerodynamic moment for the SSSL nozzle was much higher than for the SM nozzle. The hypothesis was the other way around. On the other hand, it was stated that the Isp of the SSSL nozzle would be lower than the SM nozzle during vectoring. This is correct, as the Isp of the SSSL nozzle is lower at all angles. The loss due to submergence is smaller than the loss due to the split. The hypothesis on the vectoring performance and the overall mass difference were correct.

8

Results and discussion of amplification factor research

In this chapter the results from the research on the amplification factor is presented. The results from chapter 7 of the SSSL nozzle with expansion ratio of 12 will also be used for this chapter. The outcome of this research is an output that Nammo has requested. The rest of the contour plots can be found in appendix D. At the end there is a discussion on the results. The nozzle flow in all the figures in this chapter goes from left to right.

8.1. Results

In this section, the results of the investigation on the amplification factor are presented. The designs for the SSSL nozzle with expansion ratio 45 will have the following naming scheme: The SSSL nozzle with the split located at an expansion ratio of 1.75 and a total expansion ratio of 45 is called SSSL-45 design A. The SSSL nozzle with the split located at an expansion ratio of 2.25 and a total expansion ratio of 45 is called SSSL-45 design B.
The designs for the scaled down nozzle with expansion ratio 6.5 will have the following naming scheme: The scaled down SSSL nozzle with the split located at an expansion ratio of 1.75 and a total expansion ratio of 6.5 is called SSSL-6 design A. The scaled down SSSL nozzle with the split located at an expansion ratio of 2.25 and a total expansion ratio of 6.5 is called SSSL-6 design B.

8.1.1. Convergence check

The convergence check for the nozzles: SSSL-e45 design A and B and SSSL-e6 design A and B can be found in table 8.1

Table 8.1: Convergence test matrix to determine if the simulation has been converged for the nozzles: SSSL-e45 design A and B and SSSL-e6 design A and B, with expansion ratio 45 and 6. R is residuals, $\dot{m}_i$ is mass flow in, $\dot{m}_o$ is mass flow out, $\dot{m}_{tot}$ is mass flow total, X-Y-Z is the X-Y-Z forces and AM is the aerodynamic moment.

Simulation	R	$\dot{m}_i$	$\dot{m}_o$	$\dot{m}_{tot}$	X-Y-Z	AM	Convergence	Notes
SSSL-e45 design A 0deg	√	√	√	√	√	√	√	-
SSSL-e45 design A 2.5deg	√	√	√	√	√	√	√	-
SSSL-e45 design A 5deg	√	√	√	√	√	√	√	-
SSSL-e45 design B 0deg	~	√	√	√	√	√	√	As all other criteria than the residuals are converged the total simulation is deemed converged.
SSSL-e45 design B 2.5deg	~	√	√	√	√	√	√	As all other criteria than the residuals are converged the total simulation is deemed converged.
SSSL-e45 design B 5deg	~	√	√	√	√	√	√	As all other criteria than the residuals are converged the total simulation is deemed converged.
SSSL-e6 design A 0deg	X	√	√	√	√	√	√	As all other criteria than the residuals are converged the total simulation is deemed converged.
SSSL-e6 design A 2.5deg	X	√	√	√	√	√	√	As all other criteria than the residuals are converged the total simulation is deemed converged.
SSSL-e6 design A 5deg	X	√	√	√	√	√	√	As all other criteria than the residuals are converged the total simulation is deemed converged.
SSSL-e6 design B 0deg	~	√	√	√	√	√	√	As all other criteria than the residuals are converged the total simulation is deemed converged.
SSSL-e6 design B 2.5deg	~	√	√	√	√	√	√	As all other criteria than the residuals are converged the total simulation is deemed converged.
SSSL-e6 design B 5deg	X	√	√	√	√	√	√	As all other criteria than the residuals are converged the total simulation is deemed converged.

8.1.2. Nozzle performance and amplification factor change for expansion ratio 12

All the performance parameters and contour plots of the three SSSL nozzle designs A, B and C have been presented in the previous chapter. However, this section of the results deals with what the effect on the amplification factor is when moving the split to a higher expansion ratio. In figure 8.1, the amplification factor of the three designs is graphed against the split location. There is one line for the 2.5 degree case and one for the 5 degree case. The lines are only indicating a possible trend. It can be seen that the amplification factor increases when moving the split to a higher expansion ratio. It increases from 1.52 to 1.59 when going from design A to C. It can also be seen that the amplification ratio is higher at a lower vectoring angle. The amplification factor is 1.57 for design A and 1.66 for design C.

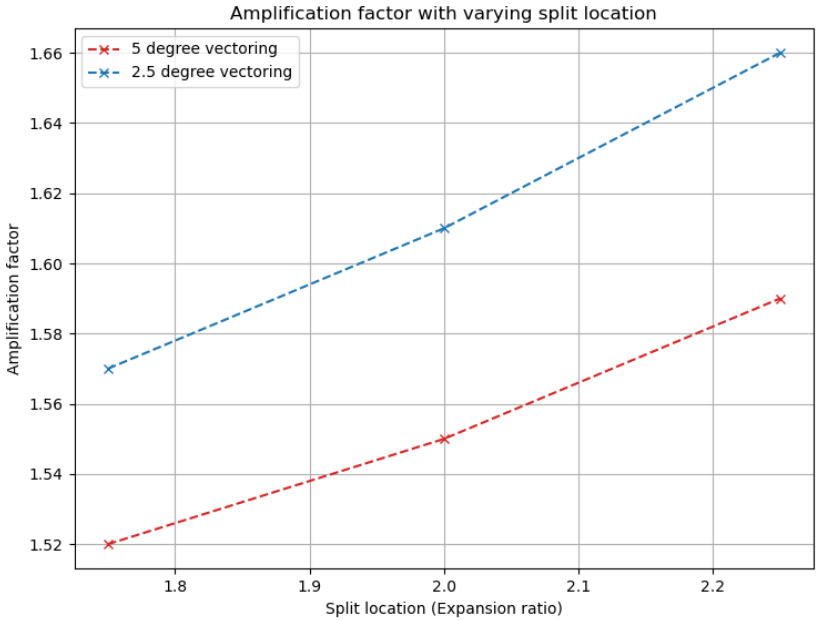

Figure 8.1: Graph showing the change in amplification factor when moving the split

8.1.3. Influence of mass flow on the amplification factor

The mass flow was altered for two SSSL designs to see what the influence of the mass flow is on the amplification factor. The simulation was based on the scenario when the rocket engine is throttling. For this purpose, design A and C were chosen. The designs were tested at 5 degree thrust vectoring with three sets of mass flows. The mass flow was altered by changing the total pressure of the simulation. The three pressure settings were 35, 32.5 and 30 bar. The results are presented in table 8.2.

Table 8.2: SSSL nozzle performance at different mass flow settings for the 5 degree thrust vector angle case. D-A is SSSL nozzle design A, D-C is SSSL nozzle design C and AF is amplification factor.

Parameter	D-A 35bar	D-C 35bar	D-A 32.5bar	D-C 32.5bar	D-A 30bar	D-C 30bar
Thrust	101.70 kN	101.08 kN	94.43 kN	93.87 kN	87.14 kN	86.64 kN
Isp	289.90 s	288.07 s	289.87 s	288.13 s	289.83 s	288.10 s
Mass flow	35.76 kg/s	35.76 kg/s	33.21 kg/s	33.21 kg/s	30.65 kg/s	30.65 kg/s
AF	1.52	1.59	1.52	1.59	1.52	1.59

The results that are shown in table 8.2 show that the amplification factor does not change with mass flow and stays constant at 1.52 and 1.59 for design A and C respectively. It can be noted that only the

thrust changes a significant amount between the different mass flows. The thrust reduces with 14.31% when reducing the total pressure from 35e5 Pa to 30e5 Pa.

8.1.4. Nozzle performance and amplification factor change for upper stage nozzle

In this section, the performance and the amplification factors of the SSSL nozzle with expansion ratio 45 are presented. The nozzle simulates a second stage nozzle for a launch vehicle. The results of the higher expansion ratio nozzle is compared to the results for the same split locations for the SSSL nozzle with an expansion ratio of 12. Additionally, the flow field of the larger expansion ratio nozzle are presented.

The performance of the nozzle designs SSSL-45 design A and SSSL-45 design B can be seen in tables 8.3 to 8.5. From the tables, it can be seen that the thrust and the Isp of the larger expansion ratio nozzles increases with 8.96% and 8.93% respectively. This is due to the gases being expanded more and therefore the nozzles are better adapted to the ambient pressure. It can be noted that the amplification factor for the larger expansion ratio nozzles is reduced to 1.28 and 1.32 for SSSL-e45 design A and B respectively. This is a reduction of 0.16% and 0.17%. The reduction is an indication that the split location may not be optimal for a high amplification factor for the high expansion ratio nozzles. A similarity with the low expansion ratio nozzles is that the thrust and Isp is reduced when vectoring, 0.22% and 0.23% respectively for SSSL-e45 design A. This increases to 0.43% and 0.42% for SSSL-e45 nozzle design B. The loss in percentage is less than the low expansion ratio nozzles.

Table 8.3: Nozzle performance parameters for the 5 degree thrust vector angle case for the SSSL nozzle with expansion ratio 45.

Parameter	**SSSL-45 design A**	**SSSL-45 design B**
Thrust	111.46 kN	111.45 kN
Isp	317.60 s	317.59 s
Thrust vector angle	0 deg	0 deg
Amplification factor	1	1
Mass flow	35.77 kg/s	35.77 kg/s
Aerodynamic moment	0.49 Nm	2.39 Nm

Table 8.4: Nozzle performance parameters for the 2.5 degree thrust vector angle case for the SSSL nozzle with expansion ratio 45.

Parameter	**SSSL-45 design A**	**SSSL-45 design B**
Thrust	111.27 kN	111.19 kN
Isp	317.11 s	316.865 s
Thrust vector angle	3.29 deg	3.36 deg
Amplification factor	1.31	1.34
Mass flow	35.77 kg/s	35.77 kg/s
Aerodynamic moment	1344.79 Nm	1416.91 Nm
Thrust loss	0.17%	0.22%
Isp loss	0.15%	0.21%

Table 8.5: Nozzle performance parameters for the 5 degree thrust vector angle case for the SSSL nozzle with expansion ratio 45.

Parameter	SSSL-45 design A	SSSL-45 design B
Thrust	111.21 kN	110.98 kN
Isp	316.94 s	316.25 s
Thrust vector angle	6.40 deg	6.58 deg
Amplification factor	1.28	1.32
Mass flow	35.77 kg/s	35.77 kg/s
Aerodynamic moment	2326.82 Nm	2499.45 Nm
Thrust loss	0.22%	0.43%
Isp loss	0.23%	0.42%

When comparing the results of the SSSL nozzle with expansion ratio 45 to the performance program it shows the same trend as for the SSSL nozzle with expansion ratio 12. The CFD simulations have predicted a little lower performance than the performance program has done.

Table 8.6: Nozzle performance parameters for the 0 degree thrust vector angle case for the SSSL nozzle with expansion ratio 45 compared to the performance program.

Parameter	SSSL-45 design A	Performance program	Percentage difference
Thrust	111.46 kN	113.99 kN	2.22%
Isp	317.60 s	321.28 s	1.14%
Mass flow	35.77 kg/s	36.17 kg/s	1.11%
Mach number	3.833	3.928	2.42%
Pressure	8827.10 Pa	8351.51 Pa	5.69%

In figure 8.2, it can be seen that extending the nozzle to a larger expansion ratio has the effect of lowering the amplification factor to 1.28 and 1.32 for SSSL-e45 design A and B respectively at 5 degree thrust vectoring. Both the low and high expansion ratio nozzle has an increasing amplification factor when increasing the expansion ratio at the split. When looking at the Mach number contour in figure 8.3 of both SSSL nozzle design C and SSSL-45 design B there is a clear difference. The higher expansion ratio nozzle has a more symmetrical flow. The effect of the split is dissipated as the flow is expanded.

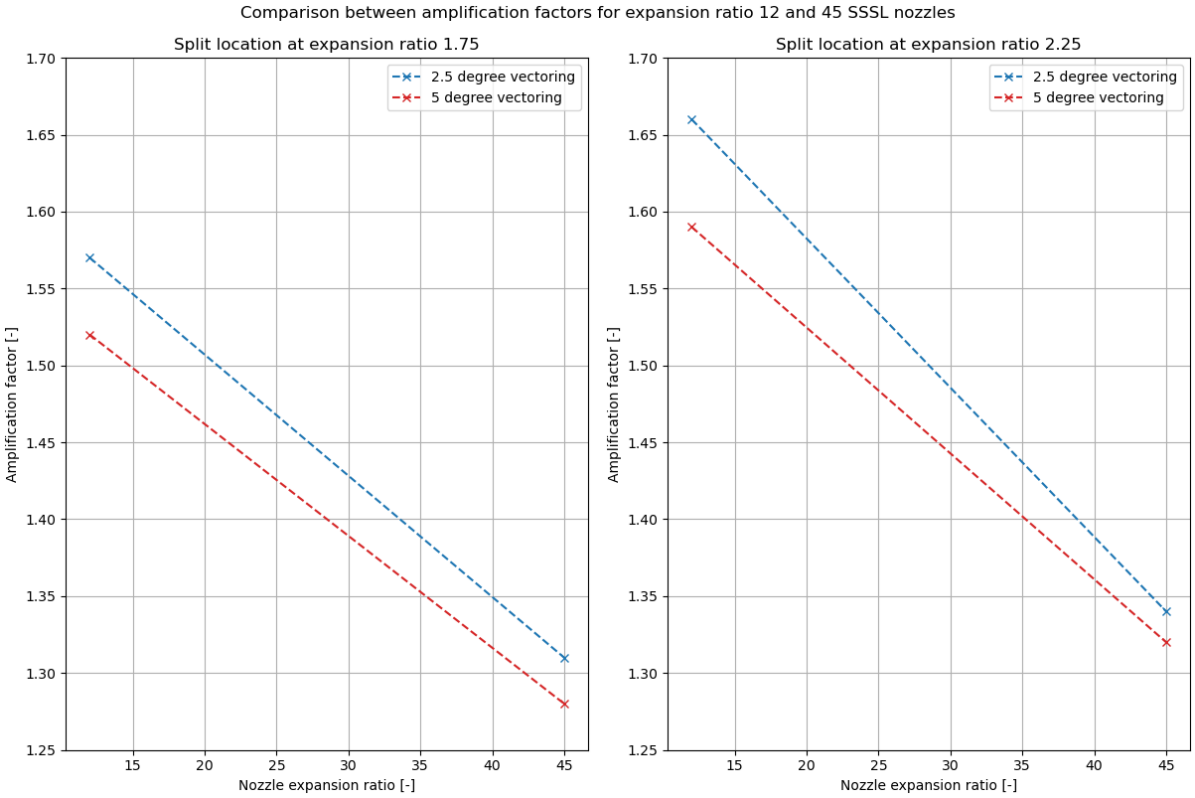

Figure 8.2: Graph showing the change in amplification factor when extending the SSSL nozzle to a higher expansion ratio

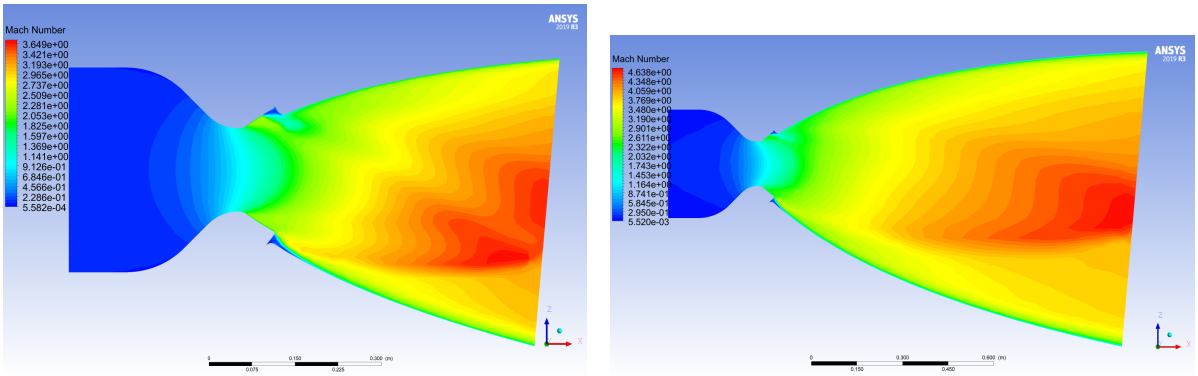

(a) SSSL nozzle design C at 5 degree vectoring

(b) SSSL nozzle SSSL-45 design B at 5 degree vectoring

Figure 8.3: Mach number contour of the SSSL nozzle design C and SSSL-45 design B at 5 degrees of thrust vectoring

8.1.5. Nozzle performance and amplification factor change for scaled down nozzle

In this section, the performance and the amplification factors of the scaled down SSSL nozzle with expansion ratio 6.5 are presented. The nozzle simulates a sounding rocket. The results of the scaled down nozzle is compared to the results for the same split locations for the SSSL nozzle with expansion ratio 12. Additionally, the flow field of scaled down nozzle is presented.

The performance of the nozzle designs SSSL-6 design A and SSSL-6 design B can be seen in tables 8.7 to 8.9. It can be seen that the scaled down nozzle obtains an amplification factor of 1.82 and 2.01 for SSSL-e6 design A and B respectively. Furthermore, the thrust and Isp loss is much larger for the scaled down nozzle. The loss increases to 1.94% for the thrust and 1.92% for the Isp for SSSL-e6 design C at 5 degree thrust vectoring.

Table 8.7: Nozzle performance parameters for the 0 degree thrust vector angle case for the scaled down SSSL nozzle.

Parameter	SSSL-6 design A	SSSL-6 design B
Thrust	31.70 kN	31.67 kN
Isp	275.86 s	275.64 s
Thrust vector angle	0 deg	0 deg
Amplification factor	1	1
Mass flow	11.71 kg/s	11.71 kg/s
Aerodynamic moment	0.14 Nm	0.26 Nm

Table 8.8: Nozzle performance parameters for the 2.5 degree thrust vector angle case for the scaled down SSSL nozzle.

Parameter	SSSL-6 design A	SSSL-6 design B
Thrust	31.52 kN	31.34 kN
Isp	274.18 s	272.72 s
Thrust vector angle	4.830 deg	5.401 deg
Amplification factor	1.93	2.16
Mass flow	11.71 kg/s	11.71 kg/s
Aerodynamic moment	218.83 Nm	265.17 Nm
Thrust loss	0.56%	1.06%
Isp loss	0.61%	1.06%

Table 8.9: Nozzle performance parameters for the 5 degree thrust vector angle case for the scaled down SSSL nozzle.

Parameter	SSSL-6 design A	SSSL-6 design B
Thrust	31.35 kN	31.06 kN
Isp	272.62 s	270.34 s
Thrust vector angle	9.13 deg	10.02 deg
Amplification factor	1.82	2.01
Mass flow	11.71 kg/s	11.71 kg/s
Aerodynamic moment	377.97 Nm	430.91 Nm
Thrust loss	1.10%	1.94%
Isp loss	1.17%	1.92%

When comparing the results of the SSSL nozzle with expansion ratio 6.5 to the performance program it shows the same trend as for the SSSL nozzle with expansion ratio 12 and 45. The CFD simulations have predicted a slightly lower performance than the performance program has done.

Table 8.10: Nozzle performance parameters for the 0 degree thrust vector angle case for the scaled down SSSL nozzle with expansion ratio 6.5 compared to the performance program.

Parameter	SSSL-6 design A	Performance program	Percentage difference
Thrust	31.70 kN	32.22 kN	1.61%
Isp	275.86 s	277.15 s	0.46%
Mass flow	11.71 kg/s	11.85 kg/s	1.18%
Mach number	2.777	2.827	1.77%
Pressure	96574.93 Pa	92253.40 Pa	4.68%

When looking at the Mach number contour in figure 8.4 of both SSSL nozzle design C and SSSL-6 design B there is a clear difference. The SSSL nozzle SSSL-e6 design B has a more asymmetrical flow distribution than SSSL nozzle design C. The shock wave and expansion wave have an even larger effect on the nozzle flow at the exit than for the larger SSSL nozzle. Additionally, comparing the Mach number contour of SSSL-e6 design A and B, presented in figure 8.5. It can be seen that moving the split to a higher expansion ratio has a drastic effect on the flow field. This is indicated in the figure with circles around the effects of the split. For SSSL-e6 design B, the effect of the split penetrates further downstream than for SSSL-e6 design A. The even larger distortion of the flow field has the effect of increasing the thrust and Isp loss by 0.84% and 0.75% respectively.

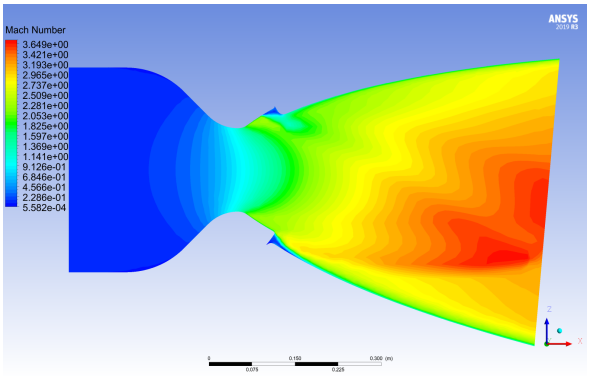

(a) SSSL nozzle design C at 5 degree vectoring

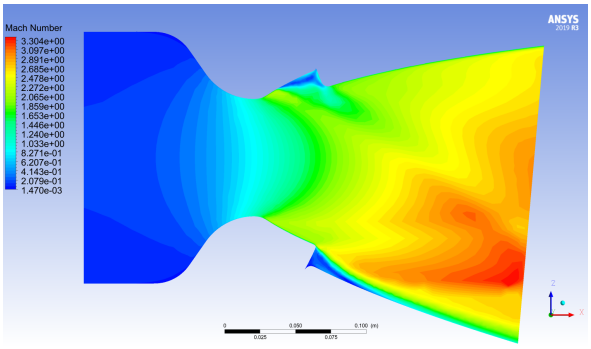

(b) SSSL nozzle SSSL-6 design B at 5 degree vectoring

Figure 8.4: Mach number contour of the SSSL nozzle design C and SSSL-6 design B at 5 degrees of thrust vectoring

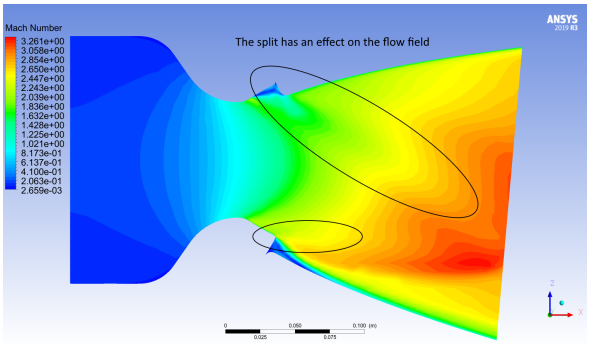

(a) SSSL nozzle SSSL-6 design A at 5 degree vectoring

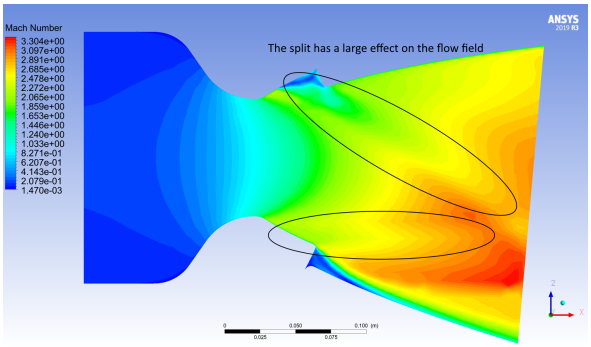

(b) SSSL nozzle SSSL-6 design B at 5 degree vectoring

Figure 8.5: Mach number contour of SSSL-e6 nozzle design A and SSSL-6 design B at 5 degrees of thrust vectoring

8.1.6. Trend of amplification factor

A trend of the amplification factor with respect to the ratio of split location to the total expansion ratio can be constructed. Using the data from the scaled down nozzle can be used for this trend as well.

Unfortunately the scaling down of the nozzle should have been done on a nozzle with an expansion ratio of 12. This is to be able to distinct the effect of scaling and the effect of changing the ratio of split location to the total expansion ratio. However, the requirements by Nammo were that the nozzle had the expansion ratio at 6.5. In figure 8.6 the trend of the amplification factor with respect to the ratio of the expansion ratio at the split to the total expansion ratio of the nozzle. The ratio of split location to the total expansion ratio of the nozzle is defined in equation (8.1):

$$\epsilon_{\text{Ratio}} = \frac{\epsilon_{\text{Split location}}}{\epsilon_{\text{Nozzle}}} \tag{8.1}$$

Where ϵ is the expansion ratio. Two figures are constructed. The figure on the left is the trend with the scaled down nozzle data included and the one on the right is the trend without the scaled down nozzle data. The two figures are made as the amplification factor of the scaled down SSSL nozzle is very high compared to the other SSSL nozzles and to literature [11, 15, 19, 23, 43]. The trend indicates a nearly linear relation ship between the ϵ_{Ratio} and the amplification factor. However more data points are needed in order to validate the trend.

The data for the scaled down nozzle can have a combined effect of scaling and increasing the ϵ_{Ratio}. Hence, it is hard to distinguish between the direct effect of scaling and the effect of changing the ϵ_{Ratio}. As increasing the ϵ_{Ratio} will increase the amplification factor as can be seen in figure 8.6 Therefore, hypothesis 5 is hard to answer with the current data.

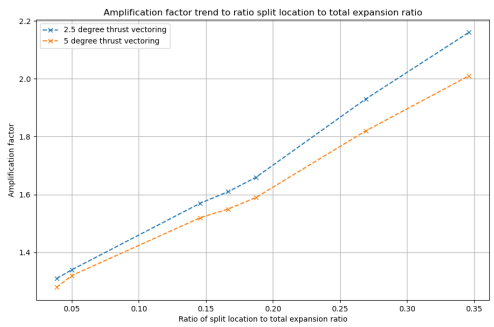

(a) Trend of the amplification factor when increasing the ϵ_{Ratio} including the data for the scaled down nozzle

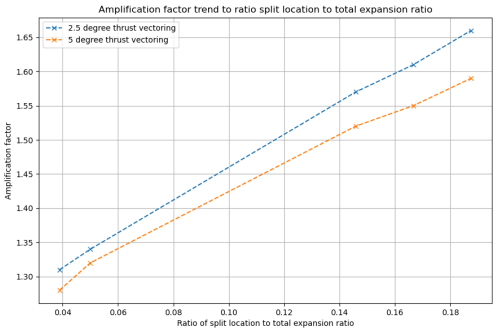

(b) Trend of the amplification factor when increasing the ϵ_{Ratio} excluding the data for the scaled down nozzle

Figure 8.6: Trend of the amplification factor when increasing the ϵ_{Ratio}

8.1.7. Validation of amplification factor research

In order to validate the amplification factors obtained from the simulations, they are compared to literature. The values obtained from the CFD simulations and the values from literature are shown in table 8.11. From the table it can be seen that the values obtained for the SSSL nozzle with expansion ratio 12 and 45 fit nicely within the values obtained from literature. However, the values for the scaled down nozzle are relatively large in comparison to the values from literature.

Table 8.11: Amplification factors obtained and values from reference material

SSSL nozzle design	CFD values	Nammo SSSL study [43]	SEP SSSL study [23]	Snecma SSSL study [11]
SSSL e12 design A to C	1.52 - 1.66	1.3 - 1.6	1.25 - 1.6	1.3 - 1.7
SSSL e45 design A to B	1.28 - 1.34	1.3 - 1.6	1.25 - 1.6	1.3 - 1.7
SSSL e6 design A to B	1.82 - 2.16	1.3 - 1.6	1.25 - 1.6	1.3 - 1.7

8.1.8. Summary of results to amplification factor research

The results of the amplification factor research has shown that when moving the split further downstream has the effect of increasing the amplification factor. Moving the split further downstream does

however decrease nozzle performance more when vectoring. Furthermore, when increasing the overall expansion ratio the amplification factor decreased when having the same split locations. The effect of scaling was difficult to observe as at the same time the ratio of expansion ratios was altered due to changing the overall expansion ratio of the nozzle to 6.5. The amplification factor of the nozzles with expansion ratio 12 and 45 achieved comparable results to literature, while the expansion ratio 6.5 had a slightly high amplification factor.

8.2. Discussion on amplification factor research

The second part of this thesis researched the amplification factor. The research focussed on the split location, changing the mass flow, increasing the total expansion ratio and scaling down the nozzle. The expansion ratios of the split locations tested were 1.75, 2 and 2.25 for the SSSL nozzle with expansion ratio 12. It can be noted from figure 8.1 that the amplification factor increases when moving the split towards a higher expansion ratio. Since the amplification factor does increase with a higher expansion ratio, hypothesis number 2 is partly proven correct however, the maximum of the amplification factor has not yet been found for the SSSL nozzle. In order to find the trend and the maximum amplification factor more simulations are needed.
Even though the amplification factor increases when moving the split, it also has an effect on the performance of the nozzle. The performance drop can clearly be seen in tables 7.3 and 7.4. The naming scheme of the nozzle designs is reused (expansion ratio 1.75 is design A, 2 is design B and 2.25 is design C). For both design B and C the performance drop when vectoring is larger than the performance drop is for design A. Hence it is recommended to do a trade off on the value of the amplification factor against the performance loss of the nozzle when selecting a SSSL nozzle design. It is not only the performance parameters that are reduced, also the mass of the nozzle increases when comparing it to a SM nozzle.
When changing the mass flow of the nozzle it had no effect on the amplification factor. The only effect of changing the mass flow was to lower the thrust of the engine. It might be that for a real engine the amplification factor does change when altering the mass flow. However, this effect is not captured by the CFD simulations. Thereby hypothesis number 3 is disproved as it predicted that the amplification factor would increase with a lower mass flow.
This makes the results from the scaled down nozzle possibly seem unrealistic. It might however be that the combination of split location and total expansion ratio is just right to produce very high amplification factors. As the amplification factor obtained from the CFD simulations for the two larger nozzles are close to that of literature, it can be said that the results of the research are partially validated. In order to increase the accuracy of the result and validate the results for the scaled down nozzle, experimental tests should be done.

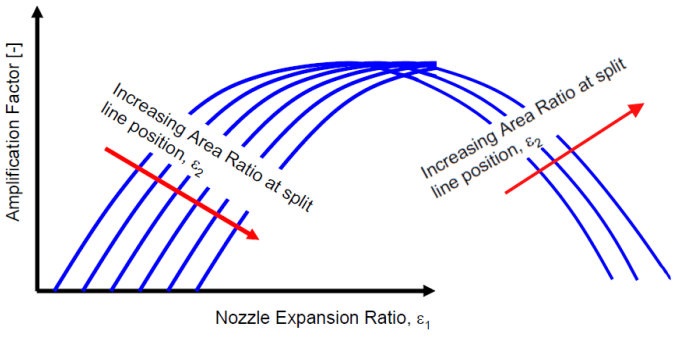

Figure 8.7: Trend of the amplification factor with increasing expansion ratio, figure adapted from [43].

In section 1.4.5 a figure from the study by Ørbekk is presented [43]. When looking closely at the figure by Ørbekk, it can be seen that the amplification factor should go down when moving the split further down stream. This contradicts the results of this work. However, if the figure is extended the trend turns around and the amplification factor increases with moving the split further down stream. This can

be seen in figure 8.7. If the trend continues the way that Ørbekk has indicated, then the results from this work further supports the theory by Ørbekk. However, this needs to be supported by more data in order to fully confirm this trend. One way is to extend to this work by keeping the same split location but changing the overall expansion ratio. The effect of changing the total expansion ratio of the nozzle is that the amplification factor is reduced. The amplification factor is reduced by 45-49% for the various designs. The same patterns as the for the lower expansion ratio nozzle are seen. The amplification factor increases with an increasing expansion ratio at the split. Additionally, the amplification factor is the largest at small angles. The flow field of the larger expansion ratio nozzle found in figure 8.3 shows that as the nozzle becomes longer, the flow field becomes more symmetrical. As the flow field becomes more symmetrical the additional side force is also reduced. The results of the higher expansion ratio nozzle supports hypothesis number 4 as the amplification factor is reduced and thereby the maximum point has moved further down stream. Hypothesis 4 also states that the effect of the shock will dissipate further downstream, this is exactly what is seen in figure 8.3. The results of the investigation into the higher expansion ratio nozzle supports thereby hypothesis 4.

9

Results and discussion on temperature distribution and heat flux

In this chapter, the results of the temperature distribution and the heat flux calculations are presented. The temperature and the heat flux is of interest as the SSSL nozzle has been reported to have problems with high heat around the split area. Firstly, the results of the temperature along the nozzle wall are shown. Secondly, the temperature contours of the nozzles are presented. Thirdly, the heat flux contours and the values for the heat flux are given. Finally, the results are discussed.

9.1. Results

The temperature along the nozzle wall and the heat flux estimate are presented in this section. The heat flux was estimated with the methods described in chapter 5. The heat flux of the various nozzles was found to be very similar and hence only a few of the contour plots are shown. The rest of the contour plots of the heat flux are shown in appendix D. Note that the contour plots of the heat flux are made on the nozzle wall and a cut through the middle is made in order to see the inside of the nozzle.

9.1.1. Nozzle wall temperature

The temperature along the wall for SSSL nozzle design A for 0 degree vectoring and 5 degree vectoring can be seen in figure 9.1. The split is indicated with a green dotted line and the throat is indicated with a orange dotted line. It can clearly be seen that the split has a large effect on the temperature along the nozzle wall. At the split, the temperature sharply rises back to 2700K before returning to a lower temperature further down the nozzle. The little bend backwards at the split is due to the temperature trace following the nozzle wall and at the split the wall turns back towards the combustion chamber. The difference between the 5 degree and the 0 degree case are quite large as the upper wall has a shock wave that suddenly increases the temperature before the split. The lower wall has the expansion waves that extend the high temperature region behind the split. Additionally, the temperature remains different for the two walls all the way to the exit.

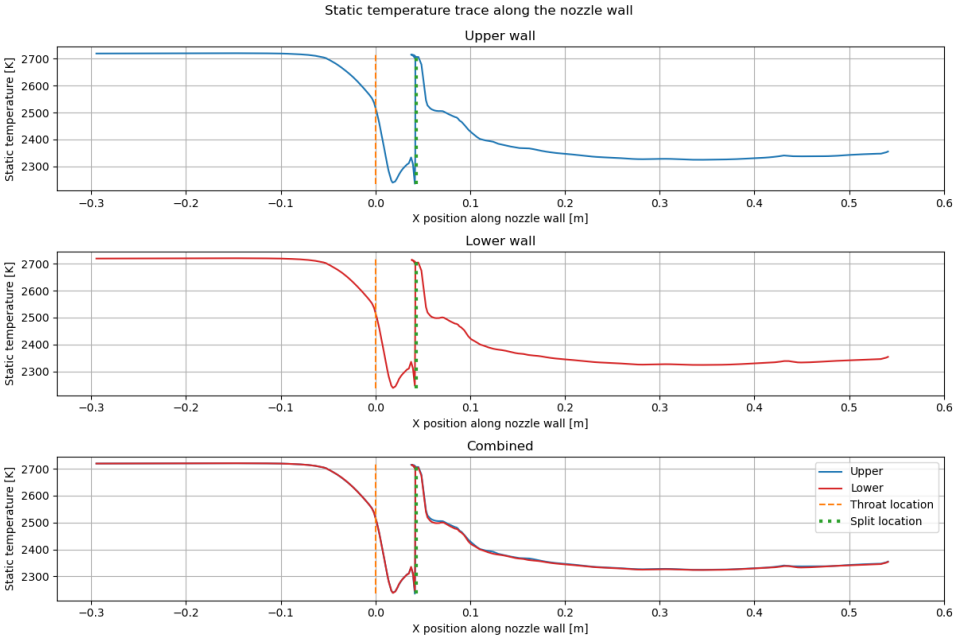

(a) SSSL nozzle design A at 0 degree vectoring

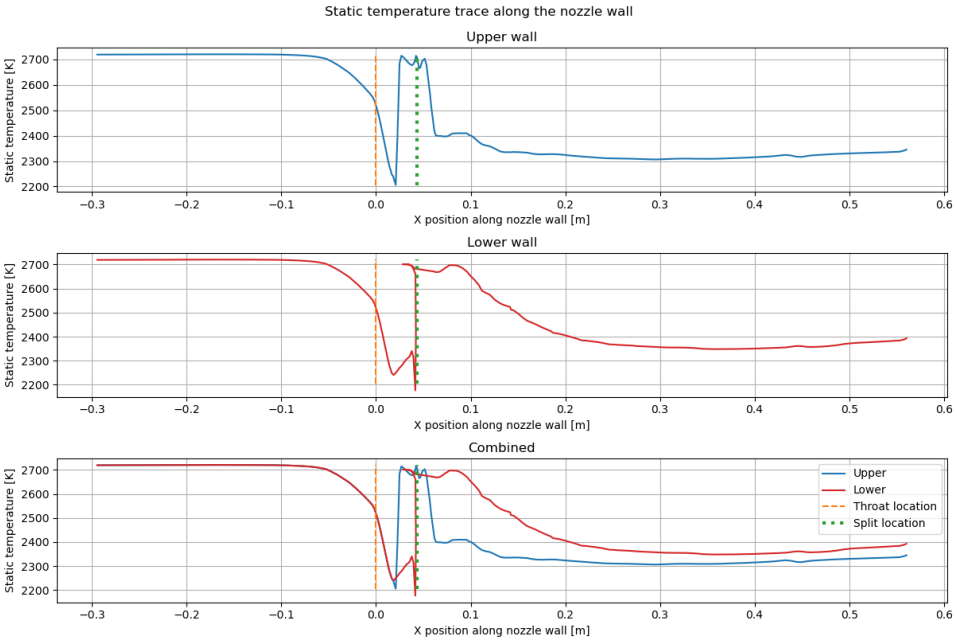

(b) SSSL nozzle design A at 5 degree vectoring

Figure 9.1: Temperature trace along nozzle wall for SSSL nozzle design A at 0 and 5 degree vectoring.

When comparing the temperature trace of the SSSL nozzle to the temperature trace of the SM nozzle it can be seen that the SM nozzle does not have a sudden peak at around the split and keeps a lower temperature than the SSSL nozzle until the exit. It can be noted that the weak shock wave formed right after the throat does increase the temperature a bit but far less than the shock introduced by the split. The SM nozzles temperature trace does not change significantly when going from 0 degree vectoring to 5 degree vectoring. The only difference is a bit more turbulent temperature trace after the throat. This is due to the increased turbulence induced by the vectoring. The increased turbulence can seen in figure 7.7.

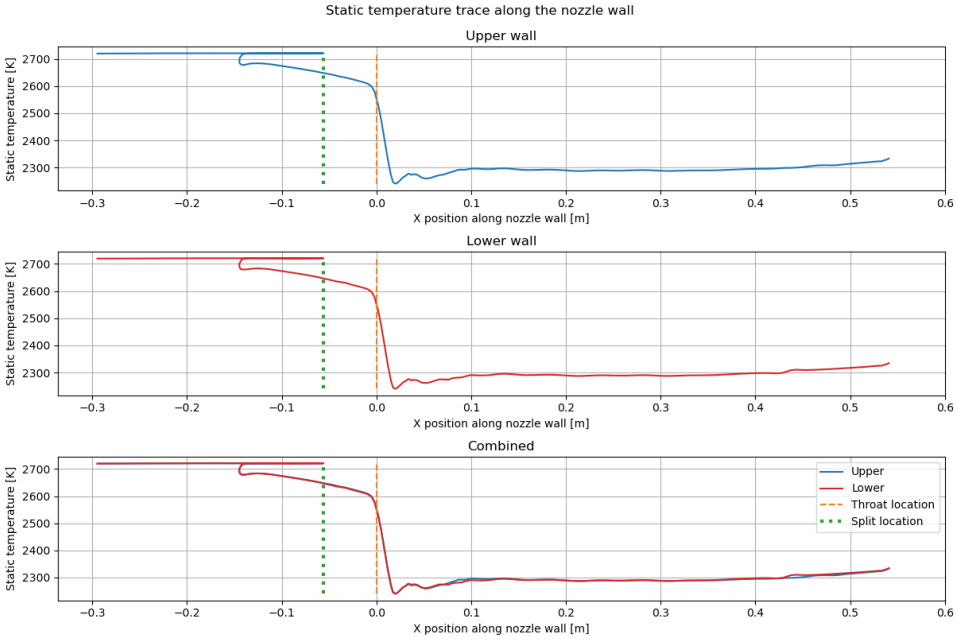

(a) SM nozzle at 0 degree vectoring

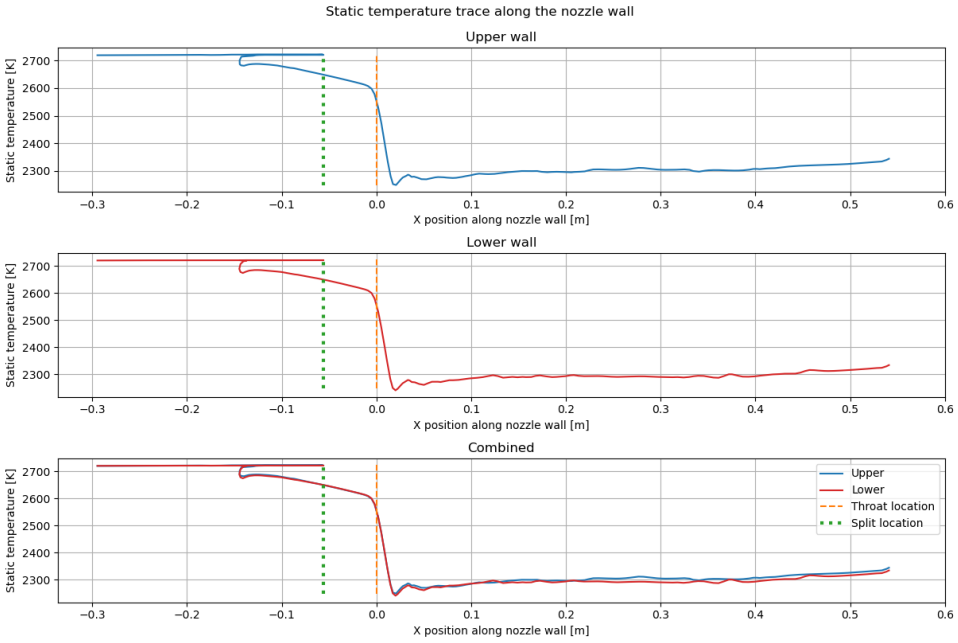

(b) SM nozzle at 5 degree vectoring

Figure 9.2: Temperature trace along nozzle wall for the SM nozzle at 0 and 5 degree vectoring.

The temperature trace along the nozzle wall for the SSSL-e45 design A and SSSL-e6 design A can be seen in figure 9.3. The temperature traces resemble the trace from the SSSL e12 design A however, the trace for the e45 nozzle is a bit longer and the lowest temperature is around 100K lower. For the SSSL e6 nozzle the lowest temperature is around 100K higher than the SSSL e12 design. What can be noted is the bump in temperature right before the throat of the nozzle. This might indicate that the nozzle design is not optimal for the flow contraction from the combustion chamber.

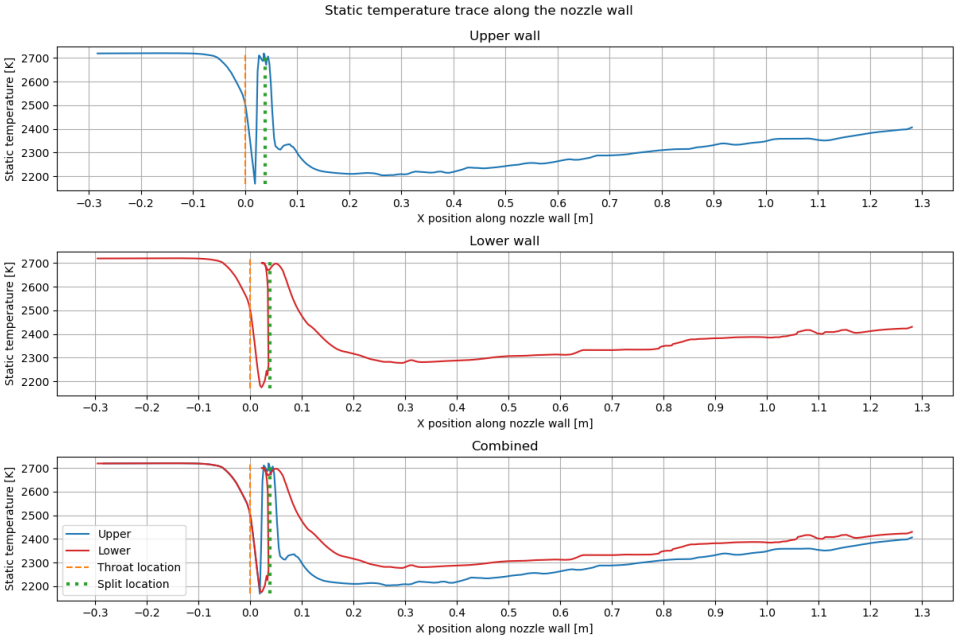

(a) SSSL-e45 design A at 5 degree vectoring

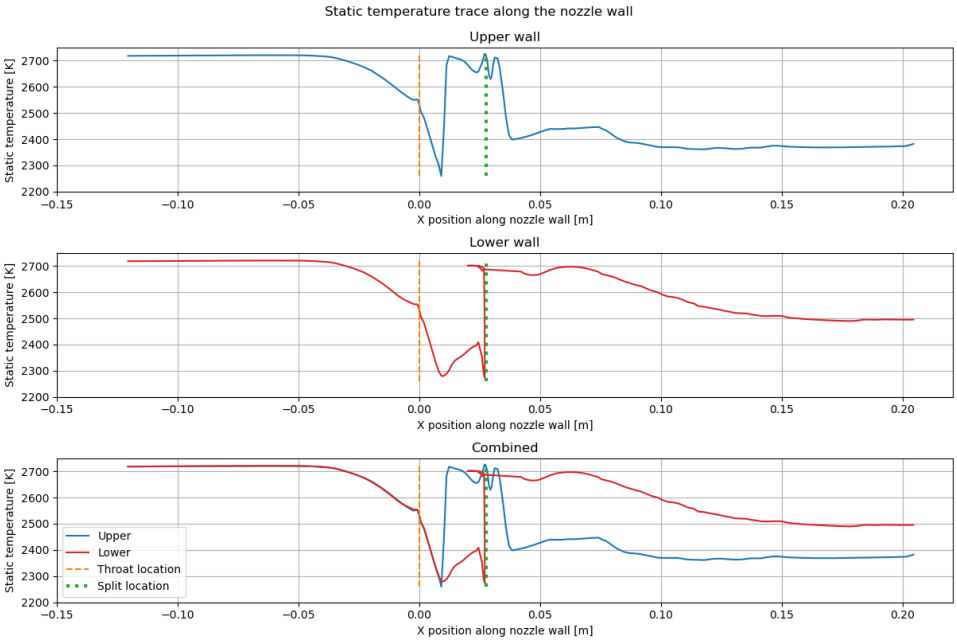

(b) SSSL-e6 design A at 5 degree vectoring

Figure 9.3: Temperature trace along nozzle wall for SSSL-e45 design A and SSSL-e6 design A at 5 degree vectoring.

9.1.2. Temperature distribution through the nozzle

When looking at the temperature contour for the 5 degree case of SSSL nozzle design A it can be seen that around the split there are high temperature areas. This is shown in figure 9.4. The circles indicate the split areas with high temperature. Due to the slightly coarse mesh the wall function has trouble to calculate the temperature at exactly the wall. Therefore, it seems like the wall has a very hot layer. In the previous section the correct wall temperature was shown. The red temperature areas around the split have a temperature of around 2700 K. The same can be seen for the higher expansion ratio nozzle and the scaled down nozzle in figure 9.5. Both areas around the split have a temperature of around 2700 K. In figure 9.6 the temperature contour of the SM nozzle is shown. It can be seen that the SM nozzle does not have any extra hot areas as the SSSL nozzle has.

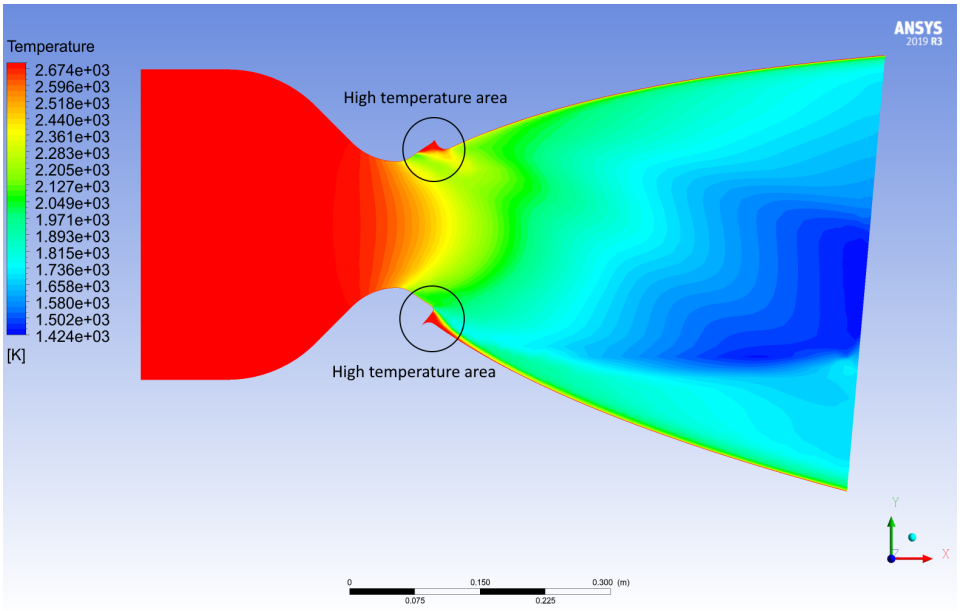

Figure 9.4: Temperature contour of SSSL nozzle design A with indications of high temperature at the split.

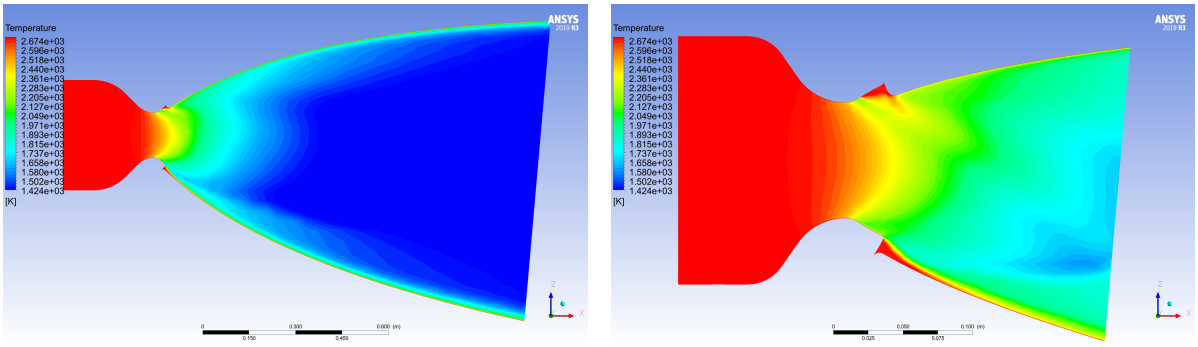

(a) SSSL-e45 design A at 5 degree vectoring

(b) SSSL-e6 design A at 5 degree vectoring

Figure 9.5: Temperature contour for SSSL-e45 design A and SSSL-e6 design A at 5 degree vectoring.

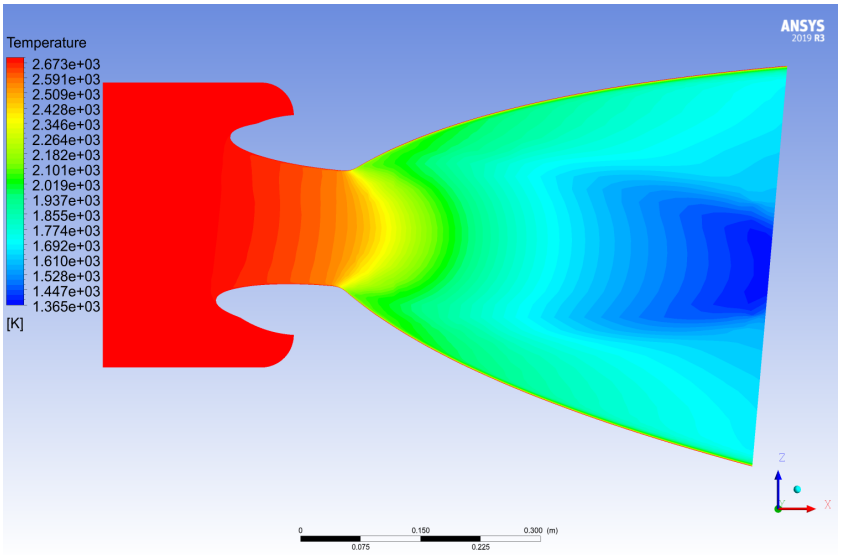

Figure 9.6: Temperature contour of the SM nozzle at a thrust vectoring angle of 5 degrees.

9.1.3. Heat flux estimation

The heat flux for the different nozzles was very similar, all the nozzles had a total heat flux of around 3.8-4.1 MW/m^2 for the e12 and e45 nozzles. The heat flux is calculated by the method described in chapter 5. The scaled down nozzle had a maximum total heat flux of around 3.1 MW/m^2. For the 5 degree thrust vectoring case the shock wave and expansion wave create local hot spots with higher heat flux. However, the location with the highest heat flux can be found right before the throat, with a maximum of 3.90 MW/m^2 for SSSL nozzle design A. However, SSSL-e6 design B at 5 degree thrust vectoring was the only nozzle that had the maximum heat flux around the split area This can be seen in figure 9.11. In figure 9.7 the convective and radiative heat flux is shown. It can be seen that around the split the shock wave creates an area with higher heat flux for the convective and radiative heat flux. This is indicated with a circle. The total heat flux and the combination of the two effects can be seen in figure 9.8. The distribution of heat flux is 36% from radiation and 64% from convection. For the larger expansion ratio nozzle the heat flux was around the same as the lower expansion ratio nozzle. The SM nozzle had the highest heat flux of all the nozzles with a heat flux of 4.1 MW/m^2. The SM nozzle does not experience the additional hot spots as the SSSL nozzle. The total heat flux of the SM nozzle is shown in figure 9.9. When comparing the heat flux in the throat area for the SM and SSSL nozzle design A at 5 degrees thrust vectoring, the SM nozzle had a total heat flux of 4.1 MW/m^2 and the SSSL nozzle design A had 3.8 MW/m^2. If the heat flux is compared at the split location of the SSSL nozzle, the SM nozzle has a heat flux of 1.95 MW/m^2 and the SSSL nozzle design A has a heat flux of 3.2 MW/m^2. This is a large difference.
For the scaled down nozzle the maximum heat flux was 3.1 MW with 42% from radiation and 58% from convection. The effect of the shock wave is more obvious for the scaled down nozzle. The heat flux for the scaled down nozzle can be seen in figures 9.10 and 9.11

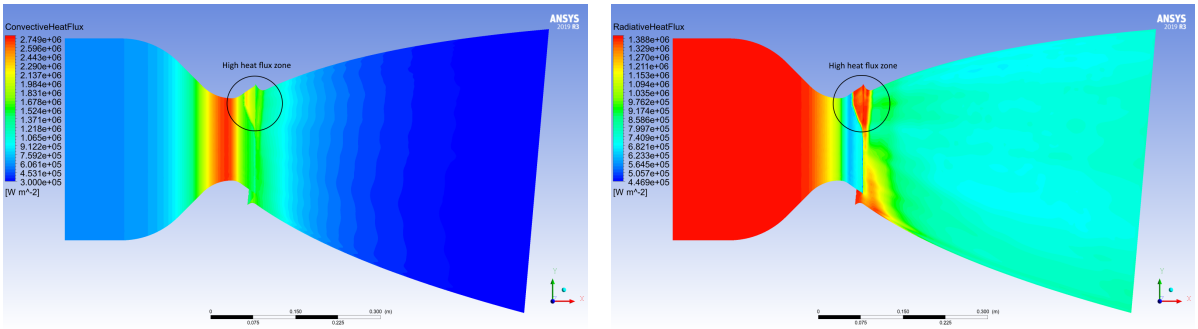

(a) Convective heat flux

(b) Radiative heat flux

Figure 9.7: Heat flux contours for SSSL nozzle design A at 5 degree thrust vectoring.

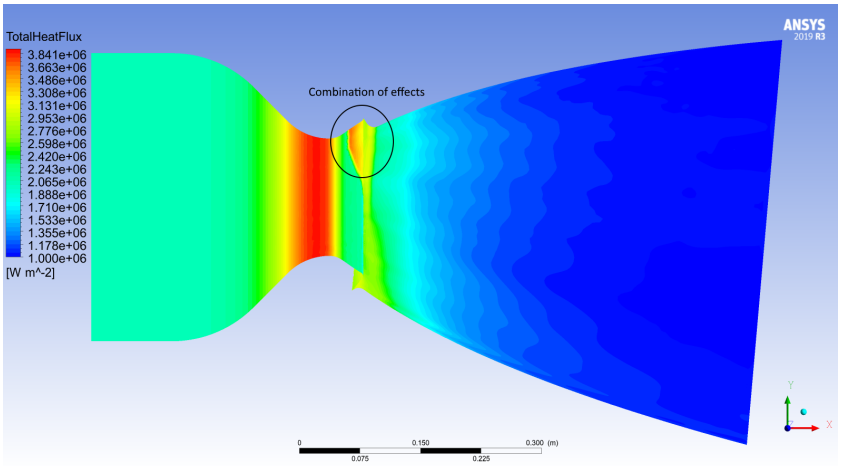

Figure 9.8: Heat flux contour for convective and radiative combined for SSSL nozzle design A at 5 degree thrust vectoring.

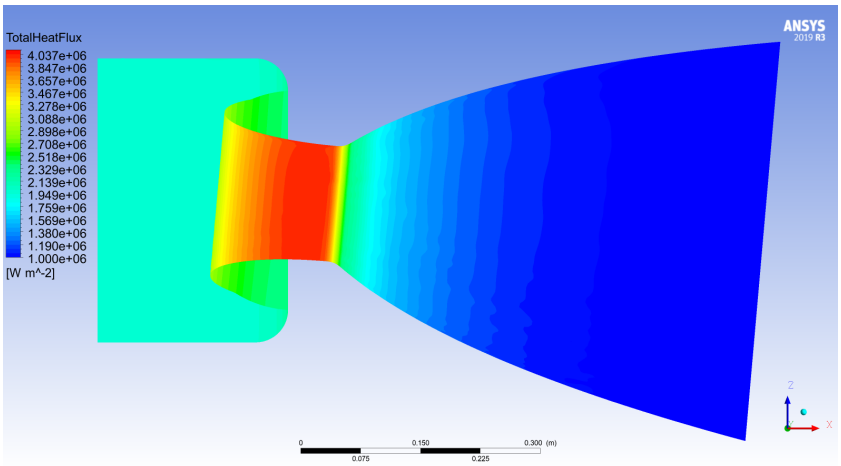

Figure 9.9: Heat flux contour for convective and radiative combined for the SM nozzle at 5 degree thrust vectoring.

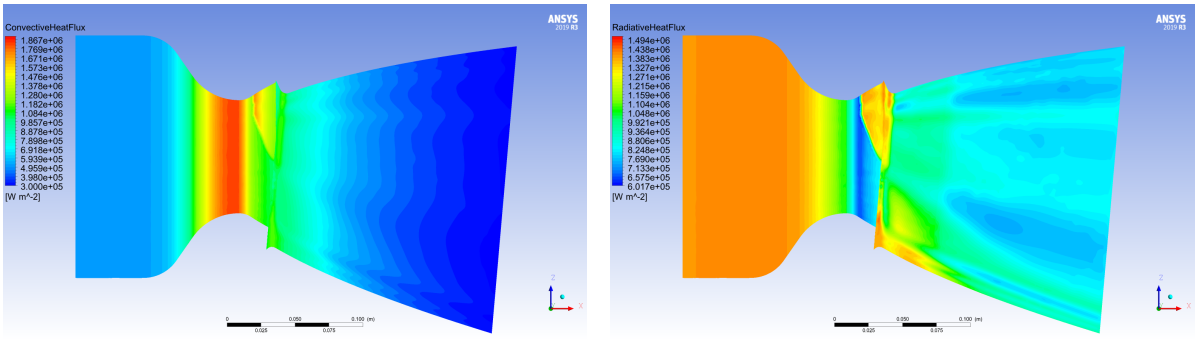

(a) Convective heat flux (b) Radiative heat flux

Figure 9.10: Heat flux contours for SSSL-e6 design A at 5 degree thrust vectoring.

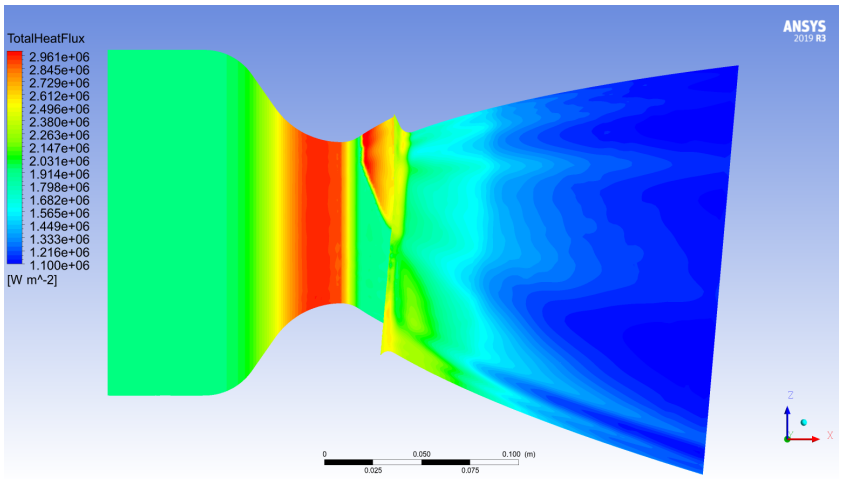

Figure 9.11: Heat flux contour for convective and radiative combined for SSSL-e6 design A at 5 degree thrust vectoring.

9.1.4. Summary of temperature and heat flux calculations

The results of the temperature investigation and heat flux investigation has shown that the temperature at the split for the SSSL nozzle is very high, up to 2700 K. The split induces shock waves that in turn raises the temperature. The heat flux in the region around the split is also increased due to the shock waves. The SM nozzle has no hotspots after the throat and the temperature drops throughout the nozzle. Additionally, the SM nozzle has a slightly higher heat flux in the throat region. When comparing the heat flux of the SM and SSSL nozzle the SM has the highest heat flux, but the SSSL nozzle has a much higher heat flux at the split location as the same location for the SM nozzle.

9.2. Discussion

As the SSSL nozzle has shown from literature that the split location has problems with high temperatures, extra care has to be taken when designing a SSSL nozzle [15, 19, 23, 43, 52].
The temperature along the nozzle wall for the SSSL nozzle show that the split has a large impact of the temperature along the nozzle wall. This is true for both the un-vectored and vectored state of the nozzle. In the vectored state the nozzle wall stays hotter for longer than for the un-vectored state. When comparing to the SM nozzle, the SSS nozzle has a much warmer region around the split which may need additional cooling or structural reinforcement. This could reduce the mass difference between the two nozzles as the SSSL nozzle might need additional reinforcement around the split.
The heat flux was calculated using the Bartz equation [10]. This equation is only an estimate based on empirical data for nozzles without a split. It might be that the heating due to convection in the area around the split is higher than the calculated value. The highest heat flux can be found in the throat region which is the area that according to literature has the highest heat flux [13, 24, 40]. The heating

from radiation is calculated to be around 36-42% of the total heat flux. The high contribution from the radiative heat flux is a little higher than the expected value of around 25-30% [13, 24]. This is most likely due to the simple method of calculation the radiative heat flux and the estimation of the emissivity of the gas.
When looking at the figures for the convective and radiative heat flux for the SSSL nozzle in figure 9.7 it can be seen that the shock wave and the expansion wave cause the heat flux of both radiative and convective to change. The convective heat flux and the radiative heat flux suddenly increase due to the large temperature change over the shock wave. When combining the two effects into the total heat flux which can be seen in figure 9.8, the two effects amplify each other and the area around the split receives a high heat flux. This was already expected as literature on the SSSL nozzle described extra hot regions around the split area [11, 15, 23, 43, 52].

10

Conclusion and recommendations

In this chapter, the concluding remarks of the thesis are presented. The research questions formulated in the introduction are answered and recommendations for expanding or improving the research is discussed.

10.1. Conclusion

The research conducted has focussed on comparing the SSSL nozzle and the SM nozzle. The two nozzles were simulated using CFD software. With the developed mass model, the two nozzles were compared by looking at how much mass they would add to a rocket. Additionally, further investigation into the amplification factor of the SSSL nozzle was conducted. The parameters examined were the split location, mass flow, total nozzle expansion ratio and nozzle scale. The aim was to find the effect on the amplification factor when changing these parameters. Each research question is dealt with separately.

What is the mass difference between the SSSL nozzle and the SM nozzle for a 100kN hybrid rocket motor with a burn time of 90s?

In order to answer the first research question, the two nozzles needed to be modelled. This was achieved by firstly creating the basic nozzle shape with ideal rocket theory. From the basic nozzle shape the design of the SSSL nozzle and the SM nozzle were performed in a CAD program. The two nozzles could then be simulated using CFD software.

In order to compare the two nozzles, a model was created that compared the nozzles on their mass addition to the rocket system. The masses that were considered were; nozzle mass, TVC mass and propellant penalty all these masses can be found in tables 7.8 to 7.10. This model was created using numbers from literature. From the CFD simulations, the required inputs for the mass model were created. The results of the mass model show that the mass difference between a SSSL nozzle system and a SM nozzle system depends on the angle of thrust vectoring and duty cycle of the TVC. For a duty cycle of 0.25 the SSSL nozzle system is 13.41 kg (37%) lighter than the SM nozzle system. The SSSL nozzle system is the lighter option due to its higher vectoring performance and lower structural weight. It was also observed that the high aerodynamic moment and lower Isp for the SSSL nozzle were the main components for increasing the SSSL nozzle system mass. Furthermore, the SM nozzle had slightly better performance with respect to thrust and Isp at higher angles of thrust vectoring.

To conclude, the SSSL nozzle is the lighter option when the aerodynamic effects are considered. Other effects such as the interstage length and thermal protection of the split were not considered in this study, but these might have an influence on the overall system mass for the SSSL nozzle. In the sensitivity analysis is was found that changing the empty mass and the burn time will increase the mass of the SSSL nozzle more than the SM nozzle, but the SSSL nozzle remained the lighter option even with an increase in the burn time to 180s.

What is the effect on the amplification factor when changing the parameters of the nozzle and the engine?

The second research question has several parts, the first part is: What is the effect on the amplification factor when moving the split, while keeping everything else constant? From the results, it was found that moving the split location further downstream has the effect of increasing the amplification factor. This can be seen in tables 7.2 to 7.4.

To conclude, when moving the split further downstream the amplification factor increases, but at the cost of a higher thrust and Isp loss with respect to the un-vectored state. When deciding on the split location for a SSSL nozzle a careful consideration should be made on the benefit of a higher amplification factor. In comparison to the SM nozzle and considering the mass of the nozzle system the split should be located where the Isp loss is minimized.

The second part was: What is the effect on the amplification factor when changing the mass flow, while keeping the split at a constant location? To answer this question the total pressure of the CFD simulation was altered for design A and C and the results can be found in table 8.2. The result from the investigation found that the amplification factor does not change when the mass flow changes. The only effect is that the thrust becomes lower.

To conclude, by throttling the engine the amplification factor did not change since the velocity at the nozzle exit did not change.

The third part consists of the question: What is the effect on the amplification factor when increasing the expansion ratio of the nozzle, while keeping the same throat area and mass flow rate? In order to answer this question, the SSSL nozzle was redesigned with a higher expansion ratio. The results of this investigation can be found in tables 8.3 to 8.5. It was found that the amplification factor decreases when increasing the expansion ratio. Combining the results from the lower expansion ratio nozzle with the results for the higher expansion ratio nozzle a relationship between the ratio of expansion ratio at the split to the total expansion ratio of the nozzle could be made. It was found that for the range of expansion ratios simulated, a linear trend could be made. The amplification factor was increasing when the ratio of the expansion ratios increased.

To conclude, the trend that Ørbekk created for the amplification factor in figure 1.3 is confirmed. This is under the assumption that the trend continues as shown in figure 8.7. However, more data points are needed to fully confirm this trend.

The final research question was: What is the effect on the amplification factor when decreasing the scale of the nozzle down to a 29kN engine? This question is to find the effect of scaling the nozzle. To answer this, a new SSSL nozzle was designed with the requirements from Nammo. Two nozzle designs were made. From the results, that can be found in tables 8.7 to 8.9, it was found that the amplification factor increases with scaling down the nozzle. However, as the scaled down engine both changed the scale of the nozzle and the ratio of the expansion ratios it was not possible to find the effect of scaling alone.

To conclude, by scaling down the nozzle the amplification factor increased however the results could not be separated from the effect of increasing the ratio of expansion ratios. Additionally, the amplification factors of the scaled down nozzles did not compare to any nozzles in literature and should be investigated further.

Temperature and heat flux

All the nozzles were also analysed for their heat flux and temperature. It was found that the SSSL nozzles had a hot spot at around the split, which had temperature of around 2700 K in the split area. This hot spot also increased the heat flux at the split location. The SM nozzle did not experience a higher heat flux at the split location.

To conclude, the split area of the SSSL nozzle will have to be designed with care in order to keep the temperature as low as possible, additionally the SSSL nozzle could potentially need additional thermal insulation and structural reinforcement around the split area to withstand the high temperatures. This could affect the mass difference between the SM and SSSL nozzle systems.

Conclusion on methods used

The mass model that was created for this work is only suited for the comparison between the SSSL an SM nozzle systems, it was not created for the use of sizing one of the nozzles. The mass model

will still be able to compare the nozzles when changing the burn time and thrust level. The scaling of the nozzle mass will not hold for nozzles that are much larger than the nozzles used in this study. The performance program uses ideal rocket theory and produced the expected results. The limitation of ideal rocket theory is that it does not take into account any losses. Ansys was very suited to the task of simulation the nozzles however the limitation of the student licence means that the results are not as accurate as they could be.

10.2. Recommendations

In this section, the recommendations for future research are presented and summarized. Each recommendation is handled separately.

The CFD calculations were performed with a student license for Ansys. The student license sets a limit on how many mesh nodes can be used. This limit is 512000 nodes. Therefore, it can not be concluded that mesh convergence has been found in this thesis. The recommendation is to perform a mesh convergence study to determine the error of using a student license.
Additionally, the residuals for the CFD calculations were oscillating at the end of each simulation. This indicates that either the mesh is to coarse or that there is transient behaviour in the fluid domain. It is recommended to perform a transient analysis to determine if there are transient features in the flow.

The design of the pivot point and the design of the nozzle in general was not optimized for this thesis. Both nozzles have several aspects that could be changed, such as the shape around the split and the shape of the inlet to the SM nozzle. Additionally, the SSSL nozzle could benefit from a forward pivot point as this could reduce the aerodynamic torque. With a reduction in the aerodynamic torque the mass of the SSSL nozzle system would decrease. These design optimizations are recommended as a point for further study.

The relationship of the ratio of expansion ratios has only a couple of data points, to extend the trend more data points are needed. Therefore, it is recommended to extend the data set, with either data from literature or data from additional simulations in order to create a design guideline on where to position the split. Additionally, extending the range of angles tested would make a more robust relationship between the amplification factor and the angle of thrust vectoring.

The effect of scale on the amplification factor could not be distinguished from the effect of changing the ratio of expansion ratios. Therefore, it is recommended that the scaled down nozzle is redesigned to have a expansion ratio of 12. This allows to find the effect of scaling alone.

The rounding at the split of the SSSL nozzle should be further investigated in order to minimize the effect of the split on the flow field. Aspects to take in mind are, rounding shape, rounding radius and if a rounding is needed at all.

The actuator placement of the SM and SSSL nozzle was not optimized for the comparison in this work. It would be interesting to see the effect of a more optimal actuator placement. Additionally, the inertia of the nozzle has not been taken into account in this study. With the SSSL nozzle having to move much less material the influence of the inertia could have an impact on the mass difference for the actuator. Therefore it is recommended to explore this topic in detail

The CFD simulations performed in this work are steady state. It would be interesting to do a transient CFD analysis coupled with a thermal analysis to observe how the heat propagates through the SSSL nozzle and especially around the split. This could influence the amount of insulation needed or the need for additional cooling techniques, which could influence the mass budget for a SSSL nozzle.

The final recommendation is to perform an experimental test of the SSSL nozzle and SM nozzle designed in this thesis. This will help to validate the conclusions drawn from this thesis.

Bibliography

[1] A. Prince, R. McCauley, T. Kibbey, L. McCollum, B. Oglesby, P. Stefanski. Mars ascent vehicle (mav)solid motor technology plans. NASA archive, Sept 2019. Retrieved at 22-10-2019 from https://ntrs.nasa.gov/archive/nasa/casi.ntrs.nasa.gov/20190002124.pdf.

[2] Michael Alberti, Roman Weber, and Marco Mancini. Gray gas emissivities for h2o-co2-co-n2 mixtures. *Journal of Quantitative Spectroscopy and Radiative Transfer*, 219:274 – 291, 2018. ISSN 0022-4073. doi: https://doi.org/10.1016/j.jqsrt.2018.08.008. URL http://www.sciencedirect.com/science/article/pii/S0022407318304618.

[3] J.D. Anderson. *Fundamentals of Aerodynamics*. McGraw-Hill Education, 2016. ISBN 9781259129919. URL https://books.google.nl/books?id=D1ZojgEACAAJ.

[4] Ansys. Ansys, 2020. Retrieved at 10-09-2020 from, https://www.ansys.com/.

[5] Ansys. Ansys, 2020. Retrieved at 10-09-2020 from, https://www.ansys.com/products/fluids/ansys-fluent.

[6] Ansys. Ansys faq, 2020. Retrieved at 10-09-2020 from, https://www.cfd-online.com/Wiki/Ansys_FAQ#My_steady_state_solution_converges_for_a_while_but_stops_converging_before_reaching_my_convergence_criteria.

[7] Inc. ANSYS. Ansys fluent tutorial guide, July 2020. http://support.ansys.com/documentation.

[8] Raman Baidya, Apostolos Pesyridis, and Maxim Cooper. Ramjet nozzle analysis for transport aircraft configuration for sustained hypersonic flight. *Applied Sciences*, 8(4):574, Apr 2018. ISSN 2076-3417. doi: 10.3390/app8040574. URL http://dx.doi.org/10.3390/app8040574.

[9] A. Balabel, A.M. Hegab, M. Nasr, and Samy M. El-Behery. Assessment of turbulence modeling for gas flow in two-dimensional convergent–divergent rocket nozzle. *Applied Mathematical Modelling*, 35(7):3408 – 3422, 2011. ISSN 0307-904X. doi: https://doi.org/10.1016/j.apm.2011.01.013. Retrieved at 10-09-2020 from, http://www.sciencedirect.com/science/article/pii/S0307904X11000266.

[10] D.R. Bartz. "a simple equation for rapid estimation of rocket nozzle convective heat transfer coefficients". *ARS Journal*, Jan 1957.

[11] Michel" "Berdoyes. "snecma propulsion solide advanced technology srm nozzles. history and future.". *"42nd AIAA/ASME/SAE/ASEE Joint Propulsion Conference & Exhibit"*, 2006. doi: 10.2514/6.2006-4596. https://arc.aiaa.org/doi/pdf/10.2514/6.2006-4596 retrieved at 30-04-2019.

[12] James Braun, Jorge Sousa, and Guillermo Paniagua. Numerical assessment of the convective heat transfer in rotating detonation combustors using a reduced-order model. *Applied Sciences*, 8, 05 2018. doi: 10.3390/app8060893. Retrieved at 10-09-2020 from, https://www.researchgate.net/publication/325451130_Numerical_Assessment_of_the_Convective_Heat_Transfer_in_Rotating_Detonation_Combustors_Using_a_Reduced-Order_Model.

[13] B.T.C Zandbergen. AE4-S01 Thermal Rocket Propulsion (version 2.07). TU Delft readers, August 2018. Lecture notes in the course AE4-S01 Thermal Rocket Propulsion given at TU Delft.

[14] K.H.J" "Buschow. *"Encyclopedia of materials: science and technology"*. Elsevier, 2001.

[15] P. Donguy" "C.A. Yezzi. "thrust vector control technology demonstration". *"22nd AIAA/ASME/SAE/ASEE Joint Propulsion Conference"*, 1986. https://arc.aiaa.org/doi/pdf/10.2514/6.1986-1642 retrieved at 30-04-2019.

[16] Aleksandr Chikitkin, Mikhail Petrov, Roman Dushkov, and Ernest Shifrin. Aerodynamic design of a laval nozzle for real gas using hodograph method. *Aerospace*, 5(3):96, 2018. doi: 10.3390/aerospace5030096.

[17] COMSOL. Sutherlands law, 2020. Retrieved at 10-12-2020 from, https://books.google.nl/books?id=woeqa4-a5EgC.

[18] Charles R. Cooke. Development and demonstration of an own i axi al flexible seal movable nozzle for thrust vector control (u), 1967. Retrieved at 22-01-2021 from, https://ia903102.us.archive.org/5/items/DTIC_AD0385084/DTIC_AD0385084.pdf.

[19] "D. Crapiz". "improvements in composite tactical solid rocket motor technology. *"26nd AIAA/ASME/SAE/ASEE Joint Propulsion Conference"*, 1990. https://arc.aiaa.org/doi/pdf/10.2514/6.1990-1975 retrieved at 30-10-2019.

[20] Gael DEE, Tillo VANTHUYNE, Alessandro POTINI, Ignasi PARDOS, and Guerric DE CROMBRUGGHE. Electromechanical thrust vector control systems for the vega-c launcher. *Proceedings of the 8th European Conference for Aeronautics and Space Sciences*, 2019. doi: 10.13009/EUCASS2019-186. URL https://www.eucass.eu/doi/EUCASS2019-0186.pdf.

[21] Thiokol Chemical Corporation Wasatch Division. Thrust vector control tvc system study program. NASA Technical Reports Server, June 1970. Retrieved at 25-10-2019 from https://ntrs.nasa.gov/archive/nasa/casi.ntrs.nasa.gov/19700027043.pdf.

[22] James Donat. Solid rocket motor nozzle flexseal design. *Aerospace Design Conference 1993*, 1993. doi: 10.2514/6.1993-1122. retrieved at 23-10-2019 from https://arc.aiaa.org/doi/abs/10.2514/6.1993-1122.

[23] R. Ellis and M. Berdoyes. Supersonic splitline (SSSL) flexseal nozzle technology evaluation program. *33rd Joint Propulsion Conference and Exhibit*, 1997. doi: 10.2514/6.1997-2721. Retrieved at 01-04-2019 https://arc.aiaa.org/doi/pdf/10.2514/6.1997-2721.

[24] Russel A. Ellis. Solid Rocket Motor Nozzles. *Solid Rocket Motor Nozzles. NASA SP-8115, 126 pages, published by NASA, Washington, D.C.*, 1975. Retrieved at 23-10-2019 from https://ntrs.nasa.gov/archive/nasa/casi.ntrs.nasa.gov/19760013126.pdf.

[25] L. H. Erickson, T. L. Nickens, P. C. Sottosanti, and J. L. Sutton. Thrust vector control study for large (260 inch) rocket motor applications. NASA Technical Reports Server, April 1970. Retrieved at 01-04-2019 from https://ntrs.nasa.gov/archive/nasa/casi.ntrs.nasa.gov/19700032883.pdf.

[26] Martina Faenza, Adrien J. Boiron, Bastien Haemmerli, and Constans J. Verberne. The nammo nucleus launch: Norwegian hybrid sounding rocket over 100km. *AIAA Propulsion and Energy 2019 Forum*, 2019. doi: 10.2514/6.2019-4049. URL https://arc.aiaa.org/doi/abs/10.2514/6.2019-4049.

[27] Yukio Fukushima, Hiroyuki Nakatsuzi, Ryuji Nagao, Kenji Kishimoto, Keiichi Hasegawa, Takashi Koganezawa, and Shogo Warashina. Development status of le-7a and le-5b engines for h-iia family. *Acta Astronautica*, 50(5):275 – 284, 2002. ISSN 0094-5765. doi: https://doi.org/10.1016/S0094-5765(01)00165-5. URL http://www.sciencedirect.com/science/article/pii/S0094576501001655.

[28] Kadir Gok, Sermet Inal, Arif Gok, and Eyyup Gulbandilar. Comparison of effects of different screw materials in the triangle fixation of femoral neck fractures. *Journal of Materials Science: Materials in Medicine*, 28, 05 2017. doi: 10.1007/s10856-017-5890-y.

[29] Qiang Cai" "Haifeng Hu, Futing Bao. "coupling heat transfer and fluid flow solvers for high area ratio rocket nozzle". *"2012 International Conference on Image, Vision and Computing"*, 50, 2012. ISSN 1270-9638. doi: 10.7763/IPCSIT.2012.V50.25. Retrieved at 30-10-2019 from https://pdfs.semanticscholar.org/a299/59772b574f7988ded996bd9115d0332647fa.pdf.

[30] Stefan Hickel. Lecture notes cfd for aerospace engineers, ae. TU Delft lecture slides, 2018. Lecture slides in the course AE4202 CFD for aerospace engineers given at TU Delft.

[31] Ogawa Hideaki and Boyce Russell R. Physical insight into scramjet inlet behavior via multi-objective design optimization. *AIAA Journal*, 50(8):1773–1783, 2012. doi: 10.2514/1.J051644. Retrieved at 10-09-2020 from, https://doi.org/10.2514/1.J051644.

[32] D. K. Huzel and D. H. Huang. Design of liquid propellant rocket engines second edition, nasa-sp-125. *NASA technical reports server*, January 1971. Retrieved at 15-04-2020 from https://ntrs.nasa.gov/archive/nasa/casi.ntrs.nasa.gov/19710019929.pdf.

[33] R. Ramesh Kumar and Yuvarajan Devarajan. Cfd simulation analysis of two-dimensional convergent-divergent nozzle. *International Journal of Ambient Energy*, page 1–11, 2018. doi: 10.1080/01430750.2018.1517683. Retrieved at 10-09-2020 from, https://www.tandfonline.com/doi/pdf/10.1080/01430750.2018.1517683?needAccess=true.

[34] R. LLOYD and G. THORP. A review of thrust vector control systems for tactical missiles. *14th Joint Propulsion Conference*, 1978. doi: 10.2514/6.1978-1071. Retrieved at 05-06-2019 from https://arc.aiaa.org/doi/abs/10.2514/6.1978-1071.

[35] Mitsubishi Heavy Industries Ltd. □-□□□ user's manual, February 2015. Retrieved at 10-09-2020 from, https://www.mhi.com/jp/products/pdf/manual.pdf.

[36] Baker Mary. Understanding critical dynamic loads fro nozzle and nozzle extension design. In *AIAA/ASME/SAE/ASEE Joint Propulsion Conference*, 07 2011. Retrieved at 10-09-2020 from, https://www.researchgate.net/publication/268506997_Understanding_Critical_Dynamic_Loads_fro_Nozzle_and_Nozzle_Extension_Design.

[37] MIT. Defenition of bézier curve and its properties, December 2009. Retrieved at 10-09-2020 from, http://web.mit.edu/hyperbook/Patrikalakis-Maekawa-Cho/node12.html.

[38] NASA. Mars ascent propulsion system (maps). Federal Buisness Opportunities, Sept 2019. Retrieved at 22-10-2019 from https://www.fbo.gov/index?s=opportunity&mode=form&tab=core&id=3edde27df24304dde150bfd7827b81a1.

[39] Nassir, Chellou, Maamar, Guendez, Abdallah, and Benarous. Cooling of the vulcain nozzle□s divergent wall. In *Journal of Mechanics Engineering and Automation 5*, 2015. Retrieved at 22-01-2021 from, https://pdfs.semanticscholar.org/81ca/2b1b18e058eb8229aaebd4f3e7804c738e64.pdf.

[40] Sutton George P. and Biblarz Oscar. *Rocket Propulsion Elements (9th Edition)*. "John Wiley & Sons", 2017. ISBN 978-1-118-75365-1. URL https://app.knovel.com/hotlink/toc/id:kpRPEE001A/rocket-propulsion-elements/rocket-propulsion-elements.

[41] Prosun Roy, Abhijit Mondal, Biswanath Barai. CFD Analysis Of Rocket Engine Nozzle. *International Journal of Advanced Engineering Research and Science (IJAERS)*, January 2016. Retrieved at 30-01-2020 from https://www.academia.edu/21513123/CFD_Analysis_Of_Rocket_Engine_Nozzle?auto=download.

[42] G.V.R. Rao. Exhaust nozzle contour for optimum thrust. *Journal of Jet Propulsion*, 28(6), June 1958.

[43] Dr. Erland Ørbekk. SuperSonic Split Line TVC Technology and Testing at Nammo Raufoss AS. *42nd AIAA/ASME/SAE/ASEE Joint Propulsion Conference and Exhibit*, 2006. doi: 10.2514/6.2006-4940. Retrieved at 11-04-2019 https://arc.aiaa.org/doi/pdf/10.2514/6.2006-4940.

[44] R.J. Zeamer R.F.H. Woodberry. Solid Rocket Thrust Vector Control. *Solid Rocket Thrust Vector Control. NASA SP-8114, 190 pages, published by NASA, Washington, D.C.*, 1974. Retrieved at 23-10-2019 from https://ntrs.nasa.gov/archive/nasa/casi.ntrs.nasa.gov/19760010106.pdf.

[45] M.J. Riedl. *Optical Design Fundamentals for Infrared Systems*. SPIE tutorial texts. Society of Photo Optical, 2001. ISBN 9780819440518. URL https://books.google.nl/books?id=i35NCLLiglIC.

[46] Rocketdyne. Space shuttle main engine orientation, 1998. Retrieved at 10-09-2020 from, http://large.stanford.edu/courses/2011/ph240/nguyen1/docs/SSME_PRESENTATION.pdf.

[47] Ravnan S. The supersonic split line nozzle and its advantages over a submerged movable nozzle for a 100kn hybrid rocket motor, 2020. TU Delft, Aerospace engineering, AE4010 Research Methodologies.

[48] Ravnan Sigurd. Ae4020 literature study, 2020. TU Delft, Aerospace engineering, AE4020 Literature study.

[49] DEWEY M. SMITH. A comparison of experimental heat-transfer coefficients in a nozzle with analytical predictions from bartz's methods for various combustion chamber pressures in a solid propellant rocket motor, 1970. Retrieved at 20-02-2021 from, https://ntrs.nasa.gov/api/citations/19710011726/downloads/19710011726.pdf.

[50] Safran Snecma. Vulcain 2, 2011. Retrieved at 22-01-2021 from, https://www.safran-aircraft-engines.com/sites/snecma/files/fiche_vulcain2_ang_2011.pdf.

[51] Moog Space and defence group. Data sheet electromechanical actuators, 2020. Retrieved at 10-12-2020 from, https://www.moog.com/content/dam/moog/literature/Space_Defense/spaceliterature/actuationmechanisms/Moog-ElectromechanicalActuators-Datasheet.pdf.

[52] R. K. Strome. Test firing of a supersonic split-line nozzle. NASA Technical Reports Server, October 1969. Retrieved at 01-04-2019 from https://apps.dtic.mil/dtic/tr/fulltext/u2/865977.pdf.

[53] Onno Verberne, Adrien J. Boiron, Martina G. Faenza, and Bastien Haemmerli. Development of the north star sounding rocket: Getting ready for the first demonstration launch. In *51st AIAA/SAE/ASEE Joint Propulsion Conference*, 07 2015. Retrieved at 01-04-2019 https://arc.aiaa.org/doi/pdf/10.2514/6.2015-4045.

[54] Lukas Werling, Till Horger, Helmut Ciezki, and Stefan Schlechtriem. Experimental and theoretical analysis of the combustion efficiency and the heat loads on a n2o/c2h4 green propellant combustion chamber. In *8th European Conference for Aeronautics and Space Sciences*, 2019.

[55] Fujii K. Suzuki Y. and Mugitani T. Electric actuators for h-iia rocket tvc systems. *Spacecraft Guidance, Navigation and Control Systems, Proceedings of the 4th ESA International Conference*, pages 575–578, 2000. Retrieved at 10-09-2020 from, http://articles.adsabs.harvard.edu//full/2000ESASP.425..575F/0000575.000.html.

Appendices

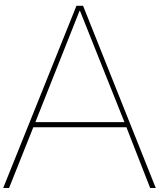

Statement of work from Nammo

Nammo	Document No.: Dokument Nr.: **2125666**	
	Version: Versjon: **1**	Date: Dato: **24 Jan 2020**

Document type / Dokumenttype:

Technical Specification

Title / Tittel:

SOW SSSL study

Project / Prosjekt:

FLPP Phase 4

Prepared by : Utarbeidet av :	Reviewed by: Kontrollert av:	Approved by : Godkjent av :
Faenza, Martina Development Engineer	**Haemmerli, Bastien** Development Engineer	**Lium, Kristian** Section Manager

Statement of Work

For master thesis work on TVC solution based on Nammo's SSSL

Revision History

Date of next revision:

Revision	Revision Date	Previous revision	Previous Revision Date	Summary of Changes
1	20.01.2020	-	-	-

Table of contents

1. SCOPE

In the framework of its hybrid rocket propulsion development, Nammo is interested in the future implementation of thrust vector control features to its motors. The Super Sonic Split Line (SSSL) TVC technology has been investigated by Nammo in the past primarily for defence applications based on solid rocket motors and is considered as a suitable technology to implement on its hybrid motors.
It is of interest to perform a preliminary feasibility study, to characterize the peculiarities and performance of the SSSL when applied to the hybrid motor and its requirements.
This document provides a description of the proposed work in order to perform such a characterization. This work is suitable to be covered as a master thesis work.

2. REFERENCE DOCUMENTS

[RD1] E. Ørbekk: *SuperSonic Split Line TVC Technology and Testing at Nammo Raufoss AS*; 42nd AIAA/ASME/SAE/ASEE Joint Propulsion Conference and Exhibit, 2006, Sacramento (CA).
[RD2] G. P. Sutton: *Rocket Propulsion Elements*; John Wiley & Sons Inc, 7th ed, 2001.

3. ABBREVIATIONS

NAMMO	Nammo Raufoss AS – Aerospace Propulsion (Purchaser)
SOW	Statement of work
SSSL	Super Sonic Split Line
ESA	European Space Agency
NOSA	NOrwegian Space Agency

4. INTRODUCTION

Nammo Raufoss AS, Norwegian defense and space company, has been developing hybrid rocket motors for the past 20 years with the support of ESA and NOSA. The development started initially with small scale engines (1-1.5 kN) and moved thereafter to upscaling (30 kN), first in battleship and then in flight weight configuration. The development of Nammo's 30 kN motor culminated in September 2018 in the launch of the sounding rocket Nucleus, a technology demonstrator based on the 30 kN hybrid motor. The maturation of Nammo's hybrid technology is continuing beyond this successful achievement both with optimization of the motor design towards industrialization as well as with gradual maturation of the needed building blocks for microlauncher applications based on the hybrid technology.
Nammo believes in fact its hybrid rocket technology to be suitable for both sounding rocket and microlauncher applications. When the microlauncher application is considered, a further upscaling of the engine towards the 80-100 kN thrust class is needed; moreover, some extra features/capabilities of the engine are needed, such as long burning time and TVC.
In this context, a very attractive TVC technology identified as suitable for the hybrid motor is the SSSL ([RD1]). This vectoring technology is of the movable nozzle kind and, as the name suggests, is based on the possibility to move only the supersonic part of the nozzle, the exit cone, by means of a split line introduced downstream the throat in the nozzle assembly. Such a technology is expected to be competitive in addressing the vectoring capabilities typically required for attitude control in space applications, whilst guaranteeing an overall lighter and less complex TVC system when compared to other more conventional technologies.
Before a detailed design of this TVC solution can be performed, a mapping of the achievable performance is needed by means first of all of extensive CFD characterization. A detailed design would further require thermal and structural analysis as well as prototype production and demonstrator testing.

5. WORK DESCRIPTION

Nammo is interested in obtaining a mapping of the SSSL characteristics and performance when applied to the specific requirements and motor dimensions relevant for the hybrid rocket application. Chapter 6 provides a summary of the basic requirements to perform the study. If applicable, further requirements mandatory to perform the study could be shared dedicatedly in a second stage.
CFD is expected to be the primary tool to be used for this task. Steady state simulations are preferred.
In chapter 6, the reference requirements for both designing the nozzle inner contour and setting up the CFD simulations are provided.
The SSSL performance mapping shall aim at characterizing:

- Vectoring effect: effective thrust vectoring obtained in comparison to the angular rotation applied on the exit cone;
- Performance loss due to vectoring: thrust coefficient, cF, penalty introduced by the vectoring;
- Temperature and pressure field distribution, especially in the area around the split;
- Estimation of the heat transfer coefficient at the wall.

The mapping shall be performed as a function of:

- Nozzle vectoring angle: at least 3 angle positions in the range from 0° to the maximum nozzle deflection angle shall be analysed;
- Split position along the exit cone: at least 3 split positions shall be analysed.

Once the performance mapping is obtained on the reference geometry, scaling effects shall be evaluated. Two approaches are proposed:

1. Change in flow conditions: the effect on performance of changes in mass flow rate (thus total pressure P0) on the same nozzle geometry are evaluated, selecting 2 or more different nozzle configurations among the ones already analysed for the performance mapping to run new simulations at different total pressure levels.
2. Change in geometry dimension:
    a. Increased expansion ratio maintaining the same nozzle throat: this case corresponds to the configuration needed for a second stage motor in a microlauncher application. 2 or more combinations of deflection angle and split position shall be selected and the vectoring performance shall be compared between long and short exit cone without changing the position of the split.
    b. Reduced scale nozzle: this case corresponds to the configuration needed for mesosphere sounding rocket applications. 2 or more combinations of deflection angle and split position shall be selected and the vectoring performance shall be analysed with the new nozzle dimensions in order to compare the obtain performance between two different nozzle scales.

If the analyses at point 2a and 2b cannot be both performed, due to time constraints, a discussion shall be held with Nammo in due time, in order to perform a trade-off between the two options and choosing the one with the most values for all the stakeholders.
Figure 1 shows the workflow based on the proposed work description.
All the results shall be documented in written form and delivered to Nammo. If the results are reported in their entirety in a master thesis, the thesis can be considered as an accepted final report by Nammo.
The CAD and mesh files as well as the simulation setup reports shall be delivered to Nammo as well, if possible without infringing intellectual property rights.

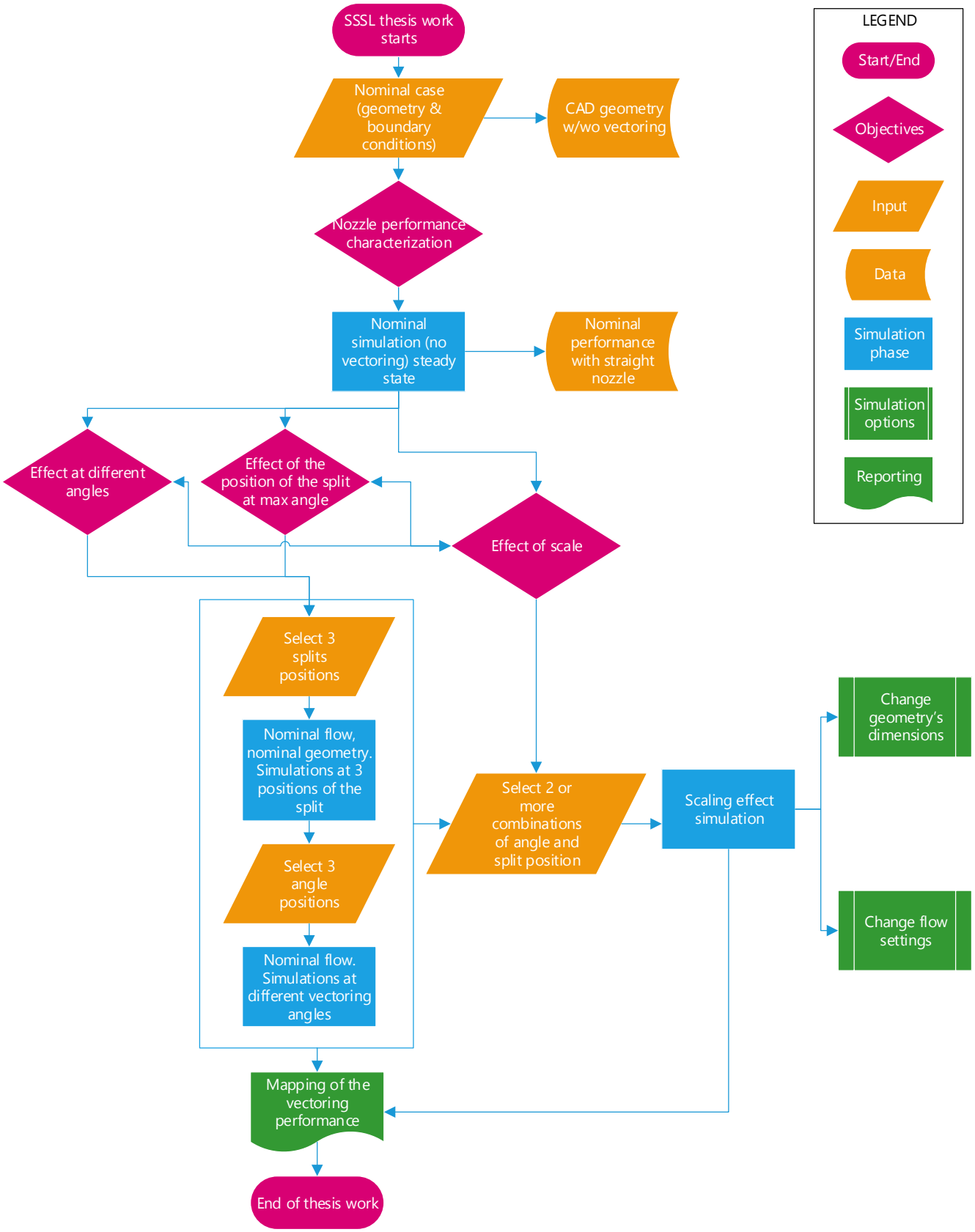

Figure 1. Work flow for performance mapping of the SSSL technology.

6. REQUIREMENTS

In this section, the preliminary requirements needed for the CFD characterization are provided.

Table 1. Motor and TVC specifications

Theoretical vacuum Thrust, F	100 kN
Burning time, tb	90 s
Theoretical vacuum Isp	289.5 s
Maximum nozzle deflection angle, alpha	± 5°
Nozzle exit cone profile	Bell shape, 80% length of the ideal conical shape ([RD2]).
Constant wall temperature**, Tw	1200 °C

*From NASA-CEA thermochemical software, assuming thermochemical equilibrium.
**For boundary conditions and heat transfer coefficient calculation.

Table 2. Nozzle Input Parameters, nominal case

Total temperature*, T0	2721 K
Total pressure, P0	35 bar
Molar mass reacting mixture*, Mm	22 g/mol
Gamma	1.13
Mixture composition, molar fractions [mass fraction]*	CO 0.02654 [3.3%] CO2 0.16195 [31.9%] OH 0.01668 [1.3%] O2 0.01237 [1.8%] H2O to get to unity (~0.78246) [~61.2%]
Nozzle throat diameter, Dt	0.145 m
Nozzle expansion ratio, AR	12
Total mass flow rate**, dm	35.2kg/s

*From NASA-CEA thermochemical software, assuming thermochemical equilibrium.
**Redundant information.

Table 3. Nozzle Additional Input Parameters, scaling effect evaluation

*a. Nozzle exit cone extension**	
Theoretical vacuum Thrust, F	107.7 kN
Theoretical vacuum Isp	311.8 s
Nozzle expansion ratio, ARII**	45
b. Nozzle downscaling*	
Theoretical vacuum Thrust, F	29.0 kN
Burning time, tb	39 s
Theoretical vacuum Isp	275.4 s
Nozzle throat diameter, Dt1	0.083 m
Nozzle expansion ratio, AR1	6.5
Total mass flow rate***, dm	10.75 kg/s

* The values given in Table 1 and Table 2 shall be considered valid if not modified by the values in Table 3
** Even if not optimal, the bell profile contour could be maintained unchanged from the nominal geometry up to AR and the exit cone simply extended up to ARII, in order to reduce the CAD-ing/meshing effort. A comparison between the profile so obtained and the optimal one that would be needed for ARII should be provided for completeness.
*** Redundant information.

DISCLAIMER

The work described in this document addresses a specific and concrete interest identified by Nammo in connection to the possible use of the SSSL TVC technology in hybrid rocket applications. As such, Nammo is available to provide the required support needed in order to perform the described work.
The work described in this document does not pretend to be a full description of a thesis work but rather a clear identification of a work package that can be included in a thesis work.

B

Emissivity charts

In this appendix the emissivity chats are found that are used for the calculation of the emissivity of the hot gas flow. The charts have been adapted from [1]

[1] Michael Alberti, Roman Weber, and Marco Mancini. *Gray gas emissivities for h2o co2 co n2 mixtures. Journal of Quantitative Spectroscopy and Radiative Transfer* doi: https://doi.org/10.1016/j.jqsrt.2018.08.008. URL http://www.sciencedirect.com/science/article/pii/S0022407318304618.

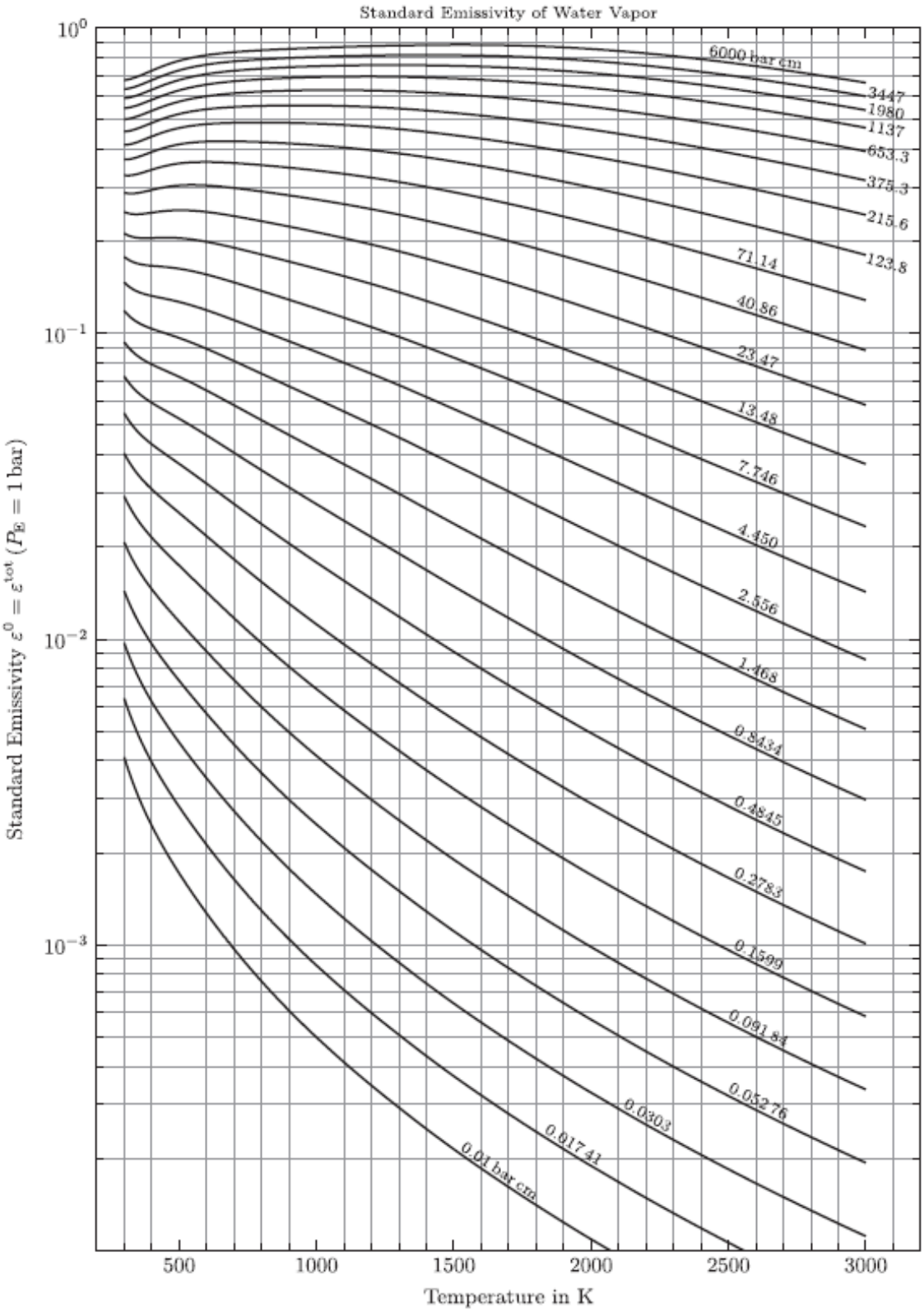

Fig. A1. Standard emissivity of water vapor.

Figure B.1: Emissivity of water vapour at different pressure path lengths and temperatures

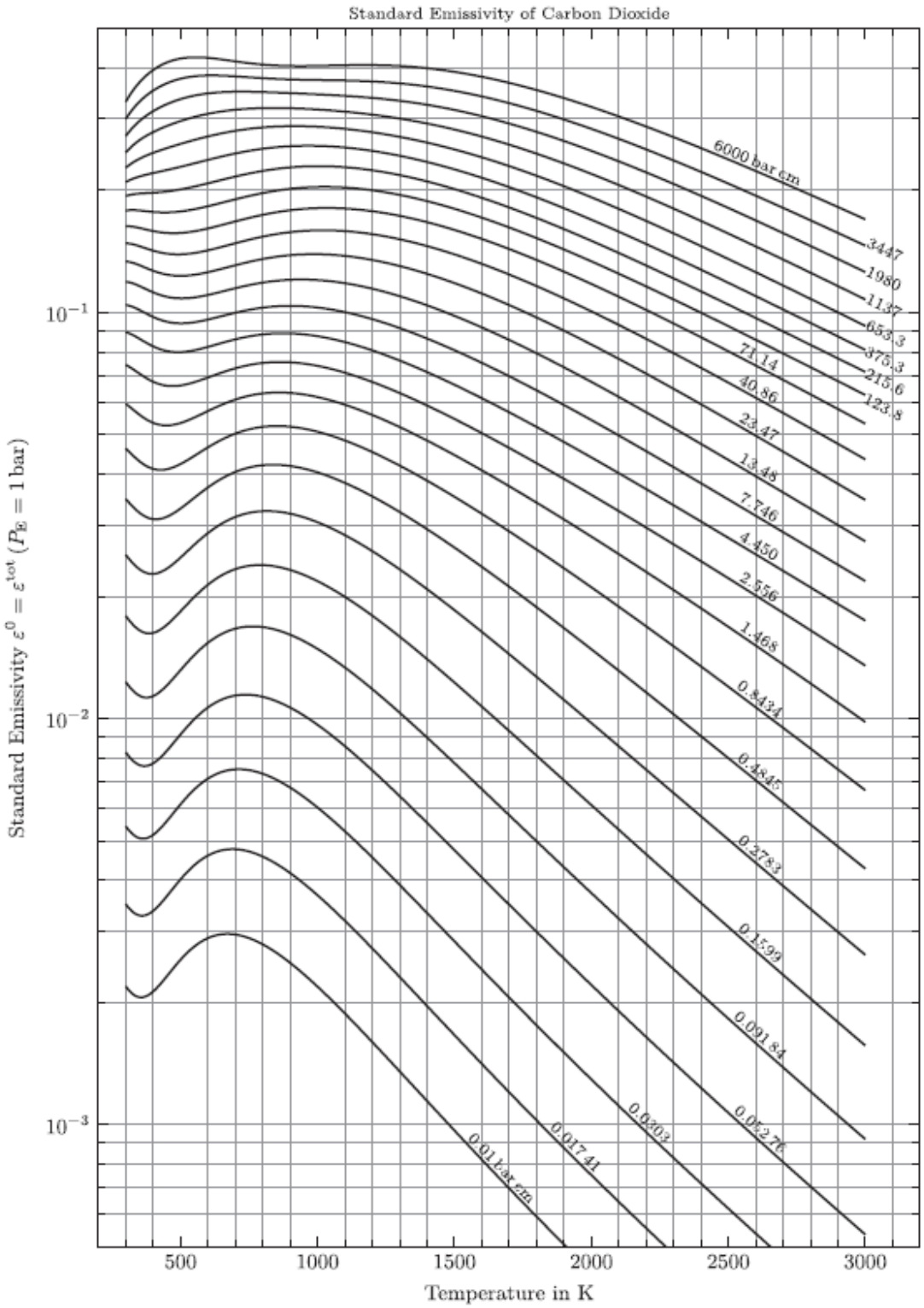

Fig. A3. Standard emissivity of carbon dioxide.

Figure B.2: Emissivity of carbon di-oxide at different pressure path lengths and temperatures

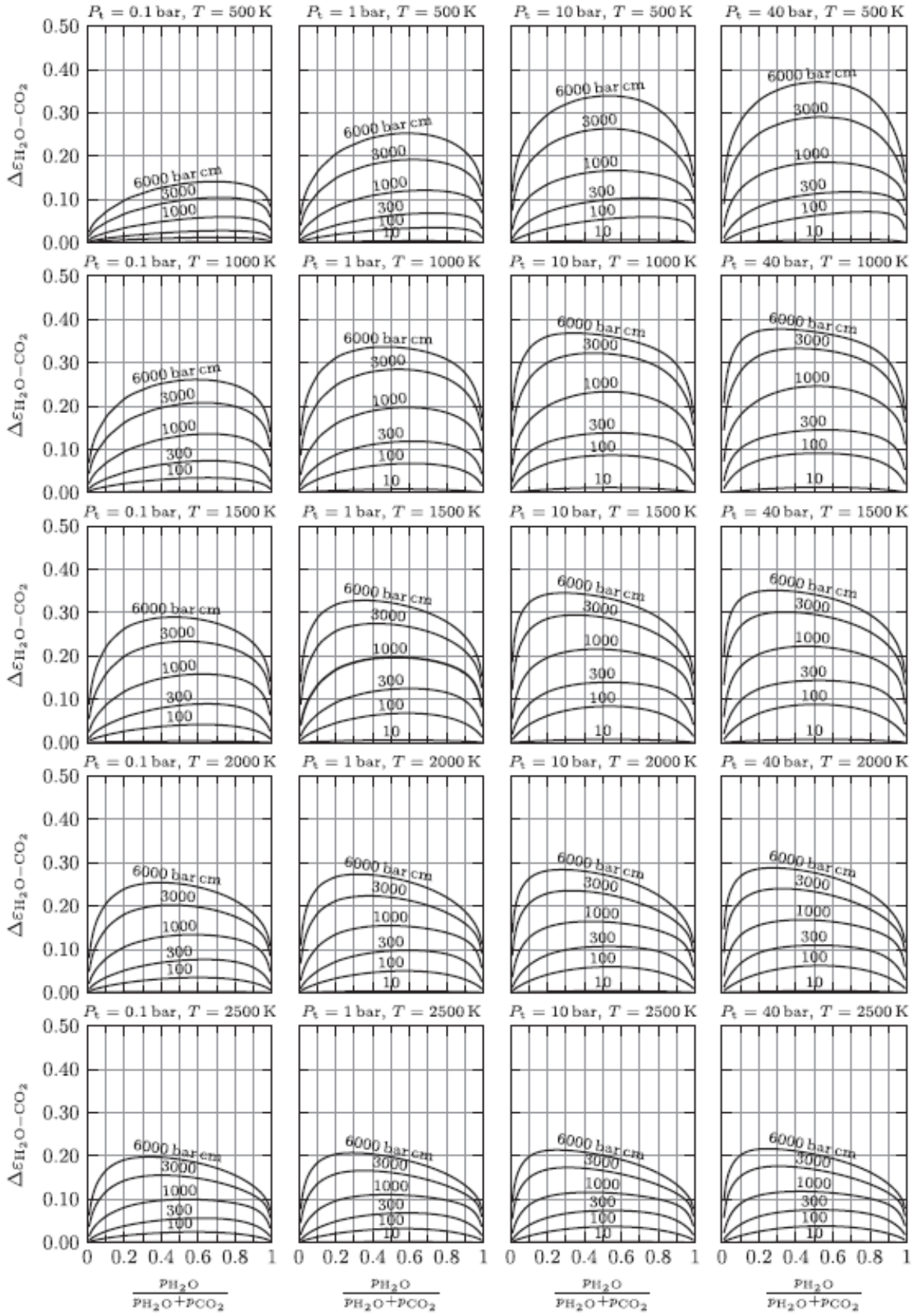

Fig. A7. Binary overlap correction for $H_2O - CO_2$-mixtures.

Figure B.3: Emissivity correction factor of water vapour and carbon-dioxide at different molar fractions and temperatures

C

Shape approach 1

In order to calculate the shape of the nozzle the methods by Sutton and by Zandbergen are used [1],[2]. The calculated shape corresponds to the shape from the throat towards the exit. The nozzle shape directly after the throat will be approximated by a circular arc. This arc is defined as a constant multiplied by the throat radius. This constant is taken to be 0.382 as described by Huzel and Huang [3]. At a defined point in this arc the convergent parabolic shape starts. The starting point is the initial angle of the parabolic, while the endpoint of this parabolic has the exit angle of the nozzle. Since the requirements states that the nozzle should have a length of 80% of a reference 15°conical nozzle, the nozzle length is already fixed. Also, the throat radius and the expansion ratio has been defined in the requirements. Therefore the only two design parameters are the two angles mentioned earlier. The initial angle of the nozzle can be found by the use of the following figure, see figure C.1

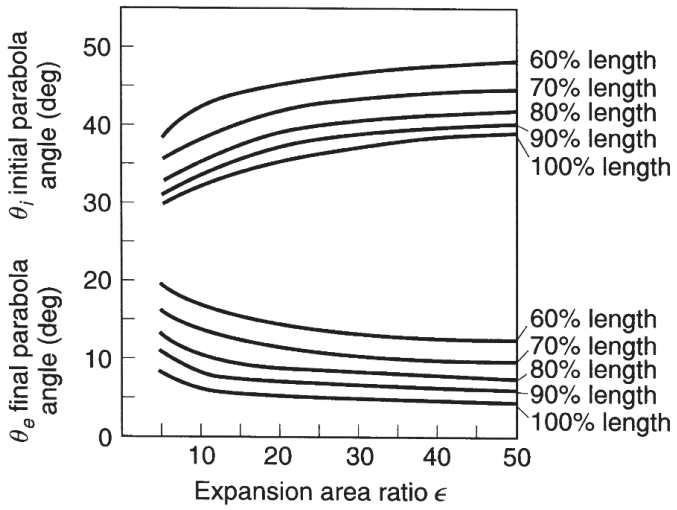

Figure C.1: Figure showing the nozzle entry and exit angles for a certain expansion ratio. The length percentage is the length of the bell nozzle compared to a 15°conical nozzle. Source for the image[2].

In order to compute the final angle of the nozzle a set of equations are created in order to solve for the exit angle. A parabolic equation is used to find the x-position as a function of the y-position. By

[1]B.T.C Zandbergen. AE4S01 *Thermal Rocket Propulsion (version 2.07)*, TU Delft readers, August 2018. Lecture notes in the course AE4S01 Thermal Rocket Propulsion given at TU Delft.

[2]Biblarz Oscar and Sutton George P. *Rocket Propulsion Elements (9th Edition)*. "John Wiley & Sons", 2017. ISBN 9781118753651. URL https://app.knovel.com/hotlink/toc/id: kpRPEE001A/rocketpropulsionelements/ rocketpropulsionelements.

[3]D. K. Huzel and D. H. Huang. *Design of liquid propellant rocket engines second edition, nasasp125.* NASA technical reports server, January 1971. Retrieved at 15-04-2020 from https: //ntrs.nasa.gov/archive/nasa/casi.ntrs.nasa.gov/19710019929.pdf.

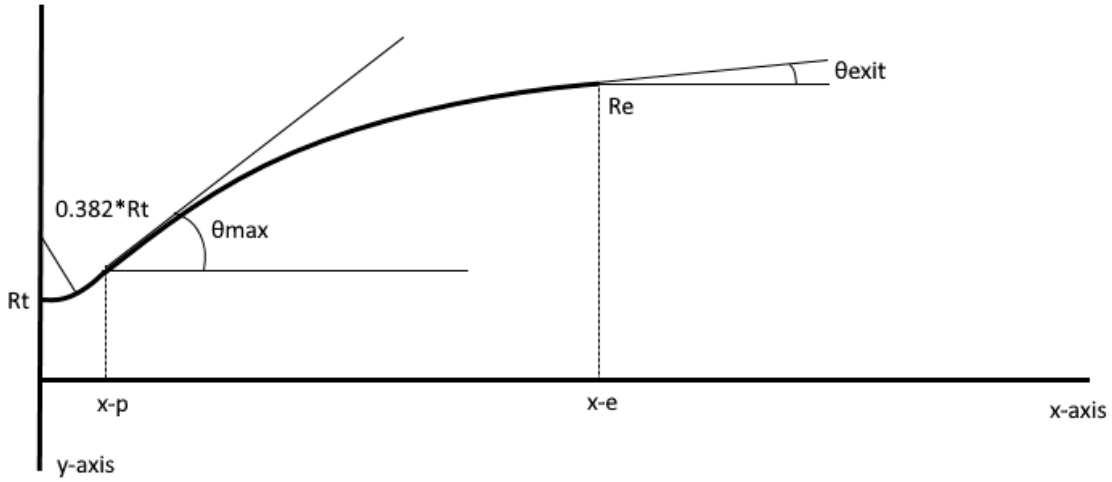

Figure C.2: Showing the various locations and angles on an example nozzle, Rt is the throat radius, the figure is not to scale.

using the boundary conditions at x-p and x-e and the derivative of the parabolic equation, a solution can be found for the exit angle. The definition of point x-e and x-p are found in figure C.2. The parabolic equation is given in equation (C.1). Where a, b and c are constants. The derivative of the parabolic equation is given in equation (C.2), and since the derivative is equal to the tangent of the curve it can be used to solve for the exit angle of the nozzle. When all the unknowns are found the shape of the nozzle can be drawn in the python program.

$$x = a \cdot y^2 + b \cdot y + c \tag{C.1}$$

$$\frac{dx}{dy} = 2a \cdot y + b = tan(\frac{\pi}{2} - \theta) \tag{C.2}$$

D

Contour plots from the flow field of the various nozzles

In this appendix the flow field from all the nozzle simulations are presented. Each nozzle design at each thrust vector angle will be displayed in its own section. For all nozzle representations the flow of gases goes from the left to the right. All the nozzles tested are at vacuum conditions. The naming convention is as following. The supersonic split line (SSSL) nozzle with the split at an expansion ratio of 1.75 is design A, the one at 2 is design B and the one at 2.25 is design C. This is for the SSSL nozzle with exspantion ratio 12. The SSSL nozzle with a total expansion ratio of 45 with the split at an expansion ratio of 1.75 is SSSL-e45 design A and the one at 2.25 is SSSL-e45 design B. The SSSL nozzle with a total expansion ratio of 6.5 with the split at an expansion ratio of 1.75 is SSSL-e6 design A and the one at 2.25 is SSSL-e6 design B. In table D.1 are all the different nozzles tested are presented:

Table D.1: List simulations that were performed. The split location is the area expansion ratio at the location of the split. Where multiple angles are mentioned one simulation for each of the angles were performed.

Type nozzle	Expansion ratio	Split location	Angle (degree)
SM nozzle	12	-	0, 2.5, 5
SSSL nozzle	12	1.75	0, 2.5, 5
SSSL nozzle	12	2	0, 2.5, 5
SSSL nozzle	12	2.25	0, 2.5, 5
SSSL nozzle	45	1.75	0, 2.5, 5
SSSL nozzle	45	2.25	0, 2.5, 5
SSSL nozzle	6.5	1.75	0, 2.5, 5
SSSL nozzle	6.5	2.25	0, 2.5, 5

Each of the simulated cases are presented with the following contour plots:

- Mach number contour
- Pressure contours
- Temperature contour
- Turbulence contour
- Total temperature contour
- Heat flux contours

- Pressure and temperature trace along nozzle wall
- Residual plots

D.1. SSSL nozzle design A 0 degree thrust vectoring

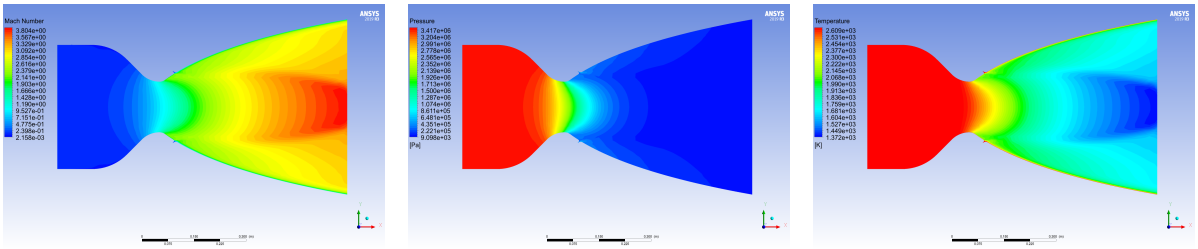

(a) Mach number contour (b) Pressure contour (c) Temperature contour

Figure D.1: Contour plots for Mach number, pressure and temperature for the SSSL nozzle design A at 0 degree thrust vectoring

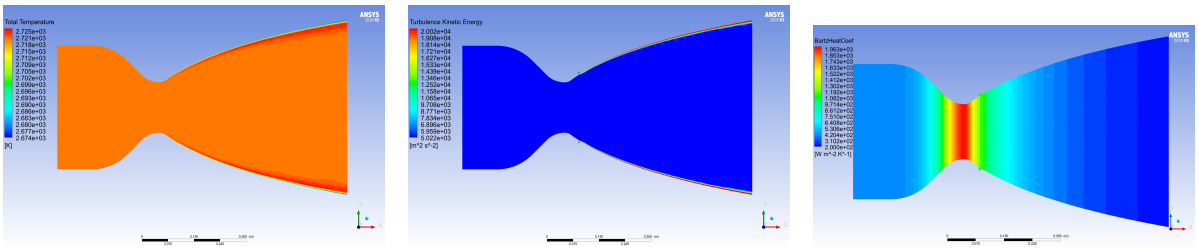

(a) Total temperature contour (b) Turbulence contour (c) Bartz heat coefficient contour

Figure D.2: Contour plots for total temperature, turbulence and Bartz heat coefficient for the SSSL nozzle design A at 0 degree thrust vectoring

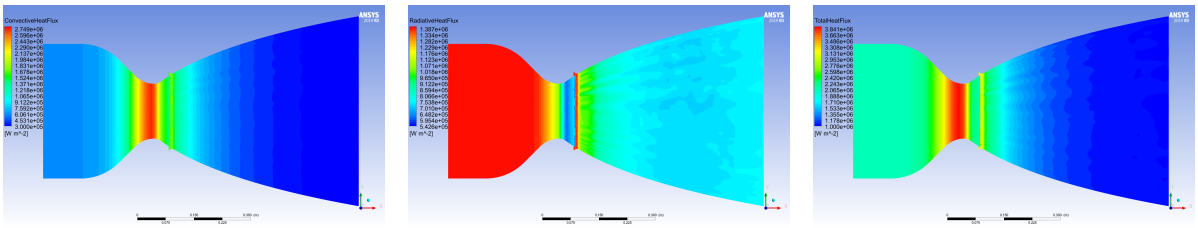

(a) Convective heat flux contour (b) Radiative heat flux contour (c) Total heat flux contour

Figure D.3: Contour plots for convective heat flux, radiative heat flux and total heat flux for the SSSL nozzle design A at 0 degree thrust vectoring

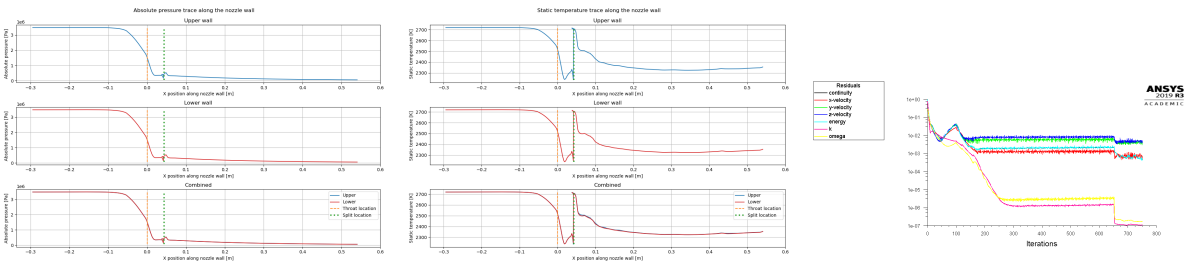

(a) Pressure along the nozzle wall (b) Temperature along the nozzle wall (c) Residual plot

Figure D.4: Temperature and pressure traces along the nozzle wall and residual plot for the SSSL nozzle design A at 0 degree thrust vectoring

D.2. SSSL nozzle design B 0 degree thrust vectoring

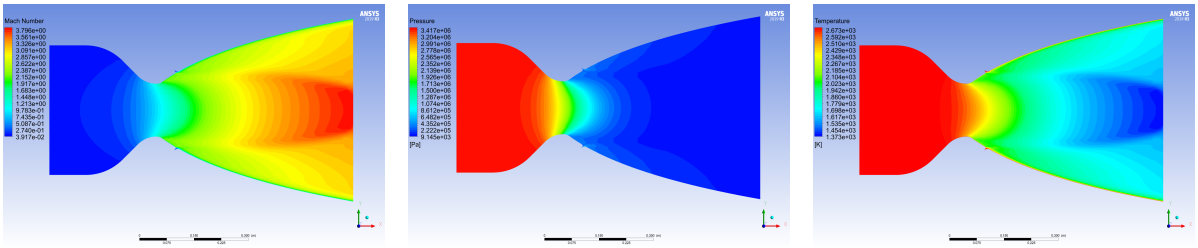

(a) Mach number contour (b) Pressure contour (c) Temperature contour

Figure D.5: Contour plots for Mach number, pressure and temperature for the SSSL nozzle design B at 0 degree thrust vectoring

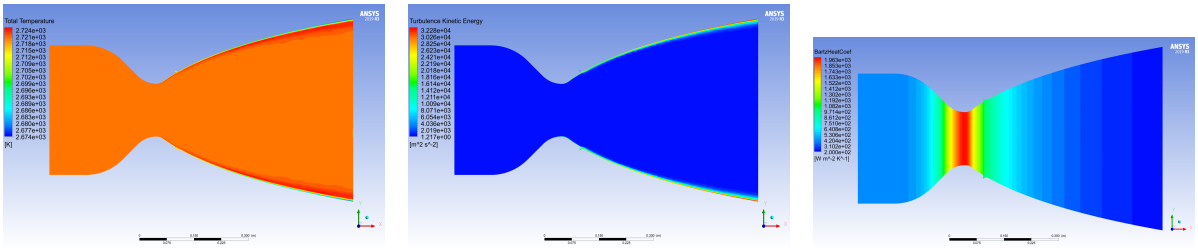

(a) Total temperature contour (b) Turbulence contour (c) Bartz heat coefficient contour

Figure D.6: Contour plots for total temperature, turbulence and Bartz heat coefficient for the SSSL nozzle design B at 0 degree thrust vectoring

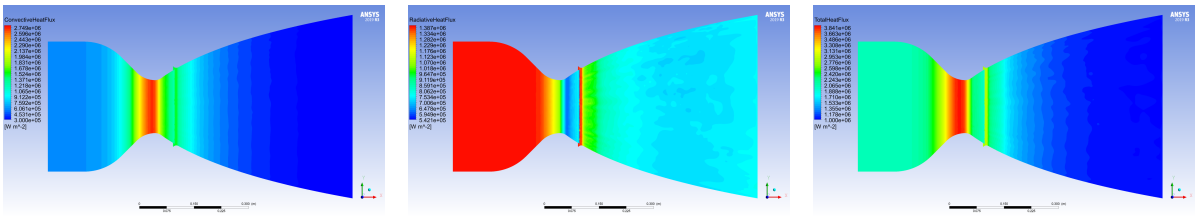

(a) Convective heat flux contour (b) Radiative heat flux contour (c) Total heat flux contour

Figure D.7: Contour plots for convective heat flux, radiative heat flux and total heat flux for the SSSL nozzle design B at 0 degree thrust vectoring

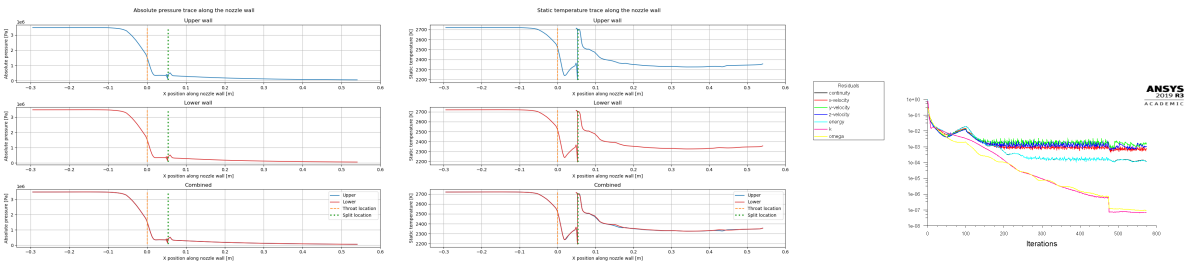

(a) Pressure along the nozzle wall (b) Temperature along the nozzle wall (c) Residual plot

Figure D.8: Temperature and pressure traces along the nozzle wall and residual plot for the SSSL nozzle design B at 0 degree thrust vectoring

D.3. SSSL nozzle design C 0 degree thrust vectoring

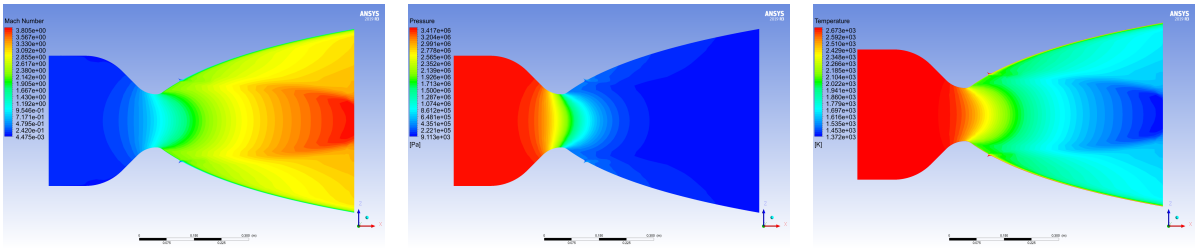

(a) Mach number contour (b) Pressure contour (c) Temperature contour

Figure D.9: Contour plots for Mach number, pressure and temperature for the SSSL nozzle design C at 0 degree thrust vectoring

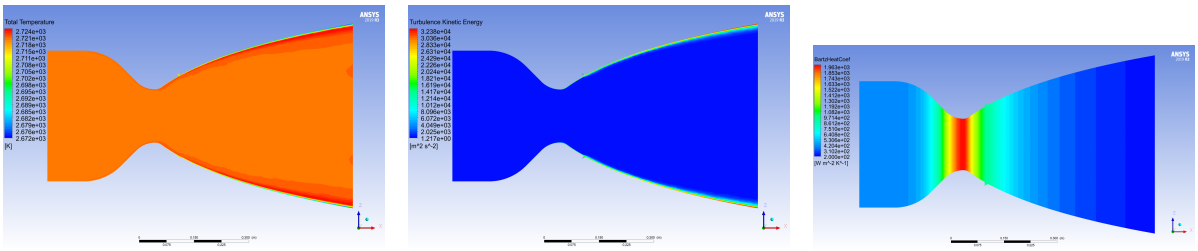

(a) Total temperature contour (b) Turbulence contour (c) Bartz heat coefficient contour

Figure D.10: Contour plots for total temperature, turbulence and Bartz heat coefficient for the SSSL nozzle design C at 0 degree thrust vectoring

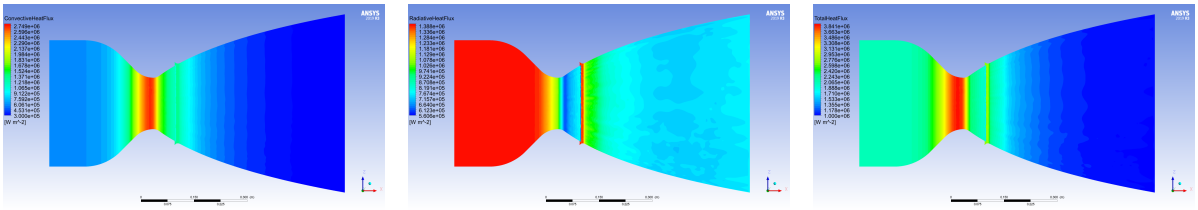

(a) Convective heat flux contour (b) Radiative heat flux contour (c) Total heat flux contour

Figure D.11: Contour plots for convective heat flux, radiative heat flux and total heat flux for the SSSL nozzle design C at 0 degree thrust vectoring

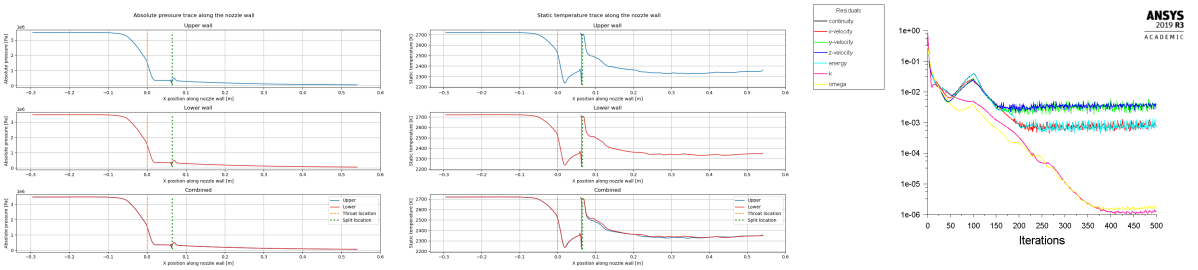

(a) Pressure along the nozzle wall (b) Temperature along the nozzle wall (c) Residual plot

Figure D.12: Temperature and pressure traces along the nozzle wall and residual plot for the SSSL nozzle design C at 0 degree thrust vectoring

D.4. SM nozzle at 0 degree thrust vectoring

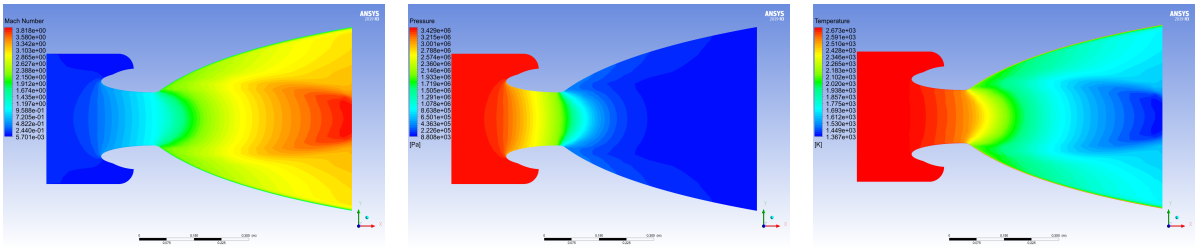

(a) Mach number contour (b) Pressure contour (c) Temperature contour

Figure D.13: Contour plots for Mach number, pressure and temperature for the SM nozzle at 0 degree thrust vectoring

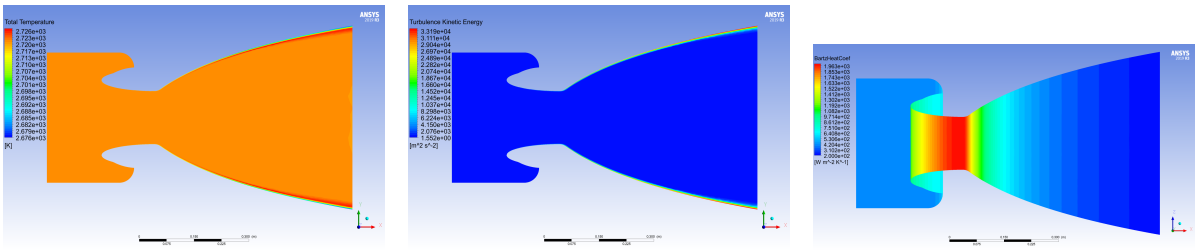

(a) Total temperature contour (b) Turbulence contour (c) Bartz heat coefficient contour

Figure D.14: Contour plots for total temperature, turbulence and Bartz heat coefficient for the SM nozzle at 0 degree thrust vectoring

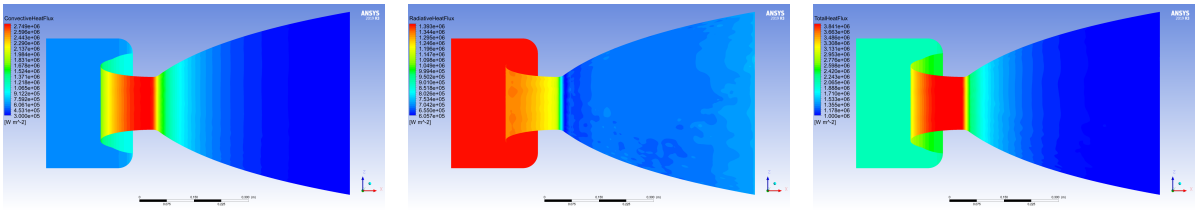

(a) Convective heat flux contour (b) Radiative heat flux contour (c) Total heat flux contour

Figure D.15: Contour plots for convective heat flux, radiative heat flux and total heat flux for the SM nozzle at 0 degree thrust vectoring

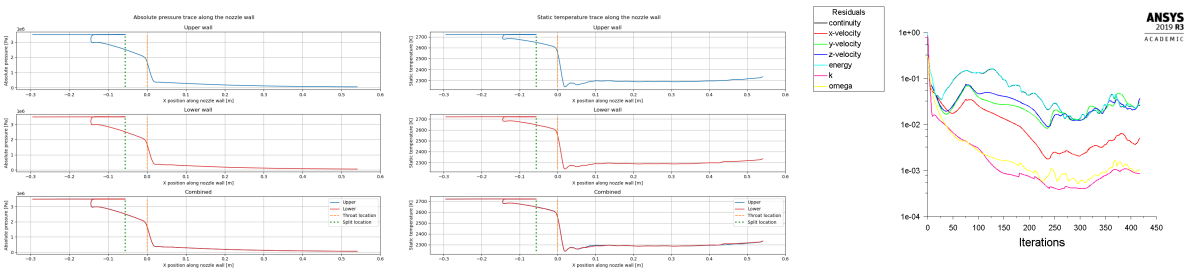

(a) Pressure along the nozzle wall (b) Temperature along the nozzle wall (c) Residual plot

Figure D.16: Temperature and pressure traces along the nozzle wall and residual plot for the SM nozzle at 0 degree thrust vectoring

D.5. SSSL nozzle design A 2.5 degree thrust vectoring

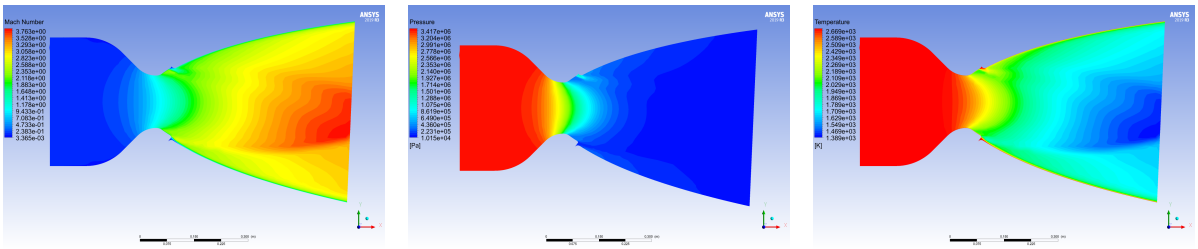

(a) Mach number contour (b) Pressure contour (c) Temperature contour

Figure D.17: Contour plots for Mach number, pressure and temperature for the SSSL nozzle design A at 2.5 degree thrust vectoring

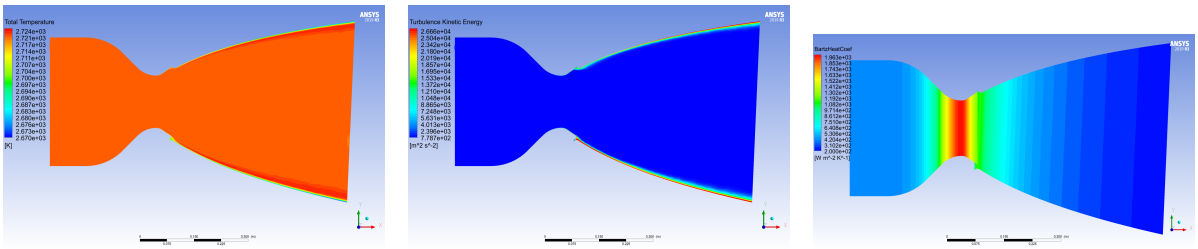

(a) Total temperature contour (b) Turbulence contour (c) Bartz heat coefficient contour

Figure D.18: Contour plots for total temperature, turbulence and Bartz heat coefficient for the SSSL nozzle design A at 2.5 degree thrust vectoring

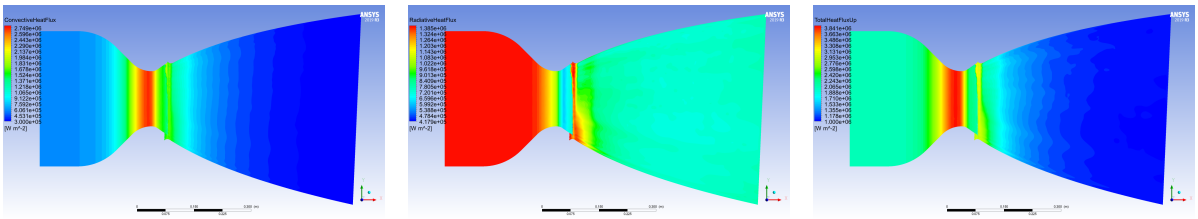

(a) Convective heat flux contour (b) Radiative heat flux contour (c) Total heat flux contour

Figure D.19: Contour plots for convective heat flux, radiative heat flux and total heat flux for the SSSL nozzle design A at 2.5 degree thrust vectoring

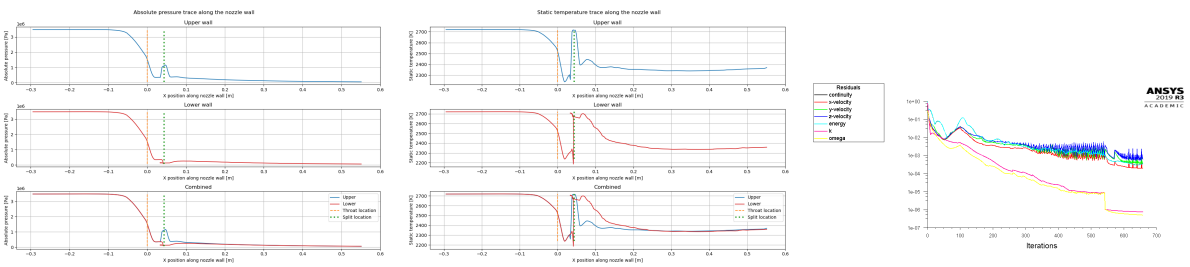

(a) Pressure along the nozzle wall (b) Temperature along the nozzle wall (c) Residual plot

Figure D.20: Temperature and pressure traces along the nozzle wall and residual plot for the SSSL nozzle design A at 2.5 degree thrust vectoring

D.6. SSSL nozzle design B 2.5 degree thrust vectoring

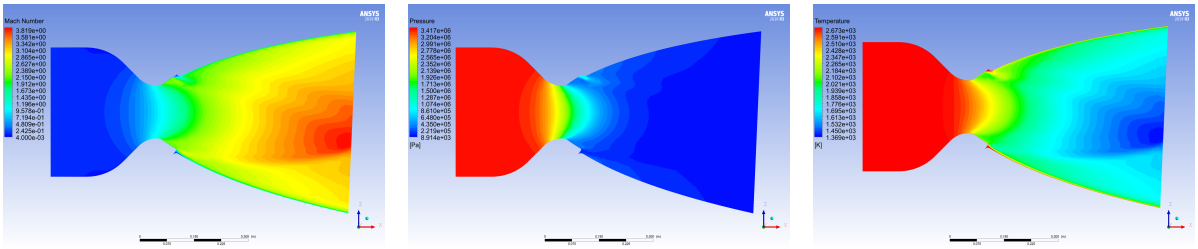

(a) Mach number contour (b) Pressure contour (c) Temperature contour

Figure D.21: Contour plots for Mach number, pressure and temperature for the SSSL nozzle design B at 2.5 degree thrust vectoring

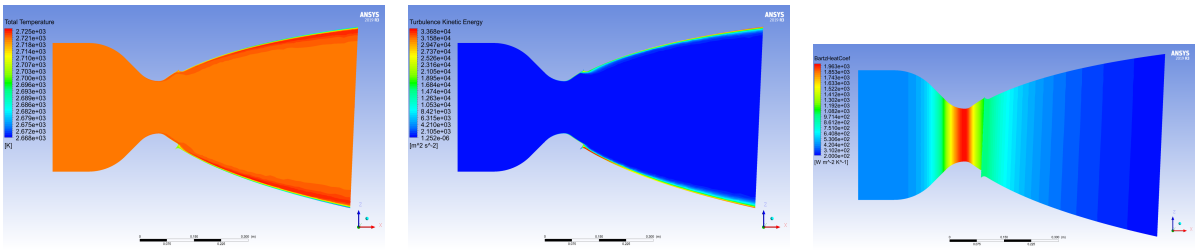

(a) Total temperature contour (b) Turbulence contour (c) Bartz heat coefficient contour

Figure D.22: Contour plots for total temperature, turbulence and Bartz heat coefficient for the SSSL nozzle design B at 2.5 degree thrust vectoring

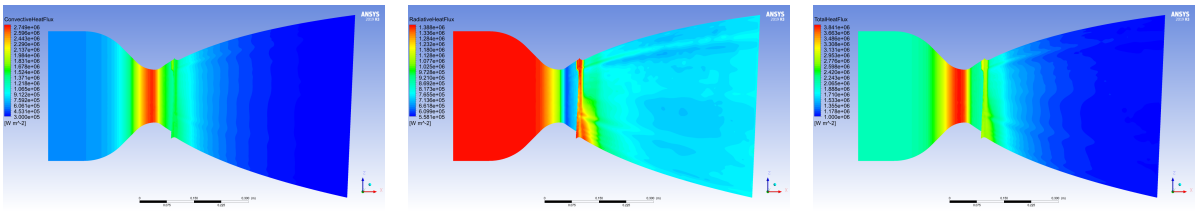

(a) Convective heat flux contour (b) Radiative heat flux contour (c) Total heat flux contour

Figure D.23: Contour plots for convective heat flux, radiative heat flux and total heat flux for the SSSL nozzle design B at 2.5 degree thrust vectoring

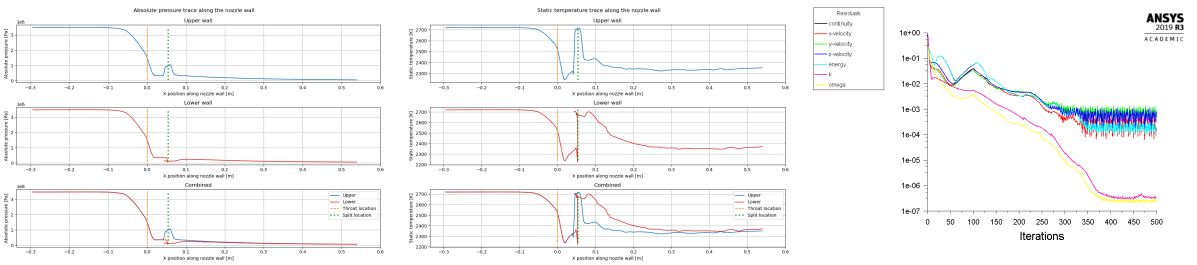

(a) Pressure along the nozzle wall (b) Temperature along the nozzle wall (c) Residual plot

Figure D.24: Temperature and pressure traces along the nozzle wall and residual plot for the SSSL nozzle design B at 2.5 degree thrust vectoring

D.7. SSSL nozzle design C 2.5 degree thrust vectoring

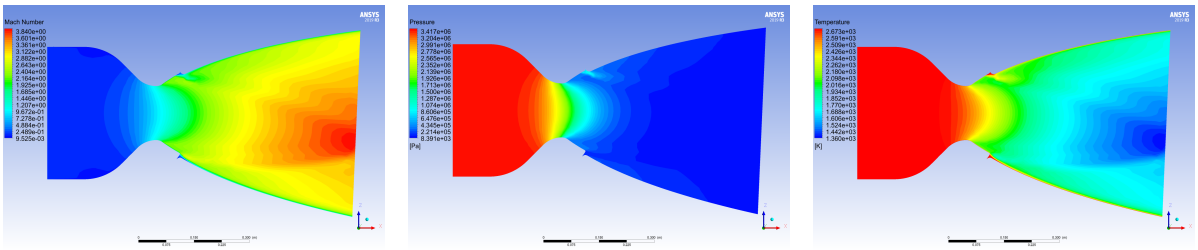

(a) Mach number contour (b) Pressure contour (c) Temperature contour

Figure D.25: Contour plots for Mach number, pressure and temperature for the SSSL nozzle design C at 2.5 degree thrust vectoring

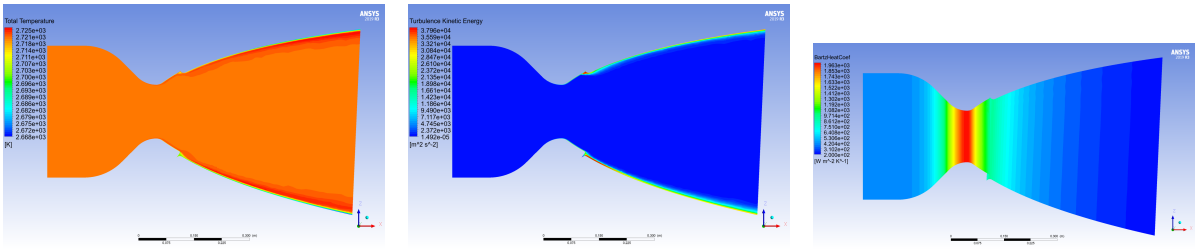

(a) Total temperature contour (b) Turbulence contour (c) Bartz heat coefficient contour

Figure D.26: Contour plots for total temperature, turbulence and Bartz heat coefficient for the SSSL nozzle design C at 2.5 degree thrust vectoring

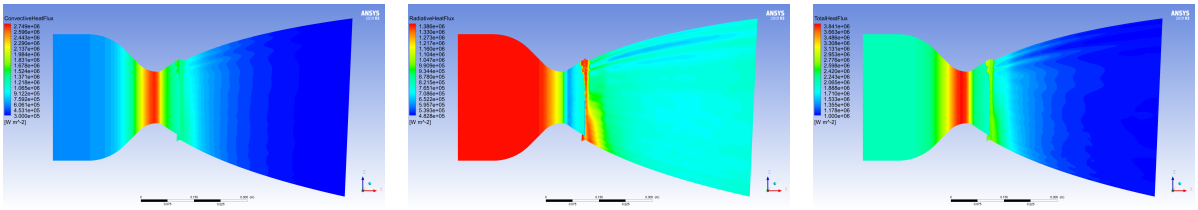

(a) Convective heat flux contour (b) Radiative heat flux contour (c) Total heat flux contour

Figure D.27: Contour plots for convective heat flux, radiative heat flux and total heat flux for the SSSL nozzle design C at 2.5 degree thrust vectoring

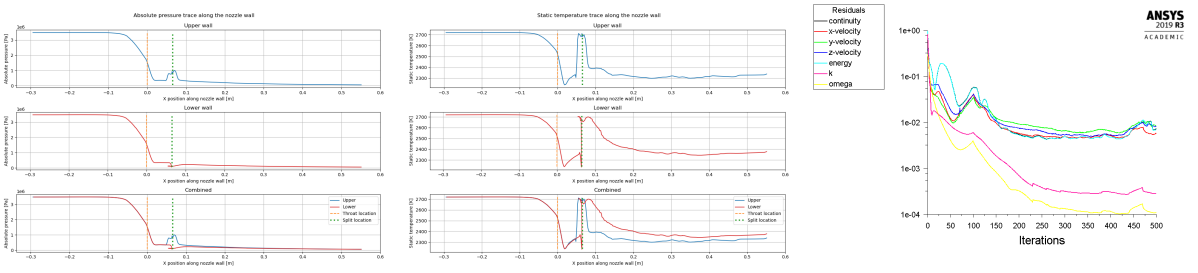

(a) Pressure along the nozzle wall (b) Temperature along the nozzle wall (c) Residual plot

Figure D.28: Temperature and pressure traces along the nozzle wall and residual plot for the SSSL nozzle design C at 2.5 degree thrust vectoring

D.8. SM nozzle at 2.5 degree thrust vectoring

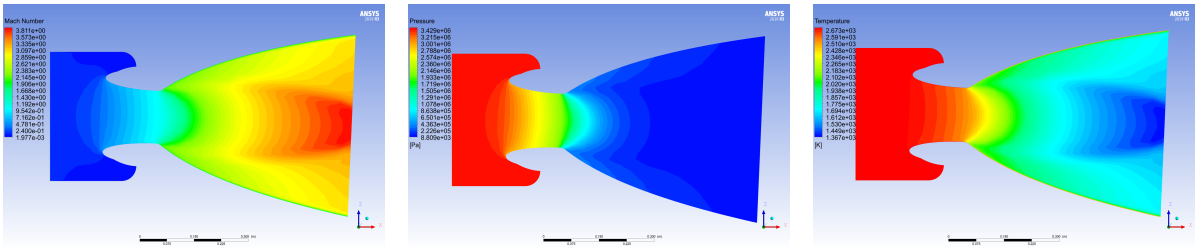

(a) Mach number contour (b) Pressure contour (c) Temperature contour

Figure D.29: Contour plots for Mach number, pressure and temperature for the SM nozzle at 2.5 degree thrust vectoring

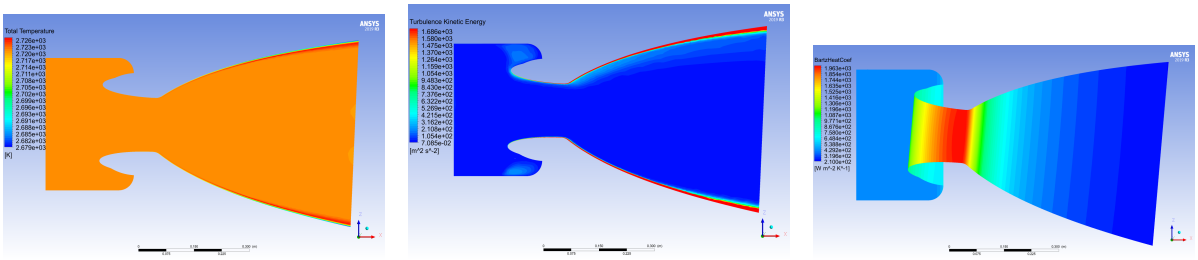

(a) Total temperature contour (b) Turbulence contour (c) Bartz heat coefficient contour

Figure D.30: Contour plots for total temperature, turbulence and Bartz heat coefficient for the SM nozzle at 2.5 degree thrust vectoring

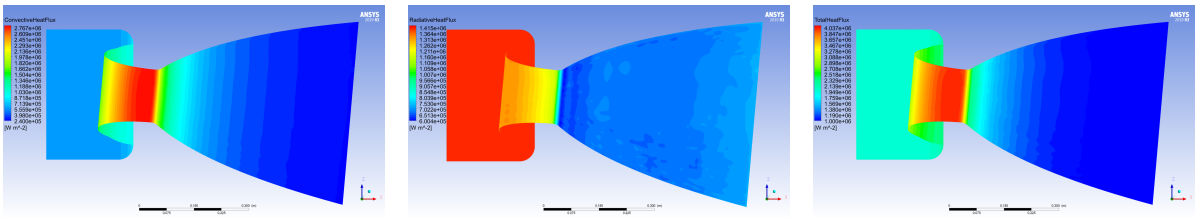

(a) Convective heat flux contour (b) Radiative heat flux contour (c) Total heat flux contour

Figure D.31: Contour plots for convective heat flux, radiative heat flux and total heat flux for the SM nozzle at 2.5 degree thrust vectoring

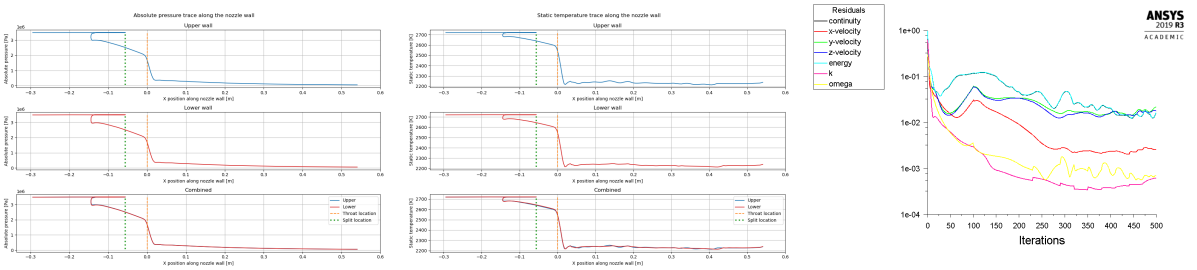

(a) Pressure along the nozzle wall (b) Temperature along the nozzle wall (c) Residual plot

Figure D.32: Temperature and pressure traces along the nozzle wall and residual plot for the SM nozzle at 2.5 degree thrust vectoring

D.9. SSSL nozzle design A 5 degree thrust vectoring

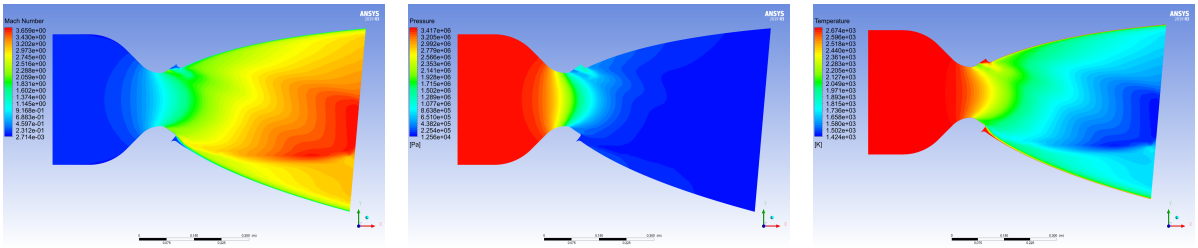

(a) Mach number contour (b) Pressure contour (c) Temperature contour

Figure D.33: Contour plots for Mach number, pressure and temperature for the SSSL nozzle design A at 5 degree thrust vectoring

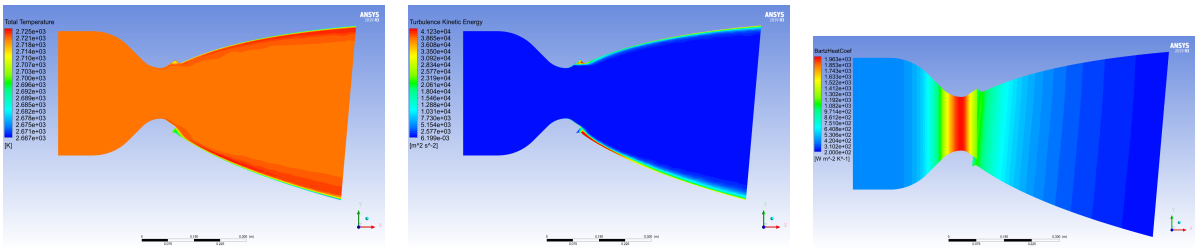

(a) Total temperature contour (b) Turbulence contour (c) Bartz heat coefficient contour

Figure D.34: Contour plots for total temperature, turbulence and Bartz heat coefficient for the SSSL nozzle design A at 5 degree thrust vectoring

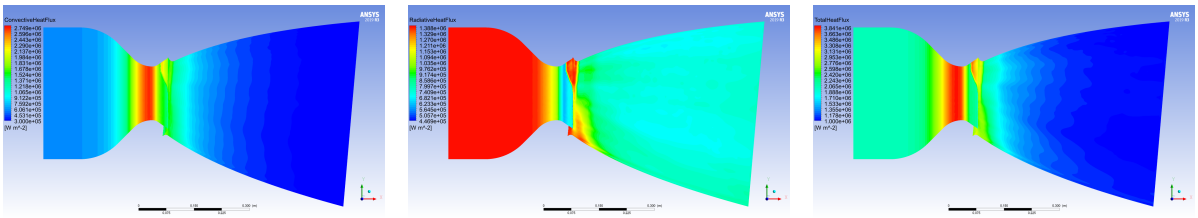

(a) Convective heat flux contour (b) Radiative heat flux contour (c) Total heat flux contour

Figure D.35: Contour plots for convective heat flux, radiative heat flux and total heat flux for the SSSL nozzle design A at 5 degree thrust vectoring

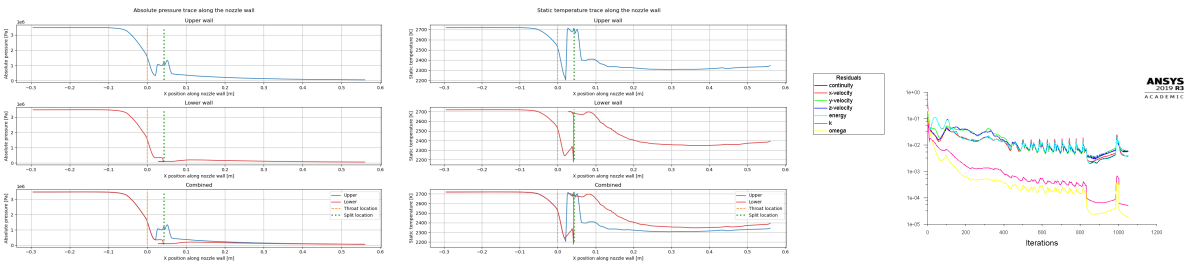

(a) Pressure along the nozzle wall (b) Temperature along the nozzle wall (c) Residual plot

Figure D.36: Temperature and pressure traces along the nozzle wall and residual plot for the SSSL nozzle design A at 5 degree thrust vectoring

D.10. SSSL nozzle design B 5 degree thrust vectoring

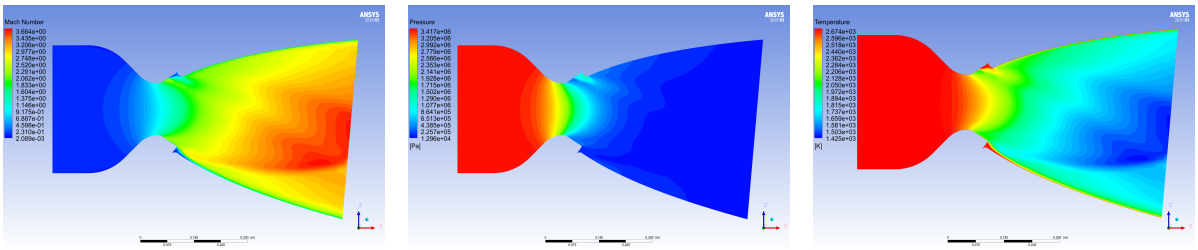

(a) Mach number contour (b) Pressure contour (c) Temperature contour

Figure D.37: Contour plots for Mach number, pressure and temperature for the SSSL nozzle design B at 5 degree thrust vectoring

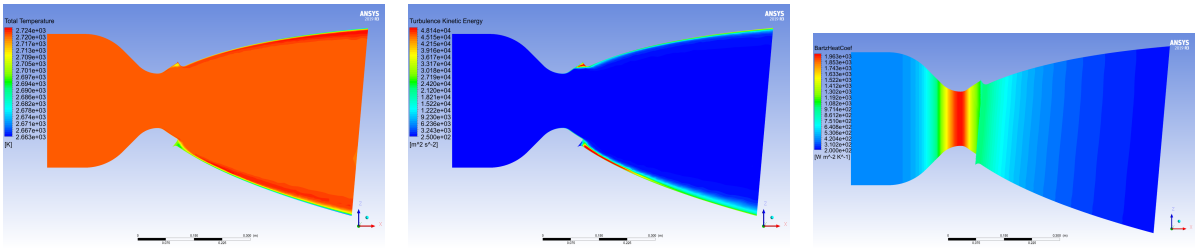

(a) Total temperature contour (b) Turbulence contour (c) Bartz heat coefficient contour

Figure D.38: Contour plots for total temperature, turbulence and Bartz heat coefficient for the SSSL nozzle design B at 5 degree thrust vectoring

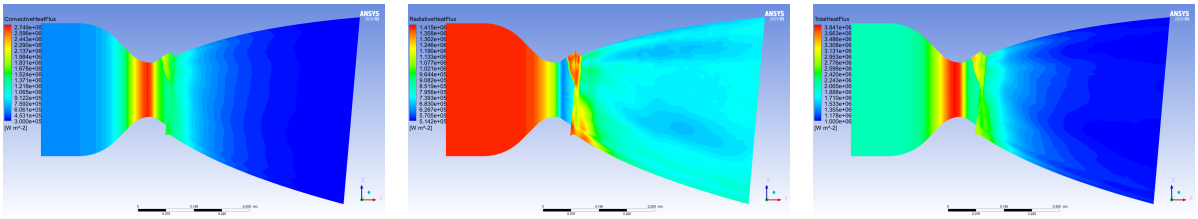

(a) Convective heat flux contour (b) Radiative heat flux contour (c) Total heat flux contour

Figure D.39: Contour plots for convective heat flux, radiative heat flux and total heat flux for the SSSL nozzle design B at 5 degree thrust vectoring

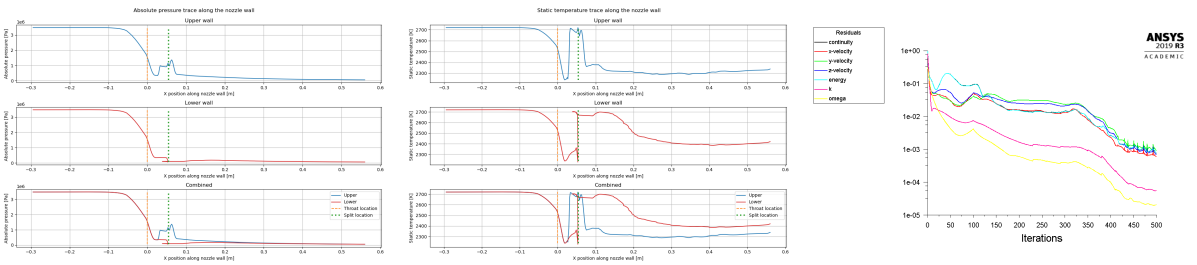

(a) Pressure along the nozzle wall (b) Temperature along the nozzle wall (c) Residual plot

Figure D.40: Temperature and pressure traces along the nozzle wall and residual plot for the SSSL nozzle design B at 5 degree thrust vectoring

D.11. SSSL nozzle design C 5 degree thrust vectoring

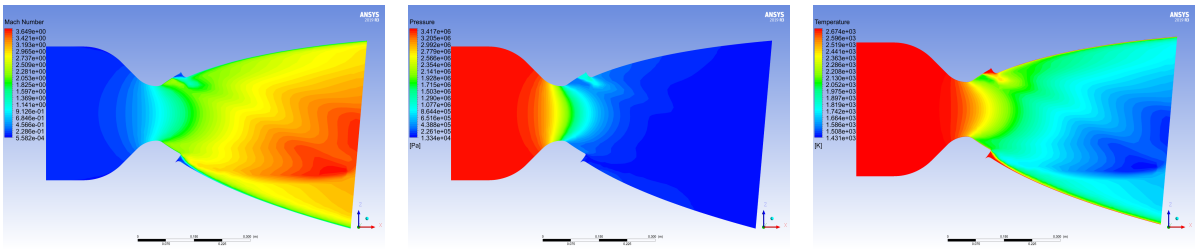

(a) Mach number contour (b) Pressure contour (c) Temperature contour

Figure D.41: Contour plots for Mach number, pressure and temperature for the SSSL nozzle design C at 5 degree thrust vectoring

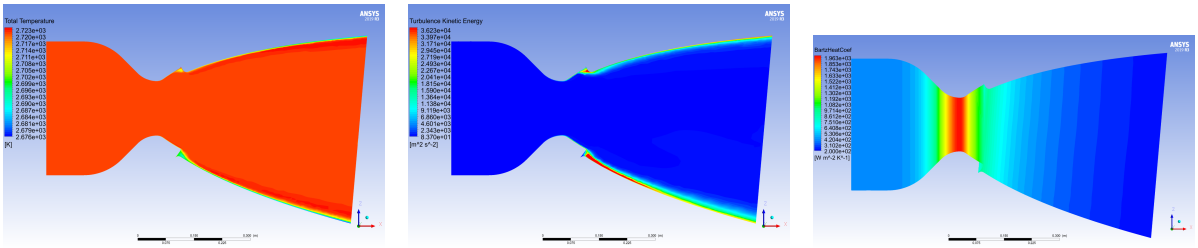

(a) Total temperature contour (b) Turbulence contour (c) Bartz heat coefficient contour

Figure D.42: Contour plots for total temperature, turbulence and Bartz heat coefficient for the SSSL nozzle design C at 5 degree thrust vectoring

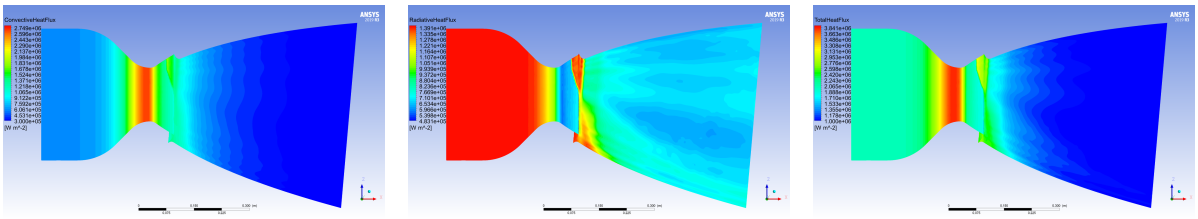

(a) Convective heat flux contour (b) Radiative heat flux contour (c) Total heat flux contour

Figure D.43: Contour plots for convective heat flux, radiative heat flux and total heat flux for the SSSL nozzle design C at 5 degree thrust vectoring

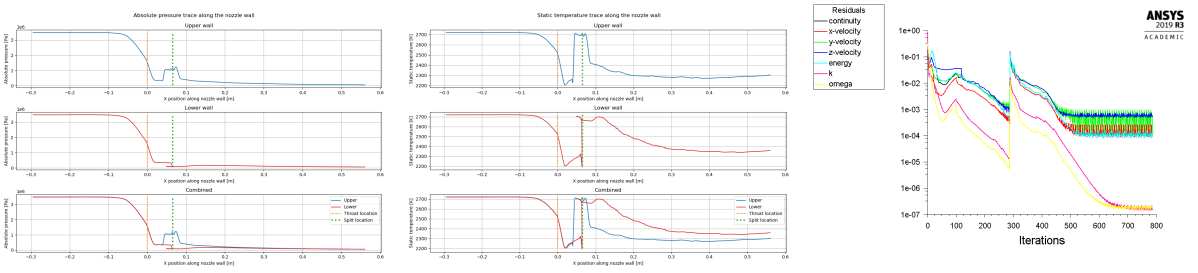

(a) Pressure along the nozzle wall (b) Temperature along the nozzle wall (c) Residual plot

Figure D.44: Temperature and pressure traces along the nozzle wall and residual plot for the SSSL nozzle design C at 5 degree thrust vectoring

D.12. SM nozzle at 5 degree thrust vectoring

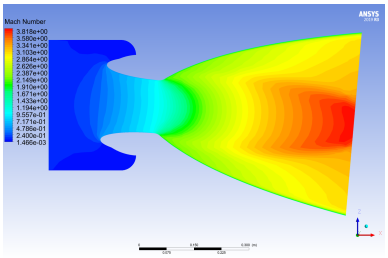

(a) Mach number contour (b) Pressure contour (c) Temperature contour

Figure D.45: Contour plots for Mach number, pressure and temperature for the SM nozzle at 5 degree thrust vectoring

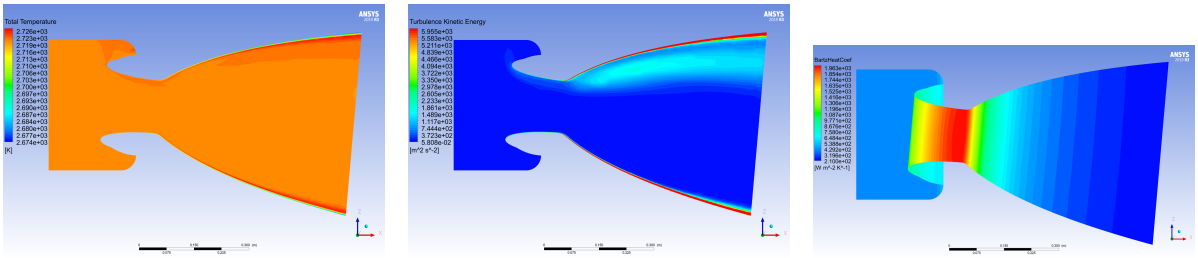

(a) Total temperature contour (b) Turbulence contour (c) Bartz heat coefficient contour

Figure D.46: Contour plots for total temperature, turbulence and Bartz heat coefficient for the SM nozzle at 5 degree thrust vectoring

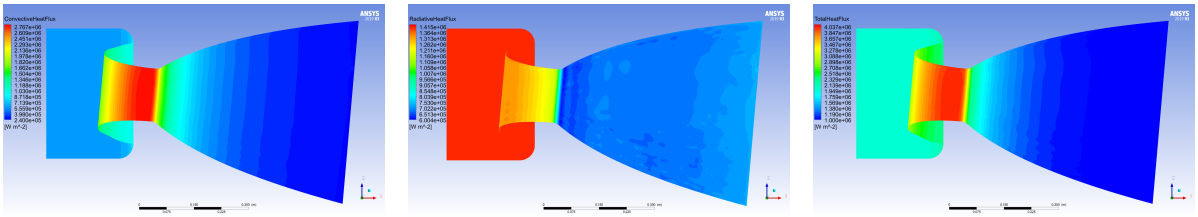

(a) Convective heat flux contour (b) Radiative heat flux contour (c) Total heat flux contour

Figure D.47: Contour plots for convective heat flux, radiative heat flux and total heat flux for the SM nozzle at 5 degree thrust vectoring

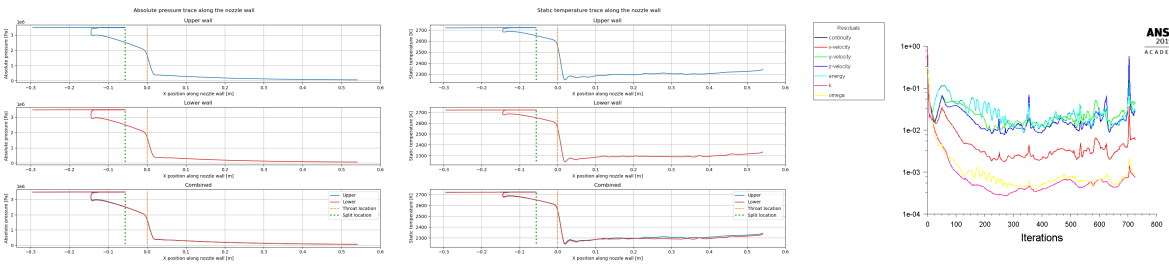

(a) Pressure along the nozzle wall (b) Temperature along the nozzle wall (c) Residual plot

Figure D.48: Temperature and pressure traces along the nozzle wall and residual plot for the SM nozzle at 5 degree thrust vectoring

D.13. SSSL nozzle SSSL-e45 design A 0 degree thrust vectoring

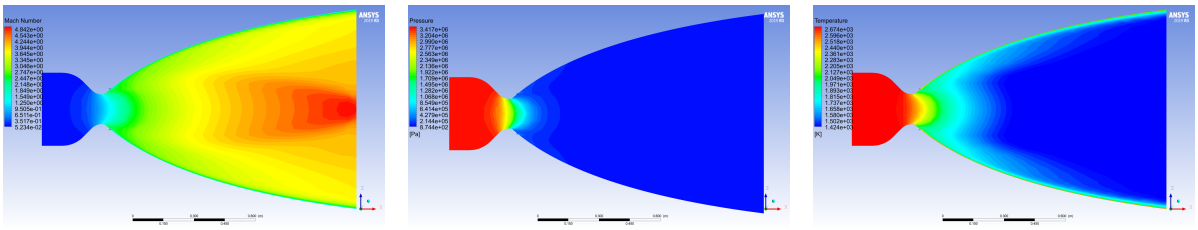

(a) Mach number contour (b) Pressure contour (c) Temperature contour

Figure D.49: Contour plots for Mach number, pressure and temperature for the SSSL nozzle SSSL-e45 design A at 0 degree thrust vectoring

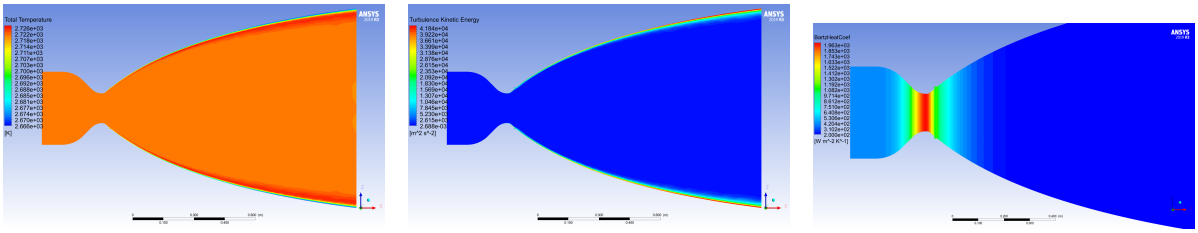

(a) Total temperature contour (b) Turbulence contour (c) Bartz heat coefficient contour

Figure D.50: Contour plots for total temperature, turbulence and Bartz heat coefficient for the SSSL nozzle SSSL-e45 design A at 0 degree thrust vectoring

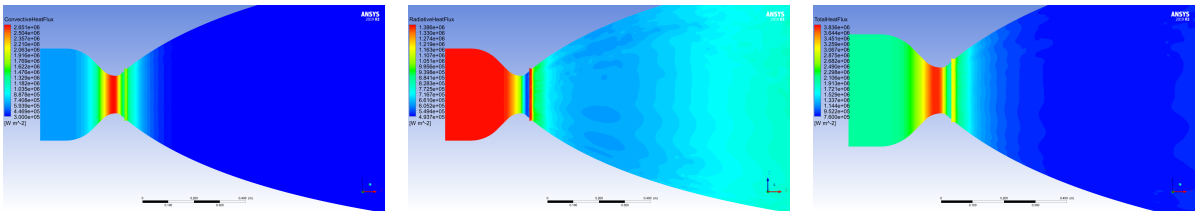

(a) Convective heat flux contour (b) Radiative heat flux contour (c) Total heat flux contour

Figure D.51: Contour plots for convective heat flux, radiative heat flux and total heat flux for the SSSL nozzle SSSL-e45 design A at 0 degree thrust vectoring

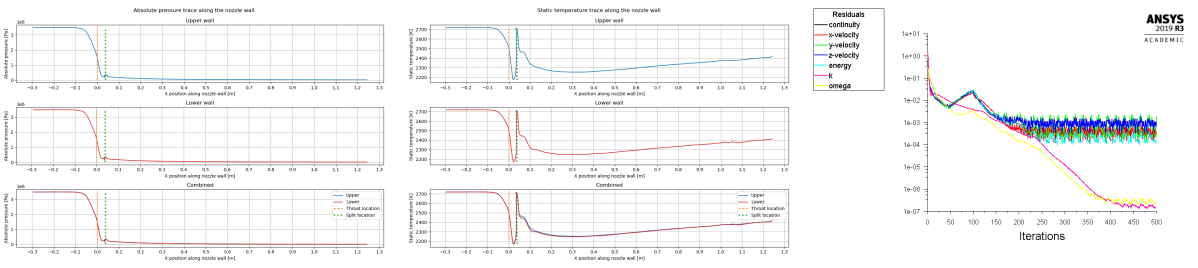

(a) Pressure along the nozzle wall (b) Temperature along the nozzle wall (c) Residual plot

Figure D.52: Temperature and pressure traces along the nozzle wall and residual plot for the SSSL nozzle SSSL-e45 design A at 0 degree thrust vectoring

D.14. SSSL nozzle SSSL-e45 design B 0 degree thrust vectoring

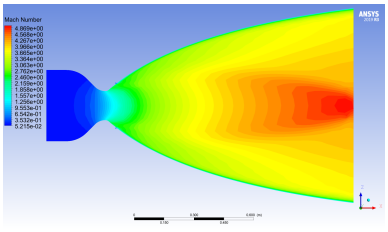

(a) Mach number contour

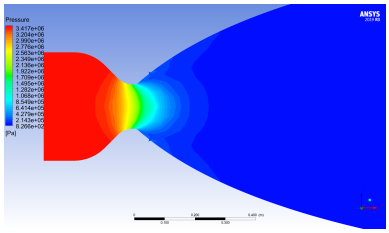

(b) Pressure contour

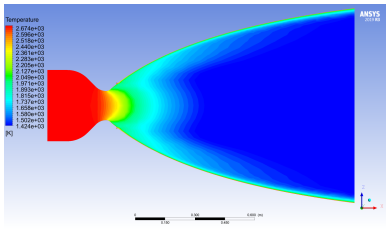

(c) Temperature contour

Figure D.53: Contour plots for Mach number, pressure and temperature for the SSSL nozzle SSSL-e45 design B at 0 degree thrust vectoring

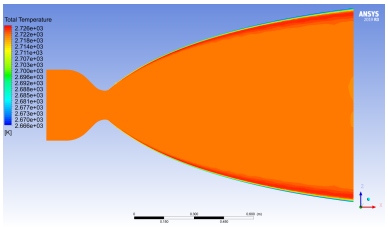

(a) Total temperature contour

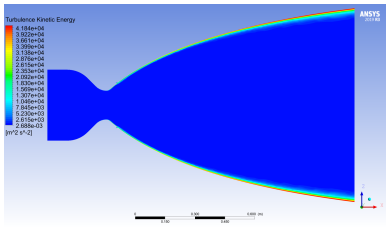

(b) Turbulence contour

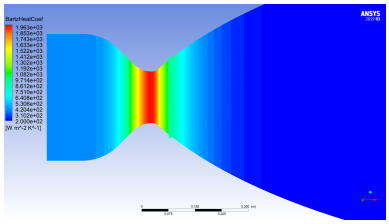

(c) Bartz heat coefficient contour

Figure D.54: Contour plots for total temperature, turbulence and Bartz heat coefficient for the SSSL nozzle SSSL-e45 design B at 0 degree thrust vectoring

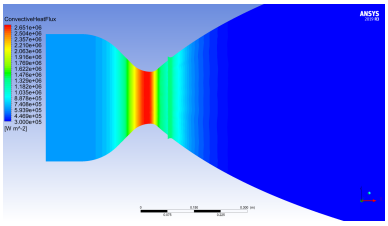

(a) Convective heat flux contour

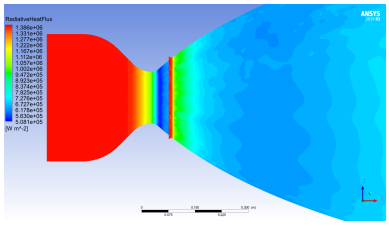

(b) Radiative heat flux contour

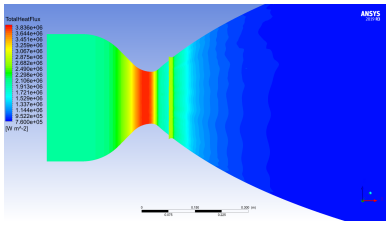

(c) Total heat flux contour

Figure D.55: Contour plots for convective heat flux, radiative heat flux and total heat flux for the SSSL nozzle SSSL-e45 design B at 0 degree thrust vectoring

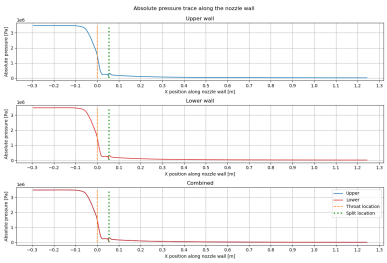

(a) Pressure along the nozzle wall

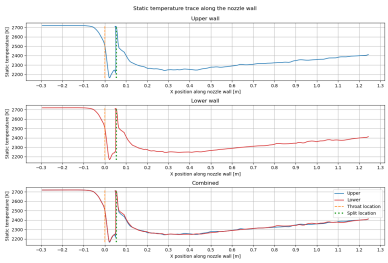

(b) Temperature along the nozzle wall

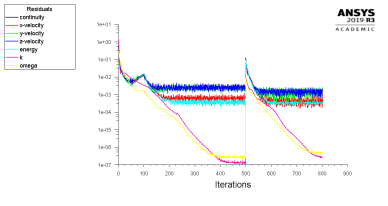

(c) Residual plot

Figure D.56: Temperature and pressure traces along the nozzle wall and residual plot for the SSSL nozzle SSSL-e45 design B at 0 degree thrust vectoring

D.15. SSSL nozzle SSSL-e45 design A 2.5 degree thrust vectoring

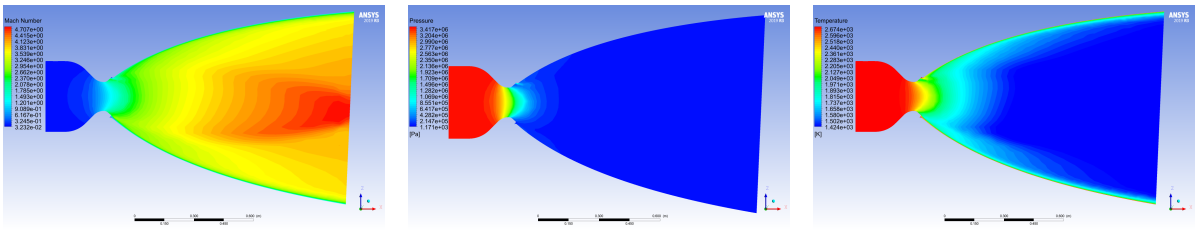

(a) Mach number contour (b) Pressure contour (c) Temperature contour

Figure D.57: Contour plots for Mach number, pressure and temperature for the SSSL nozzle SSSL-e45 design A at 2.5 degree thrust vectoring

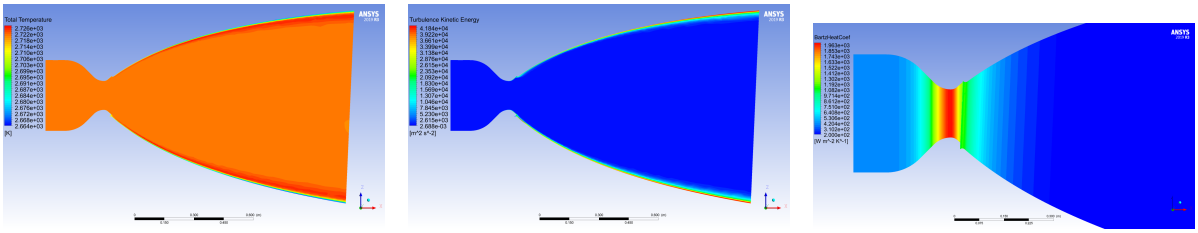

(a) Total temperature contour (b) Turbulence contour (c) Bartz heat coefficient contour

Figure D.58: Contour plots for total temperature, turbulence and Bartz heat coefficient for the SSSL nozzle SSSL-e45 design A at 2.5 degree thrust vectoring

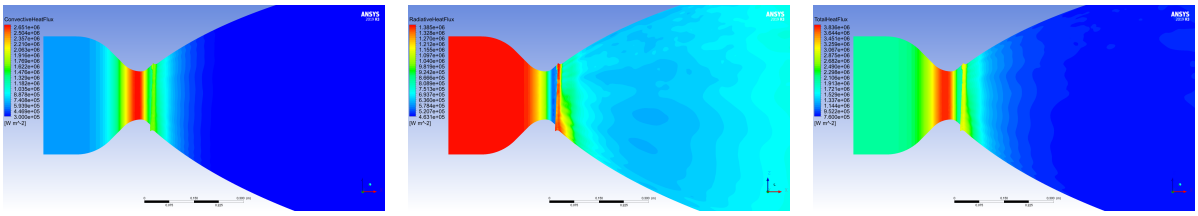

(a) Convective heat flux contour (b) Radiative heat flux contour (c) Total heat flux contour

Figure D.59: Contour plots for convective heat flux, radiative heat flux and total heat flux for the SSSL nozzle SSSL-e45 design A at 2.5 degree thrust vectoring

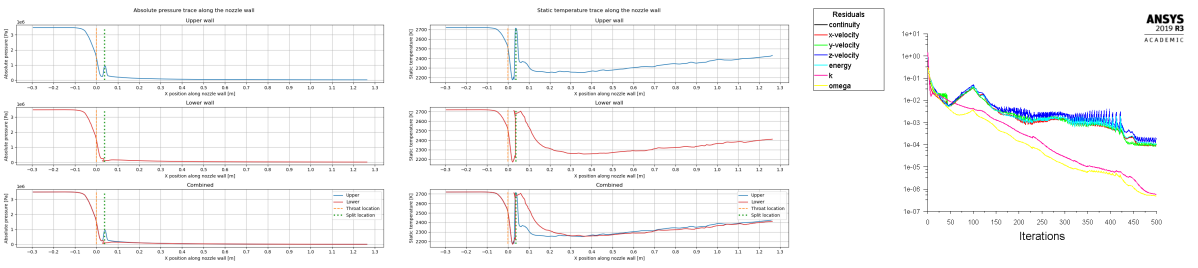

(a) Pressure along the nozzle wall (b) Temperature along the nozzle wall (c) Residual plot

Figure D.60: Temperature and pressure traces along the nozzle wall and residual plot for the SSSL nozzle SSSL-e45 design A at 2.5 degree thrust vectoring

D.16. SSSL nozzle SSSL-e45 design B 2.5 degree thrust vectoring

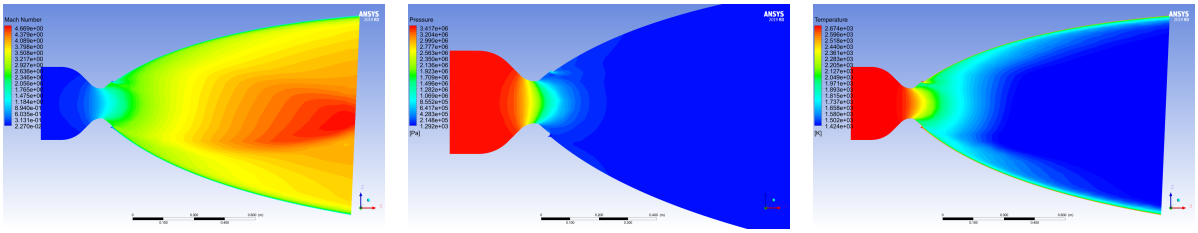

(a) Mach number contour (b) Pressure contour (c) Temperature contour

Figure D.61: Contour plots for Mach number, pressure and temperature for the SSSL nozzle SSSL-e45 design B at 2.5 degree thrust vectoring

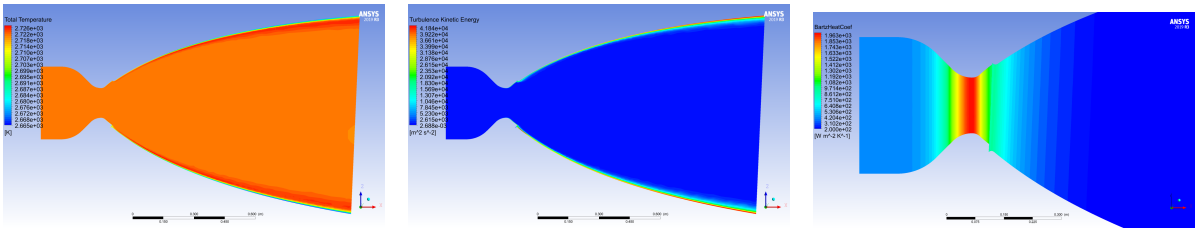

(a) Total temperature contour (b) Turbulence contour (c) Bartz heat coefficient contour

Figure D.62: Contour plots for total temperature, turbulence and Bartz heat coefficient for the SSSL nozzle SSSL-e45 design B at 2.5 degree thrust vectoring

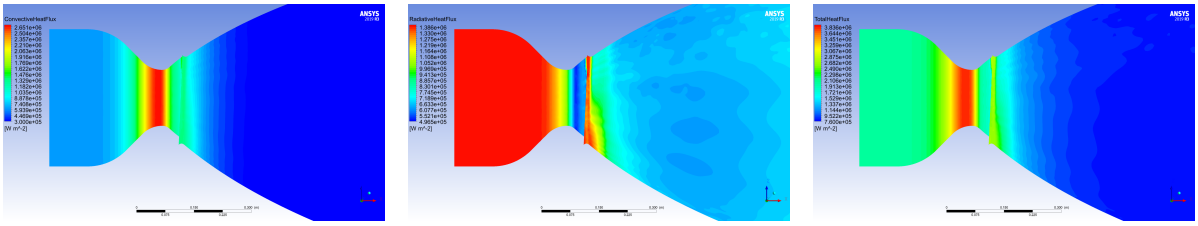

(a) Convective heat flux contour (b) Radiative heat flux contour (c) Total heat flux contour

Figure D.63: Contour plots for convective heat flux, radiative heat flux and total heat flux for the SSSL nozzle SSSL-e45 design B at 2.5 degree thrust vectoring

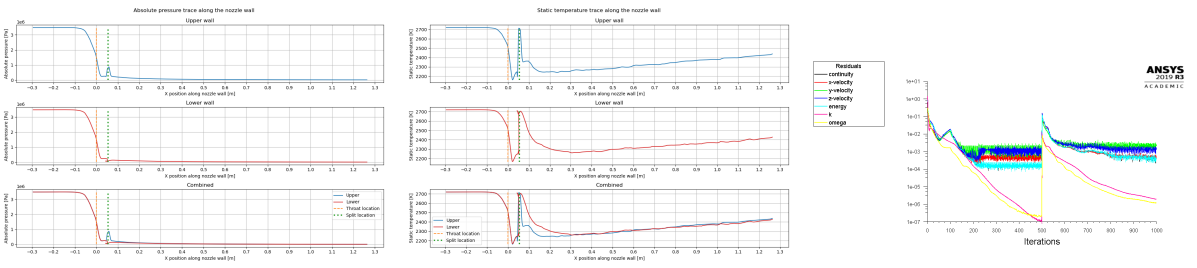

(a) Pressure along the nozzle wall (b) Temperature along the nozzle wall (c) Residual plot

Figure D.64: Temperature and pressure traces along the nozzle wall and residual plot for the SSSL nozzle SSSL-e45 design B at 2.5 degree thrust vectoring

D.17. SSSL nozzle SSSL-e45 design A 5 degree thrust vectoring

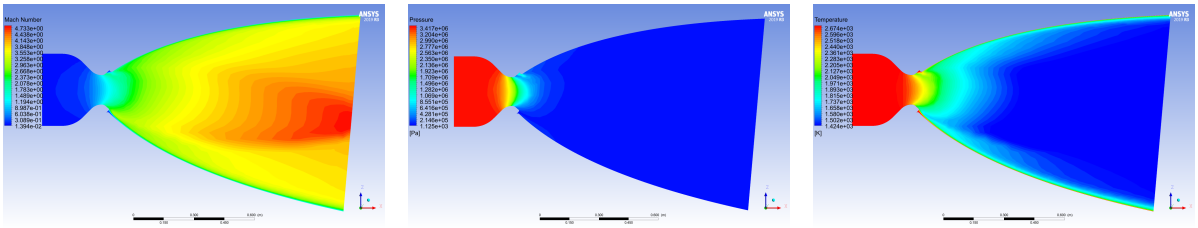

(a) Mach number contour (b) Pressure contour (c) Temperature contour

Figure D.65: Contour plots for Mach number, pressure and temperature for the SSSL nozzle SSSL-e45 design A at 5 degree thrust vectoring

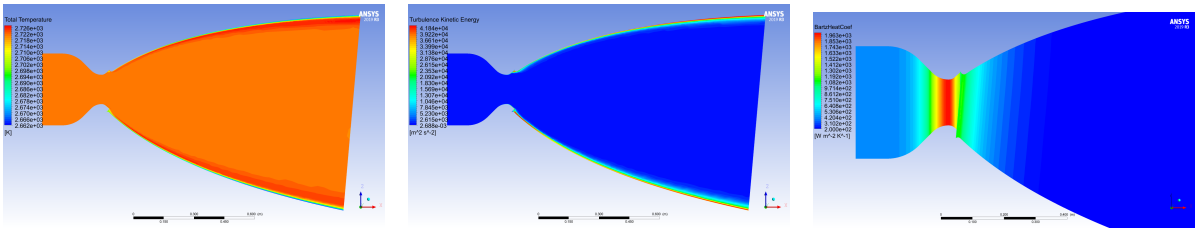

(a) Total temperature contour (b) Turbulence contour (c) Bartz heat coefficient contour

Figure D.66: Contour plots for total temperature, turbulence and Bartz heat coefficient for the SSSL nozzle SSSL-e45 design A at 5 degree thrust vectoring

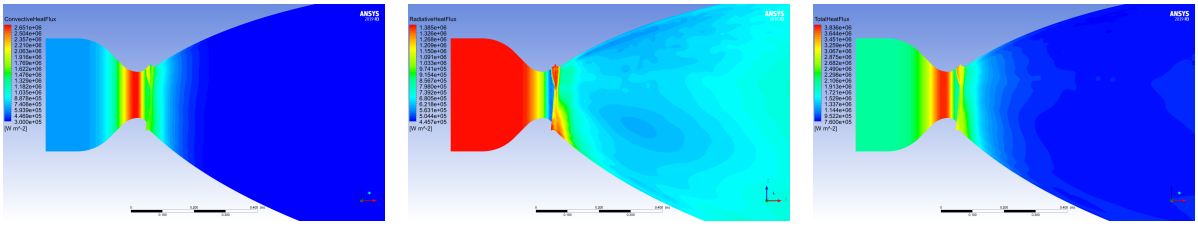

(a) Convective heat flux contour (b) Radiative heat flux contour (c) Total heat flux contour

Figure D.67: Contour plots for convective heat flux, radiative heat flux and total heat flux for the SSSL nozzle SSSL-e45 design A at 5 degree thrust vectoring

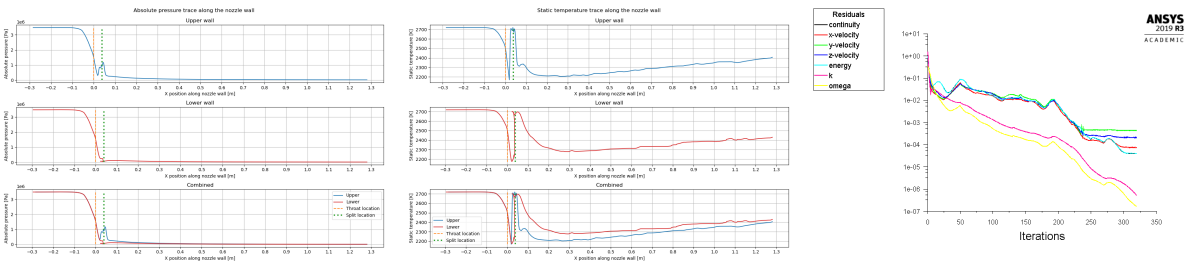

(a) Pressure along the nozzle wall (b) Temperature along the nozzle wall (c) Residual plot

Figure D.68: Temperature and pressure traces along the nozzle wall and residual plot for the SSSL nozzle SSSL-e45 design A at 5 degree thrust vectoring

D.18. SSSL nozzle SSSL-e45 design B 5 degree thrust vectoring

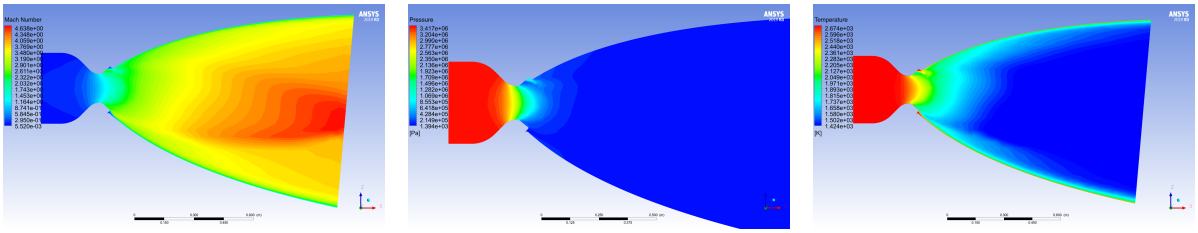

(a) Mach number contour (b) Pressure contour (c) Temperature contour

Figure D.69: Contour plots for Mach number, pressure and temperature for the SSSL nozzle SSSL-e45 design B at 5 degree thrust vectoring

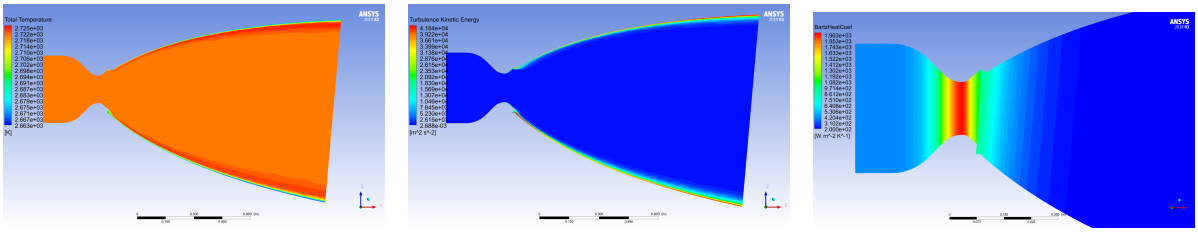

(a) Total temperature contour (b) Turbulence contour (c) Bartz heat coefficient contour

Figure D.70: Contour plots for total temperature, turbulence and Bartz heat coefficient for the SSSL nozzle SSSL-e45 design B at 5 degree thrust vectoring

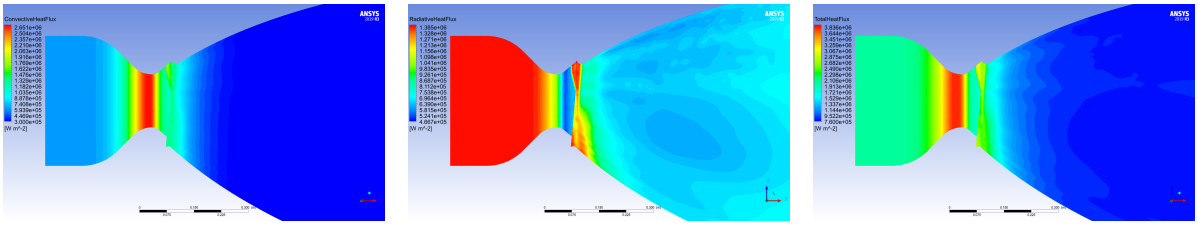

(a) Convective heat flux contour (b) Radiative heat flux contour (c) Total heat flux contour

Figure D.71: Contour plots for convective heat flux, radiative heat flux and total heat flux for the SSSL nozzle SSSL-e45 design B at 5 degree thrust vectoring

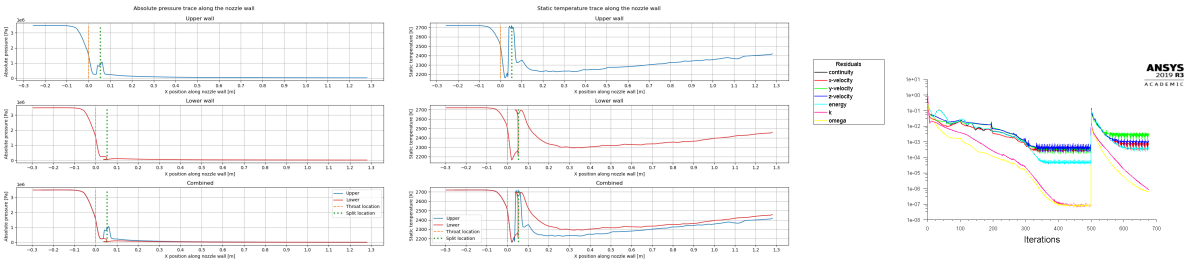

(a) Pressure along the nozzle wall (b) Temperature along the nozzle wall (c) Residual plot

Figure D.72: Temperature and pressure traces along the nozzle wall and residual plot for the SSSL nozzle SSSL-e45 design B at 5 degree thrust vectoring

D.19. SSSL nozzle SSSL-e6 design A 0 degree thrust vectoring

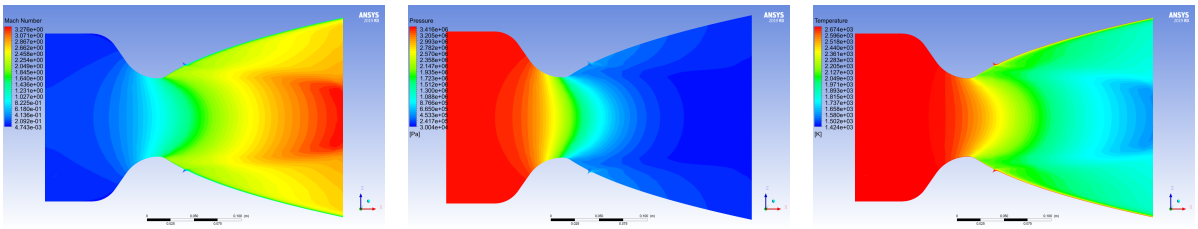

(a) Mach number contour (b) Pressure contour (c) Temperature contour

Figure D.73: Contour plots for Mach number, pressure and temperature for the SSSL nozzle SSSL-e6 design A at 0 degree thrust vectoring

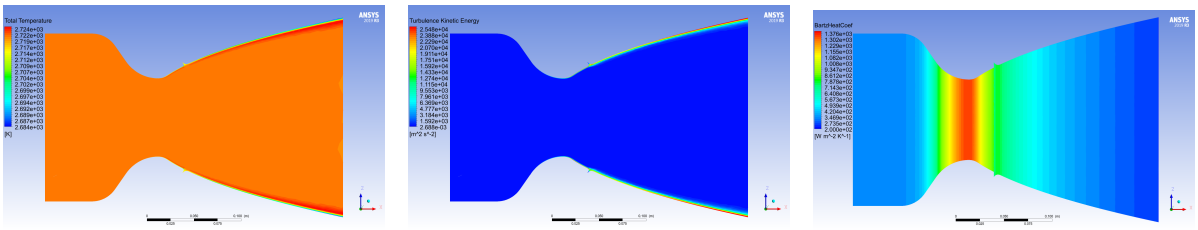

(a) Total temperature contour (b) Turbulence contour (c) Bartz heat coefficient contour

Figure D.74: Contour plots for total temperature, turbulence and Bartz heat coefficient for the SSSL nozzle SSSL-e6 design A at 0 degree thrust vectoring

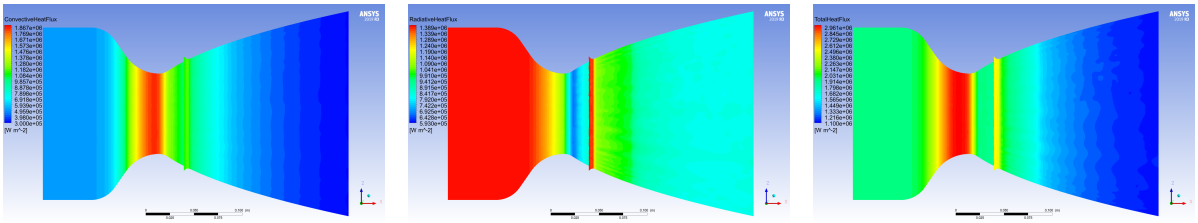

(a) Convective heat flux contour (b) Radiative heat flux contour (c) Total heat flux contour

Figure D.75: Contour plots for convective heat flux, radiative heat flux and total heat flux for the SSSL nozzle SSSL-e6 design A at 0 degree thrust vectoring

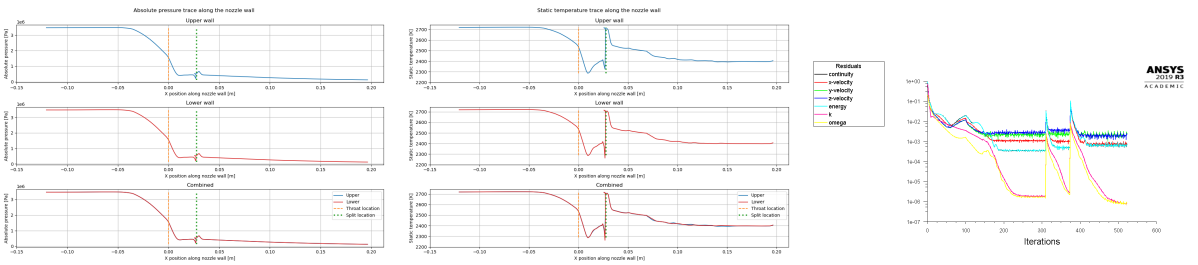

(a) Pressure along the nozzle wall (b) Temperature along the nozzle wall (c) Residual plot

Figure D.76: Temperature and pressure traces along the nozzle wall and residual plot for the SSSL nozzle SSSL-e6 design A at 0 degree thrust vectoring

D.20. SSSL nozzle SSSL-e6 design B 0 degree thrust vectoring

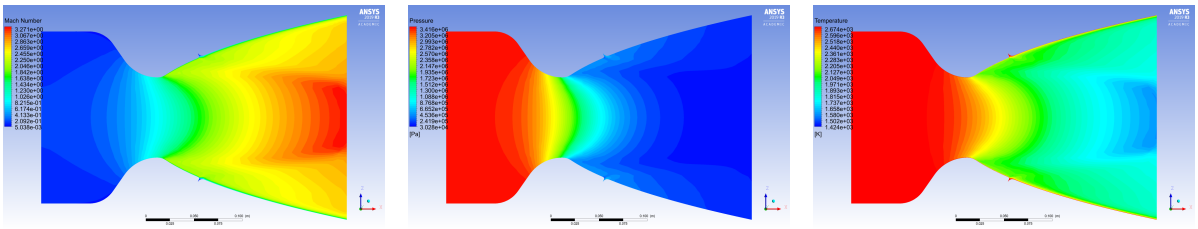

(a) Mach number contour (b) Pressure contour (c) Temperature contour

Figure D.77: Contour plots for Mach number, pressure and temperature for the SSSL nozzle SSSL-e6 design B at 0 degree thrust vectoring

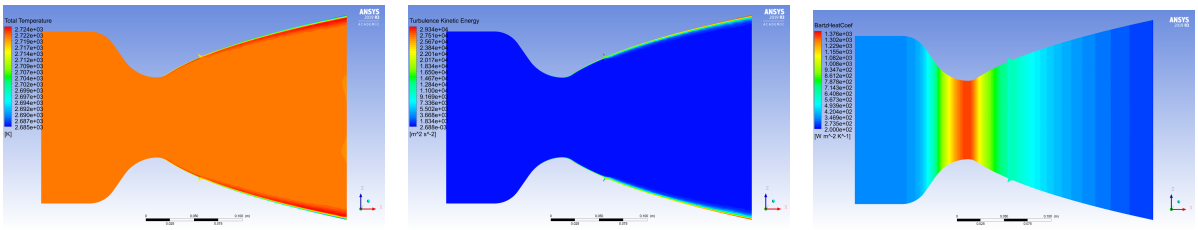

(a) Total temperature contour (b) Turbulence contour (c) Bartz heat coefficient contour

Figure D.78: Contour plots for total temperature, turbulence and Bartz heat coefficient for the SSSL nozzle SSSL-e6 design B at 0 degree thrust vectoring

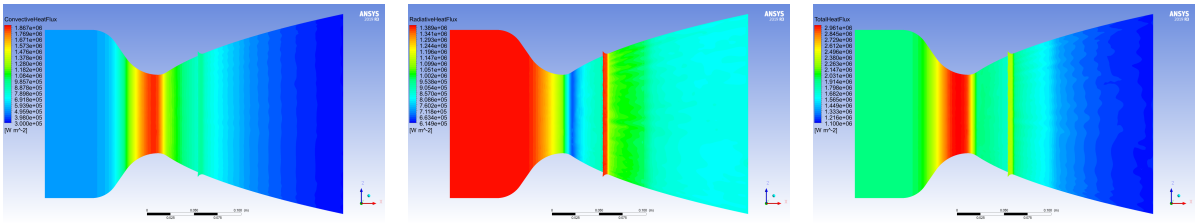

(a) Convective heat flux contour (b) Radiative heat flux contour (c) Total heat flux contour

Figure D.79: Contour plots for convective heat flux, radiative heat flux and total heat flux for the SSSL nozzle SSSL-e6 design B at 0 degree thrust vectoring

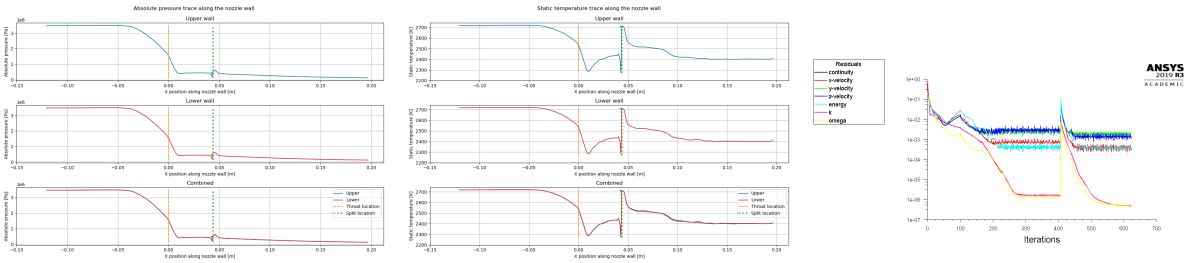

(a) Pressure along the nozzle wall (b) Temperature along the nozzle wall (c) Residual plot

Figure D.80: Temperature and pressure traces along the nozzle wall and residual plot for the SSSL nozzle SSSL-e6 design B at 0 degree thrust vectoring

D.21. SSSL nozzle SSSL-e6 design A 2.5 degree thrust vectoring

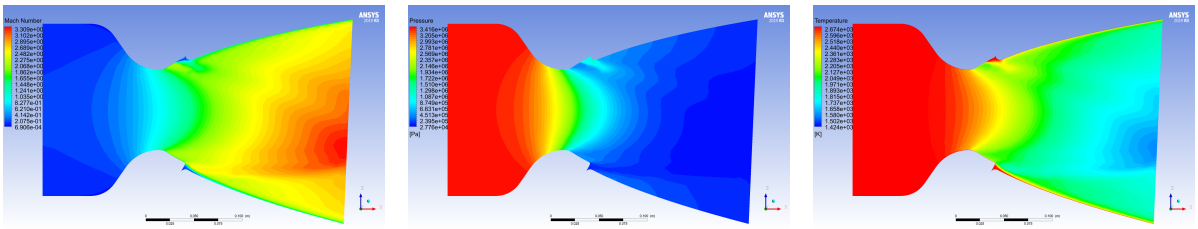

(a) Mach number contour (b) Pressure contour (c) Temperature contour

Figure D.81: Contour plots for Mach number, pressure and temperature for the SSSL nozzle SSSL-e6 design A at 2.5 degree thrust vectoring

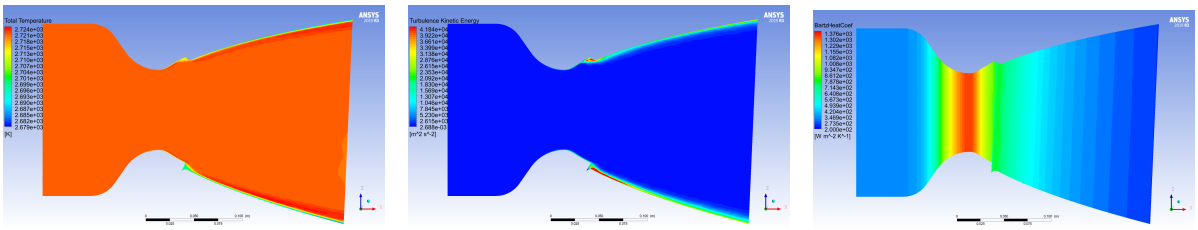

(a) Total temperature contour (b) Turbulence contour (c) Bartz heat coefficient contour

Figure D.82: Contour plots for total temperature, turbulence and Bartz heat coefficient for the SSSL nozzle SSSL-e6 design A at 2.5 degree thrust vectoring

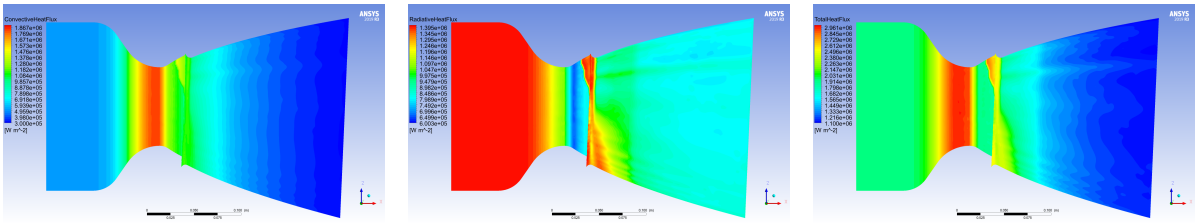

(a) Convective heat flux contour (b) Radiative heat flux contour (c) Total heat flux contour

Figure D.83: Contour plots for convective heat flux, radiative heat flux and total heat flux for the SSSL nozzle SSSL-e6 design A at 2.5 degree thrust vectoring

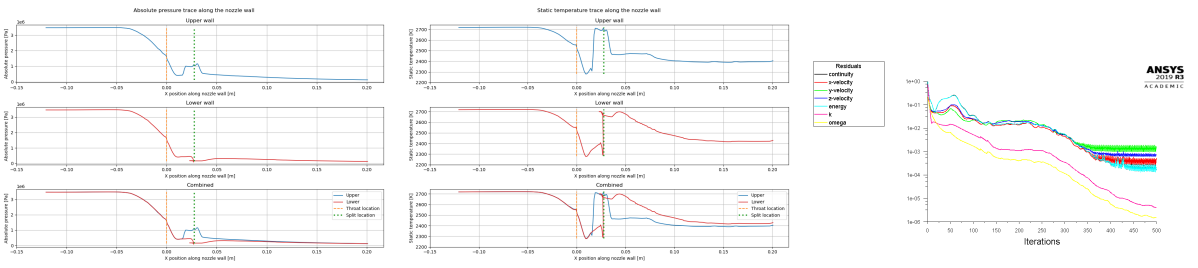

(a) Pressure along the nozzle wall (b) Temperature along the nozzle wall (c) Residual plot

Figure D.84: Temperature and pressure traces along the nozzle wall and residual plot for the SSSL nozzle SSSL-e6 design A at 2.5 degree thrust vectoring

D.22. SSSL nozzle SSSL-e6 design B 2.5 degree thrust vectoring

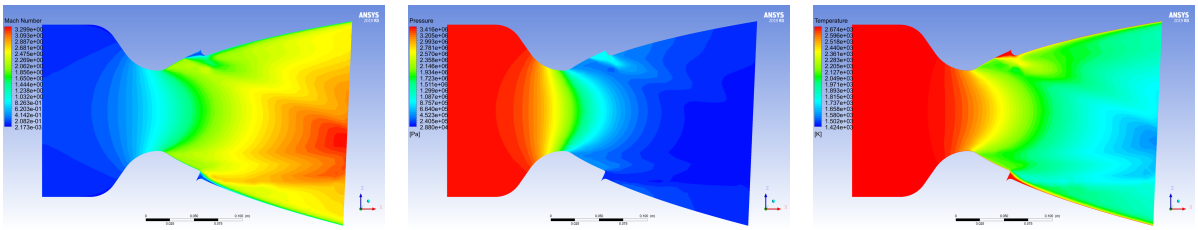

(a) Mach number contour (b) Pressure contour (c) Temperature contour

Figure D.85: Contour plots for Mach number, pressure and temperature for the SSSL nozzle SSSL-e6 design B at 2.5 degree thrust vectoring

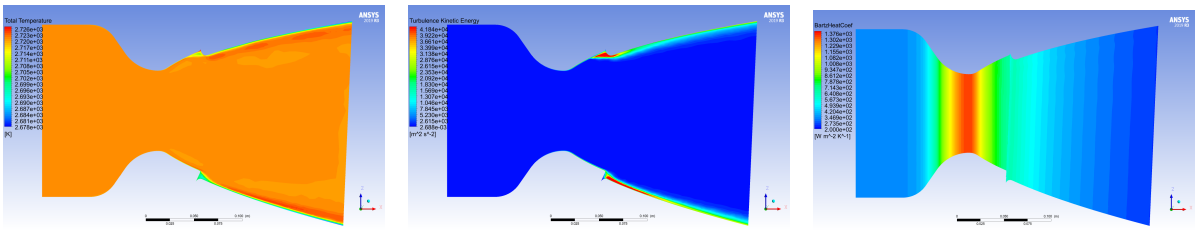

(a) Total temperature contour (b) Turbulence contour (c) Bartz heat coefficient contour

Figure D.86: Contour plots for total temperature, turbulence and Bartz heat coefficient for the SSSL nozzle SSSL-e6 design B at 2.5 degree thrust vectoring

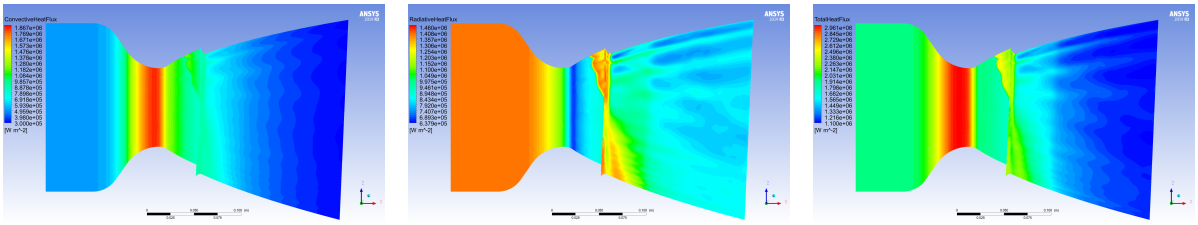

(a) Convective heat flux contour (b) Radiative heat flux contour (c) Total heat flux contour

Figure D.87: Contour plots for convective heat flux, radiative heat flux and total heat flux for the SSSL nozzle SSSL-e6 design B at 2.5 degree thrust vectoring

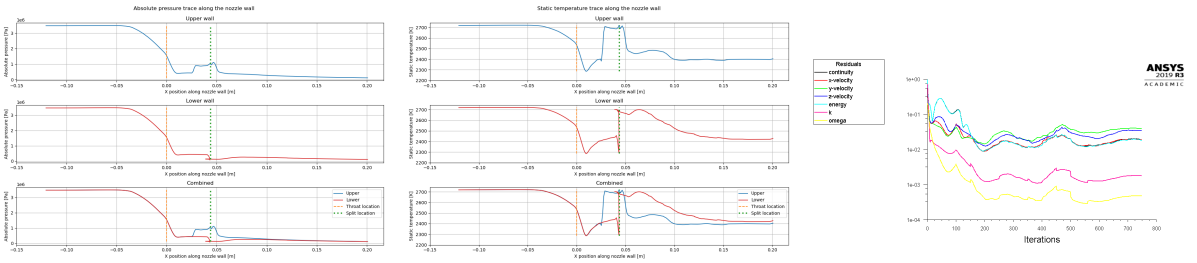

(a) Pressure along the nozzle wall (b) Temperature along the nozzle wall (c) Residual plot

Figure D.88: Temperature and pressure traces along the nozzle wall and residual plot for the SSSL nozzle SSSL-e6 design B at 2.5 degree thrust vectoring

D.23. SSSL nozzle SSSL-e6 design A 5 degree thrust vectoring

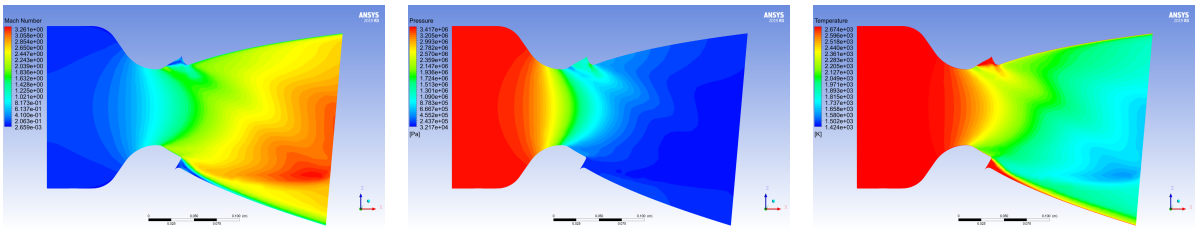

(a) Mach number contour (b) Pressure contour (c) Temperature contour

Figure D.89: Contour plots for Mach number, pressure and temperature for the SSSL nozzle SSSL-e6 design A at 5 degree thrust vectoring

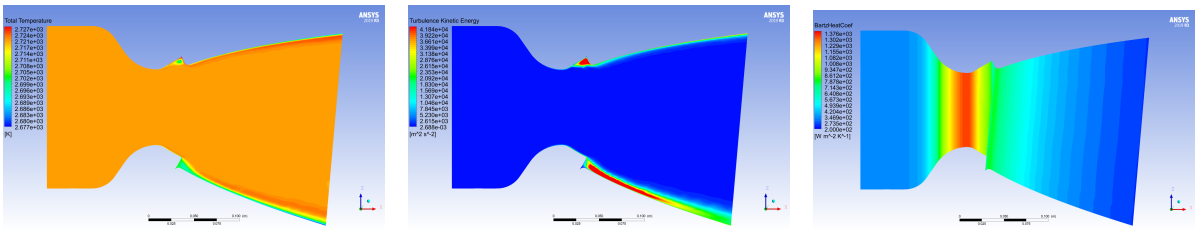

(a) Total temperature contour (b) Turbulence contour (c) Bartz heat coefficient contour

Figure D.90: Contour plots for total temperature, turbulence and Bartz heat coefficient for the SSSL nozzle SSSL-e6 design A at 5 degree thrust vectoring

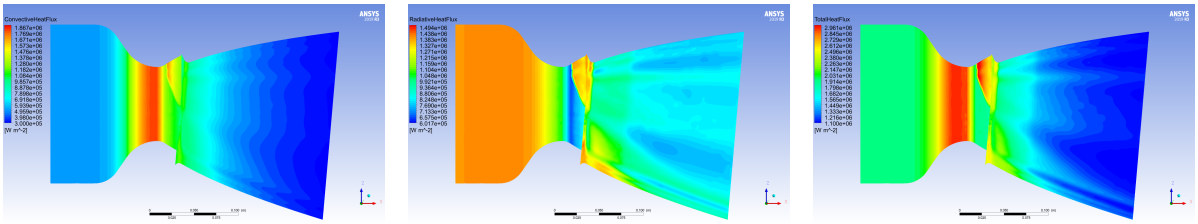

(a) Convective heat flux contour (b) Radiative heat flux contour (c) Total heat flux contour

Figure D.91: Contour plots for convective heat flux, radiative heat flux and total heat flux for the SSSL nozzle SSSL-e6 design A at 5 degree thrust vectoring

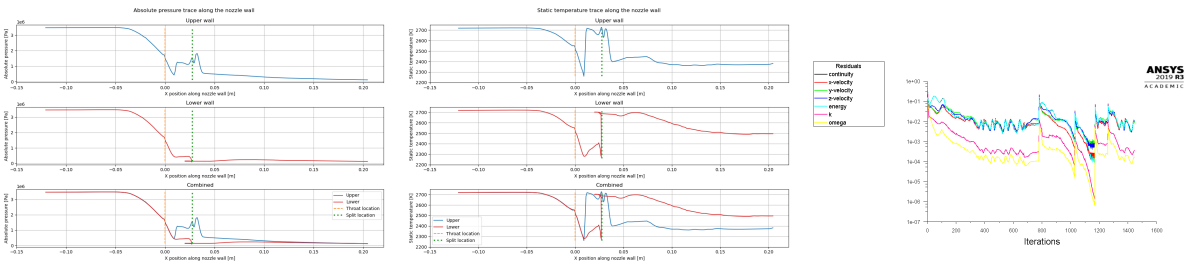

(a) Pressure along the nozzle wall (b) Temperature along the nozzle wall (c) Residual plot

Figure D.92: Temperature and pressure traces along the nozzle wall and residual plot for the SSSL nozzle SSSL-e6 design A at 5 degree thrust vectoring

D.24. SSSL nozzle SSSL-e6 design B 5 degree thrust vectoring

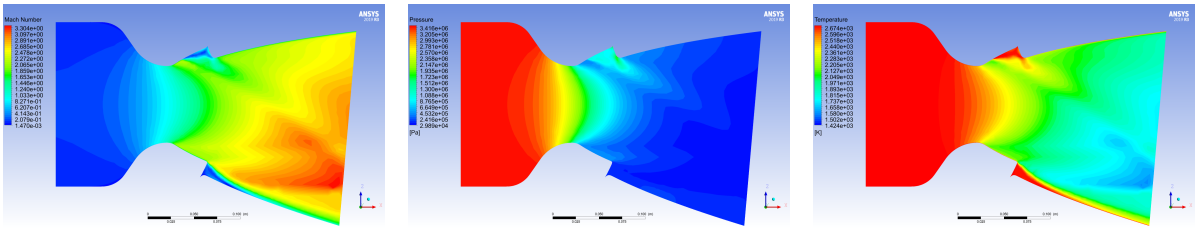

(a) Mach number contour (b) Pressure contour (c) Temperature contour

Figure D.93: Contour plots for Mach number, pressure and temperature for the SSSL nozzle SSSL-e6 design B at 5 degree thrust vectoring

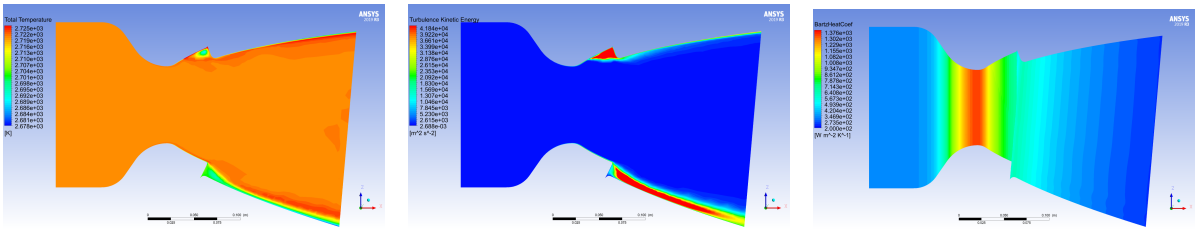

(a) Total temperature contour (b) Turbulence contour (c) Bartz heat coefficient contour

Figure D.94: Contour plots for total temperature, turbulence and Bartz heat coefficient for the SSSL nozzle SSSL-e6 design B at 5 degree thrust vectoring

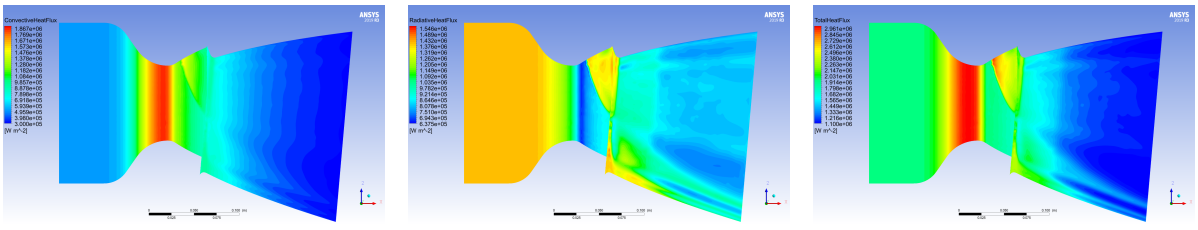

(a) Convective heat flux contour (b) Radiative heat flux contour (c) Total heat flux contour

Figure D.95: Contour plots for convective heat flux, radiative heat flux and total heat flux for the SSSL nozzle SSSL-e6 design B at 5 degree thrust vectoring

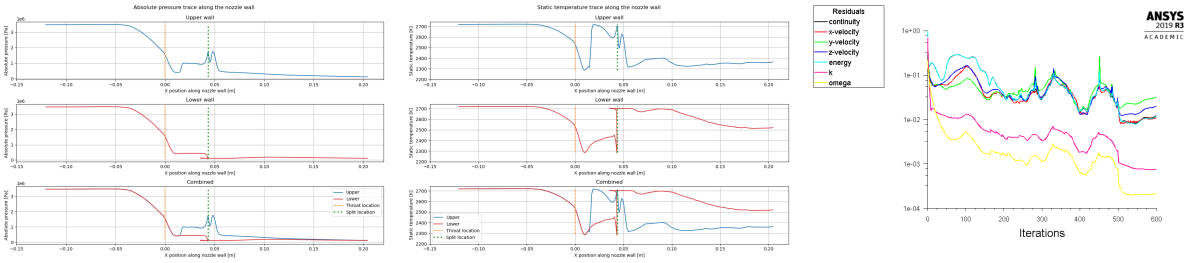

(a) Pressure along the nozzle wall (b) Temperature along the nozzle wall (c) Residual plot

Figure D.96: Temperature and pressure traces along the nozzle wall and residual plot for the SSSL nozzle SSSL-e6 design B at 5 degree thrust vectoring